UNIVERSITY OF SOUTHAMPTON
FACULTY OF ENGINEERING AND APPLIED SCIENCE
INSTITUTE OF SOUND AND VIBRATION RESEARCH

THE NON-LINEAR MODELLING OF SQUEEZE FILM DAMPED ROTOR-DYNAMIC SYSTEMS: AN EFFICIENT INTEGRATED APPROACH

by

Philip Bonello

A thesis submitted for the degree of
Doctor of Philosophy

July 2002

UNIVERSITY OF SOUTHAMPTON

ABSTRACT

FACULTY OF ENGINEERING AND APPLIED SCIENCE
INSTITUTE OF SOUND AND VIBRATION RESEARCH

Doctor of Philosophy

THE NON-LINEAR MODELLING OF SQUEEZE FILM DAMPED ROTOR-DYNAMIC SYSTEMS: AN EFFICIENT INTEGRATED APPROACH

by Philip Bonello

Squeeze film dampers (SFDs) are non-linear elements used in rotor assemblies such as aero-engines to attenuate vibrations and transmitted forces, and to improve stability. However, undesirable non-linear side effects under rotating unbalance excitation necessitate an effective predictive tool for the resulting dynamics. The main contribution of this thesis is the development of an efficient integrated non-linear modelling technique for the solution of the unbalance response problem. It consists of the following three complementary blocks, each of which is tractable to practical systems with many degrees of freedom:

(1) A Receptance Harmonic Balance method for the determination of periodic solutions. In this method, the receptance functions of the rotating linear part of the system are used in the non-linear analysis of the complete system.

(2) Stability analysis of these periodic solutions. This is done by applying Floquet theory to a limited number of the perturbed modal equations of the system.

(3) Numerical integration of the modal equations, when necessary.

With such an approach, linear rotor-dynamic software packages used in industry can be used to analyse the linear subsystem for receptance functions and modal parameters. The latter quantities can then be used in a detailed non-linear analysis of the whole system that can be implemented using standard mathematical software. The integrated model is tested on three squeeze film damped rotor-dynamic systems, of increasing complexity. The SFD forces are obtained from an extant model for the SFD that assumes a short incompressible film that cavitates at absolute zero pressure. In each case studied, excellent correlation between the results from the above mentioned modelling blocks is achieved. Depending on the operating conditions, the systems considered are shown to exhibit undesirable non-linear phenomena such as: amplitude jumps; periodic motion containing sub-harmonics and their integer multiples; quasi-periodic motion containing combination frequencies; motion that appears to be chaotic; and sub-critical super-harmonic resonance. The overall correlation with experiment is also good. The validated integrated model is thus shown to be a valuable tool in both the study and the design of squeeze film damped rotating systems.

ACKNOWLEDGEMENTS

I would like to thank:

- My supervisors, Professor Michael J. Brennan and Emeritus Professor Roy Holmes, for all their help and advice during the course of this project.
- All those members of the University technical staff who helped in setting up the experimental facilities, particularly Mr. Peter Wheeler (School of Engineering Sciences) for his useful advice.
- The Institute of Sound and Vibration Research and the Faculty of Engineering and Applied Science, who provided the scholarship for this research.
- Universities UK, who partially supported this research through the Overseas Research Student scholarship.
- Last but not least, family and friends, for their support, particularly my partner Richard who has put up with me during these last three years, and my mother.

CONTENTS

GLOSSARY OF TERMS

DEFINITION OF COMMONLY USED TERMS

Attractor	A bounded region in state space to which regions of initial conditions shrink as time progresses.
Bifurcation	A qualitative change in the dynamics that occurs as a system control parameter is changed.
Dynamical system	A continuous-time dynamical system is a physical system whose dynamics can be modelled by a set of first order differential equations.
Equilibrium solution	Solutions to the dynamical system equations that are non-transient i.e. exhibit long-term steady-state behaviour.
Forced system	Dynamical system subjected to external time-varying excitation.
Journal	Ring fixed to the outer race of a rolling-element bearing and mechanically prevented from rotating relative to the shaft axis. Forms inner surface of SFD.
K-frequency quasi-periodic motion	Motion that is composed of a mixture of K periodic motions that have irrationally related fundamental frequencies.
Linear subsystem	Linear part of system, specifically, the system minus the squeeze film dampers.
Non-linear degrees of freedom	Those degrees of freedom of the linear subsystem that are associated with the non-linear forces.
Receptance	Frequency response function that, for a given frequency, relates the force/moment applied in the direction of one degree of freedom with the consequent response of another degree of freedom.
Sprung SFD	SFD with parallel retainer spring.
Squeeze film damper (SFD)	Annulus of oil filling the clearance between the journal and the inner surface of the bearing housing.
Stability	An equilibrium solution is said to be stable if small linearised perturbations from it decay to zero as time progresses.

State space	A space that is used to specify the instantaneous values of the dynamical variables (displacements and velocities) and (for a forced system) the associated value of the independent variable (i.e. time).
Unsupported SFD	An unsprung SFD in which the journal is fully eccentric within the radial clearance under the static load in the static condition.

COMMONLY USED ABBREVIATIONS

EO	Engine order: 1EO denotes the synchronous frequency component in the frequency spectrum of the vibration time history
DFT	Discrete Fourier transform, computed by the fast Fourier transform (FFT) algorithm
FE	Finite element
MI	Mechanical impedance
RHB	Receptance harmonic balance
SFD	Squeeze film damper

LIST OF SYMBOLS FOR PRINCIPAL PARAMETERS

The following list is not exhaustive. However, all parameters are defined in the main text. Greek letter symbols are listed towards the end. Vectors and matrices are in bold typeface (vectors in lower case and matrices in upper case).

$a_{XB}^{(s)}$, $a_{YB}^{(s)}$, $a_{XJ}^{(s)}$, $a_{YJ}^{(s)}$...etc.	cosine coefficients in Fourier expansions of X_B, Y_B, X_J, Y_J...etc.
$A_{PQ}^{(xr)}$, $A_{PQ}^{(yr)}$	r^{th} modal constants of rotor receptances $\alpha_{PQ}(\omega)$, $\beta_{PQ}(\omega)$ respectively, equal to $\phi_P^{(xr)}\phi_Q^{(xr)}$, $\phi_P^{(yr)}\phi_Q^{(yr)}$ (kg^{-1})
$A_{B_iB_j}^{(Sxr)}$, $A_{B_iB_j}^{(Syr)}$	r^{th} modal constants of receptances $\alpha_{B_iB_j}(\omega)$, $\beta_{B_iB_j}(\omega)$ respectively, equal to $\phi_{B_i}^{(Sxr)}\phi_{B_j}^{(Sxr)}$, $\phi_{B_i}^{(Syr)}\phi_{B_j}^{(Syr)}$ (kg^{-1})
$\mathbf{A_0}$	zero frequency value of accelerance matrix **A**, eq. (5.27)
$b_{XB}^{(s)}$, $b_{YB}^{(s)}$, $b_{XJ}^{(s)}$, $b_{YJ}^{(s)}$...etc.	sine coefficients in Fourier expansions of X_B, Y_B, X_J, Y_J...etc.

$\hat{B}$	non-dimensional viscosity parameter used in Chapter 4, defined in eq. (4.21a)
c	radial clearance of damper (m)
d_{groove}	depth of oil supply groove of SFD (m)
d_{gap}	width of gap at outlet of SFD (m)
$\mathbf{D}$	diagonal matrix of squares of natural frequencies (eq. (5.31))
e	instantaneous eccentricity of J from B (m)
e_{0x}, e_{0y}	static offset of J from B in x and y directions respectively (m)
$\mathbf{f}$	$P\times 1$ vector of forces external to linear subsystem
$\mathbf{f}_{\mathrm{L}}$	$P\times 1$ vector of unbalance forces and static loads (if taken into account)
$\mathbf{f}_{\mathrm{N}}$	for RHB, $\mathbf{f}_{\mathrm{N}}$ comprises the non-linear (i.e. SFD) forces only; for the time domain analysis, $\mathbf{f}_{\mathrm{N}}$ generally comprises all damping forces (linear, as well as non-linear) and any gyroscopic moments
$\tilde{\mathbf{f}}$	complex amplitude of $\mathbf{f}$ for $\mathbf{f}$ harmonic (eq. (5.6b))
$\mathbf{f}_{\mathrm{C}}$, $\mathbf{f}_{\mathrm{S}}$	cosine and sine coefficient vectors of $\mathbf{f}$ for $\mathbf{f}$ harmonic (eq. (5.6b))
$\bar{\mathbf{f}}$, $\mathbf{f}_{\mathrm{C}}^{(s)}$, $\mathbf{f}_{\mathrm{S}}^{(s)}$	Fourier coefficient vectors of $\mathbf{f}$
$\bar{\mathbf{f}}_{\mathrm{N}}$, $\mathbf{f}_{\mathrm{NC}}^{(s)}$, $\mathbf{f}_{\mathrm{NS}}^{(s)}$	Fourier coefficient vectors of $\mathbf{f}_{\mathrm{N}}$
$g\left(\hat{\mathbf{v}},\hat{\Omega},\sigma\right)$	arc-length function, eq. (5.23)
$\mathbf{g}$	vector of "linear" degrees of freedom
$\bar{\mathbf{g}}$, $\mathbf{g}_{\mathrm{C}}^{(s)}$, $\mathbf{g}_{\mathrm{S}}^{(s)}$	Fourier coefficient vectors of $\mathbf{g}$
$\mathbf{G}$	monodromy matrix, eqs. (3.16), (3.20), (3.22)
$\mathbf{h}$	vector of non-linear degrees of freedom (at SFDs)
$\mathbf{h}_0$	static value of $\mathbf{h}$
$\bar{\mathbf{h}}$, $\mathbf{h}_{\mathrm{C}}^{(s)}$, $\mathbf{h}_{\mathrm{S}}^{(s)}$	Fourier coefficient vectors of $\mathbf{h}$
H	total number of modes considered in modal solution
$\mathbf{H}$, $\mathbf{H}_{\mathrm{N}}$, $\mathbf{H}_{\mathrm{L}}$	modal matrices defined in eqs. (5.30), (5.33)
$\mathbf{H}_{\mathrm{H}}$	matrix comprising H rows of $\mathbf{H}$
$\mathbf{I}_n$	$n\times n$ unit diagonal matrix i.e. with 1's on leading diagonal

K_B	equivalent stiffness of support structure at B (Chapter 6) (N/m)
K_{xB_i}, K_{yB_i}	equivalent stiffness of support structure at B_i in x and y directions (Chapter 8) (N/m)
L	SFD land length (m)
m	total number of harmonics taken in RHB solution
$M_{R,J}$	equivalent mass of rigid rotor at J (Chapters 4 and 6) (kg)
M_B	equivalent mass of support structure at B (Chapter 6) (kg)
M_{xB_i}, M_{yB_i}	equivalent mass of support structure at B_i in x and y directions (Chapter 8) (kg)
n	dimension of dynamical variables vector s
n_{SFD}, n_U	number of squeeze film dampers, unbalance discs, respectively
N	positive integer, $(=\Omega/\varpi)$
$p(\theta,z)$	instantaneous SFD pressure distribution (gauge, Pa)
p_c	cavitation pressure (gauge, Pa)
$p_t(\theta,z)$	truncated SFD pressure distribution (gauge, Pa)
p_S	supply pressure (gauge, Pa)
$p_x^{(s)}$, $p_y^{(s)}$, $p_{xi}^{(s)}$, $p_{yi}^{(s)}$	sine coefficients in Fourier expansions of Q_x, Q_y, Q_{xi}, Q_{yi}
$\mathbf{p}(\hat{\mathbf{v}},\hat{\Omega})$	left hand side of RHB vector equation (5.18)
P	total number of degrees of freedom
P_N	number of degrees of freedom associated with $\mathbf{f_N}$
P_L	$= P - P_N$
P_x, P_y,	unbalance forces in x, y directions (N)
P_{xk}, P_{yk}	unbalance forces at U_k in x, y directions (N)
$q_x^{(s)}$, $q_y^{(s)}$, $q_{xi}^{(s)}$, $q_{yi}^{(s)}$	sine coefficients in Fourier expansions of Q_x, Q_y, Q_{xi}, Q_{yi}
q_{xr}, q_{yr}	r^{th} modal coordinates for rotor vibration in xz and yz planes respectively (Chapter 7)
q_{Rxr}, q_{Ryr}	r^{th} modal coordinates for rotor vibration in xz and yz planes respectively (Chapter 8)
q_{Sxr}, q_{Syr}	r^{th} modal coordinates for support structure vibration in xz and yz planes respectively (Chapter 8)

$\mathbf{q}$	vector of modal coordinates $q_1 \ldots q_H$
$\mathbf{q}_E$	vector of modal coordinates of equilibrium periodic solution $\mathbf{u}_E$
Q_R, Q_T	radial and tangential SFD forces on journal (N)
Q_x, Q_y	Cartesian components of SFD forces on J (N)
Q_{xi}, Q_{yi}	Cartesian components of SFD forces on J_i (N)
$\overline{Q}_x$, $\overline{Q}_y$, $\overline{Q}_{xi}$, $\overline{Q}_{yi}$	mean terms in Fourier expansions of Q_x, Q_y, Q_{xi}, Q_{yi}
R	SFD bearing housing bore (m)
$\mathbf{R}$	receptance matrix
Re	gap Reynolds number
s	positive integer, equal to the order of a harmonic in RHB solution
$\mathbf{s}$	vector of dynamical variables, equal to $\begin{bmatrix}\mathbf{u}\\ \dot{\mathbf{u}}\end{bmatrix}$ or $\begin{bmatrix}\mathbf{u}\\ \mathbf{u}'\end{bmatrix}$ or $\begin{bmatrix}\mathbf{q}\\ \dot{\mathbf{q}}\end{bmatrix}$ or $\begin{bmatrix}\mathbf{q}\\ \mathbf{q}'\end{bmatrix}$
$\mathbf{s}_E$	equilibrium solution for $\mathbf{s}$
$\mathbf{S}$	matrix of receptances pertaining to non-linear degrees of freedom
$\mathbf{S}_0$	zero frequency value of $\mathbf{S}$
t	time (s)
T	period of rotation ($= 2\pi/\Omega$) (s)
$\mathbf{T}$	matrix of receptances pertaining to linear degrees of freedom
$\mathbf{T}_0$	zero frequency value of $\mathbf{T}$
$\mathbf{u}$, $\mathbf{u}_L$, $\mathbf{u}_N$	degrees of freedom vectors, defined in eq. (5.4)
$\mathbf{u}_E$	equilibrium periodic solution for $\mathbf{u}$
$\mathbf{u}_{HE}$	vector of RHB responses at H degrees of freedom
$\tilde{\mathbf{u}}$	complex amplitude of $\mathbf{u}$ for $\mathbf{u}$ harmonic (eq. (5.6a))
$\mathbf{u}_C$, $\mathbf{u}_S$	cosine and sine coefficient vectors of $\mathbf{u}$ for $\mathbf{u}$ harmonic (eq. (5.6a))
$\overline{\mathbf{u}}$, $\mathbf{u}_C^{(s)}$, $\mathbf{u}_S^{(s)}$	Fourier coefficient vectors of $\mathbf{u}$
U, U_k	unbalance at positions U, U_k (kgm)
$U_{eq,J}$	equivalent unbalance at J for rigid rotors of Chapters 4 and 6 (kgm)
$\hat{U}$	non-dimensional dynamic load parameter for rigid rotors of Chapters 4 and 6, defined in eqs. (4.21c), (4.18)

$\mathbf{U}(\tau)$	periodic matrix defined in eq. (5.45a)
$\mathbf{v}$	vector of unknown Fourier coefficients in $\overline{\mathbf{h}}$, $\mathbf{h}_{\mathrm{C}}^{(s)}$, $\mathbf{h}_{\mathrm{S}}^{(s)}$
$\hat{\mathbf{v}}$	$= \mathbf{v}/c$
$\hat{\mathbf{w}}$	$= \begin{bmatrix} \hat{\mathbf{v}} \\ \hat{\Omega} \end{bmatrix}$
$\mathbf{V}(\tau)$	periodic matrix defined in eq. (5.45b)
W, W_i	equivalent static load on SFD or SFD no. i, (N)
$\hat{W}$	non-dimensional dynamic load parameter for rotors of Chapters 4 and 6, defined in eq. (4.21b)
$\mathbf{W}(\tau)$	coefficient matrix of perturbation equations, defined in eqs. (3.13), (5.44)
x, y, z	Cartesian coordinate system
$\mathbf{x}$	$= \begin{bmatrix} \mathbf{z} \\ \mathbf{z}' \end{bmatrix}$
X_B, Y_B, X_{B_i}, Y_{B_i}	Cartesian displacements of housing centre B or B_i (m)
X_J, Y_J, X_{J_i}, Y_{J_i}	Cartesian displacements of journal centre J or J_i (m)
X_P, Y_P, X_{P_R}, Y_{P_R}	displacements of arbitrary position P or P_R on rotor (m)
X_{rel}, Y_{rel}, X_{rel_i}, Y_{rel_i}	$X_{rel} = X_J - X_B$, $Y_{rel} = Y_J - Y_B$, $X_{rel_i} = X_{J_i} - X_{B_i}$, $Y_{rel_i} = Y_{J_i} - Y_{B_i}$
$\overline{X}_B$, $\overline{Y}_B$, $\overline{X}_J$, $\overline{Y}_J$...etc.	mean terms in Fourier expansions of X_B, Y_B, X_J, Y_J...etc.
z	axial coordinate of SFD (m) or global Cartesian axis
$\mathbf{z}$	$= \mathbf{q} - \mathbf{q}_{\mathrm{E}}$ (i.e. vector of perturbations in $\mathbf{q}$)
$\alpha_{PQ}(\omega)$, $\beta_{PQ}(\omega)$	x, y receptances between positions P and Q (m/N)
$\alpha_{BB}(\omega)$, $\beta_{BB}(\omega)$	x, y point receptances of support structure at B (m/N) (Chapter 6)
$\alpha_{B_iB_j}(\omega)$, $\beta_{B_iB_j}(\omega)$	x, y receptances between positions B_i and B_j on support structure, $i, j = 1, 2$ (m/N) (Chapter 8)
$\breve{\alpha}_{B_iB_j}(\omega)$, $\breve{\beta}_{B_iB_j}(\omega)$	accelerance functions $= -\omega^2\alpha_{B_iB_j}(\omega)$, $-\omega^2\beta_{B_iB_j}(\omega)$ ($\mathrm{ms^{-2}N^{-1}}$) (Chapter 8)
δ_{Ns}	equal to 0 for $s \neq N$ and equal to 1 for $s = N$
ε	non-dimensional instantaneous eccentricity of J from B ($= e/c$)

ε_{0x}, ε_{0y}	non-dimensional x, y static offsets of SFD journal centre J from housing centre B ($=e_{0x}/c$, e_{0y}/c)
θ	angular position around the SFD, measured from the maximum film thickness position (rad)
ψ	attitude angle of SFD journal (rad)
$\varphi(\mathrm{s},t)$	non-linear vector function of s and t on the right hand side of the dynamical equations (3.1)
$\phi_P^{(xr)}$, $\phi_P^{(yr)}$	r^{th} mass-normalised mode shapes of rotor in Chapter 7 at position P in xz, yz planes ($\mathrm{kg}^{-0.5}$)
$\phi_{P_R}^{(Rxr)}$, $\phi_{P_R}^{(Ryr)}$	r^{th} mass-normalised mode shapes of rotor in Chapters 6 and 8 at position $\mathrm{P_R}$ in xz, yz planes ($\mathrm{kg}^{-0.5}$)
$\phi_B^{(Sxr)}$, $\phi_B^{(Syr)}$, $\phi_{B_i}^{(Sxr)}$, $\phi_{B_i}^{(Syr)}$	r^{th} mass-normalised mode shapes of support structure at position B or B_i in xz, yz planes ($\mathrm{kg}^{-0.5}$)
$\phi^{(h)}$	mass-normalised mode shape vector ($h=1\ldots H$)
γ_k	phase shift of unbalance at U_k (rad)
λ_l	leading eigenvalue of $\mathbf{G}$ (leading Floquet multiplier)
η	dynamic viscosity of oil (Nsm^{-2})
$\hat{\eta}_{xB_i}$, $\hat{\eta}_{yB_i}$	structural damping loss factors for support structure vibration at B_i
τ	$=\varpi t$, non-dimensional time
ς	$=\Omega t$, non-dimensional time
ϖ	fundamental frequency of equilibrium periodic solution (rad/s)
ω	general frequency (rad/s)
ω_0	lowest undamped natural frequency with SFD locked (rad/s)
ω_h	undamped natural frequency in mode $h=1\ldots H$ (rad/s)
ω_{xr}, ω_{yr}	undamped natural frequencies of rotor (Chapter 7) in mode r in xz and yz planes (rad/s)
ω_{Rxr}, ω_{Ryr}	undamped natural frequencies of rotor (Chapter 8) in mode r in xz and yz planes (rad/s)
ω_{Sxr}, ω_{Syr}	undamped natural frequencies of support structure (Chapter 8) in mode r in xz and yz planes (rad/s)
σ	arc length parameter
Ω	rotor rotational speed (rad/s)

$\hat{\Omega}$	non-dimensional speed parameter ($=\Omega/\omega_0$)
Γ	period of equilibrium periodic solution $(=NT)$ (s)
$\mathbf{0}_{i\times j}$	$i\times j$ matrix of zeros
diag[ ]	diagonal matrix with vector [ ] on the leading diagonal
Re( ), Im( )	real and imaginary parts of ( )
$(\,)^*$	complex conjugate of ( )
$(\,)^R$, $(\,)^I$	applied to a matrix: real and imaginary parts of ( ) respectively
$(\,)^T$	applied to a matrix or a vector ( ): transpose of ( )
$\dot{(\,)}$	$d(\,)/dt$
$(\,)'$	$d(\,)/d\tau$ or $d(\,)/d\varsigma$

LIST OF FIGURES

LIST OF TABLES

1 INTRODUCTION

Squeeze film dampers are non-linear elements used in rotor assemblies, particularly aero-engines, to attenuate vibrations and transmitted forces, and to improve stability. Figure 1.1 shows a schematic of a squeeze film damper (SFD) assembly. The inner surface of the damper is formed by the "journal" which is a ring fixed to the outer race of a rolling-element bearing. The journal is prevented from rotating relative to the shaft axis, but is free to orbit in the oil-filled annular clearance in the bearing housing, forming the SFD. A retainer spring, usually in the form of a squirrel cage (not shown in Figure 1.1) is optionally placed in parallel with the SFD. This design is referred to here as the "sprung SFD". The spring might be inserted to tune the system natural frequencies. However, the primary function of the spring is to support the static load on the journal (normally the gravity load). It also serves to prevent the journal from rotating. Preloading of the spring is used in an effort to centralise the journal in the housing, thus obtaining circular and concentric journal orbits, synchronous with the rotational speed. However, in practice, there will be some degree of static eccentricity of the journal within the bearing housing due to preloading error, omission of the preloading mechanism for constructional simplicity, or, in extreme cases, partial failure of the retainer spring in service. This offset results in non-circular orbits, with increased likelihood of non-synchronous frequency components. In some engine designs, the retainer spring is dispensed with altogether, as in Figure 1.1. This design is referred to here as the "unsprung SFD". In this design, the journal is prevented from rotating by anti-rotation pins or dogs (in the schematic of Figure 1.1, dogs projecting from the right hand end of the journal engage with similar ones on the right hand end-plate with sufficient clearance so as not to obstruct relative movement in the x-y plane). The resulting simpler mechanical design avoids problems of fatigue in the retainer spring and reduces manufacturing costs. If, in the static condition, the journal of an unsprung SFD is fully eccentric under the static load of the rotor, then the SFD is referred to as "unsupported". When in operation, the unsupported SFD is effectively in series with the bearing pedestal flexibility and performs the additional function of a bearing (i.e. supports the static load). Paradoxically however, this is not possible if there is no relative vibration between the journal and the housing since, in such a case, the two would remain in contact. Hence, to operate, an unsupported SFD makes use of the ever-

present residual unbalance in the rotating system. An unsupported SFD is inherently non-linear. Moreover, as will be shown later in this thesis, despite the unbalance excitation, the journal can still "bottom" within the clearance under the gravity load over certain operating regimes due to minimal relative vibration across the damper. Apart from wear problems, such a condition introduces additional non-linear effects as a result of the ineffective SFD behaving like a piecewise-linear (bilinear) spring wherein the journal experiences different linear stiffnesses along the $-y$ and $+y$ axes.

The undesirable non-linear side effects introduced by SFDs are jump phenomena, non-synchronous vibrations, and, indirectly, bilinear oscillator effects. A jump phenomenon is a sudden jump-up or jump-down in amplitude upon increasing or decreasing the speed and is associated with the non-linear spring-like characteristic of a SFD. In this thesis, "non-synchronous vibration" is taken to mean any vibration that contains frequency components that are not equal to (and hence not synchronous with) the excitation frequency, which, for unbalance excitation is the rotational speed. This vibration therefore includes: (a) periodic vibration containing super-harmonics (of the excitation frequency) or sub-harmonics (of the excitation frequency) and their integer multiples; (b) quasi-periodic vibration containing combination (sum and difference) frequency components; and (c) chaotic motion, with its continuous frequency spectrum. Sub-synchronous flexural vibrations are undesirable in rotors since they give rise to cyclic stresses, aggravating fatigue problems. It will also be seen later that when an unsupported SFD degenerates into a bilinear oscillator, sub-critical super-harmonic resonances and super-critical sub-harmonic resonances result. This myriad of non-linear phenomena necessitates an effective predictive tool for the dynamics of unbalanced squeeze film damped rotating systems. It is only the forced response problem that is of interest since a SFD cannot introduce instability of the type that results in self-excited vibration, unlike hydrodynamic journal bearings. It is in this respect that SFDs are said to offer improved stability. Jump and sub-synchronous vibration phenomena in a system with SFDs are the result of the instability of pre-existing, externally forced periodic oscillations. Rotor unbalance is the major source of the external excitation. Moreover, the state of balance can degrade progressively during service and change sharply as a result of minor damage.

SFDs introduce non-linear motion-dependent forces into an otherwise linear rotor-dynamic system. The techniques used for the determination of the unbalance response of such systems can be broadly divided into two categories: periodic solution techniques and

time-marching methods. Periodic solution techniques are used to determine equilibrium solutions (i.e. steady-state, non-transient solutions) of the periodic type, usually of assumed period. These periodic solutions can be either (asymptotically) stable (forming periodic attractors in state space) or unstable. Oscillations of the latter variety are not observed in practice. Time-marching methods involve numerical integration of the system equations from given initial conditions over sufficiently long integration times for transients to die out and a stable equilibrium solution (attractor in state space) to be reached which need not necessarily be periodic. While periodic solution techniques are essentially much faster than time-marching methods, the solutions obtained need to be tested for stability and time-marching becomes the only method of solution when no periodic attractor exists.

The main contribution of this thesis is the development of an efficient integrated non-linear modelling technique for the solution of the unbalance response problem. The integrated model consists of the following three complementary blocks, each of which is tractable to systems with many degrees of freedom:

(1) The determination of the periodic solutions: a *receptance harmonic balance* (RHB) method is proposed for such a purpose. In this method, the receptance functions of the rotating linear part of the system are used in the non-linear analysis of the complete system.

(2) Stability analysis of these periodic solutions. This is done by applying Floquet theory to a limited number of the perturbed modal equations of the system.

(3) Numerical integration of the modal equations, when necessary.

During the course of this project, discussions with engineers in the UK aircraft industry revealed that little or no non-linear analysis of squeeze film damped aero-engine systems is performed. Instead, the SFDs are modelled as linear elements that can be incorporated into industrial linear rotor-dynamic software packages. With the integrated model presented in this thesis, these software packages can be used to analyse the linear subsystem for receptance functions and modal parameters. These two sets of data can then be used in a detailed non-linear analysis of the complete system that can be implemented using standard mathematical software.

The integrated model is tested on three rotor-dynamic systems, of increasing complexity:

(A) Rigid rotor with one unsupported SFD in flexible housing.

(B) Flexible rotor with one rigidly housed SFD, with and without retainer spring.

(C) Flexible rotor with two unsupported SFDs in flexible housings.

The SFD forces are obtained from an extant model for the SFD suitable for the short, unsealed dampers considered. This SFD model assumes a short incompressible film that cavitates (ruptures) at absolute zero pressure. The fundamental objectives of each test are two-fold. The first objective is to demonstrate the correlation between the simulation results from the three complementary modelling blocks (i.e. RHB, stability analysis, time-marching). The second objective is to assess the ability of the modelling technique to predict and explain observed non-linear phenomena. Hence, where available, evidence from experimental rigs for configurations (A), (B), and (C) is presented to validate the study. Configurations (A) and (C) are based on aero-engine designs. Configuration (B) is typical of a small centrifugal pump. With the exception of (C), these configurations had been analysed analytically and experimentally in the literature. However, the lack of a comprehensive non-linear model did not allow an adequate study of the non-linear effects highlighted above. Hence, the analytical and experimental findings should shed new light on the non-linear behaviour of squeeze film damped rotating systems. Moreover, the study should provide useful additional validation of the model used to compute the SFD forces, since, despite being generally considered the best available from a physical and practical viewpoint, this SFD model is not definitive.

This chapter concludes in the next section (1.1) with a summary of the thesis objectives and contributions. A critical review of previous research is given in Chapter 2. Chapter 3 outlines basic concepts in non-linear dynamics, with emphasis on stability and bifurcation of periodic oscillations. In Chapter 4, the non-linear force expressions for a SFD, based on existing theory, are presented. These expressions are illustrated by simulations for a simple rotor system. The integrated model is developed in Chapter 5 for a general squeeze film damped rotor-dynamic system and the advantages of this model over current models are explained. The model is applied to configurations (A), (B), and (C) in Chapters 6 to 8 respectively. The general conclusions are drawn in Chapter 9, along with recommendations for future research.

1.1 THESIS OBJECTIVES AND CONTRIBUTIONS

The thesis objectives were:

- The development of an efficient integrated modelling technique for the solution of the unbalance response problem of rotor-dynamic systems with squeeze film dampers.

- Validation of the integrated model in simulation for three squeeze film damped rotor-dynamic configurations (A), (B), and (C).
- To assess the ability of the model to predict and explain non-linear performance. To achieve this aim, experimental work is performed on test rigs for (B) and (C). Limited experimental results from a test rig for (A) are reproduced from the literature.

The thesis contributions are:

- An integrated non-linear modelling technique that provides a comprehensive solution to the unbalance response problem of squeeze film damped rotor-dynamic systems over a wide range of operating conditions, that is efficient for systems with many degrees of freedom, and that can be interfaced with linear rotor-dynamic modelling techniques used in industry.
- Extension of research in the area of non-linear rotor-dynamics by applying the modelling technique to predict and explain experimentally observed undesirable non-linear phenomena in squeeze film damped systems.
- To a limited extent, as an outcome of the previously listed contribution, the provision of additional experimental validation for the existing oil film model used to compute the squeeze film damper forces.

It should be noted that the integrated model can be easily adapted to cover other types of non-linearities in rotor-dynamic systems by using the appropriate non-linear forcing functions.

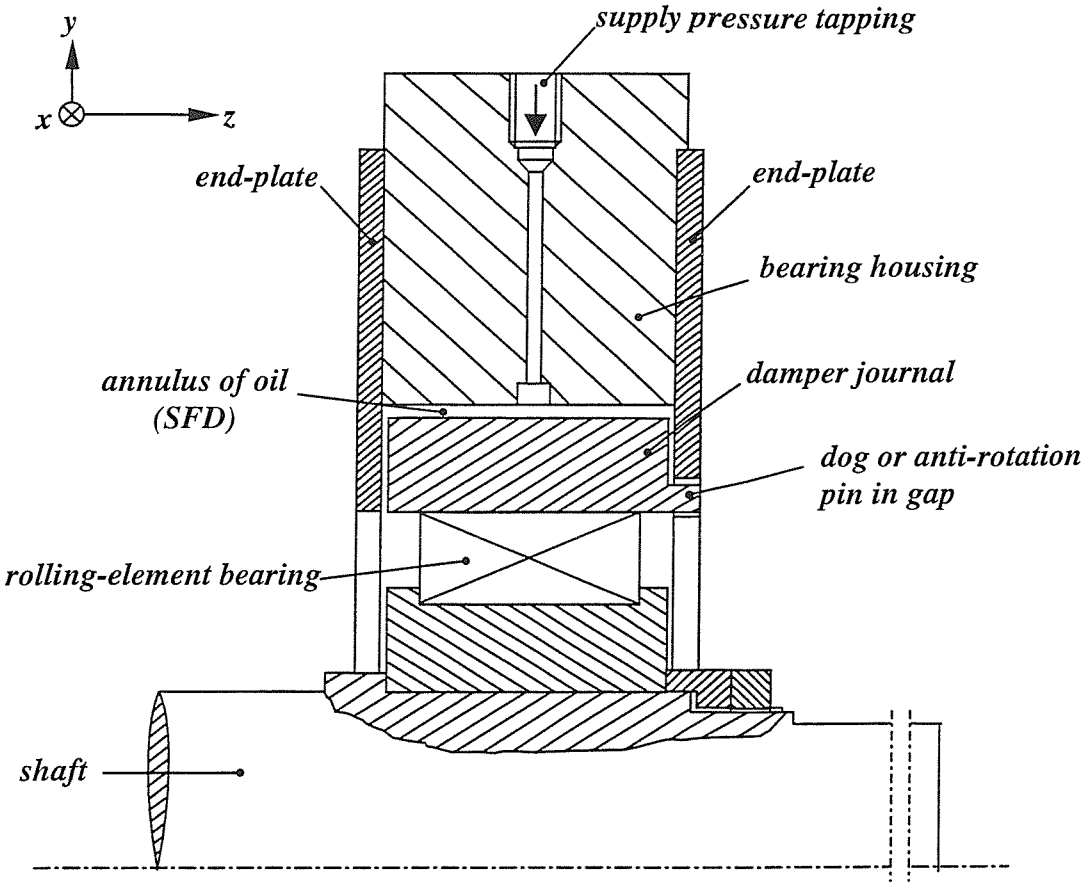

Figure 1.1: *Schematic of a squeeze film damper (SFD) assembly*

2 REVIEW OF PREVIOUS RESEARCH

2.1 INTRODUCTION

In this chapter a critical review of previous research relating to squeeze film damped rotor-dynamic systems is presented. The first part of this review deals with solution techniques for the unbalance response. The second part deals with reported studies on the non-linear phenomena in such systems. Existing research into the models used for squeeze film damper (SFD) force estimation is outlined in Chapter 4.

2.2 SOLUTION TECHNIQUES FOR THE UNBALANCE RESPONSE

Ever since Cooper [1] first patented a squeeze film damper bearing in 1964, efforts have been made to develop efficient modelling techniques for the unbalance response of rotor-dynamic systems fitted with such non-linear components. Time-marching (i.e. the numerical integration of the differential equations of motion from given initial conditions) has been applied to simple rigid rotors on non-linear supports for many years e.g. Craven and Holmes [2] in 1972, Gunter *et al.* [3] in 1977, Cookson and Kossa [4] in 1979. However, the need for faster solutions resulted in the development of non-linear rotor-dynamic periodic solution techniques. The theoretical analysis of centrally preloaded dampers with circular, concentric, and synchronous rotor motion is well documented [5-7]. The example considered by McLean and Hahn [6], was a symmetric flexible rotor mounted on identical sprung SFDs and the solution procedure was reduced to the solution of a single non-linear algebraic equation. The stability problem for such computed orbits was considered by McLean and Hahn [7]. This was done by considering small linearised perturbations from the equilibrium orbit. By virtue of the circular and synchronous nature of the orbit, the stability problem was reduced to a simple eigenvalue problem by writing the perturbed time domain equations of motion with respect to a *rotating* frame of reference, thus obtaining a system of linear differential equations with *constant* coefficients. As evidenced by the unexpected instabilities discovered by McLean and Hahn in this simplest of rotor configurations, the stability analysis of periodic solutions is an essential requirement.

As discussed in the Introduction, some offset of varying degree will exist in sprung SFDs, and unsupported SFDs are also used. For such situations, attempts have been made to obtain periodic solutions by equivalent linearisation of the damper forces by Holmes and Dogan [8], Hahn [9], Chen and Liu [10], and El-Shafei and Eranki [11]. These methods enable the equivalent damping, stiffness and/or inertia coefficients to be used in conjunction with existing linear rotor-dynamic modelling techniques. However, such solutions assume synchronous motion and make no allowance for the possibility of sub-harmonic and super-harmonic frequency components. More recently, it has been shown that reasonably accurate periodic solutions with non-synchronous frequency components can be obtained by the harmonic balance (HB) method [12] or the analogous trigonometric collocation (TC) method [13, 14]. In particular, Chen *et al.* [12] successfully analysed a symmetric rigid rotor with a rigidly housed unsupported SFD at either end using harmonic balance for periodic solutions with sub-harmonic fundamental frequencies. While HB and TC are different in the detail, they are fundamentally similar in that both approximate the periodic motion with a truncated Fourier series with m harmonics of an assumed fundamental frequency $\varpi = \Omega/N$ where Ω rad/s is the rotational speed and N is a positive integer. Both methods ultimately result in a system of non-linear algebraic equations with the unknowns being the Fourier coefficients of the degrees of freedom at the non-linear elements. Hence, these unknowns total $P_N(2m+1)$ where P_N is the number of non-linear degrees of freedom of the system. In either case, the system of equations is soluble (by iteration) so long as a solution of fundamental frequency ϖ exists. For computational reasons, only a finite number of harmonics m can be considered, so the periodic solution will be, strictly speaking, approximate. However, in most practical problems, where N is small, the solution always converges after a manageable number of harmonics m [12, 15]. However, Chen *et al.* [12] found that convergence was difficult to achieve for oscillations with large N, since many harmonics needed to be taken. In such situations it was considered more economical to use time-marching. Moreover, the work in [12] showed that time-marching could be used with HB to help locate different stable equilibrium solution possibilities. Zhao *et al.* [13] used arc-length continuation [16] with TC to negotiate regions of the unbalance response curve where more than one solution was possible for a given rotational speed (as in bistable regions). The stability analysis of non-circular periodic orbits with non-synchronous frequency components was considered in [12, 13, 15]. The perturbed time domain equations

of motion were written in terms of a *stationary* frame, resulting in a system of linear differential equations with *periodic* coefficients, which was then analysed by Floquet theory.

The extension of accurate periodic solution techniques employing TC or HB to practical systems with many degrees of freedom has been studied in [14, 15, 17, 18]. The common strategy was to regard the forces from the non-linear elements as external, acting on the rotating linear part. Hahn and Chen [15] modelled the linear part by the finite element (FE) method and the HB method was applied to the FE time domain equations of motion of the system (which are of the general form $\mathbf{M}\ddot{\mathbf{u}} + \mathbf{C}\dot{\mathbf{u}} + \mathbf{K}\mathbf{u} = \mathbf{f}$, where **M**, **C**, and **K** are the mass, damping/gyroscopic and stiffness matrices respectively and **u** and **f** are the vectors of the degrees of freedom and the external forces/moments respectively). This resulted in a very large set of non-linear algebraic equations with $P(2m+1)$ unknowns where P was the total number of degrees of freedom of the system. This number was then reduced to $P_N(2m+1)$ (where P_N = number of non-linear degrees of freedom) by applying a condensation technique involving the inversion of potentially large FE matrices (of the order $P \times P$). The stability of the solution was tested by applying Floquet theory to the perturbed FE equations of motion, again resulting in potentially large matrices. The work by Shiao and Jean [17] was similar to that in [15], except that complex notation was used and no stability analysis was performed. Such FE-based periodic solution and stability techniques are clearly not useful for practical systems with many degrees of freedom. Nataraj and Nelson [14], adopted a component mode synthesis approach. The TC method was applied to the modal equations of the system, making the technique tractable to large order systems. This required the solution of the eigen-problem of the rotating linear part and modal truncation. However, as observed by Shiao and Jean [17], this needs to be done at each rotational speed if gyroscopic effects are significant. More recently, Liew *et al.* [18] obtained the HB equations of non-linear rotor-bearing systems by applying the transfer matrix (TM) method. While this method is efficient, it is limited by its exclusive use of the TM method, which, as discussed by Bonello and Brennan [19], is not effective at including the dynamics of the support structure.

With time-marching methods, as with periodic solution techniques, the SFD forces are included in the external force vector **f**. However, the integration of the FE equations of motion is clearly impractical for large order systems. This is mostly due to the fact that the step size required by the integration scheme to maintain the local error within a prescribed tolerance is determined by the shortest period of the system, which corresponds to the highest

frequency mode. Hence, the step size decreases with increasing numbers of degrees of freedom [20]. It may be considered to simplify the physical model by lumping mass in order to reduce the number of degrees of freedom. However, this can seriously limit the range of reliability of the results. For example, in order to overcome computing limitations, Chu and Holmes [21] modelled a squeeze film damped flexible rotor rig (rig (B) described in the Introduction and considered in Chapter 7) as a lumped parameter system with three masses. Upon fixing the locations of two of the masses, the location of the third was chosen such that the first two undamped critical speeds of the equivalent system matched those of the actual continuous system, which had been previously estimated by the transfer matrix method. The static influence coefficients of the simplified system were determined experimentally from the rig. Despite this arduous simplification, the results obtained from such a model were considered reliable only within a frequency range of 0-50 Hz. This not only restricted the operating speed of the rig, which could otherwise be driven up to 100 rev/s, but must have affected the super-synchronous frequency content of the predictions within the speed range considered (0-50 rev/s). The only viable and accurate time-marching approach for large systems (i.e. systems with many degrees of freedom) is the numerical integration of an adequate number of the modal equations [20]. Becker and Steinhardt [22], and Armentrout and Gunter [23] demonstrated how the transient response of a squeeze film damped rotating system can be computed by numerically integrating the modal equations. However, apart from these two demonstrations, to the author's knowledge no modal time-marching studies of such systems have yet been reported.

In the time marching approach, the differential equations of motion (whether in modal or FE form) can be integrated using any convenient numerical integration scheme. SFD researchers have tended to use the 4^{th} order Runge-Kutta (RK) method [8, 12, 24]. However, the RK method is not suitable in situations where the system of equations is "stiff" (i.e. the highest natural frequency is very high). In this situation, the step size required by the RK method to maintain the local error within the prescribed tolerance is exceedingly small, resulting in a very time consuming process that will most likely crash due to overload of the computer memory. In [2], a method based on the trapezoidal integration rule was presented in order to overcome this problem. This integration scheme was used in [21]. Moreover, *MATLAB*® (version 5 and later) [25] has a whole suite of functions dedicated to the solution of stiff systems.

2.3 RESEARCH INTO NON-LINEAR PHENOMENA

The benefits of a squeeze film damper in attenuating vibrations in the critical speed regions are illustrated in the work by Holmes and Dogan [8]. Chu and Holmes [26] used a simple numerical example to show how a SFD, by virtue of the extra damping provided by its non-linearity, can control instability introduced by components such as seals by limiting the amplitude of the self-excited vibration. However, it is understandable that most research has concentrated on the negative side effects introduced by the non-linearity of the SFD on the unbalance response. These non-linear phenomena were listed in Chapter 1 as jump phenomena, non-synchronous vibration, and, indirectly, bilinear oscillator effects.

Jump phenomena, resulting from non-linear spring characteristics of cavitated squeeze film dampers have been reported by many researchers. Spring-hardening characteristics (i.e. jump-down in amplitude on run-up in speed, Figure 2.1(a)) were reported by many researchers in both theoretical and experimental work [6, 7, 13, 24, 27, 28-30]. In all these works, this spring hardening characteristic was associated with the parallel combination of a SFD and some flexibility. This flexibility was the retainer spring in [6, 7, 13, 24, 27]. In [28-30] it was the engine carcass (i.e. support structure) flexibility. In [28, 29] the carcass flexibility was located at a different bearing but was still effectively in parallel with the SFD. Stability analysis for sprung dampers in [7, 13, 27] showed that, when three solutions existed at one rotor speed, the middle solution was unstable while the upper and lower ones were stable (hence the *bistable* regions in Figure 2.1). Spring-softening characteristics (i.e. jump-up in amplitude on run-up in speed, Figure 2.1(b)) were reported in [8, 31], both with horizontal rotor rigs involving rigidly housed unsupported SFDs carrying appreciable rotor weight. A similar effect was obtained in [28, 32] with unsupported SFDs in flexibly mounted housings.

Many researchers have observed super-harmonics and sub-harmonics (with integer multiples) in the vibration signals from squeeze film damped rotating systems. Nikolajsen and Holmes [33] reported sub-harmonics down to one quarter of the rotational speed (i.e. 1EO/4, where 1EO refers to the synchronous frequency component – "EO" standing for "engine order") from a flexible rotor rig. Sykes and Holmes [28] demonstrated the existence of severe sub-harmonics equal to 1EO/2 as well as strong super-harmonics, under various conditions of static offset. A theoretical study on the sub-harmonic motion of a simple rigid rotor in unsprung SFDs was done by Chen *et al.* [12]. Among other things it was concluded that a resultant static load on the journal appeared necessary for sub-harmonic motion. This

analysis was limited since it did not include the effect of the bearing pedestal flexibility (i.e. the dynamic deflection of the bearing housing), which is often significant for practical gas turbines [8] and was shown in various works [8, 28, 31, 32] to be highly influential in the dynamics of unsupported SFDs. Using elementary analysis, Holmes and Box [30] showed that, for a rigid rotor with an unsupported SFD that is in series with the pedestal flexibility, a 1EO/2 sub-harmonic was expected to be excited when the speed was close to the undamped natural frequency. On the other hand, for a rigid rotor with a rigidly housed SFD in parallel with a spring (or equivalent flexibility), the 1EO/2 sub-harmonic was expected when the rotational speed was just around twice the undamped natural frequency. These results have been confirmed in [8, 31] for the unsupported SFD and in [30] for the sprung SFD.

The bifurcation of periodic motion in a general non-linear system into quasi-periodic motion is described in standard non-linear dynamics text books, for example [16, 34, 35]. As shown in Chapter 3, a quasi-periodic signal is an aperiodic signal composed of two (or more) periodic signals having irrationally related fundamental frequencies, one of which is normally the excitation frequency. This motion is hard to distinguish from periodic motion with very many sub-harmonics [34]. In 1976, Botman [36] observed what looked like quasi-periodic motion on a high-speed oil film damper rig run by Pratt and Whitney of Canada Ltd. In that very early research, this motion was given the general term "non-synchronous". Reference to Botman's observations was made in the work by Li and Taylor [37], which was the first to analyse numerically quasi-periodic motions in SFDs. This work considered a simple rigid rotor with sprung SFDs and the same term as Botman was used to describe quasi-periodicity (i.e. "non-synchronous"). When the computed quasi-periodic response was sampled at intervals equal to the period of excitation and the samples plotted[1], a closed curve resulted. This agrees with standard non-linear dynamics theory and is the hall-mark of quasi-periodic motion with two fundamental frequencies [34, 38]. Li and Taylor concluded that the quasi-periodic motion could be changed or suppressed into a periodic motion of period NT (where T is the period of rotation and N a positive integer) by the introduction of a unidirectional static force onto the otherwise centrally preloaded rotor. They also made the important observation that the sub-synchronous phenomena in a system with SFDs are not self-excited since their existence directly relates to the external excitation (unbalance force). The term "quasi-periodic" was first used in the context of SFDs by Zhao *et al.* [13, 24, 27], who used Poincaré maps and frequency spectra to analyse the aperiodic motion. In [13] they examined

[1] A plot of such samples is referred to as a Poincaré map [13, 24, 27, 34, 38].

theoretically a symmetric flexible rotor in identical centrally preloaded SFDs. Well beyond the jump phenomenon described earlier, they discovered that the synchronous periodic motion bifurcated into quasi-periodic motion that persisted over a limited speed range beyond twice the pin-pin critical speed of the shaft. The effect of introducing a static offset in the SFDs was to introduce a period-doubling bifurcation soon after the first pin-pin critical speed such that there was stable periodic motion of period $2T$ (where T is the period of rotation) over a short speed range. Additional theoretical work on quasi-periodic and sub-harmonic motion was done by Zhao *et al.* in [24, 27] on a symmetric rigid rotor in identical eccentric sprung SFDs. In [24], chaotic motions were also found to occur and were identified by the fractal nature of the Poincaré Map. To the author's knowledge, the work in [24] is the only work related directly to SFDs where chaotic motion was investigated numerically.

The quasi-periodic motion in [13, 24, 27] was found to contain combination (or "sum and difference") frequency components of the general form $n_1 f_1 + n_2 f_2$ where n_1 and n_2 are integers (positive, negative or zero) and f_1 and f_2 are the two irrationally related fundamental frequencies of the motion. This feature of quasi-periodic motion is described in the text-book by Ott [35]. Ehrich [39] observed combination frequencies in a General Electric gas turbine engine. It was noted that two fundamental frequencies were involved – one synchronous with the rotor rotation, associated with the unbalance, and an asynchronous frequency that was attributed to fluid trapped in the rotor. It was concluded by Ehrich that the source of the combination frequencies was the truncation of vibration, probably due to the rotor being located eccentrically in a bearing clearance. Combination frequencies were also observed experimentally by Holmes and Dede [31] in a twin rotor configuration coupled through a SFD. This time however, the two fundamental frequencies were both due to unbalance excitations, one on each rotor, and the generation of the combination frequencies was attributed to the non-linearity of the coupling between the rotors.

Before leaving the subject of the SFD proper, two important issues are discussed: (a) the correlation between experiment and theory, and (b) the practical significance of the SFD systems studied in the literature. Of course, the correlation between experiment and theory will be influenced by the actual model used to compute the SFD forces. As shall be seen in Chapter 4, a major source of uncertainty is the modelling of the cavitation effect within the SFD. The idealised "π film" model applies for an externally unpressurised, short, and unsealed damper in which the oil film is assumed to cavitate (rupture) at atmospheric pressure. This leads to closed form expressions for the SFD forces, which are easy to use. A

more realistic model called the "variable film" model allows for the supply pressure and assumes cavitation at some sub-atmospheric pressure, usually absolute zero pressure. However, the instantaneous SFD forces need to be computed numerically by double integration. Most work reviewed in this section, pertaining to the non-linear dynamics of SFD systems, can be divided into two contrasting categories. The first includes the works by Zhao *et al.* [13, 24, 27], Chen *et al.* [12], and McLean and Hahn [6, 7], which apply all the non-linear dynamics tools available (i.e. periodic solution computation, stability and bifurcation analysis, time-marching, Poincaré maps, and frequency spectra) to analyse theoretical models of both rigid rotor and flexible rotor systems. These works used a "π film" model for the SFD and no experimental verification was undertaken. The second category involves the work done by Holmes with various co-researchers [8, 28, 31, 32] which was restricted to the time-marching of the differential equations of motion of rigid rotor models and the examination of the orbital motion, amplitude-speed plots, and frequency spectra from the results obtained. However, these works used the variable film model and were backed up by experimental work. Moreover, unlike the workers in the first category, the rigid rotor systems considered by Holmes *et al.* included those with flexible pedestals (housings). According to Holmes and Box [20], practical squeeze film damped rotating assemblies can be classified into one of two types of simple configurations, as a rough first approximation: (i) rigid rotor-flexible housing systems, such as military aero-engines and turbo-chargers, and (ii) flexible rotor-rigid housing systems like civil aero-engines and air compressors. What appears to be lacking in the literature is an advanced non-linear study, on a par with those performed by researchers in the first category mentioned above, on systems of type (i) and (ii), that is backed by experimental evidence.

Bilinear oscillator effects, which are not exclusive to SFDs, are now discussed. Ehrich [40, 41] did considerable research on unbalanced rotors operating eccentrically within a clearance and in local contact with the stator. The rotor-stator interaction was modelled by a piecewise-linear spring that was softer for the vertical motion of the rotor from its rest position into the clearance and harder for the vertical motion from the rest position into the direction of contact. This is illustrated in Figure 2.2. In [40], Ehrich cited a rotor just bottomed in the squeeze film damper/bearing clearance as a typical example. Hence, the non-linear SFD force expressions were replaced by the piecewise-linear spring characteristic. The resulting oscillator was said to behave as a bilinear oscillator [41]. Simulations on a simple unbalanced Jeffcott rotor [40, 41] showed that, for the direction of the non-linearity

(i.e. vertical direction), super-critical sub-harmonic resonance at exactly $1/n$ of the excitation frequency (n is a positive integer) occurred whenever the excitation frequency (the rotational speed) was in the region of n times the natural frequency. Similarly, sub-critical super-harmonic resonance at exactly n times the excitation frequency occurred whenever the excitation was in the region of $1/n$ times the natural frequency. It was also found that there was a zone of characteristically chaotic behaviour located midway of each transition zone between successive resonances. The results from the numerical simulation were used to explain data collected from an aircraft gas turbine engine.

It appears from the literature that a direct correlation between SFDs and bilinear oscillator effects has yet to be made i.e. the prediction of such effects using the SFD force expressions, without recourse to piecewise-linear spring models. This is important since, by neglecting the SFD forces, Ehrich [40, 41] assumed that the piecewise-linear spring model was applicable over the entire operating range of the rotational speed. However, in a real system, it is reasonable to expect that over part(s) of the operating range the SFD forces will create sufficient sustained lift to counter the rotor offset within the clearance, thus rendering the piecewise-linear spring model invalid.

2.4 CONCLUSION

The previous research into the analysis of the dynamics of unbalanced squeeze film damped rotating systems has been reviewed in this chapter. The first part of this review (section 2.2) dealt with solution techniques for the unbalance response. The second part (section 2.3) dealt with reported studies on the non-linear phenomena in such systems. An integrated model has been recently developed by the author [42] to overcome the shortcomings highlighted in section 2.2. This forms the basis of this thesis. This model will be used to extend the existing research into the non-linear phenomena presented in section 2.3.

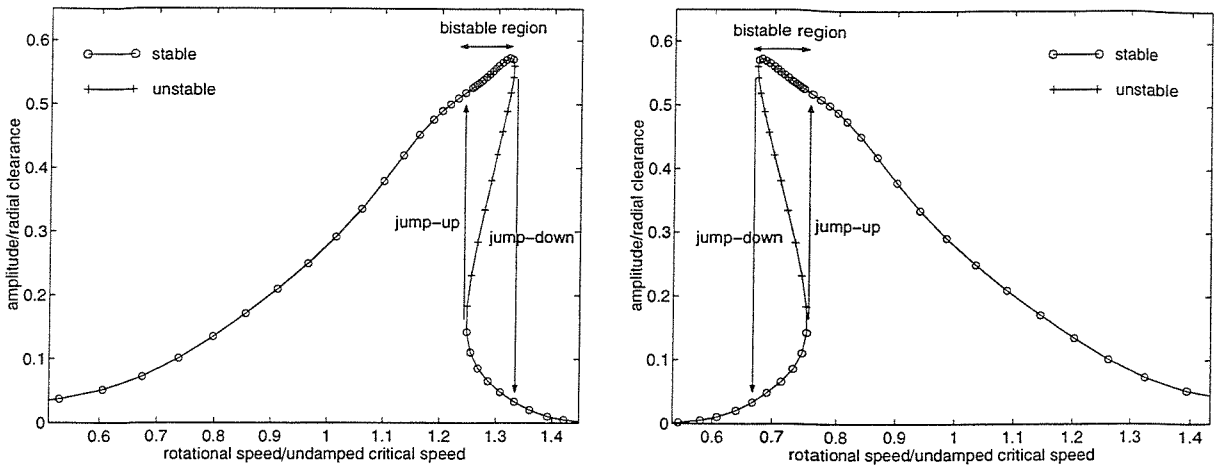

(a) hardening spring characteristic (b) softening spring characteristic

Figure 2.1: *Non-linear spring characteristics of a SFD*

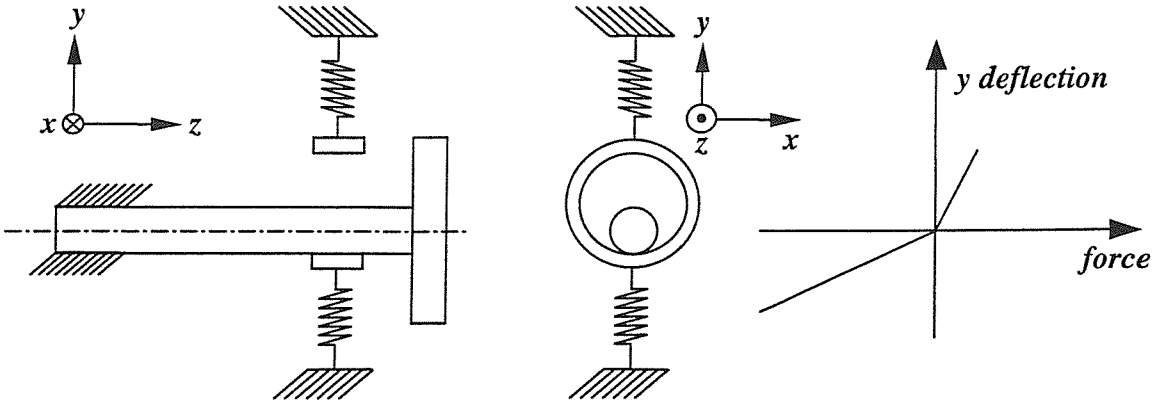

Figure 2.2: *Piecewise-linear spring characteristic of a rotor operating eccentrically in a bearing clearance and in local contact with the stator*
(case shown is for rotor just contacting stator in static condition, after Ehrich [40, 41])

3 BACKGROUND NON-LINEAR DYNAMICS THEORY

3.1 INTRODUCTION

This chapter describes the background non-linear dynamics theory relevant to this thesis. Emphasis is placed on the stability and bifurcation of periodic oscillations of forced dynamical systems. A description of quasi-periodic motion is given and the occurrence of combination frequencies explained. This is followed by a brief discussion of chaos. A short note on unforced systems is also given in this chapter. While this is not relevant to the squeeze film damper (SFD) problem, it helps to explain the benefit of using a device like the SFD over other fluid film devices. The chapter concludes with a note on the issue of "numerical stability" i.e. the "stability" of numerical integration methods.

A dynamical system can be either a continuous-time system or a discrete-time system. This thesis is concerned with the former. A continuous-time dynamical system can be modelled as a set of n first order differential equations. For a non-autonomous system, the independent time variable t appears explicitly in the dynamical equations, so these are of the form:

$$\dot{\mathbf{s}} = \varphi(\mathbf{s}, t) \tag{3.1}$$

For an autonomous system, the independent time variable t does not appear explicitly in the dynamical equations and so, these are of the form:

$$\dot{\mathbf{s}} = \varphi(\mathbf{s}) \tag{3.2}$$

φ is an $n \times 1$ vector function of the dependent variable $\mathbf{s} = [s_1 \quad \cdots \quad s_n]^T$ and (for a non-autonomous system) the independent variable t:

$$\varphi(\mathbf{s}, t) = [\varphi_1(s_1, \ldots, s_n, t) \quad \cdots \quad \varphi_n(s_1, \ldots, s_n, t)]^T \tag{3.3}$$

$$\boldsymbol{\varphi}(\mathbf{s}) = [\varphi_1(s_1,\ldots,s_n) \quad \cdots \quad \varphi_n(s_1,\ldots,s_n)]^T \tag{3.4}$$

The dynamical system (and its governing system of equations) is said to be "non-linear" if $\boldsymbol{\varphi}$ is a non-linear function of the dependent variable $\mathbf{s}$ i.e. the element functions of $\boldsymbol{\varphi}$ are non-linear in the elements of $\mathbf{s}$.

In the present context of structural dynamics, eqs. (3.1) or (3.2) are the equations of motion: eq. (3.1) corresponds to the forced case (i.e. a system subjected to time-varying external excitation, for example the rotor unbalance force in a rotor-dynamic system) and eq. (3.2) to the unforced case (i.e. a system not subjected to time-varying external excitation). Except for the short notes on unforced non-linear systems in section 3.3 of this chapter and in section 4.7 of Chapter 4, this thesis is confined to the study of non-linear systems with time-varying external excitation that is harmonic with frequency Ω rad/s and period $T = 2\pi/\Omega$. For an unbalanced rotor-dynamic system Ω is the rotational speed and the amplitude of the unbalance forces is proportional to Ω^2 for a given state of unbalance. $\mathbf{s}$ is an $n\times 1$ vector of generalised coordinates and their time derivatives. Depending upon whether the original second order differential equations of motion are cast in finite element (FE) or modal form:

$$\mathbf{s} = [s_1 \quad \cdots \quad s_n]^T = \begin{bmatrix}\mathbf{u}\\ \dot{\mathbf{u}}\end{bmatrix} \text{ (FE form), or } \begin{bmatrix}\mathbf{q}\\ \dot{\mathbf{q}}\end{bmatrix} \text{ (modal form)} \tag{3.5}$$

where $\mathbf{u}$ is the vector of degrees of freedom (as in the FE equations of page 9) and $\mathbf{q}$ is the vector of modal coordinates (see Chapter 5, section 5.4). The first $n/2$ equations of (3.1) or (3.2) are hence $[\dot{s}_1 \quad \cdots \quad \dot{s}_{n/2}]^T = [s_{n/2+1} \quad \cdots \quad s_n]^T$. The remaining equations are then the (originally second order) differential equations of motion. For the unforced system in eq. (3.2), the $n\times 1$ vector $\mathbf{s}$ is referred to as the state vector. The specification of the state of the forced system requires knowledge of both $\mathbf{s}$ and t (or Ωt). Hence, in this case, the state vector is defined as the augmented vector $\mathbf{s}_{aug}$

$$\mathbf{s}_{aug} = \begin{bmatrix}\Omega t\\ \mathbf{s}\end{bmatrix} \tag{3.6}$$

The elements of the state vector are the state variables and the associated n or $(n+1)$-dimensional space is the state space. For the forced system, when visualising plots of trajectories of $\mathbf{s}(t)$ from given initial conditions $\mathbf{s}(t_0)$ in the state space, the independent state variable Ωt is an *angular* coordinate [16, 34]. In this way, a periodic solution to equation (3.1) of period NT, where N is a positive integer i.e. $\mathbf{s}(t)=\mathbf{s}(t+NT)$ will appear as a *closed* loop in the state space since $\Omega(t+NT)$ $(=\Omega t+N2\pi)$ will then represent the same angle as Ωt.

A Poincaré map is obtained by sampling the trajectory of $\mathbf{s}(t)$ in state space at discrete times t_k, $k=0,1,2,\ldots$, according to certain rules which are different for forced and unforced systems [38]. The sampled points $\mathbf{s}(t_k)$ are called the "return points". For a periodically driven system, the map is a stroboscopic picture of the trajectory i.e. the trajectory is sampled at fixed intervals, usually equal to the period T of the excitation, hence $t_k=t_0+kT$ where t_0 is some arbitrarily chosen sampling start time. Hence, motion of period NT ("NT-periodic motion") appears as N discrete points on the map when the sampling interval is T. A two-dimensional Poincaré map is obtained by plotting two elements of the sampled vector $\mathbf{s}(t_k)$.

Dissipative systems are characterised by attractors. An attractor is a bounded set of points in state space which the trajectory of $\mathbf{s}(t)$ reaches after the transients due to the initial conditions $\mathbf{s}(t_0)$ die out. Regions of initial conditions in state space shrink asymptotically on to the attractor as time progresses. For a periodically driven system, an attractor may be one of the following:

(a) Periodic attractor, where $\mathbf{s}(t)=\mathbf{s}(t+\Gamma)$, Γ being the period and $\varpi=2\pi/\Gamma$ rad/s the fundamental frequency of the oscillation. Since the frequency components of this periodic motion are integer multiples of ϖ and the excitation frequency Ω is assumed to be one of these, ϖ must be equal to Ω/N where N is a positive integer, and so, the motion is NT-periodic.

(b) Quasi-periodic attractor - motion with two (or more) fundamental frequencies.

(c) Strange attractor - chaotic motion.

An attractor can be located by integrating eq. (3.1) from arbitrarily chosen initial conditions $\mathbf{s}=\mathbf{s}(t_0)$ at $t=t_0$ and allowing sufficient time for the initial transients to die out. This process is referred to as "solving the initial value problem" or "time-marching" and is done using a convenient step-by-step numerical integration scheme (e.g. Runge-Kutta, ... etc.).

Solutions to eqs. (3.1) or (3.2) that are non-transient i.e. that exhibit *long-term* steady-state behaviour ("steady-state" solutions) are referred to as equilibrium solutions [43] and are denoted by $\mathbf{s}_E(t)$. Attractors describe equilibrium solutions. The converse is not necessarily true however. Consider (equilibrium) periodic solutions to the forced equation (3.1). As discussed above, these are *NT*-periodic, such that $\mathbf{s}_E(t)=\mathbf{s}_E(t+NT)$, and form closed loops or cycles in state space. Like the static equilibria of unforced systems (section 3.3), these periodic oscillations can be either stable or unstable. A periodic oscillation is said to be asymptotically stable (or simply, stable) if trajectories starting from nearby initial conditions converge towards the cycle. A stable periodic oscillation is a periodic attractor. Conversely, an unstable periodic oscillation will repel trajectories from nearby initial conditions. Note that, since this unstable periodic oscillation *is* a solution of equation (3.1), a trajectory starting *exactly* at a point on the cycle will never leave it provided there is not the slightest fluctuation in operating conditions. Such an oscillation clearly cannot be realised in practice: even in the highly improbable case of getting conditions exactly on the cycle, the oscillation cannot be maintained due to inevitable minor fluctuations in operating conditions. Likewise, unstable periodic solutions cannot be calculated by time-marching, even in the highly improbable cases of starting with initial conditions exactly on the cycle or getting there through a stable manifold[1]. The reason for this is that the inevitable local integration error in each time step introduces minute perturbations into the computed trajectory of $\mathbf{s}(t)$, thus invariably driving it towards an attractor, which, by definition, is stable to minute perturbations. As discussed in Chapters 1 and 2, periodic solution techniques using analytical methods like harmonic balance (HB) or trigonometric collocation (TC) *pre-assume* periodic solutions of given period. Hence, the resulting solutions need to be tested to determine whether they represent stable or unstable periodic motion. It is noted in passing that an alternative periodic solution technique not mentioned in Chapter 2 is to solve eq. (3.1) as a two-point boundary value problem [16] rather than as an initial value problem. However, the resulting periodic solutions still need to be tested for stability [16]. It is customary to generate a batch of periodic solutions over a range of values of a system control parameter and plot some property of the solutions (e.g. amplitude) versus the control parameter to form a response curve of periodic solutions e.g. in rotating systems the control parameter would be the rotational speed and the resulting plot called the speed response

[1] A stable manifold, if it exists, defines a certain set of initial conditions from which a point on an unstable cycle can be reached [35].

curve of periodic solutions. The stability of each periodic solution on the response curve is then analysed.

The following section deals with the issue of stability and bifurcation of periodic solutions. A bifurcation is a qualitative change in the dynamics that occurs as a system control parameter is changed. For example, in the following section it is shown that the onset of instability of a periodic motion results in the three possible kinds of bifurcations.

3.2 STABILITY AND BIFURCATION OF PERIODIC SOLUTIONS

In this section the stability of a periodic solution of the forced system in eq. (3.1) with period Γ and fundamental frequency $\varpi = 2\pi/\Gamma$ rad/s is analysed. It is more convenient to work with non-dimensional time τ defined as $\tau = \varpi t$. The dynamical equations of the forced system are then rewritten in the form

$$\mathbf{s}' = \varphi(\mathbf{s}, \tau) \tag{3.7}$$

where $(\,)'$ denotes differentiation with respect to τ,

$$\mathbf{s} = [s_1 \quad \cdots \quad s_n]^T = \begin{bmatrix} \mathbf{u} \\ \mathbf{u}' \end{bmatrix} \text{ (FE form), or } \begin{bmatrix} \mathbf{q} \\ \mathbf{q}' \end{bmatrix} \text{ (modal form)} \tag{3.8}$$

and

$$\varphi(\mathbf{s}, \tau) = [\varphi_1(s_1, \ldots, s_n, \tau) \quad \cdots \quad \varphi_n(s_1, \ldots, s_n, \tau)]^T \tag{3.9}$$

It should be noted that the elements of the vectors $\mathbf{s}$ and φ in eqs. (3.8), (3.9) are generally different from those of $\mathbf{s}$ and φ in eqs. (3.3), (3.5). However, to economise on the use of symbols, the same symbols $\mathbf{s} = [s_1 \quad \cdots \quad s_n]^T$ and $\varphi = [\varphi_1 \quad \cdots \quad \varphi_n]^T$ have been retained. With this transformation of the independent variable, the (equilibrium) periodic solution of period $2\pi/\varpi$ in t now has a period of 2π in τ, regardless of ϖ i.e. $\mathbf{s}_E(\tau) = \mathbf{s}_E(\tau + 2\pi)$ and:

$$\mathbf{s}_E' = \varphi(\mathbf{s}_E, \tau) \tag{3.10}$$

To test the stability of $\mathbf{s}_E$, the evolution of a small perturbation $\mathbf{x}$ from $\mathbf{s}_E$ is considered:

$$\mathbf{x}(\tau) = \mathbf{s}(\tau) - \mathbf{s}_E(\tau) \tag{3.11}$$

Subtracting eq. (3.10) from eq. (3.7), expanding $\varphi(\mathbf{s}, \tau)$ into a Taylor series about $\mathbf{s} = \mathbf{s}_E$ and retaining only terms that are linear in $\mathbf{x} = \mathbf{s} - \mathbf{s}_E$, the following linearised perturbation equation is obtained:

$$\mathbf{x}' = \mathbf{W}(\tau)\mathbf{x} \tag{3.12}$$

where,
$$\mathbf{W}(\tau) = \mathbf{W}(\tau + 2\pi) = \left.\frac{\partial \varphi}{\partial \mathbf{s}}\right|_{\mathbf{s}=\mathbf{s}_E} = \left[\begin{array}{ccc} \frac{\partial \varphi_1}{\partial s_1} & \cdots & \frac{\partial \varphi_1}{\partial s_n} \\ \vdots & \vdots & \vdots \\ \frac{\partial \varphi_n}{\partial s_1} & \cdots & \frac{\partial \varphi_n}{\partial s_n} \end{array}\right]_{\mathbf{s}=\mathbf{s}_E(\tau)} \tag{3.13}$$

The theory developed from eq. (3.12) is called the linear stability theory [43]. Note that, although the independent variable τ disappears explicitly from the partial derivative expressions of the $n \times n$ Jacobian matrix $\partial\varphi/\partial\mathbf{s}$, these expressions are evaluated at $\mathbf{s} = \mathbf{s}_E(\tau)$, which is itself a periodic function of τ. Hence, $\mathbf{W}(\tau)$ must be periodic in τ, period 2π. Hence, eq. (3.12) is a system of ordinary linear homogeneous differential equations with periodically varying coefficients. The study of the stability of the equilibrium solution $\mathbf{s}_E(\tau)$ has thus been reduced to the study of the stability of such a system of equations, which can be conveniently done using Floquet theory [43, 44]. The coefficient matrix $\mathbf{W}(\tau)$ for the general squeeze film damped rotor-dynamic model is derived in Chapter 5. In the following three sections the fundamentals of Floquet theory, the computation of the Floquet transition matrix (governing stability), and the implications of instability (i.e. bifurcations) are discussed.

3.2.1 Fundamentals of Floquet Theory [43, 44]

The system of equations (3.12) will have n linearly independent solutions $\breve{\mathbf{x}}_1(\tau), \ldots\ldots, \breve{\mathbf{x}}_n(\tau)$. These can be collected into a *fundamental matrix* $\mathbf{X}(\tau)$:

$$\mathbf{X}(\tau) = [\breve{\mathbf{x}}_1(\tau) \quad \ldots \quad \breve{\mathbf{x}}_n(\tau)] \tag{3.14}$$

If, in addition, $\breve{\mathbf{x}}_1(0)=[1 \quad 0 \quad \cdots \quad 0]^T$, $\breve{\mathbf{x}}_2(0)=[0 \quad 1 \quad \cdots \quad 0]^T$, ..., $\breve{\mathbf{x}}_n(0)=[0 \quad \cdots \quad 0 \quad 1]^T$, then $\mathbf{X}(\tau)$ is referred to as the *principal fundamental matrix* $\mathbf{X}_P(\tau)$, which is unique. The solution to eq. (3.12) that satisfies the initial conditions $\mathbf{x}(0)=\mathbf{x}_0$ is thus [44]:

$$\mathbf{x}(\tau)=\mathbf{X}_P(\tau)\mathbf{x}_0 \tag{3.15}$$

In general neither $\mathbf{X}(\tau)$ nor $\mathbf{X}_P(\tau)$ is periodic. The *monodromy matrix* $\mathbf{G}$ is defined as

$$\mathbf{G}=\mathbf{X}_P(2\pi) \tag{3.16}$$

If we define $\mathbf{x}_k=\mathbf{x}(k2\pi)$, $k=0,1,2,\ldots$, then it follows from eqs. (3.15), (3.16) and the fact that $\mathbf{W}(\tau)$ is periodic with period 2π that

$$\mathbf{x}_{k+1}=\mathbf{G}\mathbf{x}_k, \quad k=0,1,2,\ldots \tag{3.17}$$

For this reason, the monodromy matrix $\mathbf{G}$ is also referred to as the *growth matrix* [45, 46] or the *Floquet transition matrix* [13]. Hence, the linear continuous-time system of eq. (3.12) has been transformed to the linear discrete-time system of eq. (3.17). By substituting into eq. (3.17) a trial solution of the form $\mathbf{x}_k=\lambda^k\mathbf{e}$ it is readily seen that λ must be an eigenvalue of $\mathbf{G}$ and $\mathbf{e}$ is an associated eigenvector. Hence, the solution to eq. (3.17) (which is the discrete solution to eq. (3.12)) is of the general form

$$\mathbf{x}_k=\sum_{i=1}^{n}c_i\lambda_i^k\mathbf{e}_i, \quad k=0,1,2,\ldots \tag{3.18}$$

where λ_i $(i=1\ldots n)$ are the eigenvalues of $\mathbf{G}$ (also known as the *Floquet multipliers*), the $\mathbf{e}_i$ are corresponding eigenvectors and c_i are arbitrary scalar constants. Hence, for the asymptotic stability of the periodic solution $\mathbf{s}_E(\tau)$ to eq. (3.1):

$$|\lambda_i|<1, \text{ for } i=1\ldots n \tag{3.19}$$

3.2.2 Computation of the Monodromy Matrix

From the previous section, it can be seen that the stability test of a given periodic solution to the dynamical equations (3.1) requires the knowledge of the associated monodromy matrix. This section deals with the computation of $\mathbf{G}$ from the coefficient matrix $\mathbf{W}(\tau)$ of the perturbation equation (3.12). Two methods are available for the computation of $\mathbf{G}$, which are referred to here as the "slow" and "fast" methods respectively.

The "slow" method is based on the definition of $\mathbf{G}$ given in the previous section, eq. (3.16). Hence, this involves solving the perturbation equation (3.12) by a numerical integration scheme (e.g. Runge-Kutta, ... etc.) over the interval $\tau = 0$ to $\tau = 2\pi$ for n initial conditions $\breve{\mathbf{x}}_1(0) = [1 \quad 0 \quad \cdots \quad 0]^T$, $\breve{\mathbf{x}}_2(0) = [0 \quad 1 \quad \cdots \quad 0]^T$, ..., $\breve{\mathbf{x}}_n(0) = [0 \quad \cdots \quad 0 \quad 1]^T$, in turn. The monodromy matrix $\mathbf{G}$ is then formed from the values of the resulting n solutions at $\tau = 2\pi$:

$$\mathbf{G} = [\breve{\mathbf{x}}_1(2\pi) \quad \ldots \quad \breve{\mathbf{x}}_n(2\pi)] \tag{3.20}$$

This method is extremely time consuming, which makes it impractical to test the stability of a whole set of periodic solutions forming a response curve. This method was used by Chen *et al.* [12] and Hahn and Chen [15].

Hsu [45, 46] developed a very fast approximate method for computing the monodromy matrix, based on impulsive parametric excitation theory. This "fast" method was used by Zhao *et al.* [13]. In this technique, the periodic interval $[0, 2\pi]$ of the periodic matrix function $\mathbf{W}(\tau)$ is divided into K equal segments $\Delta\tau$. Let τ_k, $k = 1 \ldots K$, be the value of τ at the midpoint each segment. $\mathbf{W}(\tau)$ is replaced over $[0, 2\pi]$ by a series of impulses of strength $\mathbf{W}_k \Delta\tau$ where

$$\mathbf{W}_k = \mathbf{W}(\tau_k) \tag{3.21}$$

It can be shown that $\mathbf{G}$ can be approximated by a product of matrix exponentials [45]:

$$\mathbf{G} \approx e^{\mathbf{W}_K \Delta\tau} e^{\mathbf{W}_{K-1} \Delta\tau} \ldots e^{\mathbf{W}_2 \Delta\tau} e^{\mathbf{W}_1 \Delta\tau} \tag{3.22}$$

The above product converges to the exact matrix $\mathbf{G}$ as $K \to \infty$. However, in all the simulations presented in this thesis, $K = 200$ gave highly accurate results.

3.2.3 Bifurcation of Periodic Solutions

From eq. (3.19), for the (equilibrium) periodic solution $\mathbf{s}_E(\tau)$ to be stable, all the eigenvalues of the associated monodromy matrix $\mathbf{G}$ must lie within a unit circle in the complex plane centred at the origin. The stability is hence controlled by the eigenvalue of largest absolute value (magnitude), known as the leading eigenvalue or leading Floquet multiplier, λ_l. This eigenvalue is either real or one of a complex conjugate pair (λ_l, λ_l^*)[2]. If, as a system control parameter is changed (e.g. the rotational speed Ω), the leading eigenvalue λ_l escapes from the circle, then $\mathbf{s}_E(\tau)$ becomes unstable and a bifurcation occurs. As shown in Figure 3.1, the leading eigenvalue has three possible escape routes and hence three kinds of bifurcation are possible: (a) tangent bifurcation (escape along the positive real axis); (b) period-doubling bifurcation (escape along the negative real axis); (c) secondary Hopf bifurcation (simultaneous escape of two complex conjugate leading eigenvalues). These bifurcations are explained in the following paragraphs with the aid of the Poincaré map. In what follows, the sampling interval of the map is taken as *the period of the equilibrium periodic solution* (period $2\pi/\varpi = NT$ in the t-domain and period 2π in the τ-domain) rather than that of the driving force (T in the t-domain), so that the cycle always appears as a single point on the map, regardless of N. The evolution of the return points of the trajectory for an initial small disturbance from an unstable equilibrium cycle is given by eq. (3.18) and if $\mathbf{x}_k = \mathbf{x}(k2\pi)$ is plotted rather than $\mathbf{s}(k2\pi)$, the point $(0,0)$ on the two-dimensional Poincaré map will correspond to the fixed point $\mathbf{s}_E(k2\pi)$ on the unstable equilibrium cycle.

Case (a): λ_l real and positive and $|\lambda_l| > 1$:

From eq. (3.18)

$$\mathbf{x}_k \approx c_l \lambda_l^k \mathbf{e}_l \tag{3.23}$$

From eq. (3.23), since λ_l is real, consecutive return points on a Poincaré map will lie approximately on a straight line of direction determined by the eigenvector $\mathbf{e}_l$. Since $\lambda_l > 0$,

[2] Since $\mathbf{G}$ is a real matrix, any complex eigenvalues must occur in conjugate pairs.

they will lie on the *same* side of the unstable equilibrium point (0,0) (at increasing distances from it, since $|\lambda_l| > 1$). This illustrated in Figure 3.2(a), which plots the two elements of $\mathbf{x}_k$ against each other for $\lambda_l = 1.1$, $c_l\mathbf{e}_l = [0.2 \quad 0.4]^T$. Hence, the perturbed trajectory tends to a periodic motion of the same period as the unstable equilibrium cycle. If such a periodic attractor exists in the vicinity, the return points eventually congregate at a single fixed point at one end of the line as the trajectory settles down on the attractor. The onset of this type of instability as one progresses along the response curve, marked by the escape of λ_l from the unit circle along the positive real axis, is called a saddle-node bifurcation, tangent bifurcation, or turning point bifurcation. This instability is normally associated with bistable regions of the response curve (see Figure 2.1).

Case (b): λ_l real and negative, $|\lambda_l| > 1$:

Eq. (3.23) still applies and consecutive sampled points on a Poincaré map will approximately lie on a straight line of direction determined by $\mathbf{e}_l$. However, since the leading multiplier $\lambda_l < 0$, consecutive return points flip on either side of the unstable equilibrium point (0,0) (at increasing distances from it, since $|\lambda_l| > 1$). This illustrated in Figure 3.2(b) for $\lambda_l = -1.1$, $c_l\mathbf{e}_l = [0.2 \quad 0.4]^T$ (consecutive return points are indicated by crosses and circles). Hence, the perturbed trajectory tends to a periodic motion of twice the period of the unstable equilibrium cycle. If such a periodic attractor, having a fundamental frequency $\varpi/2$ rad/s, exists in the vicinity, the return points eventually congregate at two fixed points, on either side of the unstable equilibrium point. The onset of this type of instability as one progresses along the response curve, marked by the escape of λ_l from the unit circle along the negative real axis, is called a period-doubling bifurcation or a flip bifurcation.

Case (c): λ_l complex, $|\lambda_l| = |\lambda_l^*| > 1$:

From eq. (3.18)

$$\mathbf{x}_k \approx c_1\lambda_l^k\mathbf{e}_l + c_2(\lambda_l^*)^k\mathbf{e}_l^* \tag{3.24}$$

Now $\lambda_l = |\lambda_l|e^{j\vartheta}$, hence, $\lambda_l^k = |\lambda_l|^k e^{jk\vartheta} = |\lambda_l|^k\{\cos k\vartheta + j\sin k\vartheta\}$. Just as for ordinary linear homogeneous differential equations with constant coefficients [44], it can be shown that $\mathbf{x}_k$ can be expressed as $\mathbf{x}_k = d_1\,\mathrm{Re}\{\lambda_l^k\mathbf{e}_l\} + d_2\,\mathrm{Im}\{\lambda_l^k\mathbf{e}_l\}$ where d_1, d_2 denote arbitrary scalar

constants and $\mathrm{Re}\{\ \}, \mathrm{Im}\{\ \}$ denote the real and imaginary parts of $\{\ \}$ respectively. Hence $\mathbf{x}_k$ is of the form

$$\mathbf{x}_k \approx |\lambda_l|^k \{\mathbf{d}_1 \cos k\vartheta + \mathbf{d}_2 \sin k\vartheta\} \tag{3.25}$$

where $\mathbf{d}_1$, $\mathbf{d}_2$ are real vectors and ϑ is the phase angle of λ_l $(0 \le \vartheta < 2\pi)$. Eq. (3.25) means that the return points will spiral out of the unstable equilibrium point (0,0). As an example, the two elements of $\mathbf{x}_k$ are plotted against each other for $|\lambda_l| = 1.1$, $\mathbf{d}_1 = [0.2 \quad 0.4]^T$, $\mathbf{d}_2 = [0.4 \quad 0.2]^T$ in Figures 3.3(a-d). It is seen that, as the return points spiral out around the origin, consecutive points hop from one spiral branch to the next, and that the number of branches is equal to $\breve{k}_1$ where $\vartheta \approx (\breve{k}_2/\breve{k}_1)2\pi$, $\breve{k}_1$, $\breve{k}_2$ being non-negative integers with $\breve{k}_1 > \breve{k}_2$ and having no common factor. Consecutive points are indicated by crosses and circles in Figure 3.3(b), by crosses, circles and squares in Figure 3.3(c), and by crosses, circles, squares and diamonds in Figure 3.3(d). This indicates that the perturbed trajectory tends to a motion that contains *two* fundamental frequencies: the original one at ϖ rad/s and a new one that is *approximately* $(\breve{k}_3/\breve{k}_1)\varpi$ rad/s where $\breve{k}_3$ is some positive integer that has no factor in common with $\breve{k}_1$. If such a 2-*frequency quasi-periodic* attractor exists in the vicinity, the return points stop diverging and settle down, densely filling a closed curve around the origin. The reason for this curve or "drift ring" is that the two fundamental frequencies are in general incommensurate (i.e. their ratio is an irrational number) and hence the steady motion is aperiodic (more specifically, "quasi-periodic"), with the return points never quite coinciding with each other. The onset of this type of instability as one progresses along the response curve, marked by the simultaneous escape from the unit circle of two complex conjugate leading eigenvalues, is called a secondary Hopf bifurcation. The reason for this is that the birth of the 2-frequency quasi-periodic attractor from the periodic motion is analogous to the birth of a periodic attractor from the static equilibrium point of an unforced system (primary Hopf bifurcation). Note that, in the exceptional case that ϑ is exactly equal to $(\breve{k}_2/\breve{k}_1)2\pi$, the second fundamental frequency is exactly $(\breve{k}_3/\breve{k}_1)\varpi$ and hence commensurate with the first. In this case (see Figures 3.4(a,b)), the $\breve{k}_1$ spiral branches straighten out and when steady conditions are reached, the return points congregate at $\breve{k}_1$

fixed points around the origin. In this exceptional case, the generally quasi-periodic 2-frequency motion is said to be *locked* into periodic motion of fundamental frequency $\varpi/\tilde{k}_1$. This "frequency-locking" is explained in more detail in section 3.4. Notice that the cases when ϑ is exactly equal to $(0/1)2\pi$ and $(1/2)2\pi$ correspond to the previous cases (a) and (b) respectively (Figures 3.2(a,b)).

From the above, the three types of bifurcation points on the response curve of periodic solutions are defined at the *onset* of instability and classified according to the escape route of the leading Floquet multiplier from the unit circle. However, for a general unstable periodic solution, the position of the corresponding λ_l on the complex plane is *not* by itself a definite indicator of the type of attractor on which a disturbance from it will settle down, especially if the unstable solution is well past the bifurcation point. The reason for this is that Floquet theory applies for small linearised perturbations about $\mathbf{s}_E$: hence, apart from definitely indicating that $\mathbf{s}_E$ is unstable, eq. (3.18) can only indicate the type of motion that the disturbed trajectory *tends* to in the initial stages of the perturbation when $\mathbf{x}_k$ is small, and gives no assurance that it will ultimately settle down to that motion. The attractor can only be positively identified by time-marching from unstable equilibrium initial conditions.

3.3 NOTE ON UNFORCED SYSTEMS

Unforced systems were defined in section 3.1 as systems that are not subjected to time-varying external excitation. One feature that distinguishes the unforced problem in eq. (3.2) from the forced problem of eq. (3.1) is that an additional type of equilibrium solution (i.e. steady-state solution) is possible – that describing static equilibrium. The static equilibrium states are defined by time-independent solutions to eq. (3.2), obtained by setting the right hand side of eq. (3.2) to zero and solving the resulting algebraic equation

$$\boldsymbol{\varphi}(\mathbf{s}) = \mathbf{0} \tag{3.26}$$

Each solution $\mathbf{s} = \mathbf{s}_{ES}$ to eq. (3.26) corresponds to a state of static equilibrium in the "Newtonian" sense (i.e. zero velocities and accelerations). The stability of each solution $\mathbf{s}_{ES}$ is tested by considering the evolution of small perturbations $\mathbf{x}_S = \mathbf{s} - \mathbf{s}_{ES}$, and as in section 3.2, this results in an equation of the form

$$\dot{\mathbf{x}}_S = \left.\frac{\partial \varphi}{\partial \mathbf{s}}\right|_{s=s_{ES}} \mathbf{x}_S = \mathbf{A}\mathbf{x}_S \tag{3.27}$$

where $\mathbf{A} = \partial\varphi/\partial\mathbf{s}|_{s=s_{ES}}$. However, the partial derivatives in this $n \times n$ Jacobian matrix are now evaluated at $\mathbf{s} = \mathbf{s}_{ES}$, hence $\mathbf{A}$ will be constant with respect to time. Hence, eq. (3.27) is a system of ordinary linear homogeneous differential equations with constant coefficients, the stability of which being governed directly by the eigenvalues of $\mathbf{A}$. $\mathbf{s}_{ES}$ is unstable when the real part of one or more eigenvalues is positive [35]. The perturbation equations (3.27) define the motion of the unforced system for small linearised displacements about the static equilibrium position (i.e. the usual unforced "linear system" considered in texts on linear dynamics e.g. [47, 48]). For oscillatory motion, the eigenvalues of $\mathbf{A}$ will all be complex, occurring in conjugate pairs $\zeta_i \pm \mathrm{j}\upsilon_i$, $i = 1 \ldots n/2$, where the υ_i's are the damped natural frequencies [47, 48]. Hence, as a system parameter is changed (e.g. the rotational speed Ω), the onset of instability is marked by a pair of purely imaginary conjugate eigenvalues, which defines a primary Hopf bifurcation [16]. This bifurcation marks the birth of limit cycle behaviour – "self-excited vibration". Once such *periodic* attractors have developed, the unforced system can proceed to bifurcate in one of the three ways described in section 3.2 (i.e. tangent, flip, or secondary Hopf bifurcation). In rotor-dynamics, journal bearings are known to induce self-excited vibration [48]. Since some degree of unbalance will always be present in practical rotating systems, the self-excited limit cycle will combine with the T-periodic response from the unbalance force to form (in general) quasi-periodic motion. Hence, under low levels of unbalance excitation, a primary Hopf bifurcation of the unforced system at some value of the system control parameter μ manifests itself as a secondary Hopf bifurcation of forced T-periodic oscillations at the same value of μ. It is shown in Chapter 4, section 4.7, that squeeze film dampers (SFDs) cannot introduce self-excited vibration and so, the unforced problem need not be considered in such applications. For SFDs therefore, the existence of instability of forced T-periodic solutions relates directly to the external excitation (unbalance force), as observed by Li and Taylor [37]. Certain rotor-dynamicists, unaware of the general concept of stability in non-linear dynamics, have tended to associate the concept of stability exclusively to eq. (3.27) [49].

3.4 QUASI-PERIODICITY

K-frequency motion is a mixture of K periodic motions with respective periods T_r, $r=1\ldots K$ and corresponding fundamental frequencies $\Omega_r = 2\pi/T_r$. The motion is said to be "K-frequency quasi-periodic" if its K fundamental frequencies are "incommensurate" or "rationally independent". This means that none of the frequencies Ω_r can be expressed as a linear combination of the others using coefficients that are rational numbers i.e. the relation

$$\breve{k}_1\Omega_1 + \ldots + \breve{k}_K\Omega_K = 0 \tag{3.28}$$

does not hold for *any* set of integers $\breve{k}_1 \ldots \breve{k}_K$ except for the trivial solution $\breve{k}_1 = \ldots = \breve{k}_K = 0$. A simple form of K-frequency quasi-periodic motion would be the sum of the K periodic motions, where each element of $\mathbf{s}(t) = [s_1(t) \ \cdots \ s_n(t)]^T$ would be expressed as:

$$s_i(t) = \sum_{k=-\infty}^{\infty} {}_i^1c_k e^{jk\Omega_1 t} + \ldots + \sum_{k=-\infty}^{\infty} {}_i^Kc_k e^{jk\Omega_K t} \tag{3.29}$$

Each periodic motion in (3.29) has been expressed as a complex Fourier series [35]. On taking the Fourier transform of (3.29), it is seen that the frequency spectrum consists of discrete spikes at $|k\Omega_1|,\ldots,|k\Omega_K|$ for k integer. However, in general, the mixture of the K periodic motions goes beyond mere addition and in the general form of K-frequency quasi-periodic motion, each element of $\mathbf{s}(t) = [s_1(t) \ \cdots \ s_n(t)]^T$ can be expressed as a K-tuple complex Fourier series [35]:

$$s_i(t) = \sum_{k_1,\ldots k_K=-\infty}^{\infty} {}_ic_{k_1,\ldots k_K} e^{j(k_1\Omega_1+\ldots+k_K\Omega_K)t} \tag{3.30}$$

The special case of eq. (3.29) can be obtained from the general form in (3.30) by retaining only the coefficients ${}_ic_{k_1,0,\ldots,0}$, ${}_ic_{0,k_2,0,\ldots,0}$, ..., ${}_ic_{0,\ldots,0,k_K}$ and setting the rest to zero. The Fourier transform of (3.30) reveals that the frequency spectrum consists of discrete spikes at combination ("sum and difference") frequencies $|k_1\Omega_1 + \ldots + k_K\Omega_K|$ where $k_1 \ldots k_K$ are

integers (positive, negative, or zero). Of course, each of these spikes is modulated by the corresponding amplitude, ${}_i c_{k_1,\ldots k_K}$. Consider the case of 2-frequency quasi-periodic motion

$$s_i(t) = \sum_{k_1,k_2=-\infty}^{\infty} {}_i c_{k_1,k_2} e^{j(k_1\Omega_1 + k_2\Omega_2)t} \tag{3.31}$$

Hence, the spectrum consists of spikes at $|k_1\Omega_1 + k_2\Omega_2|$. If Ω_1 and Ω_2 become commensurate (i.e. rationally related), then $\Omega_2/\Omega_1 = \breve{k}_2/\breve{k}_1$ where $\breve{k}_1$ and $\breve{k}_2$ are positive integers with no common factor. Then the frequency spikes will occur at $|k_1\breve{k}_1 + k_2\breve{k}_2|\Omega_1/\breve{k}_1$ and hence become integer multiples of $\Omega_1/\breve{k}_1$. Hence, the 2-frequency motion is said to be locked into periodic motion of fundamental frequency $\Omega_1/\breve{k}_1$. *In fact, periodic motion is merely a special case of the K-frequency motion defined by eq.* (3.30) *that occurs when the generally incommensurate K fundamental frequencies become all commensurate with each other.* Notice, that for both cases Ω_1, Ω_2 incommensurate and Ω_1, Ω_2 commensurate, the frequency spectrum is *discrete*. In eq. (3.31), by writing $\theta_r = \Omega_r t$, $r = 1, 2$:

$$s_i(t) = \sum_{k_1,k_2=-\infty}^{\infty} {}_i c_{k_1,k_2} e^{j(k_1\theta_1 + k_2\theta_2)} \tag{3.32}$$

In eq. (3.32), $s_i(t)$ is periodic in each of θ_1 and θ_2 with period 2π. Hence, regardless of the size n of $\mathbf{s}(t)$, each of its elements is fully specified by two *angle* variables θ_1, θ_2. Specification of two angles can be regarded geometrically as specifying a point on a two-dimensional toroidal surface ("2-torus"), as in Figure 3.5. In full state space, the attractor defined by eq. (3.32) is equivalent to a 2-torus (i.e. a distorted version of Figure 3.5) [35]. Since Ω_1 and Ω_2 are incommensurate, as t progresses, the trajectory of $\mathbf{s}(t)$ never closes in on itself and will eventually cover the whole surface of the 2-torus i.e. cover every possible value of θ_1, θ_2. The reason for this type of aperiodic motion is explained as follows. If $\mathbf{s}(t)$ is sampled at the period of Ω_1 i.e. $t_k = t_0 + kT_1$, $k = 0, 1, \ldots$, then $\theta_{1k} = \Omega_1 t_k = \Omega_1 t_0 + k2\pi$. Hence, the times t_k are the instances when the trajectory $\mathbf{s}(t)$ passes the cross-section of the 2-torus in Figure 3.5 at $\theta_1 = \Omega_1 t_0$. Substituting for t_k into eq. (3.32):

$$s_i(t_k) = \sum_{k_1,k_2=-\infty}^{\infty} \left({}_i c_{k_1,k_2} e^{jk_1\Omega_1 t_0} \right) e^{jk_2\theta_{2k}} \tag{3.33}$$

where $$\theta_{2k} = \Omega_2 t_k = \Omega_2 t_0 + k2\pi(\Omega_2/\Omega_1), \quad k = 0,1,\ldots \tag{3.34}$$

As k progresses, the sampled vector $\mathbf{s}(t_k)$ will then trace a closed curve, densely filled with drifting return points since θ_{2k} covers all geometrically distinct angle values of θ_2 if the ratio Ω_2/Ω_1 in eq. (3.34) is irrational. In the special case where Ω_1 and Ω_2 are commensurate, $\Omega_2/\Omega_1 = \breve{k}_2/\breve{k}_1$ (as previously explained) and eq. (3.34) reduces to $\theta_{2k} = \Omega_2 t_0 + k2\pi(\breve{k}_2/\breve{k}_1)$. Hence, as k progresses, θ_{2k} covers only $\breve{k}_1$ geometrically distinct angle values of θ_2 and the drift ring of $\mathbf{s}(t_k)$ degenerates into $\breve{k}_1$ distinct points. In this case, the trajectory of $\mathbf{s}(t)$ can still be considered to ride on the 2-torus but it does not cover its entire surface. Instead, it closes in on itself (forms a cycle) since it is locked into $\breve{k}_1 T_1$-periodic motion (fundamental frequency $\Omega_1/\breve{k}_1$). In general, an attractor describing K-frequency quasi-periodic motion is said to define a K-dimensional torus ("K-torus") i.e. a K-dimensional subspace in which it is possible to specify uniquely any point by the values of K independent angle variables. Moreover, by sampling at a fixed interval equal to the period of one of the fundamental frequencies, the return points $\mathbf{s}(t_k)$ define a torus of reduced dimension $K-1$. Since one of the fundamental frequencies is normally the excitation frequency $\Omega = 2\pi/T$, 2-frequency quasi-periodic motion manifests itself as a closed curve on a Poincaré map sampled at fixed intervals $t_k = t_0 + kT$, $k = 0,1,\ldots$. However, K-frequency quasi-periodic motion with $K \geq 3$ is hard to identify using this method.

Combination frequencies are now discussed. The frequency spectrum of the quasi-periodic response of a *non-linear* system is characterised by linear combinations of its fundamental frequencies, as in eq. (3.30). The simple form of quasi-periodic motion in eq. (3.29) does not contain combination frequencies in its frequency spectrum. When inputs of this form are fed into a *linear* system, the steady-state output (response) will be of the same form. However, when inputs of the simple form in (3.29) are fed into a *non-linear* system, the steady-state output may be of the form in (3.30). This is illustrated schematically in Figure 3.6 for a 2-frequency input of the simple form (3.29) with one harmonic of each

fundamental frequency: $y_I(t) = A_1 \sin(\Omega_1 t + \vartheta_1) + A_2 \sin(\Omega_2 t + \vartheta_2)$ where ϑ_1, ϑ_2 are phase angles. In Chapter 2, two examples were quoted from the literature where the phenomenon illustrated in Figure 3.6(b) was observed experimentally: (a) Holmes and Dede [31], in which Ω_1 and Ω_2 were the rotational speeds of two unbalanced rotors coupled non-linearly through a SFD (the input $y_I(t)$ being the sum of the two unbalance forces); (b) Ehrich [39], in which the input $y_I(t)$ was a displacement with one frequency, Ω_1, synchronous with the rotor rotation (attributed to the unbalance) and the other, Ω_2, asynchronous, attributed to some non-linear effect. Both frequencies were estimated by Ehrich from the frequency spectrum of the measured output. The non-linear operator applied by Ehrich to $y_I(t)$ was a truncation function due to the rotor operating eccentrically in the bearing clearance:

$$y_O(t) = \begin{cases} y_I(t), & y_I(t) \geq y_{\min} \\ y_{\min}, & y_I(t) < y_{\min} \end{cases} \tag{3.35}$$

where $y_{\min}$ is the truncation level. The application of this non-linear operator yielded frequency spikes at $k_1\Omega_1 + k_2\Omega_2$, k_1, k_2 integers, as observed experimentally. Note that Ehrich took $\Omega_2/\Omega_1 = 15/17$ i.e. the two frequencies were commensurate. Hence, both input and output motions were actually periodic and the combination frequencies generated by the truncation reduced to integer multiples of $\Omega_1/17$.

3.5 CHAOS

Chaotic motion is an aperiodic steady-state motion that is not quasi-periodic. The motion on a chaotic attractor displays exponentially sensitive dependence on initial conditions: this means that any two trajectories starting from nearby points on the attractor diverge exponentially in one or more directions while still remaining on the attractor, which is bounded. From geometric considerations, the described motion of adjacent trajectories can only be possible if they are free to roam in a state space of dimension of at least three [34]. Hence, if n is the size of **s**, for the forced system, eq. (3.1), $n+1 \geq 3 \Rightarrow n \geq 2$, whereas for the unforced system, eq. (3.2), $n \geq 3$. The exponential divergence of nearby trajectories on an attractor is measured by Lyaponov exponents [50]. If the spectrum of Lyaponov exponents of an attractor contains at least one that is positive, then the attractor is defined as

chaotic. Chaotic attractors are strange attractors [35, 50]. A strange attractor is a fractal i.e. an object of fractional dimension. On the other hand, K-frequency quasi-periodic attractors define K-tori and hence have an integer dimension of K. This latter statement is also true for $K = 1, 0$[3]. The return points on the Poincaré map of a chaotic attractor exhibit the fractal quality of "self-similarity" [16]. This means that a cluster of points tends to repeat itself on finer and finer scales upon increasing magnification. However, distinguishing chaotic motion from K-frequency quasi-periodic motion with $K \geq 3$ is not so straightforward using the Poincaré map. An alternative method to identify chaotic motion is to examine the frequency spectrum [35, 38]. Chaotic motion is characterised by a continuous component in the frequency spectrum with off-lifting spikes at the dominant frequencies. For experimental data, this continuum is well above the noise level [35]. However, as observed in [38], for systems having many degrees of freedom, the spectrum sometimes appears continuous because so many frequencies are involved in the response. The leakage effect from frequency spikes at close proximity results in a fake continuum in the spectrum. Indeed, this may also be a problem with quasi-periodic motion, which should otherwise have a discrete frequency spectrum. The only definite way of proving chaos is by computing the Lyapunov exponents. This can be done by two alternative methods [50]: (a) direct from the differential equations of motion (3.1) or (3.2); (b) from a time history of one dynamical variable $s_i(t)$ of $\mathbf{s}$. Method (a) is highly impractical. Method (b) requires large amounts of very accurate data, and the state space must be of low dimension. This method is the subject of intensive research, as evidenced by various alternative methods, each claiming to introduce further improvements [51]. For this reason, the computation of Lyaponov exponents is outside the scope of this thesis. In the author's opinion, the formal proof of chaotic motion is a highly academic issue. Moreover, as shall be seen in the following discussion, K-frequency quasi-periodic motion is unlikely to be stable for $K \geq 3$, anyway.

Routes to chaos are now discussed. Various routes to chaos are known to non-linear dynamicists [16, 34, 38] e.g. via successive period-doubling bifurcations, via quasi-periodicity. The results presented in this thesis indicate that, for the cases studied, it is the latter route that is relevant. It should be emphasised that quasi-periodicity is a *potential* route to chaos and does not necessarily lead to it. 2-frequency quasi-periodicity can lead to chaos in two possible ways: (a) bifurcation of the 2-torus [16], (b) frequency-locking [34]. The

[3] A 1-torus defines periodic motion (i.e. a cycle in state space) and a 0-torus defines a static equilibrium state of an unforced system (i.e. a point in state space).

scenarios (a) and (b) are likely to lead to chaos, but not necessarily so [34]. Route (a) is called the Newhouse-Ruelle-Takens route. [16] states that this theory is supported by both theoretical and experimental results and this theory is also credited in [34, 38]. According to this theory, should a system parameter be changed such that a tertiary Hopf bifurcation occurs (i.e. the addition of a third fundamental frequency to the existing two), the resulting 3-torus is most *likely* to be unstable: a small perturbation of the motion is likely to destroy the motion on the torus and lead to chaos and a strange attractor. Hence, in practice, only two fundamental frequencies are apparent before chaos sets in: when the third fundamental frequency is about to appear, chaos is more likely than bifurcation into a 3-torus. However, Ott [35] disputes the generality of this scenario and cites the results of some numerical experiments in which, below a critical level of non-linearity, 3-frequency quasi-periodic motion can be stable. Route (b) is based on the "sine-circle map" [34], which models the interaction between two non-linear voltage oscillators. According to this theory, given 2-frequency quasi-periodic motion with frequencies Ω_1 and Ω_2 in a non-linear system of fixed non-linearity, regions of quasi-periodicity (Ω_2/Ω_1 irrational) alternate with regions of frequency-locking (Ω_2/Ω_1 rational) over the operating range of the excitation frequency Ω_1. As the level of non-linearity is increased, the range of the control parameter Ω_1 over which the ratio Ω_2/Ω_1 is locked into any given rational number gets wider and, above some critical level of non-linearity, chaos becomes likely. In the numerical simulations presented in this thesis, once the destruction of the 2-torus is evident from the Poincaré map, no attempt is made to formally investigate the resulting motion for chaos. Consequently, the results are not formally analysed for routes (a) or (b).

3.6 NOTE ON THE DYNAMICS OF NUMERICS

When eqs. (3.1) or (3.2) are solved by time-marching, a numerical integration technique is used. In general, this technique is a "$\breve{n}$-step method" which means that the approximation $\mathbf{s}_k$ for $\mathbf{s}(t_k)$ is obtained from the approximations $\mathbf{s}_{k-\breve{n}} \ldots \mathbf{s}_{k-1}$ for $\mathbf{s}(t)$ at $\breve{n}$ previous times $t_{k-\breve{n}} \ldots t_{k-1}$ e.g. for the commonly used 1-step methods, which are self-starting for given initial conditions t_0, $\mathbf{s}_0$:

$$\mathbf{s}_k = F\{\Delta t, t_{k-1}, \mathbf{s}_{k-1}\} \tag{3.36}$$

where $\Delta t = t_k - t_{k-1}$ is the step size and $\boldsymbol{F}$ an operator, depending on the type of 1-step integration technique chosen (e.g. 4th order Runge-Kutta, trapezoidal integration, ... etc.). Hence, numerical integration involves the approximation of the original continuous-time system, eq. (3.1) or (3.2), by a discrete-time system (or "map"), like eq. (3.36). In general, the map in eq. (3.36) will have its own peculiar dynamics, and in particular, its own stability characteristics, which are dependent on both the step size Δt and the type of operator $\boldsymbol{F}$ [52]. The stability of steady-state solutions to the map in eq. (3.36) is referred to as "numerical stability". Of course, a good integration scheme should ensure that the map in eq. (3.36) faithfully reproduces the dynamics of the original continuous-time system in eqs. (3.1) or (3.2) and not introduce numerical artefacts into the results (e.g. spurious bifurcations). Hence, the following standard precautions are taken in this thesis:

(1) Automatic step size adjustment in each step to ensure that the computed estimate of the approximation error over the step ("local integration error") is within a specified tolerance.

(2) Appropriate choice of integration technique, based on the type of equations to be integrated (e.g. as mentioned in Chapter 2, Runge-Kutta methods are not suitable for stiff systems of equations).

The study of the stability characteristics of numerical integration techniques is referred to as the "dynamics of numerics" in [52] and is the province of mathematicians rather than engineering researchers. The precautions (1) and (2) above ensure that numerical stability is not an issue in this thesis and the term "stability" is taken exclusively to mean the stability of equilibrium solutions of the physical, continuous-time system.

3.7 CONCLUSION

In this chapter, the general concepts of non-linear dynamics, relevant to the subject of this thesis, have been elucidated. Special emphasis was placed on the stability and bifurcation of equilibrium periodic oscillations of forced systems, based on Floquet theory. Quasi-periodicity and the generation of combination frequencies were discussed in some detail. Chaos was briefly discussed. Additionally, short notes on the stability of the static equilibria of unforced systems and the numerical stability of time-marching techniques were given.

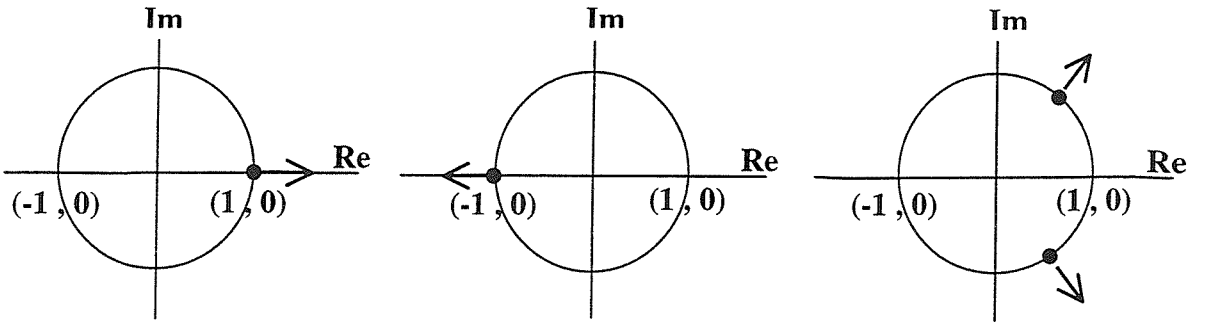

(a) tangent bifurcation (b) flip bifurcation (c) secondary Hopf bifucation

Figure 3.1: *Possible escape routes for the leading Floquet multiplier* λ_l

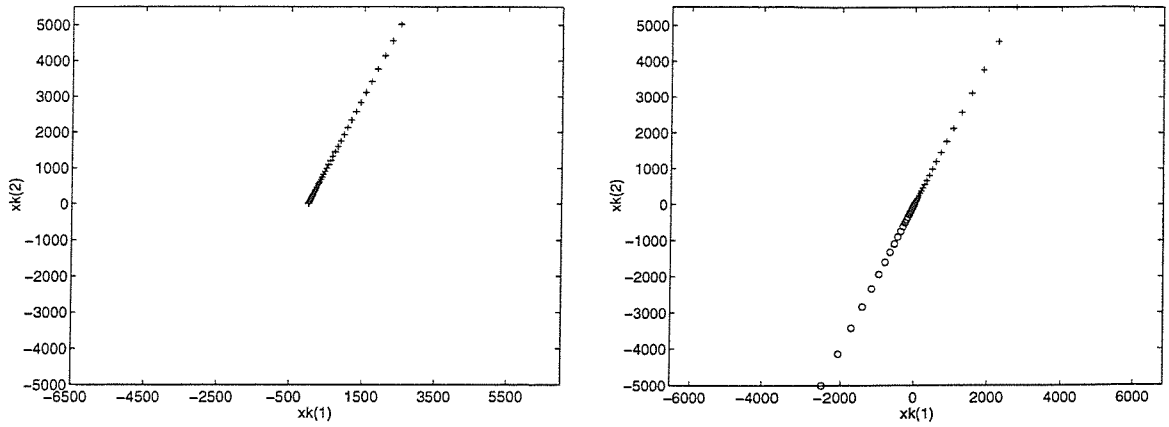

(a) λ_l positive (b) λ_l negative

Figure 3.2: *Behaviour of return points for* λ_l *real,* $|\lambda_l| > 1$

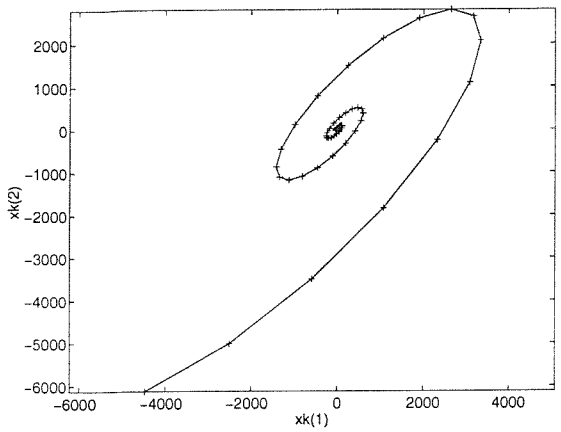

(a) $\vartheta = 0.3491 \approx (0/1)2\pi$

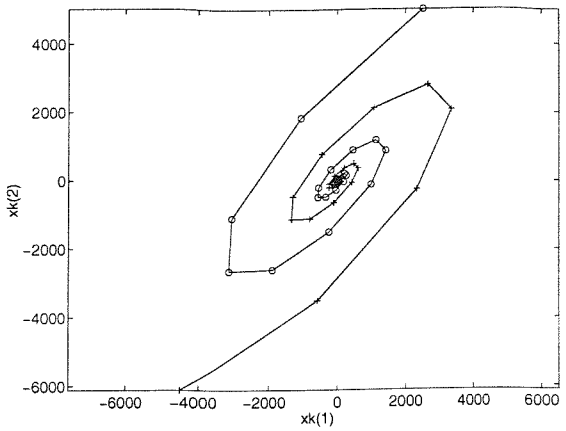

(b) $\vartheta = 3.4907 \approx (1/2)2\pi$

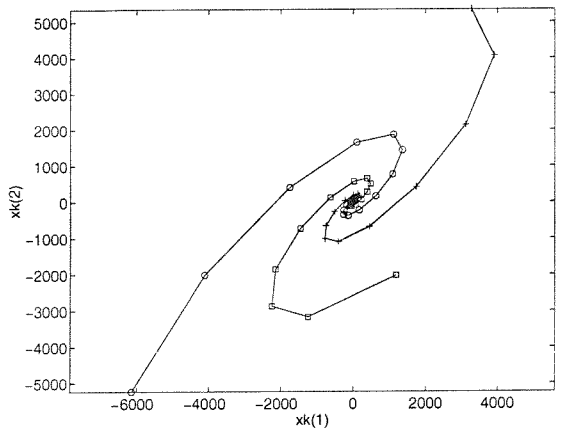

(c) $\vartheta = 4.0000 \approx (2/3)2\pi$

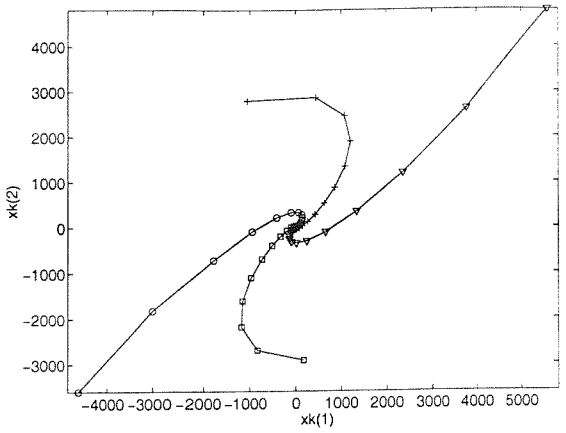

(d) $\vartheta = 4.6432 \approx (3/4)2\pi$

Figure 3.3: *Behaviour of return points for* λ_1 *complex,* $|\lambda_1| > 1$ (ϑ is the phase of λ_1)

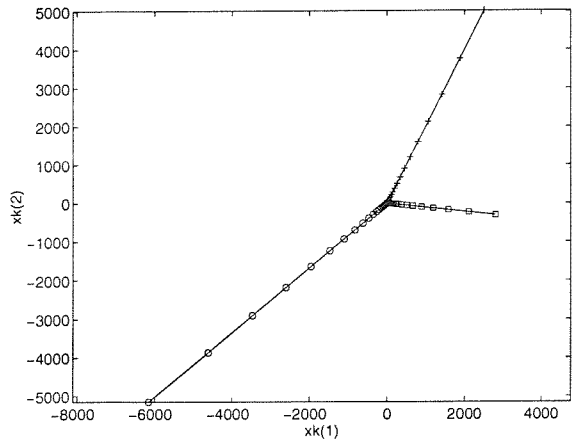

(a) $\vartheta = (2/3)2\pi$

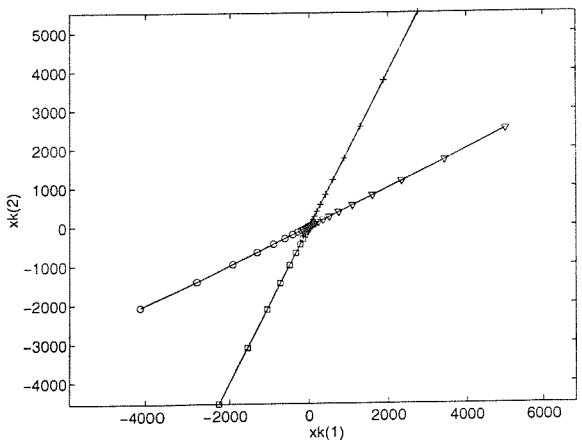

(b) $\vartheta = (3/4)2\pi$

Figure 3.4: *Behaviour of return points for* λ_1 *complex,* $|\lambda_1| > 1$: *frequency-locking case* (ϑ is the phase of λ_1; cf. Figures 3.3(c,d))

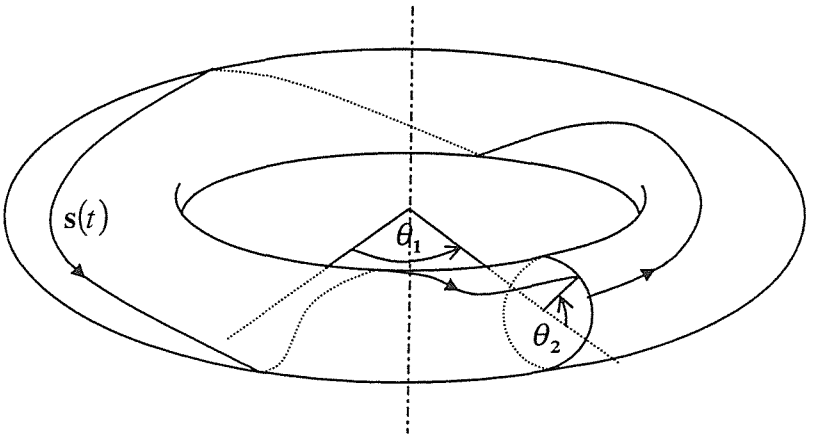

Figure 3.5: *2-torus representation of 2-frequency quasi-periodic motion*

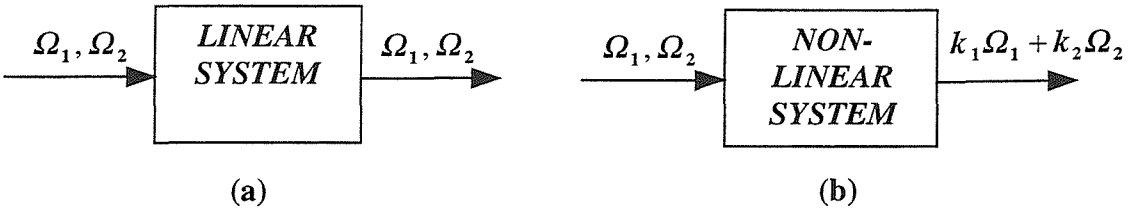

Figure 3.6: *Contrast between linear and non-linear systems for a 2-frequency input* (one harmonic of each fundamental in input)

4 SQUEEZE FILM DAMPER MODEL

4.1 INTRODUCTION

This chapter gives an outline of the model used for the estimation of the forces exerted by the non-linear element of the rotor-dynamic system i.e. the squeeze film damper (SFD). This damper is a non-linear element since its forces are non-linear functions of the relative displacements and velocities across it. In this introduction, the basic modelling assumptions are stated and the fundamental expressions presented. The short unsealed damper is then considered. The SFD modelling is illustrated for the simple case of a symmetrical rigid rotor on identical unsupported SFDs in rigidly mounted housings. In this thesis, *unless otherwise stated, all pressures are gauge pressures.* Moreover, in line with standard SFD design, the rolling-element bearing of the SFD journal assembly (Figure 1.1) is taken to be radially rigid with respect to the oil film.

Schematics of the cross-section of a SFD in the axial (xz or yz) plane are shown in Figures 4.1(a,b). In each case, the SFD is supplied by oil through holes symmetrically placed around a central circumferential groove. The one in Figure 4.1(a) is unsealed at its ends, and the one in Figure 4.1(b) is provided with end-plates, as in Figure 1.1. These end-plates can provide a degree of sealing by partially restricting the oil flow. This sealing is used to increase the damping, and the degree of sealing is controlled by the end-plate gap d_{gap}. In cases where the end-plates are required to prevent the journal from rotating (as in Figure 1.1), and for axial location of the journal (Chapter 8), the unsealed condition of Figure 4.1(a) is achieved by shimming the end-plates of Figure 4.1(b) such that the end-plate gap d_{gap} is at least of the order of the radial clearance c [53]. In this thesis, the SFD is modelled as comprising two independent lands supplied by oil at constant pressure p_S from a deep groove of depth d_{groove}. This "two-land model" is claimed to be valid provided [54]

$$d_{groove}/c > 9 \tag{4.1}$$

This condition is satisfied for the SFDs used in this thesis. It is further assumed that the lands are of equal length L, as in Figure 4.1. Figure 4.2 shows the transverse cross-section of the SFD. The analysis of the pressure distribution within a dynamically loaded SFD is identical to that of dynamically loaded circular bore hydrodynamic journal bearings [48] except that in the latter case the journal rotates integrally with the shaft. Hence, with reference to Figures 4.1 and 4.2, the Reynolds laminar lubrication equation for each land of the SFD, wherein the journal is prevented from rotating, is given by [53]

$$\frac{1}{R^2}\frac{\partial}{\partial\theta}\left\{h^3\frac{\partial p}{\partial\theta}\right\}+\frac{\partial}{\partial z}\left\{h^3\frac{\partial p}{\partial z}\right\}=12\eta c\left(\dot{\varepsilon}\cos\theta+\varepsilon\dot{\psi}\sin\theta\right) \tag{4.2}$$

where

$$h=c(1+\varepsilon\cos\theta) \tag{4.3}$$

is the oil film thickness. $\varepsilon=e/c$ is the non-dimensional eccentricity of the journal centre J from the bearing housing centre B and ψ is the attitude angle. R is the bearing housing bore radius. Among other things [48, 55], the Reynolds equation (4.2) assumes no fluid inertia, an incompressible fluid (i.e. density independent of pressure) and constant viscosity η. Eq. (4.2) can be solved for given boundary conditions to obtain the pressure distribution $p(\theta,z)$ at any instant in time. This solution depends on whether the damper is unsealed or sealed. The instantaneous radial and tangential squeeze film forces Q_R, Q_T respectively, acting on the journal (Figure 4.2), are obtained by integrating the pressure distribution $p(\theta,z)$ after truncating it below a minimum pressure at which the oil film is assumed to cavitate (i.e. rupture due to the formation of bubbles):

$$Q_R=-2R\int_{-L/2}^{L/2}\int_0^{2\pi}p_t(\theta,z)\cos\theta\ d\theta\ dz \qquad Q_T=-2R\int_{-L/2}^{L/2}\int_0^{2\pi}p_t(\theta,z)\sin\theta\ d\theta\ dz \tag{4.4a,b}$$

where the factor 2 accounts for the two lands and the truncated pressure distribution $p_t(\theta,z)$ is defined as

$$p_t(\theta,z)=\begin{matrix}p(\theta,z)\ , & p(\theta,z)>p_c\\ p_c\ , & p(\theta,z)\le p_c\end{matrix} \tag{4.5}$$

The film cavitation can be either vaporous or gaseous [55]. The former involves oil vaporisation together with the release of dissolved gases. The latter involves ambient air entering the oil film.

Since fluid inertia is neglected, the Reynolds equation (4.2) still applies when B is moving (Figure 4.2). The SFD forces are thus (non-linear) functions of the *relative* displacements and velocities across the damper. Let (X_J, Y_J) and (X_B, Y_B) be *absolute* Cartesian displacements of J and B respectively (i.e. the positions of J and B are measured from some fixed point in the *xy* plane of the SFD). Referring to Figure 4.2, the squeeze film forces Q_x, Q_y in the *x*, *y* directions respectively on the journal are given by resolving the radial and tangential forces Q_R, Q_T:

$$Q_x = Q_x\left(X_{rel}, Y_{rel}, \dot{X}_{rel}, \dot{Y}_{rel}\right) = -\left\{Q_R(\varepsilon, \dot{\varepsilon}, \dot{\psi})\sin\psi + Q_T(\varepsilon, \dot{\varepsilon}, \dot{\psi})\cos\psi\right\} \tag{4.6a}$$

$$Q_y = Q_y\left(X_{rrel}, Y_{rel}, \dot{X}_{rel}, \dot{Y}_{rel}\right) = Q_R(\varepsilon, \dot{\varepsilon}, \dot{\psi})\cos\psi - Q_T(\varepsilon, \dot{\varepsilon}, \dot{\psi})\sin\psi \tag{4.6b}$$

where $X_{rel} = X_J - X_B$, $Y_{rel} = Y_J - Y_B$, $\dot{X}_{rel} = \dot{X}_J - \dot{X}_B$, $\dot{Y}_{rel} = \dot{Y}_J - \dot{Y}_B$ are the Cartesian relative displacements and velocities across the damper and the conversion to the relative polar coordinates and their time derivatives is achieved through the relations:

$$e = \sqrt{\left(X_{rel}^2 + Y_{rel}^2\right)},\ \varepsilon = e/c,\ \dot{\varepsilon} = \frac{1}{ec}\left(X_{rel}\dot{X}_{rel} + Y_{rel}\dot{Y}_{rel}\right) \tag{4.7a,b,c}$$

$$\sin\psi = X_{rel}/e,\ \cos\psi = -Y_{rel}/e,\ \dot{\psi} = \frac{1}{e^2}\left(X_{rel}\dot{Y}_{rel} - Y_{rel}\dot{X}_{rel}\right) \tag{4.7d,e,f}$$

Additionally, since fluid inertia is neglected, the forces on the bearing housing are $-Q_x$, $-Q_y$.

Expressions for the (untruncated) pressure distribution $p(\theta, z)$ (e.g. that given in the following section for the short unsealed SFD, eq. (4.8)) show that the SFD forces are zero when there is no relative vibration across the damper i.e. $\dot{\varepsilon}, \dot{\psi} = 0$, or equivalently, $\dot{X}_{rel} = \dot{Y}_{rel} = 0$. This situation is in contrast to hydrodynamic journal bearings [48], in which

the fluid forces are of the form $\breve{Q}_{x,y}\left(X_{rel}, Y_{rel}, \dot{X}_{rel}, \dot{Y}_{rel}, \Omega\right)$ where Ω is the rotational speed, and $\breve{Q}_{x,y}\left(X_{rel}, Y_{rel}, 0, 0, \Omega\right) \neq 0$ unless $\Omega = 0$.

4.2 SHORT UNSEALED DAMPER

If the damper is unsealed and axially short ($L/(2R) \leq 0.25$ [56]), the *short bearing approximation* of the Reynolds equation applies. In this approximation, it is assumed that the pressure gradient in the circumferential (θ) direction is negligible relative to that in the axial (z) direction (i.e. $\partial p/\partial z >> \partial p/\partial \theta$) so that the first term on the left hand side of eq. (4.2) can be neglected. Integration of the resulting equation with respect to z and application of the boundary conditions $p = 0$ at $z = -L/2$, $p = p_S$ at $z = L/2$ (see Figure 4.1(a)) yields the short bearing solution for the unsealed damper as

$$p(\theta, z) = \frac{6\eta}{c^2} \frac{\{\varepsilon\dot{\psi}\sin\theta + \dot{\varepsilon}\cos\theta\}}{\{1 + \varepsilon\cos\theta\}^3}\left(z^2 - \frac{L^2}{4}\right) + p_S\left(\frac{z}{L} + \frac{1}{2}\right) \tag{4.8}$$

Three theories regarding the value of the cavitation pressure p_c in eq. (4.5), that lead to different expressions for the radial and tangential SFD forces in eqs. (4.4), are considered.

The "2π film" (or "full film") theory assumes that no cavitation occurs. Hence, in eq. (4.5), $p_c = -\infty$ and, regardless of the value of the supply pressure p_S, eqs. (4.4) reduce to the closed form expressions [57]:

$$Q_{R,2\pi} = \frac{2\eta R L^3}{c^2} \frac{\left(1 + 2\varepsilon^2\right)\pi}{\left(1 - \varepsilon^2\right)^{\frac{5}{2}}}\dot{\varepsilon} \qquad Q_{T,2\pi} = \frac{2\eta R L^3}{c^2} \frac{\pi}{\left(1 - \varepsilon^2\right)^{\frac{3}{2}}}\varepsilon\dot{\psi} \tag{4.9a,b}$$

The "π film" (or "half film") theory assumes that (a) $p_S \approx 0$, (b) cavitation occurs at atmospheric pressure (i.e. $p_c = 0$ in eq. (4.5)). From eq. (4.8) it can be deduced that $p(\theta, z)\big|_{p_S=0} \geq 0$ from $\theta = \theta_1$ to $\theta = \theta_2 = \theta_1 + \pi$, where θ_1 is located by the equations

$$\sin\theta_1 = \frac{\dot{\varepsilon}}{\sqrt{(\varepsilon\dot{\psi})^2 + \dot{\varepsilon}^2}} \quad \text{and} \quad \cos\theta_1 = -\frac{\varepsilon\dot{\psi}}{\sqrt{(\varepsilon\dot{\psi})^2 + \dot{\varepsilon}^2}} \tag{4.10a,b}$$

Hence the use of the term "π film" (or "half film"). With the two assumptions (a) and (b), eqs. (4.4) then reduce to the closed form expressions [57]:

$$Q_{R,\pi} = \frac{2\eta RL^3}{c^2}\{g_1 \varepsilon\dot{\psi} + g_2\dot{\varepsilon}\} \qquad Q_{T,\pi} = \frac{2\eta RL^3}{c^2}\{g_3 \varepsilon\dot{\psi} + g_1\dot{\varepsilon}\} \qquad (4.11a,b)$$

where

$$g_1 = -\frac{2\varepsilon\cos^3\theta_1}{\left(1-\varepsilon^2\cos^2\theta_1\right)^2} \qquad g_2 = \frac{\varepsilon\sin\theta_1\left\{3+\left(2-5\varepsilon^2\right)\cos^2\theta_1\right\}}{\left(1-\varepsilon^2\right)^2\left(1-\varepsilon^2\cos^2\theta_1\right)^2} + \frac{\left(1+2\varepsilon^2\right)}{\left(1-\varepsilon^2\right)^{\frac{5}{2}}}\alpha \qquad (4.12a,b)$$

$$g_3 = \frac{\varepsilon\sin\theta_1\left\{1-2\cos^2\theta_1+\varepsilon^2\cos^2\theta_1\right\}}{\left(1-\varepsilon^2\right)\left(1-\varepsilon^2\cos^2\theta_1\right)^2} + \frac{1}{\left(1-\varepsilon^2\right)^{\frac{3}{2}}}\alpha \qquad (4.12c,d)$$

where $$\alpha = \frac{\pi}{2} + \arctan\left\{\frac{\varepsilon\sin\theta_1}{\left(1-\varepsilon^2\right)^{\frac{1}{2}}}\right\} \qquad (4.12e)$$

The full film and half film theories are classical extremes and in reality cavitation occurs at some subatmospheric pressure $p_c \le 0$ [57]. Moreover, the zero supply pressure assumption of the half film theory is unrealistic. Hence, the numerical evaluation of the double integrals of eqs. (4.4) cannot be avoided. However, for the present case of the short unsealed damper, where $p(\theta,z)$ is given by eq. (4.8), it is possible to derive the following simpler expressions from eqs. (4.4), as follows. Since $p_c \le 0$ and $p(\theta,z) \ge 0$ from $\theta = \theta_1$ to $\theta = \theta_2 = \theta_1 + \pi$, eq. (4.4a) for Q_R can be written as:

$$Q_R = -2R\int_{-L/2}^{L/2}\int_{\theta_1}^{\theta_2} p(\theta,z)\cos\theta \; d\theta \; dz - 2R\int_{-L/2}^{L/2}\int_{\theta_2}^{\theta_2+\pi} p_t(\theta,z)\cos\theta \; d\theta \; dz \qquad (4.13)$$

Substituting eq. (4.8) for $p(\theta,z)$ in the first integral of eq. (4.13), the expression for Q_R becomes:

$$Q_R = Q_{R,\pi} + 2Rp_S L\sin\theta_1 - 2R\int_{-L/2}^{L/2}\int_{\theta_2}^{\theta_2+\pi} p_t(\theta,z)\cos\theta \; d\theta \; dz \qquad (4.14a)$$

Similarly,
$$Q_T = Q_{T,\pi} - 2Rp_S L\cos\theta_1 - 2R\int_{-L/2}^{L/2}\int_{\theta_2}^{\theta_2+\pi} p_t(\theta,z)\sin\theta \; d\theta \; dz \qquad (4.14b)$$

In eqs. (4.14) $Q_{R,\pi}$, $Q_{T,\pi}$ are the half film forces given by eqs. (4.11) and $\theta_2 = \theta_1 + \pi$ with θ_1 determined by eqs. (4.10). In this thesis, use of eqs. (4.14) instead of eqs. (4.4) was found to cut the computation time by almost half.

The general cavitation model of eq. (4.5) allows for the possibility of different values of the cavitation pressure p_c, depending on the operating conditions (e.g. unbalance force magnitude, supply pressure, ... etc.). Hence, the cavitation model of eq. (4.5) can be referred to as the "variable film extent" model. The value of p_c under particular operating conditions can be estimated experimentally from pressure probe recordings, as in [8, 58]. In the absence of experimental values, a fixed value for p_c equal to -101.325×10^3 Pa (absolute zero pressure) is taken. This is reasonable since, in most cases, this value of pressure is very close to the vapour pressure of the oil (i.e. the pressure at which it will spontaneously change phase from liquid to gas). Feng and Hahn [59], working on a simple rigid rotor rig with a centralised SFD found that better agreement between measurements and theoretical predictions was achieved when p_c was taken as -101.325×10^3 Pa rather than 0 (i.e. atmospheric pressure).

4.3 NOTE ON SEALED DAMPERS

In the case of a sealed damper, $d_{gap} < c$ in Figure 4.1(b), so that the axial flow is partially restricted by the end-plates. An expression for the pressure distribution $p(\theta,z)$ of such a two-land sealed damper was proposed in [53]. This is not presented in this thesis since it was not used the research applications presented, but it can be found in [54]. For sealed dampers, the SFD forces are computed by numerical integration from eqs. (4.4) with p_c in eq. (4.5) taken as -101.325×10^3 Pa, in the absence of experimentally determined values.

4.4 OTHER CONSIDERATIONS

In this section, factors not taken into account in the above theory are discussed. These factors are (a) tensile stresses in the oil film; (b) compressibility of the fluid; (c) fluid inertia.

The use of $p_c = -101.325\times10^3$ Pa (zero absolute) in the cavitation model of eq. (4.5) excludes the possibility of tensile stresses in the oil film. Feng and Hahn [55] cite some published works where liquid was found to be able to withstand tensile stresses in dynamic tests under controlled laboratory conditions. However, these authors also cite various conditions which reduce the likelihood of this phenomenon, including (i) badly finished solid surfaces; (ii) suspended solid particles in the liquid; (iii) large amounts of gas dissolved in the liquid; (iv) low viscosity of the liquid. Experimental recordings from a pressure probe located at the bottom of an unsupported SFD in [8, 58] revealed a tension spike immediately followed by recovery to absolute zero pressure. It was concluded that the oil film at this location momentarily supported tension prior to rupturing. In these two works, predictions were obtained by using a value of p_c in eq. (4.5) below -101.325×10^3 Pa that was an average taking into account the tension spike. However, in [58], it is stated that the area of the spike is so small that the value of p_c might as well be taken as -101.325×10^3 Pa.

The cavitation model of eq. (4.5), assumes that the oil film fully reconstitutes itself at a given location where it is ruptured when the instantaneous untruncated pressure $p(\theta,z)$ at that location is restored to a value above p_c. Feng and Hahn [56, 59] referred to such a SFD model as an "incompressible model". In that work, they stated that experimental observations on unpressurised squeeze film dampers indicate that cavitation bubbles, once formed, do not completely redissolve upon restoration of the super-cavitation pressure. Instead, one is left with a spongy compressible fluid. In [56], they assumed this fluid to be a homogeneous gas-liquid mixture and proceeded to solve the compressible form of the Reynolds equation in which density and viscosity were a function of pressure. This solution procedure is too involved to incorporate in practical rotor-dynamic solution techniques. However, in [56], theoretical results for a simple rigid rotor with a centralised SFD showed that the compressible model results gave very good agreement with the incompressible model results when p_c was taken as -101.325×10^3 Pa in the latter model. Moreover, these findings were confirmed by experiments in [59], as previously mentioned.

Fluid inertia effects are neglected in the SFD model used in this thesis. These effects were investigated by San Andres and Vance [60] for the simple case of a centralised SFD in a

fixed bearing housing. The uncavitated case was considered in [60] since inertia effects were considered to be less in a cavitated SFD. That work showed that for small amplitude oscillations, the fluid inertia effect of a short unsealed SFD was equivalent to the following mass addition to the journal:

$$M_{fluid} = 2C_I \rho R\left(L^3/c\right) \tag{4.15}$$

where the factor 2 accounts for the two lands, ρ is the oil density and the constant C_I is determined from graphs in [60], according to the regime of the gap Reynolds number Re i.e. Re small ($<<1$), Re moderate, Re large ($>>1$). Re indicates the relative magnitudes of the inertia and viscous forces and is calculated from the formula [60]:

$$Re = \rho \Omega c^2 / \eta \tag{4.16}$$

where Ω rad/s is the rotational speed of the shaft. No fluid inertia compensation is attempted in this thesis and eqs. (4.15), (4.16) are used merely to monitor fluid inertia effects, in order to ascertain that they are negligible.

4.5 SFD FORCE COMPUTATION

In order to compute the squeeze film forces Q_R, Q_T in eqs. (4.4a,b) by the general cavitation model of eq. (4.5), a function was written in *MATLAB*®. For a given value of p_c, this function generates a $2 \times \breve{n}$ matrix of radial (row 1) and tangential (row 2) forces for time histories ε, $\dot{\varepsilon}$, $\dot{\psi}$ of length $\breve{n}$ points. This means that a total of $2\breve{n}$ double integrations are performed. The double integration is performed using Simpson's rule by an array scheme outlined in [61]. For the short unsealed damper this function computes the double integrals in eqs. (4.14) and adds them to the values computed from the analytical expressions in these equations to give Q_R, Q_T. For the sealed damper the function computes the forces using the full double integration formulae in eqs. (4.4). With $\Delta\theta = 2\pi/52$ and $\Delta z = L/12$, force matrices with up to 100 columns could be generated in a fraction of a second to a sufficiently high accuracy on a 333 MHz Pentium II personal computer.

4.6 ILLUSTRATION AND DISCUSSION

In this section, the short unsealed SFD model is illustrated by considering a simple two degree of freedom system such as the rigid rotor systems in Figures 4.3(a,b). The aim is to demonstrate the validity of the cavitation model of eq. (4.5) with $p_c = -101.325\times10^3$ Pa ("absolute zero cavitation model"). The configuration in Figure 4.3(a) was considered in [57] and is symmetrical, with identical unsupported SFDs in rigid housings. The configuration in Figure 4.3(b) was considered in [8] and is pivoted at the left hand end by a self-aligning bearing and supported at the other end by a rigidly housed, unsupported SFD. Both systems are described by the following equations of motion

$$M_{R,J}\ddot{X}_J = Q_x + U_{eq,J}\Omega^2 \sin\Omega t \tag{4.17a}$$

$$M_{R,J}\ddot{Y}_J = Q_y - U_{eq,J}\Omega^2 \cos\Omega t - W \tag{4.17b}$$

where X_J, Y_J are the displacements of the journal centre J from the fixed bearing housing centre, Ω rad/s is the rotational speed, $M_{R,J}$ is the effective rotor mass at J, W is the equivalent static load at J and $U_{eq,J}$ is the equivalent unbalance at J, which can be expressed as:

$$U_{eq,J} = M_{R,J}u \tag{4.18}$$

Eqs. (4.17) can be non-dimensionalised by defining the non-dimensional time $\varsigma = \Omega t$ and dividing both sides by $M_{R,J}c\Omega^2$,

$$\hat{X}_J'' = \hat{Q}_x + \hat{U}\sin\varsigma \tag{4.19a}$$

$$\hat{Y}_J'' = \hat{Q}_y - \hat{U}\cos\varsigma - \hat{W} \tag{4.19b}$$

where $(\,)'$ denotes differentiation with respect to ς, $\hat{X}_J = X_J/c$, $\hat{Y}_J = Y_J/c$ are the non-dimensional displacements of J and $\hat{Q}_{x,y}$ are the non-dimensional squeeze film forces:

$$\hat{Q}_{x,y} = Q_{x,y}\left(X_J, Y_J, \dot{X}_J, \dot{Y}_J\right)/\left(M_{R,J}c\Omega^2\right) = Q_{x,y}\left(c\hat{X}_J, c\hat{Y}_J, c\Omega\hat{X}_J', c\Omega\hat{Y}_J'\right)/\left(M_{R,J}c\Omega^2\right) \tag{4.20}$$

where $Q_{x,y}$ are computed from eqs. (4.6). Three non-dimensional groups are defined [8, 57]:

$$\hat{B} = \frac{2\eta R}{M_{R,J}\Omega}\left(\frac{L}{c}\right)^3, \quad \hat{W} = \frac{W}{M_{R,J}c\Omega^2}, \quad \hat{U} = \frac{u}{c} \tag{4.21a,b,c}$$

and are referred to as the non-dimensional viscosity, static load and dynamic load parameters respectively. It can be shown that when the SFD forces are estimated using the full film model, or half film model, or some combination of these two models (as the "*b* factor model" discussed shortly), the response for given initial conditions is determined exclusively by the above three non-dimensional groups, eqs. (4.21) [57]. However, when $p_c \neq -\infty$ or $p_S, p_c \neq 0$ in the general cavitation model of eq. (4.5), the cavitation pressure p_c, the supply pressure p_S, and the SFD geometry become additional control parameters. The parameters used here are those of Humes and Holmes [57] (Figure 4.3(a)) and are: $M_{eq,J}$=18 kg, $W = 176.58$ N, $c = 0.2082\times10^{-3}$ m, $R = 63.5\times10^{-3}$ m, $L = 10.9\times10^{-3}$ m, $p_S = 13.8\times10^3$ Pa.

Equations (4.19) were expressed as a set of 4 first order differential equations, as in eq. (3.1) with $\mathbf{s} = \left[\hat{X}_J \quad \hat{Y}_J \quad \hat{X}_J' \quad \hat{Y}_J'\right]^T$, ς replacing *t*, and were solved for given operating parameters and initial conditions using the 4th order Runge-Kutta-Merson method with automatic step control [54, 61]. This Runge-Kutta method was adequate in this case since the number of degrees of freedom was very low and the oil viscosity was very high, ensuring no problem of (numerical) stiffness in the differential equations.

The low value of the supply pressure was found to have negligible effect on the orbital predictions obtained with the general cavitation model of eq. (4.5) and thus allowed a fair comparison of the accuracy of half film model predictions (which assume $p_S = 0$) versus alternative predictions. As a preliminary test, the load carrying capabilities of the π and 2π film models were contrasted for the same control parameters $\hat{B} = 0.61$, $\hat{W} = 0.90$, $\hat{U} = 2.26$. The transient journal orbits for the same initial conditions are shown in Figures 4.4(a) (2π film) and 4.4(b) (π film), each covering 10 shaft revolutions. In this thesis, all journal orbits relative to the housing are presented with respect to the clearance circle, to which the relative motion of the journal is confined. It can be seen that the full film gives no static load carrying capacity: the shaft simply spirals down to the bottom of the clearance circle. On the other hand, the half film result shows a definite load-carrying ability through the

development a steady-state orbit. The inability of an uncavitated film to support a static load is a well-known fact [57]. The experimental orbit, reproduced from [57] in Figure 4.4(c), is however both smaller in size and positioned at a lower level than that in Figure 4.4(b). This indicates that the cavitation pressure p_c lies somewhere between the extremes of 0 (half film) and $-\infty$ (full film). In fact, for given p_S, the lower the value of p_c, the smaller the orbit and the lower is its mean position in the clearance. In order to avoid the numerical integration of the squeeze film forces, eqs. (4.4), Humes and Holmes [57] determined the SFD forces by combining the full and half film theories using an empirical weighting factor b thus:

$$Q_R = bQ_{R,2\pi} + (1-b)Q_{R,\pi}\,,\quad Q_T = bQ_{T,2\pi} + (1-b)Q_{T,\pi} \tag{4.22a,b}$$

Comparison of predicted and experimental orbits taken from the rig used in [57] showed that $b = 0.45$ gave reliable predictions of the orbits. Unfortunately however, there is not a general value of b which may be representative over a wide range of operating parameters.

In the present research, the steady-state orbit shapes computed by both the half film model and the absolute zero cavitation model for the control parameters in Table 4.1 were compared with measurements (reproduced from [57]). The relevant figure numbers of the results obtained are included in this table.

$60\Omega/(2\pi)$ (rpm)	η ($\times 10^{-3}$ Nsm^{-2})	$\hat{B}$	$\hat{W}$	$\hat{U}$	locus no.	π film	p_c = -101325 Pa	experimental
3100	33	0.10	0.45	0.74	1	Figure 4.5(a)	Figure 4.5(b)	Figure 4.5(c)
3100	33	0.10	0.45	1.06	2	Figure 4.5(a)	Figure 4.5(b)	Figure 4.5(c)
3100	33	0.10	0.45	1.47	3	Figure 4.5(a)	Figure 4.5(b)	Figure 4.5(c)
2520	31	0.12	0.68	0.73	1	Figure 4.6(a)	Figure 4.6(b)	Figure 4.6(c)
2520	31	0.12	0.68	1.38	2	Figure 4.6(a)	Figure 4.6(b)	Figure 4.6(c)
2520	31	0.12	0.68	2.10	3	Figure 4.6(a)	Figure 4.6(b)	Figure 4.6(c)
2520	31	0.12	0.68	0.73	1	Figure 4.7(a)	Figure 4.7(b)	Figure 4.7(c)
3250	50	0.15	0.41	0.73	2	Figure 4.7(a)	Figure 4.7(b)	Figure 4.7(c)
2100	33	0.10	0.45	0.73	3	Figure 4.7(a)	Figure 4.7(b)	Figure 4.7(c)

Table 4.1: *Operating parameters for orbits in Figures 4.5 - 4.7*

Figures 4.5-4.7 show that the absolute zero cavitation predictions are invariably superior to the half film predictions (particularly evident in Figure 4.7). The intermediate orbits labelled "2" in Figures 4.5(b) and 4.6(b) still over-predicted the corresponding measured vibration in Figures 4.5(c) and 4.6(c). In these two cases, it was found that improved correlation was achieved when $p_c = -C \times 101.325 \times 10^3$Pa where C was somewhere in the range $1 < C < 2$ [54]. In fact, tensile stresses were apparent in the pressure recordings of [57] and may have been the result of the very high viscosity of the oil used. The main model applications of Chapters 7 and 8 use much thinner oils, suitable for gas turbine applications. Nonetheless, the results presented in this section provide further evidence that the absolute zero cavitation model is the best available predictive tool. This model will be used throughout this thesis, unless otherwise stated.

4.7 SFDs AND SELF-EXCITED VIBRATION

The unforced SFD problem (i.e. without unbalance force) is now briefly considered. It has already been mentioned that a SFD cannot exert a force when there is no relative vibration across the damper. Hence, the SFD does not influence the static equilibrium state of a dynamical system, if there is one. The dynamical system of eqs. (4.17), having an unsupported SFD, does not have a static equilibrium state ($U_{eq,J}$ being set to zero). This can be easily seen by noticing that, for this case, in eq. (3.26),

$$\varphi(\mathbf{s}) = \left[\dot{X}_J \quad \dot{Y}_J \quad Q_x / M_{R,J} \quad \left(Q_y - W\right)/M_{R,J}\right]^T \tag{4.23}$$

where $\mathbf{s} = \left[X_J \quad Y_J \quad \dot{X}_J \quad \dot{Y}_J\right]^T$. It is clear that the equation $\varphi(\mathbf{s}) = \mathbf{0}$ has no solution since the satisfaction of the first two equations, $\dot{X}_J, \dot{Y}_J = 0$ implies that $Q_{x,y} = 0$ and hence, the fourth equation cannot be satisfied. In practice, this simply means that the journal rests at the bottom of the clearance in the static condition, regardless of the rotational speed Ω. If a parallel retainer spring is included, the resulting dynamical system will have a static equilibrium state, determined by the spring stiffness and the static load W. In this case, upon linearising about this position, the SFD introduces the terms $\partial Q_{x,y}/\partial X_J$, $\partial Q_{x,y}/\partial Y_J$, $\partial Q_{x,y}/\partial \dot{X}_J$, $\partial Q_{x,y}/\partial \dot{Y}_J$ into the matrix $\mathbf{A}$ of eq. (3.27). Since $Q_{x,y} = Q_{x,y}\left(X_J, Y_J, \dot{X}_J, \dot{Y}_J\right)$, these partial derivative expressions do not contain any term in Ω. Moreover, these

expressions are evaluated at the static equilibrium condition $X_J = X_{JES}$, $Y_J = Y_{JES}$, $\dot{X}_J, \dot{Y}_J = 0$, which is also independent of Ω. Hence, the SFD cannot destabilise the unforced system. On the other hand, if the unsupported SFD of the dynamical system of eqs. (4.17) were replaced by a hydrodynamic journal bearing, then the system will have a static equilibrium state dependent on the rotational speed. Moreover, upon linearising about this position, since the hydrodynamic journal bearing forces are of the form $\breve{Q}_{x,y} = \breve{Q}_{x,y}\left(X_J, Y_J, \dot{X}_J, \dot{Y}_J, \Omega\right)$, the corresponding partial derivative expressions will be explicit functions of Ω even before their evaluation at the equilibrium condition. Hence, with the hydrodynamic journal bearing, the stability of the matrix **A** of eq. (3.27) is dependent on the rotational speed and this does result in instability beyond a certain speed [48].

4.8 CONCLUSION

This chapter has presented the existing model for the non-linear element of the class of rotor-dynamic systems analysed in this thesis. The model was illustrated with a simple example. The results provide confidence in a model of the SFD that assumes an incompressible oil film cavitating at absolute zero pressure. It has also been established that the SFD cannot introduce self-excited vibration, thereby justifying the focus on unbalanced SFD systems. Having established the non-linear element in this chapter and the relevant background theory of non-linear dynamical systems in the previous chapter, it is now possible to present the integrated non-linear model for a general squeeze film damped rotor-dynamic system.

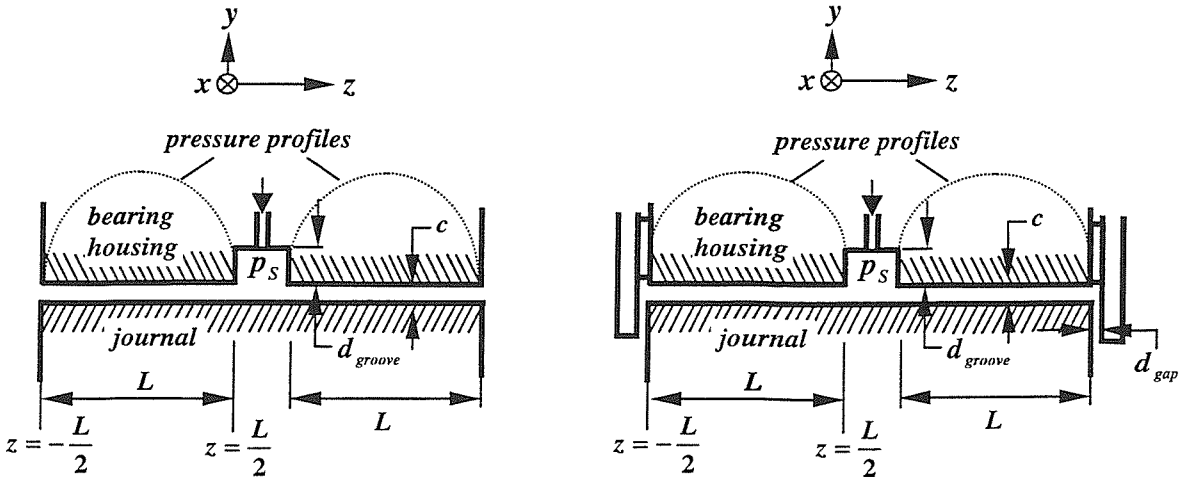

Figure 4.1: *Schematic of axial cross-section through a squeeze film damper*

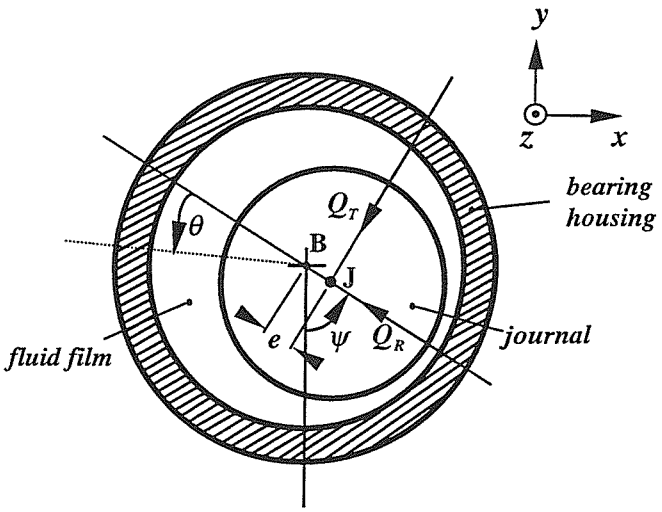

Figure 4.2: *Schematic of transverse cross-section through a squeeze film damper*

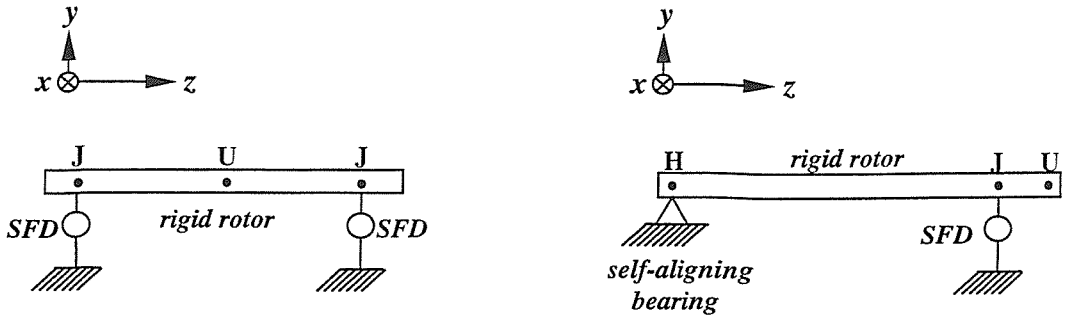

(a) after Humes and Holmes [57] (b) after Holmes and Dogan [8]

Figure 4.3: *Two degree of freedom rotor-bearing models* (unbalance applied at U)

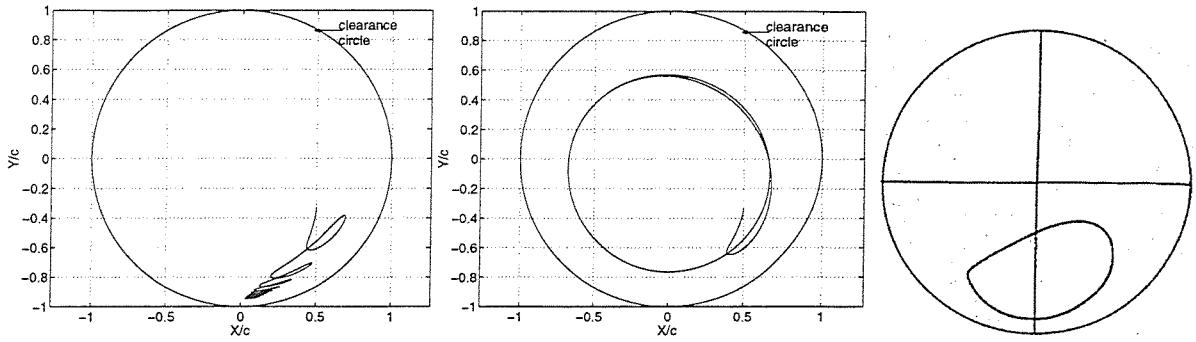

(a) full film (b) half film (c) measured (after [57])

Figure 4.4: *Comparison of load carrying ability of full film and half film models*

($\hat{B} = 0.61$, $\hat{W} = 0.90$, $\hat{U} = 2.26$)

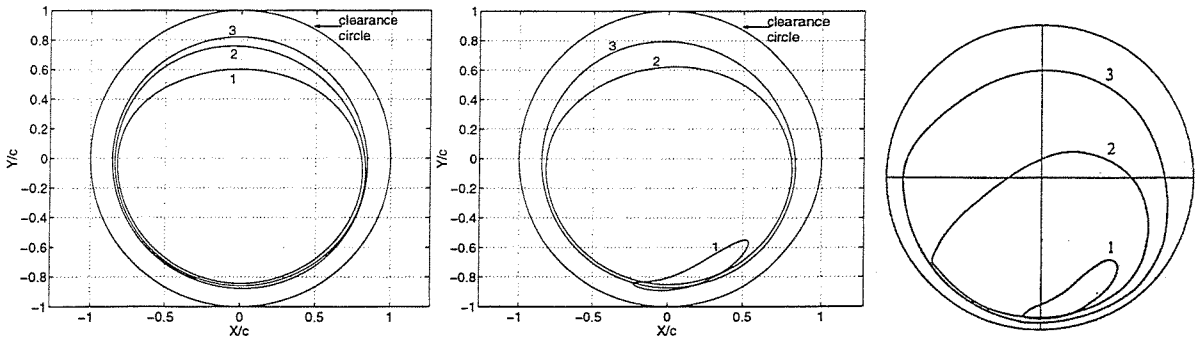

(a) half film (b) $p_c = -101.325 \times 10^3$ Pa (c) measured (after [57])

Figure 4.5: *Comparison of half film and absolute zero cavitation models*

(rows 1-3 of Table 4.1)

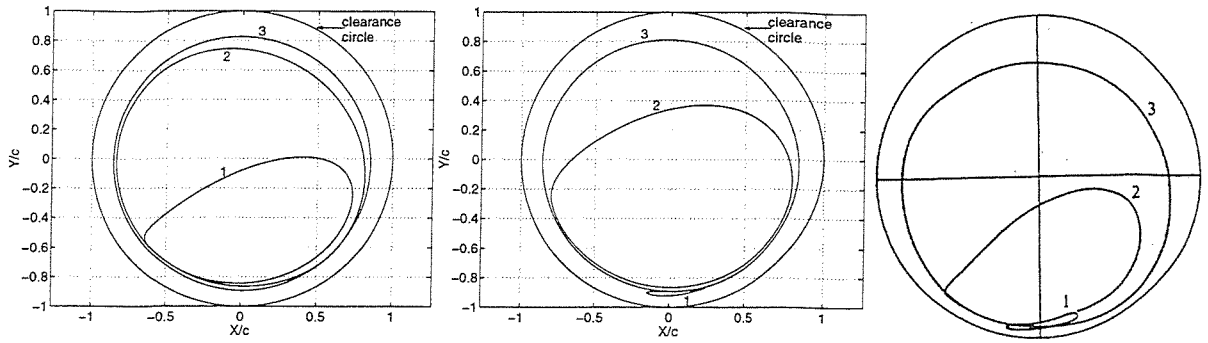

(a) half film (b) $p_c = -101.325 \times 10^3$ Pa (c) measured (after [57])

Figure 4.6: *Comparison of half film and absolute zero cavitation models*

(rows 4-6 of Table 4.1)

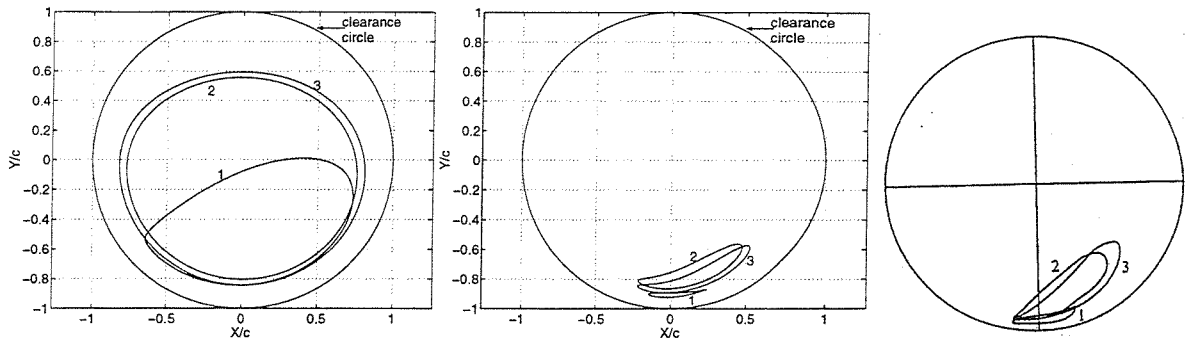

(a) half film (b) $p_c = -101.325 \times 10^3$ Pa (c) measured (after [57])

Figure 4.7: *Comparison of half film and absolute zero cavitation models*

(rows 7-8 of Table 4.1)

5 GENERAL INTEGRATED NON-LINEAR MODEL

5.1 INTRODUCTION

In this chapter, the general integrated non-linear model is developed. The representative model of the general unbalanced squeeze film damped rotor-dynamic system is first described and the fundamental assumptions stated. The receptance harmonic balance (RHB) method for the determination of forced periodic oscillations is then described. The time domain differential equations of motion in modal form are then presented, followed by the Floquet stability analysis of the periodic solutions computed by the RHB method. The application of time-marching of the modal equations to confirm the RHB and Floquet stability results, and to compute aperiodic attractors is then considered. An algorithm for the integration of the three modelling blocks (i.e. RHB, stability, and time-marching) is presented. The chapter concludes with a brief discussion of the advantages of the integrated model over current models.

5.2 REPRESENTATIVE MODEL DESCRIPTION

The representative model of the general unbalanced squeeze film damped rotor-dynamic system is shown in Figure 5.1(a). n_{SFD} squeeze film dampers (SFDs) are fitted between positions J_i and B_i, $i = 1 \ldots n_{SFD}$, on the rotor and support structure respectively. In the physical system, J_i refers to the journal centre and B_i to the bearing housing centre at SFD no. i. The bearing housings form an integral part of the support structure. For an aero-engine, the support structure is the casing, and is also referred to as the "engine carcass". It is generally non-rigid, exhibiting dynamic behaviour. A retainer spring can be optionally placed between J_i and B_i. The rotor and support structure may be linearly connected at other locations. However, these other linear connections are not shown in Figure 5.1(a). The model can additionally accommodate concentrated linear damping forces but material (hysteretic) damping is neglected. The latter restriction can be partially relaxed in the case of the RHB method only, as explained in section 5.8. The unbalance forces are assumed to be

concentrated at discs located at points U_k, $k = 1 \ldots n_U$, along the rotor and are given by (Figure 5.1(b)):

$$P_{xk} = U_k \Omega^2 \sin(\Omega t + \gamma_k), \; P_{yk} = -U_k \Omega^2 \cos(\Omega t + \gamma_k) \tag{5.1a,b}$$

where P_{xk}, P_{yk} are the unbalance forces at U_k in the x, y directions respectively. Ω (rad/s) is the rotational speed (invariant with time), and $U_k = M_{U_k} r_{U_k}$ is the unbalance at U_k (M_{U_k}, r_{U_k} being the unbalance mass and unbalance radius respectively). To avoid confusion, Ω is always taken to be positive. In Figure 5.1(a), the squeeze film forces on J_i, $i = 1 \ldots n_{SFD}$, in the x and y directions are Q_{xi}, Q_{yi}, and are calculated from equations (4.6a,b):

$$Q_{xi,yi} = Q_{x,y}\left(X_{rel_i}, Y_{rel_i}, \dot{X}_{rel_i}, \dot{Y}_{rel_i}\right) \tag{5.2a,b}$$

where $X_{rel_i} = X_{J_i} - X_{B_i}$, $Y_{rel_i} = Y_{J_i} - Y_{B_i}$, $\dot{X}_{rel_i} = \dot{X}_{J_i} - \dot{X}_{B_i}$, $\dot{Y}_{rel_i} = \dot{Y}_{J_i} - \dot{Y}_{B_i}$ are the Cartesian relative displacements and velocities at SFD no. i, and $(X_{J_i}, Y_{J_i}), (X_{B_i}, Y_{B_i})$ are the absolute Cartesian displacements of J_i and B_i respectively, both positions measured from the same fixed point in the xy plane of SFD no i. The SFD forces on B_i are $-Q_{xi}$, $-Q_{yi}$, since the inertia of the fluid film is neglected.

The *linear subsystem* is defined as the linear part of the system in Figure 5.1(a) i.e. the system in Figure 5.1(a) minus the non-linear elements (i.e. the SFDs). Let **u** and **f** be respectively the corresponding $P \times 1$ vectors of the instantaneous degrees of freedom and instantaneous external forces/moments. In general, **u** contains displacements in the x and y directions and rotations in the xz and yz planes, and **f** contains forces and moments in the corresponding directions. In general, there are 4 "non-linear" degrees of freedom associated with a SFD location: $X_{J_i}, Y_{J_i}, X_{B_i}, Y_{B_i}$. However, if the support structure is rigid at a certain SFD location (i.e. $X_{B_i}, Y_{B_i} = 0$) this number is reduced to two. In this thesis, if the support structure is flexible (rigid) at a given SFD location, then the corresponding bearing housing is said to be flexibly (rigidly) mounted, or simply, flexible (rigid). It should be noted that, while P is arbitrarily large, the vector **f** will be sparse, containing only a finite number of

non-zero elements, depending on the number of forces/moments that are taken to be external to the linear subsystem. This force vector is divided into two component vectors as follows:

$$\mathbf{f} = \begin{bmatrix} \mathbf{f}_N(\mathbf{u}_N, \dot{\mathbf{u}}_N) \\ \mathbf{0} \end{bmatrix} + \mathbf{f}_L(t) \tag{5.3}$$

where $\mathbf{f}_N$ is the $P_N \times 1$ vector of motion-dependent forces/moments and $\mathbf{u}_N$ the $P_N \times 1$ vector of the associated degrees of freedom. The $P \times 1$ vector $\mathbf{f}_L$ contains the unbalance forces and static loads (if taken into account) at the appropriate rows, and zeros elsewhere. This vector is periodic in t, period $T = 2\pi/\Omega$. The vector $\mathbf{u}$ is ordered and partitioned in accordance with the first vector on the right hand side of equation (5.3):

$$\mathbf{u} = \begin{bmatrix} \mathbf{u}_N \\ \mathbf{u}_L \end{bmatrix} \tag{5.4}$$

where $\mathbf{u}_L$ is a $P_L \times 1$ vector.

5.3 RECEPTANCE HARMONIC BALANCE (RHB) ANALYSIS

In the RHB approach, the vector $\mathbf{f}_N$ comprises the non-linear (i.e. SFD) forces only. Hence, in this analysis, $P_N = 4n_{SFD}$ if the support structure is flexible at all SFD locations, while $P_N = 2n_{SFD}$ if the support structure is rigid. The dynamics of the rotating linear subsystem at a general vibration frequency ω (rad/s) are modelled by a $P \times P$ receptance matrix $\mathbf{R}(\omega, \Omega)$ of frequency response functions, given by

$$\tilde{\mathbf{u}} = \mathbf{R}(\omega, \Omega)\tilde{\mathbf{f}} \tag{5.5}$$

$\tilde{\mathbf{u}}$ and $\tilde{\mathbf{f}}$ are the complex amplitude vectors of $\mathbf{u}$ and $\mathbf{f}$ i.e. for harmonic vibration at frequency ω, $\mathbf{u}$ and $\mathbf{f}$ are given by:

$$\mathbf{u} = \mathrm{Re}\{\tilde{\mathbf{u}}e^{j\omega t}\} = \mathbf{u}_C \cos\omega t + \mathbf{u}_S \sin\omega t, \quad \mathbf{f} = \mathrm{Re}\{\tilde{\mathbf{f}}e^{j\omega t}\} = \mathbf{f}_C \cos\omega t + \mathbf{f}_S \sin\omega t \tag{5.6a,b}$$

In general, $\mathbf{R}$ includes gyroscopic and linear damping terms and hence it is complex, non-symmetric, and dependent on the rotational speed Ω as well as the vibration frequency ω. By manipulating equations (5.5), (5.6a,b), the complex numbers can be eliminated from eq. (5.5), resulting in the following pair of equations:

$$\mathbf{u}_C = \mathbf{R}^R(\omega,\Omega)\mathbf{f}_C + \mathbf{R}^I(\omega,\Omega)\mathbf{f}_S\,, \quad \mathbf{u}_S = -\mathbf{R}^I(\omega,\Omega)\mathbf{f}_C + \mathbf{R}^R(\omega,\Omega)\mathbf{f}_S \tag{5.7a,b}$$

In (5.7a,b) the superscripts $^{R,\,I}$ respectively denote the real and imaginary parts of $\mathbf{R}$.

For the complete non-linear system, periodic solutions of fundamental frequency ϖ and period Γ are sought where

$$\varpi = \Omega/N\,, \qquad \Gamma = 2\pi/\varpi = NT \tag{5.8a,b}$$

where N is a positive integer and $T = 2\pi/\Omega$ (period of unbalance excitation), as discussed in Chapter 3, section 3.1. From eq. (5.3), if $\mathbf{u}$ is periodic, period $\Gamma = NT$, then so is $\mathbf{f}$. Hence, both $\mathbf{u}$ and $\mathbf{f}$ can be expressed as Fourier series:

$$\mathbf{u} = \bar{\mathbf{u}} + \sum_{s=1}^{m}\left(\mathbf{u}_C^{(s)}\cos s\varpi t + \mathbf{u}_S^{(s)}\sin s\varpi t\right), \quad \mathbf{f} = \bar{\mathbf{f}} + \sum_{s=1}^{m}\left(\mathbf{f}_C^{(s)}\cos s\varpi t + \mathbf{f}_S^{(s)}\sin s\varpi t\right) \tag{5.9a,b}$$

where

$$\bar{\mathbf{f}} = (1/\Gamma)\int_0^\Gamma \mathbf{f}\,dt \tag{5.10a}$$

$$\mathbf{f}_C^{(s)} = (2/\Gamma)\int_0^\Gamma \mathbf{f}\cos s\varpi t\,dt\,, \quad \mathbf{f}_S^{(s)} = (2/\Gamma)\int_0^\Gamma \mathbf{f}\sin s\varpi t\,dt \tag{5.10b,c}$$

For computational reasons, only a finite number of harmonics m of the fundamental frequency ϖ can be considered, so the solutions are, strictly speaking, approximate. Normally, this is not a problem, as discussed in Chapter 2, section 2.2. Static loads need not be considered in $\mathbf{f}$ if the elements in vectors $\mathbf{u}_N$ and $\mathbf{u}_L$ in equation (5.4) are measured from the static condition:

$$\mathbf{u}_N = \mathbf{h} - \mathbf{h}_o, \quad \mathbf{u}_L = \mathbf{g} \tag{5.11a,b}$$

where $\mathbf{h}$ is the $P_N \times 1$ vector of the "non-linear" degrees of freedom at the SFD locations:

$$\mathbf{h} = \begin{bmatrix} X_{J_1} & Y_{J_1} & \cdots & X_{J_{nSFD}} & Y_{J_{nSFD}} & X_{B_1} & Y_{B_1} & \cdots & X_{B_{nSFD}} & Y_{B_{nSFD}} \end{bmatrix}^T \tag{5.12}$$

where each degree of freedom in (5.12) is measured from the static position of the *corresponding* bearing housing centre. $\mathbf{h}_0$ is the static value of $\mathbf{h}$ and contains zeros for the degrees of freedom of the bearing housings. The remaining rows in $\mathbf{h}_0$ contain the static eccentricities of the journals in their respective housings. Bearing housings that are rigidly mounted have their degrees of freedom deleted (omitted) from $\mathbf{h}$ and $\mathbf{h}_0$. The $P_L \times 1$ vector $\mathbf{g}$ (eq. (5.11b)) contains the dynamic values of the remaining P_L degrees of freedom. The receptance matrix $\mathbf{R}$ is partitioned in a similar manner to $\mathbf{u}$ in equation (5.4):

$$\mathbf{R} = \begin{bmatrix} \mathbf{S} \\ \mathbf{T} \end{bmatrix} \tag{5.13}$$

where the matrices $\mathbf{S}$ and $\mathbf{T}$ are of dimension $P_N \times P$ and $P_L \times P$ respectively. Equations (5.7a,b) can now be applied in partitioned form to each of the Fourier coefficient vectors of the degrees of freedom $\mathbf{u}_N = \mathbf{h} - \mathbf{h}_0$, $\mathbf{u}_L = \mathbf{g}$:

$$\bar{\mathbf{h}} - \mathbf{h}_0 = \mathbf{S}_0 \bar{\mathbf{f}} \tag{5.14a}$$

$$\mathbf{h}_C^{(s)} = \mathbf{S}^R(s\varpi, \Omega)\mathbf{f}_C^{(s)} + \mathbf{S}^I(s\varpi, \Omega)\mathbf{f}_S^{(s)}, \quad s = 1 \ldots m \tag{5.14b}$$

$$\mathbf{h}_S^{(s)} = -\mathbf{S}^I(s\varpi, \Omega)\mathbf{f}_C^{(s)} + \mathbf{S}^R(s\varpi, \Omega)\mathbf{f}_S^{(s)}, \quad s = 1 \ldots m \tag{5.14c}$$

$$\bar{\mathbf{g}} = \mathbf{T}_0 \bar{\mathbf{f}} \tag{5.15a}$$

$$\mathbf{g}_C^{(s)} = \mathbf{T}^R(s\varpi, \Omega)\mathbf{f}_C^{(s)} + \mathbf{T}^I(s\varpi, \Omega)\mathbf{f}_S^{(s)}, \quad s = 1 \ldots m \tag{5.15b}$$

$$\mathbf{g}_S^{(s)} = -\mathbf{T}^I(s\varpi, \Omega)\mathbf{f}_C^{(s)} + \mathbf{T}^R(s\varpi, \Omega)\mathbf{f}_S^{(s)}, \quad s = 1 \ldots m \tag{5.15c}$$

In equations (5.14), (5.15), $\overline{\mathbf{h}}$, $\mathbf{h}_{\mathrm{C}}^{(s)}$, $\mathbf{h}_{\mathrm{S}}^{(s)}$ are the Fourier coefficients of $\mathbf{h}$ and $\overline{\mathbf{g}}$, $\mathbf{g}_{\mathrm{C}}^{(s)}$, $\mathbf{g}_{\mathrm{S}}^{(s)}$ are those of $\mathbf{g}$:

$$\mathbf{h} = \overline{\mathbf{h}} + \sum_{s=1}^{m} \left(\mathbf{h}_{\mathrm{C}}^{(s)} \cos s\varpi t + \mathbf{h}_{\mathrm{S}}^{(s)} \sin s\varpi t \right), \quad \mathbf{g} = \overline{\mathbf{g}} + \sum_{s=1}^{m} \left(\mathbf{g}_{\mathrm{C}}^{(s)} \cos s\varpi t + \mathbf{g}_{\mathrm{S}}^{(s)} \sin s\varpi t \right) \tag{5.16a,b}$$

Also, $\mathbf{S}_0$, $\mathbf{T}_0$ contain the zero frequency receptances and are real and independent of rotational speed.

Equations (5.14) define a set of $P_N(2m+1)$ non-linear algebraic equations in an equal number of unknowns contained in $\overline{\mathbf{h}}$, $\mathbf{h}_{\mathrm{C}}^{(s)}$, $\mathbf{h}_{\mathrm{S}}^{(s)}$. These unknowns are grouped into one $P_N(2m+1)\times 1$ vector $\mathbf{v}$:

$$\mathbf{v} = \begin{bmatrix} \overline{\mathbf{h}} \\ \mathbf{h}_{\mathrm{C}}^{(1)} \\ \vdots \\ \mathbf{h}_{\mathrm{C}}^{(m)} \\ \mathbf{h}_{\mathrm{S}}^{(1)} \\ \vdots \\ \mathbf{h}_{\mathrm{S}}^{(m)} \end{bmatrix} \tag{5.17}$$

For the purpose of solution, the system of eqs. (5.14) is expressed as

$$\mathbf{p}\left(\hat{\mathbf{v}}, \hat{\Omega}\right) = \mathbf{0} \tag{5.18}$$

where $\mathbf{p}$ is a $P_N(2m+1)\times 1$ non-linear vector function of $\hat{\mathbf{v}} = \mathbf{v}/c$ and $\hat{\Omega} = \Omega/\omega_0$, that is obtained by bringing all terms of eqs. (5.14) to one side:

$$\mathbf{p}\left(\hat{\mathbf{v}},\hat{\Omega}\right)=\begin{bmatrix} \mathbf{S}_0\bar{\mathbf{f}}-\left(\bar{\mathbf{h}}-\mathbf{h}_0\right) \\ \mathbf{S}^{\mathrm{R}}(\varpi,\Omega)\mathbf{f}_{\mathrm{C}}^{(1)}+\mathbf{S}^{\mathrm{I}}(\varpi,\Omega)\mathbf{f}_{\mathrm{S}}^{(1)}-\mathbf{h}_{\mathrm{C}}^{(1)} \\ \vdots \\ \mathbf{S}^{\mathrm{R}}(m\varpi,\Omega)\mathbf{f}_{\mathrm{C}}^{(m)}+\mathbf{S}^{\mathrm{I}}(m\varpi,\Omega)\mathbf{f}_{\mathrm{S}}^{(m)}-\mathbf{h}_{\mathrm{C}}^{(m)} \\ -\mathbf{S}^{\mathrm{I}}(\varpi,\Omega)\mathbf{f}_{\mathrm{C}}^{(1)}+\mathbf{S}^{\mathrm{R}}(\varpi,\Omega)\mathbf{f}_{\mathrm{S}}^{(1)}-\mathbf{h}_{\mathrm{S}}^{(1)} \\ \vdots \\ -\mathbf{S}^{\mathrm{I}}(m\varpi,\Omega)\mathbf{f}_{\mathrm{C}}^{(m)}+\mathbf{S}^{\mathrm{R}}(m\varpi,\Omega)\mathbf{f}_{\mathrm{S}}^{(m)}-\mathbf{h}_{\mathrm{S}}^{(m)} \end{bmatrix} \tag{5.20}$$

c is the radial clearance of any one of the dampers and ω_0 is some arbitrarily chosen known reference frequency of the system. In this thesis, ω_0 is taken as the lowest natural frequency of the undamped non-rotating system with the SFDs "locked" by shimming the radial clearances. For a fixed value of N, $\mathbf{p}\left(\hat{\mathbf{v}},\hat{\Omega}\right)$ can be computed for an assumed $\mathbf{v}$ at any given rotational speed Ω (since $\varpi=\Omega/N$). This enables a solution of eq. (5.18) for $\hat{\mathbf{v}}$ by iteration. The only receptance terms in $\mathbf{S}$ (eq. (5.13)) that need computation are those linking the non-linear degrees of freedom with the non-zero elements in $\mathbf{f}$. In the determination of the Fourier coefficient vectors $\bar{\mathbf{f}}$, $\mathbf{f}_{\mathrm{C}}^{(s)}$, $\mathbf{f}_{\mathrm{S}}^{(s)}$ (eqs. (5.10)), it is clear from eq. (5.3) that only the SFD force vector $\mathbf{f}_{\mathrm{N}}$ needs to be Fourier analysed at each stage of the iteration, since the unbalance forces are already harmonic at frequency $\Omega=N\varpi$. The Fourier coefficients of the SFD forces at each stage of the iteration are determined as follows. For the current value of $\mathbf{v}$ (eq. (5.17)), the time histories of the non-linear degrees of freedom $\mathbf{h}$ (eq. (5.12)) and their time derivatives are established from eq. (5.16a) and its time derivative. This enables the determination of the time histories of the SFD forces in $\mathbf{f}_{\mathrm{N}}$ by computation of the non-linear SFD force expressions, eqs. (5.2), (4.6) at a suitable number of points $\breve{n}$ over one period $\Gamma=2\pi/\varpi$. Fourier analyses of these time histories are then performed:

$$\bar{\mathbf{f}}_{\mathrm{N}}=(1/\Gamma)\int_0^{\Gamma}\mathbf{f}_{\mathrm{N}}\,dt \tag{5.21a}$$

$$\mathbf{f}_{\mathrm{NC}}^{(s)}=(2/\Gamma)\int_0^{\Gamma}\mathbf{f}_{\mathrm{N}}\cos s\varpi t\,dt,\quad \mathbf{f}_{\mathrm{NS}}^{(s)}=(2/\Gamma)\int_0^{\Gamma}\mathbf{f}_{\mathrm{N}}\sin s\varpi t\,dt \tag{5.21b,c}$$

From section 4.5, the establishment of the $\breve{n}$-point time history of the SFD force vector $\mathbf{f}_{\mathrm{N}}$ at each stage of the iteration requires $2\breve{n}$ double integrations for *each* of the n_{SFD} dampers if the general cavitation model is used. Hence, a judicious choice of $\breve{n}$ is necessary to ensure

both efficiency and accuracy. From the Nyquist criterion [47], in order to avoid error in the Fourier coefficients of $\mathbf{f}_N$ due to aliasing, the SFD forces should be sampled at a rate exceeding twice the highest frequency i.e. $\breve{n}/\Gamma > 2(m/\Gamma)$. Hence

$$\breve{n} > 2m \tag{5.22}$$

In this thesis, the number of significant harmonics does not exceed 20 and thus, a SFD force time history of 50 points is more than adequate for Fourier analysis (i.e. 100 double integrations per SFD per iteration). The single integrals in eq. (5.21) are evaluated by Simpson's rule [61].

Equation (5.18) can be solved using a predictor-corrector iterative procedure to trace out a speed response curve of *NT*-periodic solutions, where *N* is of fixed value. For a given value $\hat{\Omega}_i$ of the control parameter $\hat{\Omega}$, an initial approximation $\hat{\mathbf{v}}_i^{(0)}$ for the solution $\hat{\mathbf{v}}_i$ is provided by a linear polynomial (predictor) based on the solution(s) at one or two previous speeds, $\hat{\mathbf{v}}_{i-1}$, $\hat{\mathbf{v}}_{i-2}$ [16]. The Newton-Raphson iterative method (corrector) is then used to converge $\hat{\mathbf{v}}_i^{(0)}$ into $\hat{\mathbf{v}}_i$ [16]. However, use of $\hat{\Omega}$ as the control parameter to advance the solution procedure along the speed response curve results in failure when more than one solution $\hat{\mathbf{v}}$ is possible for a given rotational speed (as in bistable regions, see Figure 2.1). Arc-length continuation is used to overcome this problem [16]. The control parameter is changed from $\hat{\Omega}$ to an "arc-length" σ. The rotational speed becomes an unknown, $\hat{\Omega} = \hat{\Omega}(\sigma)$, and an extra equation needs to be added to the system in (5.18). Suppose that $\hat{\mathbf{v}}$ and $\hat{\Omega}$ are required for $\sigma = \sigma_i$ i.e. $\hat{\mathbf{v}}_i$, $\hat{\Omega}_i$ are required. Suppose that $\hat{\mathbf{v}}_{i-1}$, $\hat{\Omega}_{i-1}$, corresponding to $\sigma = \sigma_{i-1}$ are known. The extra equation to be added defines σ in the interval $\sigma_{i-1} \le \sigma \le \sigma_i$:

$$g(\hat{\mathbf{v}}, \hat{\Omega}, \sigma) = |\hat{\mathbf{v}} - \hat{\mathbf{v}}_{i-1}|^2 + (\hat{\Omega} - \hat{\Omega}_{i-1})^2 - (\sigma - \sigma_{i-1})^2 = 0 \tag{5.23}$$

where, for a vector $\mathbf{a} = [a_1 \quad \cdots \quad a_{n_a}]^T$, $|\mathbf{a}|^2 = a_1^2 + \ldots + a_{n_a}^2$. The system of equations to be solved for each given value of σ, σ_i, is

$$\begin{cases} \mathbf{p}\left(\hat{\mathbf{v}}, \hat{\Omega}\right) = \mathbf{0} \\ g\left(\hat{\mathbf{v}}, \hat{\Omega}, \sigma\right) = 0 \end{cases} \tag{5.24}$$

The vector of unknowns is now augmented to

$$\hat{\mathbf{w}} = \begin{bmatrix} \hat{\mathbf{v}} \\ \hat{\Omega} \end{bmatrix} \tag{5.25}$$

The solution procedure now "climbs" along the speed response curve, so that a given value of σ will correspond to just one solution $\hat{\mathbf{w}}$, thus eliminating the problem of multiple solutions. From eq. (5.23), in order to initiate the arc-length continuation procedure, one solution $\hat{\mathbf{v}}_1$, $\hat{\Omega}_1$ on the speed response curve is required. This is obtained by solving the original system of equations (5.18) for $\hat{\mathbf{v}}$ at $\hat{\Omega} = \hat{\Omega}_1$. The initial approximation to $\hat{\mathbf{v}}_1$ (i.e. $\hat{\mathbf{v}}_1^{(0)}$) is either a guessed approximation or is determined from the Fourier coefficients of a time-marching solution. For a non-degenerate rotor (see below), if $N = 1$ and $\hat{\Omega}_1$ is low, a reasonable guess is

$$\hat{\mathbf{v}}_1^{(0)} = \begin{bmatrix} \mathbf{h}_0 / c \\ \mathbf{0} \end{bmatrix} \tag{5.26}$$

since the system vibrates at small amplitude about the static condition. In degenerate rotors, namely, rotors with unsupported SFDs, guessed approximations usually result in failure in the corrector step, especially with a large number of unknowns. In such a case, $\hat{\mathbf{v}}_1^{(0)}$ is determined from the Fourier coefficients of the SFD response(s) at $\hat{\Omega} = \hat{\Omega}_1$ obtained by a time-marching solution. In eq. (5.23), σ_1 is arbitrarily set to 0. The algorithm for the solution of eqs. (5.24) by the predictor-corrector iterative procedure is presented in Appendix A1.

Upon solution of (5.18) for $\mathbf{v}$ over a range of values of Ω and determination of the associated values of $\bar{\mathbf{f}}$, $\mathbf{f}_C^{(s)}$, $\mathbf{f}_S^{(s)}$, the response in any of the remaining P_L degrees of freedom is readily available from equations (5.15). The only receptance terms in $\mathbf{T}$ that need computation are those linking the chosen degree of freedom with the non-zero elements in $\mathbf{f}$.

In equations (5.14a), (5.15a), it has been implicitly assumed that all zero frequency terms in $\mathbf{S}_0$, $\mathbf{T}_0$ exist. This condition holds when, in the *linear subsystem* (i.e. the system in Figure 5.1(a) minus the non-linear elements), the rotor is supported at not less than two positions. When, in the linear subsystem, the rotor is not connected to the support structure or has only one connection that offers no flexural resistance (i.e. a simple support), the rotor is said to be degenerate and is capable of free rigid body motion. In such a situation some or all of the terms in $\mathbf{S}_0$ and $\mathbf{T}_0$ will be undefined $(\rightarrow \pm\infty)$. In such a case, equations (5.14a) are modified as follows:

- The static load of the rotor is included in $\mathbf{f}$, concentrated at one or more of the degrees of freedom in the y direction.
- $\mathbf{h}_0$ is omitted and the displacements in $\mathbf{h}$ are measured from the static positions of the bearing housings without the rotor load acting. Similarly, the remaining degrees of freedom $\mathbf{g}$ are measured from the static condition without the rotor weight applied.
- In equation (5.14a), those k rows in $\mathbf{S}_0$ for which the receptances are undefined are replaced by the corresponding rows in the zero frequency value $\mathbf{A}_0$ of the *accelerance* matrix $\mathbf{A}$ where

$$\mathbf{A} = -\omega^2 \mathbf{S} \tag{5.27}$$

  The terms in $\mathbf{A}_0$ will be defined. The corresponding k terms on the left hand side of (5.14a) will be replaced by the corresponding zero frequency (mean) acceleration terms in the Fourier expansion of $\ddot{\mathbf{u}}$, and hence will be all zero (by differentiation of (5.9a) twice).

The resulting modified k equations in (5.14a) are a statement of the fact that, at zero frequency, the degenerate rotor will be in a state of static equilibrium under those elements in the vector $\bar{\mathbf{f}}$ that act on it and the forces from the single linear connection (if there is one) with the support structure. These equations are solved along with the remaining $P_N(2m+1)-k$ equations in (5.14) as previously described. At zero frequency, the degenerate rotor can be maintained in static equilibrium by a minimum of two linear or non-linear connections with the support structure. If the degenerate rotor has no linear connection with the support structure, $k=4$ (i.e. two unsupported SFDs) is the maximum number of modified equations that are independent. If the single linear connection is present, then $k=2$ (i.e. one unsupported SFD) is the maximum number of independent modified

equations. When $k > 4$ or 2, as the case may be, a statically indeterminate equilibrium problem at zero frequency needs to be solved within equations (5.14). A typical case is a rotor that is supported by squeeze film dampers only, without retainer springs, where the number of dampers $n_{SFD} \geq 3$. In such a case, the rotor is equivalent to a continuous beam[1] in each plane xz and yz, for which the additional independent static equilibrium equations at zero frequency can be obtained from standard texts on mechanics of materials e.g. [62]. Such cases are not considered in the model applications of Chapters 6-8.

5.4 DIFFERENTIAL EQUATIONS OF MOTION

The RHB method works exclusively in the frequency domain. However, in order to test the stability of the equilibrium solutions computed by RHB (and of course, for time-marching purposes), the time domain differential equations of motion of the non-linear system are required. A modal approach is adopted to derive these equations. In this analysis, in contrast to RHB, the vector $\mathbf{f_N}$ comprises *all* the damping forces, linear, as well as non-linear, and any gyroscopic moments (if significant). By considering all these forces/moments as external, it is possible to work with the modal parameters (i.e. natural frequencies and mode shapes) of the undamped non-rotating linear subsystem, which will be real and independent of rotational speed. The modal parameters can be obtained using any convenient linear modelling technique. As shall be illustrated in Chapters 7 and 8, receptance functions can be used to determine both the modal parameters and the number of modes required. In practice, only a limited number of modes, H, will make a significant contribution to the response. Hence

$$\mathbf{u} \approx \mathbf{H}\mathbf{q} \tag{5.28}$$

where $\mathbf{q}$ is the $H \times 1$ vector of modal coordinates:

$$\mathbf{q} = \begin{bmatrix} q_1 & \cdots & q_H \end{bmatrix}^{\mathrm{T}} \tag{5.29}$$

and $\mathbf{H}$ is the $P \times H$ modal matrix:

[1] A continuous beam is one supported at three or more locations.

$$\mathbf{H} = \left[\phi^{(1)} \quad \cdots \quad \phi^{(H)}\right] \tag{5.30}$$

where $\phi^{(h)}$, $h = 1 \ldots H$, are the mass-normalised mode shapes [47]. The corresponding natural frequencies are contained in the diagonal matrix **D**, given by

$$\mathbf{D} = \mathbf{diag}\left[\omega_1^2 \quad \cdots \quad \omega_H^2\right] \tag{5.31}$$

The modal equations of motion [23] are hence given by:

$$\ddot{\mathbf{q}} + \mathbf{D}\mathbf{q} = \mathbf{H}^{\mathrm{T}}\mathbf{f} \tag{5.32}$$

where $\mathbf{f}$ is given by eq. (5.3). By partitioning $\mathbf{H}$ in a manner similar to $\mathbf{u}$ in eq. (5.4):

$$\mathbf{H} = \begin{bmatrix} \mathbf{H}_{\mathrm{N}} \\ \mathbf{H}_{\mathrm{L}} \end{bmatrix} \tag{5.33}$$

where $\mathbf{H}_{\mathrm{N}}$ and $\mathbf{H}_{\mathrm{L}}$ are of dimension $P_N \times H$ and $P_L \times H$ respectively, $\mathbf{u}_{\mathrm{N}}$ in eqs. (5.4) and (5.3) can be expressed as

$$\mathbf{u}_{\mathrm{N}} = \mathbf{H}_{\mathrm{N}}\mathbf{q} \tag{5.34}$$

In accordance with the definition of $\mathbf{f}_{\mathrm{N}}$ for modal analysis, the vector of associated degrees of freedom $\mathbf{u}_{\mathrm{N}}$ has a more general meaning here than in the RHB approach. Notice that the modal equations are not uncoupled since $\mathbf{f}$ on the right hand side of eq. (5.32) includes the motion dependent forces/moments in $\mathbf{f}_{\mathrm{N}}$.

In all the stability and time-marching analysis, it is assumed that a sufficient number of modes H is taken to consider the transformation in eq. (5.28) to be "exact" i.e. the approximate equality sign "$\approx$" in eq. (5.28) is replaced by the equality sign "=".

5.5 STABILITY OF PERIODIC SOLUTIONS AND BIFURCATION

In this section, the coefficient matrix $\mathbf{W}(\tau)$ of the perturbation equations (3.12) is derived. As discussed in Chapter 3, this matrix is required for the stability analysis of an RHB-

computed periodic solution $\mathbf{u}_E$ of fundamental frequency ϖ. Defining $\tau = \varpi t$ and $(\,)'$ as differentiation with respect to τ, the modal equations (5.32) are rewritten as:

$$\mathbf{q}'' + \frac{1}{\varpi^2}\mathbf{D}\mathbf{q} = \frac{1}{\varpi^2}\mathbf{H}^T\left\{\begin{bmatrix}\mathbf{f}_N(\mathbf{u}_N, \dot{\mathbf{u}}_N)\\ \mathbf{0}\end{bmatrix} + \mathbf{f}_L(t)\right\} \tag{5.35}$$

where equation (5.3) has been used to substitute for $\mathbf{f}$. Now, from equation (5.28)

$$\mathbf{u}_E = \mathbf{H}\mathbf{q}_E \tag{5.36}$$

$\mathbf{u}_E$ is periodic in τ with period 2π and so is $\mathbf{q}_E$, which satisfies equation (5.35):

$$\mathbf{q}_E'' + \frac{1}{\varpi^2}\mathbf{D}\mathbf{q}_E = \frac{1}{\varpi^2}\mathbf{H}^T\left\{\begin{bmatrix}\mathbf{f}_N(\mathbf{u}_{NE}, \dot{\mathbf{u}}_{NE})\\ \mathbf{0}\end{bmatrix} + \mathbf{f}_L(t)\right\} \tag{5.37}$$

where, from equation (5.34):

$$\mathbf{u}_{NE} = \mathbf{H}_N\mathbf{q}_E \tag{5.38}$$

Defining

$$\mathbf{z} = \mathbf{q} - \mathbf{q}_E \tag{5.39}$$

and subtracting equation (5.37) from equation (5.35)

$$\mathbf{z}'' + \frac{1}{\varpi^2}\mathbf{D}\mathbf{z} = \frac{1}{\varpi^2}\left[\mathbf{H}_N^T \quad \mathbf{H}_L^T\right]\begin{bmatrix}\dfrac{\partial \mathbf{f}_N}{\partial \mathbf{u}_N}(\mathbf{u}_N - \mathbf{u}_{NE}) + \dfrac{\partial \mathbf{f}_N}{\partial \dot{\mathbf{u}}_N}(\dot{\mathbf{u}}_N - \dot{\mathbf{u}}_{NE})\\ \mathbf{0}\end{bmatrix} \tag{5.40}$$

where equation (5.33) has been used to substitute for $\mathbf{H}$ and $\mathbf{f}_N(\mathbf{u}_N, \dot{\mathbf{u}}_N)$ has been expanded in a Taylor series about $\mathbf{u}_N = \mathbf{u}_{NE}$, $\dot{\mathbf{u}}_N = \dot{\mathbf{u}}_{NE}$ and only linear terms in $(\mathbf{u}_N - \mathbf{u}_{NE})$ and $(\dot{\mathbf{u}}_N - \dot{\mathbf{u}}_{NE})$ retained. In eq. (5.40): $\dot{\mathbf{u}}_N - \dot{\mathbf{u}}_{NE} = \varpi(\mathbf{u}_N' - \mathbf{u}_{NE}')$ and $\partial \mathbf{f}_N / \partial \dot{\mathbf{u}}_N = (\partial \mathbf{f}_N / \partial \mathbf{u}_N')/\varpi$.

Therefore $(\partial \mathbf{f}_N / \partial \dot{\mathbf{u}}_N)(\dot{\mathbf{u}}_N - \dot{\mathbf{u}}_{NE}) = (\partial \mathbf{f}_N / \partial \mathbf{u}'_N)(\mathbf{u}'_N - \mathbf{u}'_{NE})$. Also, from eqs. (5.34), (5.38) and (5.39), $\mathbf{u}_N - \mathbf{u}_{NE} = \mathbf{H}_N \mathbf{z}$. Hence, eq. (5.40) becomes

$$\mathbf{z}'' + \frac{1}{\varpi^2}\mathbf{D}\mathbf{z} = \frac{1}{\varpi^2}\mathbf{H}_N^T \frac{\partial \mathbf{f}_N}{\partial \mathbf{u}_N}\mathbf{H}_N \mathbf{z} + \frac{1}{\varpi^2}\mathbf{H}_N^T \frac{\partial \mathbf{f}_N}{\partial \mathbf{u}'_N}\mathbf{H}_N \mathbf{z}' \tag{5.41}$$

Letting

$$\mathbf{x} = \begin{bmatrix} \mathbf{z} \\ \mathbf{z}' \end{bmatrix} \tag{5.42}$$

eq. (5.41) can be written in the form (3.12):

$$\mathbf{x}' = \mathbf{W}(\tau)\mathbf{x} \tag{5.43}$$

where

$$\mathbf{W}(\tau) = \begin{bmatrix} \mathbf{0}_{H\times H} & \mathbf{I}_H \\ \mathbf{U}(\tau) - \frac{1}{\varpi^2}\mathbf{D} & \mathbf{V}(\tau) \end{bmatrix} \tag{5.44}$$

$$\mathbf{U}(\tau) = \frac{1}{\varpi^2}\mathbf{H}_N^T \frac{\partial \mathbf{f}_N}{\partial \mathbf{u}_N}\mathbf{H}_N, \quad \mathbf{V}(\tau) = \frac{1}{\varpi^2}\mathbf{H}_N^T \frac{\partial \mathbf{f}_N}{\partial \mathbf{u}'_N}\mathbf{H}_N \tag{5.45a,b}$$

In eqs. (5.44), $\mathbf{0}_{H\times H}$ is an $H \times H$ matrix of zeros and $\mathbf{I}_H$ an $H \times H$ diagonal matrix with ones on the leading diagonal. Since the partial derivatives in the $H \times H$ matrices $\mathbf{U}(\tau)$ and $\mathbf{V}(\tau)$ are evaluated at the equilibrium conditions $\mathbf{u}_N = \mathbf{u}_{NE}$, $\mathbf{u}'_N = \mathbf{u}'_{NE}$, they are periodic in τ with period 2π and hence, so is the $2H \times 2H$ matrix $\mathbf{W}(\tau)$. The monodromy matrix $\mathbf{G}$ of equation (5.43) is then computed either from equation (3.20) ("slow" method) or from equation (3.22) ("fast" method). The latter method is used in this thesis. The former method is used only once, in Chapter 6, for verification purposes. In this thesis, the matrix exponentials in the product of eq. (3.22) are computed using the *MATLAB*® functions *expm*© or *expm3*© [25]. The stability of the equilibrium solution $\mathbf{u}_E$ is governed by the leading eigenvalue, λ_l, of $\mathbf{G}$, as explained in section 3.2.3.

It is worth mentioning that, strictly speaking, the monodromy matrix $\mathbf{G}$ of equation (5.43) governs the stability characteristics of $\mathbf{q}_E$. However, since the modal coordinates $\mathbf{q}$ are related to the degrees of freedom $\mathbf{u}$ by the simple linear transformation (5.28), the stability characteristics of $\mathbf{q}_E$ are identical to those of $\mathbf{u}_E$.

The above analysis shows that, to determine the stability of a RHB solution $\mathbf{u}_E$, it is only necessary to compute the RHB response at the P_N degrees of freedom contained in the vector $\mathbf{u}_{NE}$. The vector $\mathbf{u}'_{NE}$ is determined by differentiation of the relevant rows of eq. (5.9a).

5.6 TIME-MARCHING

For time-marching purposes, the system of equations (5.32) is expressed as $2H$ first order differential equations

$$\begin{bmatrix} \dot{\mathbf{q}} \\ \ddot{\mathbf{q}} \end{bmatrix} = \begin{bmatrix} \mathbf{0}_{H\times H} & \mathbf{I}_H \\ -\mathbf{D} & \mathbf{0}_{H\times H} \end{bmatrix} \begin{bmatrix} \mathbf{q} \\ \dot{\mathbf{q}} \end{bmatrix} + \begin{bmatrix} \mathbf{0} \\ \mathbf{H}^{\mathrm{T}}\mathbf{f} \end{bmatrix} \tag{5.46}$$

and integrated numerically from given initial conditions $\mathbf{q}(t=0)$, $\dot{\mathbf{q}}(t=0)$ using an integrator suitable for stiff differential equations. In [54], a numerical integration technique based on trapezoidal integration was adapted from the work by Craven and Holmes [2] for the solution of differential equations with SFD forces. It was subsequently discovered that *MATLAB*® (version 5 and later) has a whole suite of similar functions dedicated to stiff systems. The trapezoidal integration method is hence only used in Chapter 6. Chapters 7 and 8 employ the *MATLAB*® function *ode23s*© [25].

The result of the Floquet stability test for an equilibrium solution $\mathbf{u}_E$ can be confirmed by time-marching from equilibrium initial conditions $\mathbf{q}_E(t=0)$, $\dot{\mathbf{q}}_E(t=0)$. As explained in Chapter 3, if $\mathbf{u}_E$ is unstable, the time-marching trajectory will diverge from the equilibrium one. On the other hand, for $\mathbf{u}_E$ stable, both trajectories remain closely matched. This method serves to positively identify the attractor on which the disturbed trajectory will settle down, in the case of $\mathbf{u}_E$ being unstable. The initial conditions $\mathbf{q}_E(t=0)$, $\dot{\mathbf{q}}_E(t=0)$ are found by performing a modal decomposition of the RHB solution $\mathbf{u}_E$ as follows. The responses in H degrees of freedom, arbitrarily chosen, are computed with RHB. These are

contained in the $H \times 1$ vector $\mathbf{u}_{\mathrm{HE}}(t)$. The corresponding velocity vector $\dot{\mathbf{u}}_{\mathrm{HE}}(t)$ is then formed (by differentiation of the relevant rows of eq. (5.9a)). From eq. (5.36):

$$\mathbf{q}_{\mathrm{E}}(t=0) = \mathbf{H}_{\mathrm{H}}^{-1}\mathbf{u}_{\mathrm{HE}}(t=0), \quad \dot{\mathbf{q}}_{\mathrm{E}}(t=0) = \mathbf{H}_{\mathrm{H}}^{-1}\dot{\mathbf{u}}_{\mathrm{HE}}(t=0) \tag{5.47a,b}$$

where the $H \times H$ matrix $\mathbf{H}_{\mathrm{H}}$ comprises H rows of $\mathbf{H}$, respectively corresponding to the chosen H degrees of freedom in $\mathbf{u}_{\mathrm{HE}}$.

5.7 INTEGRATED MODEL ALGORITHM

This section presents an algorithm for integrating the three modelling blocks (RHB, stability analysis, time-marching). One such algorithm is summarised below:

(1) The operating conditions (the unbalances U_k, the rotational speed range, and, if applicable, the static eccentricities $\mathbf{h}_0$) are specified.

(2) A speed response curve of approximate T-periodic solutions (i.e. $N = 1$) is traced out using RHB with a suitable number of harmonics m.

(3) The resulting RHB solution set is then tested for stability using the Floquet test. Any unstable sections of the speed response curve are then classified according to the position of the leading Floquet multiplier λ_l on the complex plane.

(4) An unstable equilibrium cycle along each such section is considered. Time-marching from initial conditions on the cycle locates an attractor. If the resulting attractor is NT-periodic, then the section is reanalysed using RHB with the appropriate value for N, and steps (3)-(4) repeated. If the attractor is aperiodic then the whole branch has to be reanalysed by time-marching.

While steps (1)-(3) are obligatory, step (4) can be altered as required. For example, a speed response curve of time-marching solutions can be generated, starting from the speed at which instability of T-periodic motion was first detected in step (3). Moreover, the initial conditions for the time-marching solution at one speed can be the final conditions from the time-marching solution of the previous speed rather than the equilibrium initial conditions on the RHB solution.

Frequency spectra and Poincaré maps are used to analyse the time-marching solutions. Since the data generated by the time-marching solution process is unevenly spaced (due to automatic step adjustment for error control), linear interpolation is used to generate evenly

spaced data prior to frequency and Poincaré map analysis. The frequency spectra presented in this thesis give the modulus of the discrete Fourier transform (DFT) and are computed using the fast Fourier transform (FFT) algorithm [25]. The aim of the frequency analysis is to identify the salient frequency components of the response. Hence, the absolute level of the vertical axis of the frequency plot is of no importance: it varies with the sampling rate, data length and type of data window used. The Poincaré maps show a stroboscopic picture of the y versus x vibration trajectory (orbit) at a given location on the system at intervals of T.

5.8 ADVANTAGES OF THE INTEGRATED MODEL

The use of a combination of periodic solution technique/stability analysis/time-marching for a full solution to the unbalance response problem is not new, as discussed in Chapter 2. The contribution of the integrated model presented in this chapter lies in the individual modelling blocks, which have been devised in order to overcome the shortcomings of current techniques when applied to real systems with many degrees of freedom. These problems were highlighted on pages 9 and 10 of Chapter 2.

With RHB, harmonic balance principles are applied to the receptance model of the rotating linear part. The required non-linear algebraic equations are easily extracted in the frequency domain, without any need to condense the full number of unknowns (equal to $P(2m+1)$ where P is the total number of degrees of freedom and m is the number of harmonics) to those pertaining to the non-linear degrees of freedom (totalling $P_N(2m+1)$ where P_N is the number of non-linear degrees of freedom), as had been done in previous harmonic balance methods (that were based on the finite element (FE) equations of motion). Hence, it results in a compact and efficient model. Moreover, the receptance functions can be computed using any convenient linear rotor-dynamic modelling technique. In particular, the designer is free to use any of the various frequency-based modelling techniques that have been proposed as efficient alternatives to FE analysis for the computation of the harmonic response of linear rotating systems [19]: transfer matrices (TM); mechanical impedance (MI, or analogously, dynamic stiffness); hybrids like TM/FE, MI/FE; and hybrids involving both analytically and experimentally determined frequency response functions. The receptance formulation does not restrict the designer to the exclusive use of TM as in [18], making the proposed technique effective at including the dynamics of the rotor support structure. The receptance functions can be approximated by a truncated modal series [47]. Hence, for

highly complex systems, the receptance functions can be determined from a FE-based computation of the modal parameters of the linear part.

As regards stability analysis, Hahn and Chen [15] used an approach based on the FE equations of motion. Moreover, they used the "slow" method (eq. (3.20)) to compute the monodromy matrix **G** since they claimed that the advantages of faster methods are dubious. Zhao *et al.* [13] used the "fast" method (eq. (3.22)) to compute **G**. However, since their approach was still based on the FE equations of motion, it was still impractical since the order of the matrices in the exponents of the matrix product in eq. (3.22) is $2P \times 2P$ with the FE-based approach. In this thesis, the "fast" method is used for the computation of **G**, and the modal technique is used to reduce the size of the matrices in the exponents of eq. (3.22) to $2H \times 2H$ where $H << P$, hence making stability analysis feasible for systems with many degrees of freedom. Moreover, with both methods used in [13, 15], the matrix **G** is of size $2P \times 2P$ and, as mentioned by Hahn and Chen [15]: "the computation of the eigenvalues of **G** for large systems to a sufficient degree of accuracy may itself prove problematic." They continued by adding: "unfortunately, no simple alternative to this is known to the authors". The modal method used in this thesis to compute **G** results in a reduction of its size to $2H \times 2H$. Hence, this should facilitate the eigenvalue computation and make the results more reliable for systems with many degrees of freedom.

The RHB and the modal time-marching blocks are complementary in two peculiar aspects. The first aspect relates to the accuracy of the results. The RHB method essentially assumes a finite number of harmonics in the response. However, it does not require modal truncation. Exact (frequency-based) methods (which assume no modal truncation) can be used to compute the receptances. Even if the receptances are computed from a truncated modal series, any number of modes can be taken without affecting the number of RHB equations to be solved, which is fixed at $P_N(2m+1)$. On the other hand, the time domain differential equations of motion essentially assume modal truncation since the number of second order differential equations (5.32) has to be limited to H. However, the solution process places no restriction on the number of harmonics. Hence, if "exact" receptances are used in the RHB method, the RHB and time-marching results are "inter-checking" with respect to the respective assumptions of the number of harmonics m and the number of modes H. Notice that the reliability of the Floquet stability result depends on both m and H. The second aspect relates to computational efficiency. The RHB method becomes unwieldy when the number of non-linear elements is large, since the number of unknowns is

proportional to P_N. On the other hand, the modal time-marching method is immune to this problem since the number of second order differential equations is always equal to the number of modes H.

In section 5.2 it was stated that material (hysteretic) damping is neglected. The reason for this is that this kind of damping can only be used when the vibration is harmonic (i.e. of single frequency) [20]. In the RHB method, the motion is resolved into its component harmonics. Hence, in principle, the loss factor can be used in the evaluation of the required receptance functions (which are those of the linear subsystem); for the (non-rotating) support structure, this can be done by using a complex Young's modulus [20]. However, for the rotor, the incorporation of the loss factor is complicated since it deforms with respect to a rotating frame of reference [48]. For this reason, and to ensure parity with the time domain modal approach, the loss factor is completely neglected in this thesis. This is a reasonable assumption since this damping is likely to be minimal with respect to other sources of damping, as evidenced by the fact that none of the research works cited in Chapter 2 have taken it into account. In the model presented, distributed linear (i.e. viscous) damping can be concentrated at various locations. If the distributed viscous damping is "proportional" [20], a term $\breve{\mathbf{D}}\dot{\mathbf{q}}$ can be added to the left hand side of eq. (5.32) where $\breve{\mathbf{D}} = \mathbf{diag}[2d_1\omega_1 \ldots 2d_H\omega_H]$, d_h $(h = 1 \ldots H)$ being the modal damping ratios, and the matrices of eqs. (5.44), (5.46) amended accordingly. However, in this case, in order to retain parity between the RHB and modal approaches, one has to consider how to include these modal damping terms into the receptances used in the RHB equations. This might prove problematic.

5.9 CONCLUSION

In this chapter, the integrated non-linear model was developed for a general unbalanced squeeze film damped rotor-dynamic system. The model comprised the receptance harmonic balance method for determination of periodic solutions, a modal method for the Floquet stability analysis of the periodic solutions, and numerical integration of the modal equations when necessary. The advantages of the model, as well as its limitations were discussed. In the following chapters the model is applied to rotor-dynamic configurations of increasing complexity.

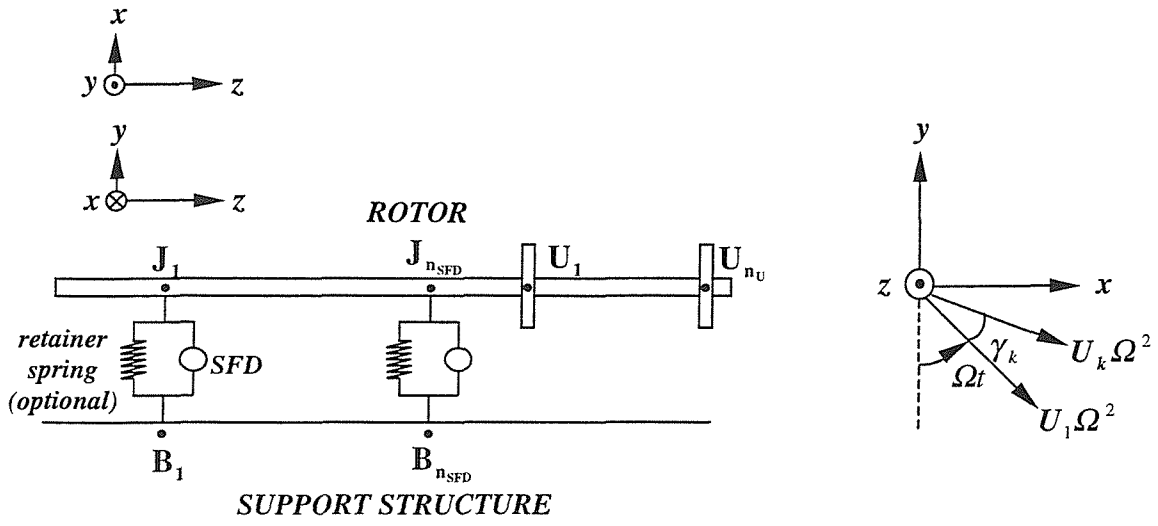

(a) general model in *xz* or *yz* plane (b) rotating out-of-balance forces

Figure 5.1: *Schematic of squeeze film damped rotor dynamic system*

6 MODEL APPLICATION A: RIGID ROTOR IN ONE FLEXIBLY HOUSED UNSUPPORTED SFD

6.1 INTRODUCTION

In this chapter, the integrated modelling approach developed in Chapter 5 is applied to a simple example taken from the literature [8, 63] and illustrated in Figure 6.1. In this configuration, a rigid rotor is supported at one end H by a rigidly mounted self-aligning bearing. The other end runs in an unsupported squeeze film damper (SFD) in which the housing is flexibly mounted. Hence, the SFD is effectively in series with the bearing housing flexibility. Unbalance excitation is applied at U. A test rig for this configuration is described in [8, 63]. The rationale of this configuration is also explained in [8, 63], where it is claimed that in many gas turbine applications the bearing pedestals are quite flexible and so, the first two rotor-support structure critical speeds essentially define "bounce modes". In these modes the rotor does not bend to any significant degree while the housings show appreciable dynamic deflection. In such systems, an oil film (SFD) is interposed between one or more of the rolling-element bearings and their housings to enable safe passage through the bounce critical speeds. In the aforementioned bounce modes, the rotor vibration is approximately symmetrical ("symmetric" bounce mode) and anti-symmetrical ("anti-symmetric" bounce mode) respectively. The configuration in Figure 6.1 is used to represent the vibration of a small gas turbine near the anti-symmetric bounce mode, the pivot (self-aligning bearing) at H representing the node of this mode. This configuration had been analysed for a limited number of rotational speeds by a time-marching method in [8]. The aims of the present analysis are three-fold:

(a) As a simple illustration of the receptance harmonic balance (RHB) technique for the determination of periodic solutions. The assumption of the rigidity of the rotor does not detract from the generality of the non-linear RHB problem since the rigid body assumption only affects the value of the receptance functions.

(b) To demonstrate the efficiency and accuracy of Hsu's fast method for the computation of the monodromy matrix **G** (i.e. the "fast" method of eq. (3.22)), in view of Hahn and Chen's claim in [15] that the advantages of such methods over the conventional method (i.e. the "slow" method of eq. (3.20)) are dubious.

(c) As a preliminary integrated analysis of non-linear effects in flexibly housed unsupported SFDs. The need for such an analysis is felt since, while periodic solution and stability analysis has been previously performed on rigid rotors in unsupported SFDs e.g. [12], the SFD housing was rigidly mounted in such studies.

6.2 MODEL APPLICATION

The linear subsystem of configuration A (Figure 6.1) consists of two uncoupled sub-subsystems: (a) the rigid rotor pivoted at H and free at J, and (b) the support structure at B. In Figure 6.1, J is the centre of the SFD journal and B that of the bearing housing. The SFD is assumed to be the only source of damping and gyroscopic effects are neglected, as in [8, 63]. Hence, the $P_N \times 1$ vector $\mathbf{f}_N$ (eq. (5.3)) is identical for both frequency domain (receptance harmonic balance (RHB)) and time domain (modal analysis) approaches:

$$\mathbf{f}_N = [Q_x \quad Q_y \quad -Q_x \quad -Q_y]^T \tag{6.1}$$

where $P_N = 4$. Q_x, Q_y are the SFD forces on J and $-Q_x$, $-Q_y$ are those on B. The SFD forces are calculated from equations (4.6a,b). Since the pinned-free rotor is degenerate (as described in Chapter 5, end of section 5.3) its static load needs to be taken into account. The vector $\mathbf{u}_N$ of degrees of freedom associated with $\mathbf{f}_N$ is then given by eq. (5.12):

$$\mathbf{u}_N = \mathbf{h} = [X_J \quad Y_J \quad X_B \quad Y_B]^T \tag{6.2}$$

where each displacement is measured from the static position of B without the rotor weight applied. As in eqs. (4.17) (Chapter 4), the rigid rotor is dynamically equivalent to an effective mass $M_{R,J}$, acted upon by equivalent unbalance forces P_x, P_y. These unbalance forces are given by (Figure 5.1(b)):

$$P_x = U_{eq,J}\Omega^2 \sin \Omega t\,, \quad P_y = -U_{eq,J}\Omega^2 \cos \Omega t \tag{6.3a,b}$$

where $U_{eq,J}$ is the equivalent unbalance at J. The support structure at B is modelled by an effective mass M_B and stiffness K_B for both the xz and yz planes, with no cross-coupling between the two planes.

In the RHB approach

$$X_J = \overline{X}_J + \sum_{s=1}^{m}\left(a_{XJ}^{(s)} \cos s\varpi t + b_{XJ}^{(s)} \sin s\varpi t\right),\; Y_J = \overline{Y}_J + \sum_{s=1}^{m}\left(a_{YJ}^{(s)} \cos s\varpi t + b_{YJ}^{(s)} \sin s\varpi t\right) \tag{6.4a,b}$$

$$X_B = \overline{X}_B + \sum_{s=1}^{m}\left(a_{XB}^{(s)} \cos s\varpi t + b_{XB}^{(s)} \sin s\varpi t\right),\; Y_B = \overline{Y}_B + \sum_{s=1}^{m}\left(a_{YB}^{(s)} \cos s\varpi t + b_{YB}^{(s)} \sin s\varpi t\right) \tag{6.4c,d}$$

and

$$Q_x = \overline{Q}_x + \sum_{s=1}^{m}\left(p_x^{(s)} \cos s\varpi t + q_x^{(s)} \sin s\varpi t\right),\; Q_y = \overline{Q}_y + \sum_{s=1}^{m}\left(p_y^{(s)} \cos s\varpi t + q_y^{(s)} \sin s\varpi t\right) \tag{6.5a,b}$$

where

$$\begin{bmatrix}\overline{Q}_x \\ \overline{Q}_y\end{bmatrix} = \frac{1}{\Gamma}\int_0^{\Gamma}\begin{bmatrix}Q_x \\ Q_y\end{bmatrix} dt\,,\quad \begin{bmatrix}p_x^{(s)} \\ p_y^{(s)}\end{bmatrix} = \frac{2}{\Gamma}\int_0^{\Gamma}\begin{bmatrix}Q_x \\ Q_y\end{bmatrix}\cos s\varpi t\; dt\,,\quad \begin{bmatrix}q_x^{(s)} \\ q_y^{(s)}\end{bmatrix} = \frac{2}{\Gamma}\int_0^{\Gamma}\begin{bmatrix}Q_x \\ Q_y\end{bmatrix}\sin s\varpi t\; dt \tag{6.6a-c}$$

In the above equations, $\Gamma = 2\pi/\varpi = NT$ (eq. (5.8b)). Hence, defining

$$\delta_{Ns} = \begin{cases}0 & s \neq N \\ 1 & s = N\end{cases} \tag{6.7}$$

the RHB equations can be written as

$$\overline{Q}_x = 0, \quad \overline{Q}_y - W = 0 \tag{6.8a1,a2}$$

$$a_{XJ}^{(s)} = \alpha_{JJ}(s\varpi)p_x^{(s)}$$

$$a_{YJ}^{(s)} = \beta_{JJ}(s\varpi)\{p_y^{(s)} - \delta_{Ns}U_{eq,J}\Omega^2\}, \quad s = 1\ldots m \tag{6.8b1,b2}$$

$$b_{XJ}^{(s)} = \alpha_{JJ}(s\varpi)\{q_x^{(s)} + \delta_{Ns}U_{eq,J}\Omega^2\}$$

$$b_{YJ}^{(s)} = \beta_{JJ}(s\varpi)q_y^{(s)}, \quad s = 1\ldots m \tag{6.8c1,c2}$$

$$\overline{X}_B = -\alpha_{BB}(0)\overline{Q}_x, \quad \overline{Y}_B = -\beta_{BB}(0)\overline{Q}_y \tag{6.8d1,d2}$$

$$a_{XB}^{(s)} = -\alpha_{BB}(s\varpi)p_x^{(s)}, \quad a_{YB}^{(s)} = -\beta_{BB}(s\varpi)p_y^{(s)}, \quad s = 1\ldots m \tag{6.8e1,e2}$$

$$b_{XB}^{(s)} = -\alpha_{BB}(s\varpi)q_x^{(s)}, \quad b_{YB}^{(s)} = -\beta_{BB}(s\varpi)q_y^{(s)}, \quad s = 1\ldots m \tag{6.8f1,f2}$$

In eqs. (6.8a1,a2), W is the equivalent static load at J. This pair of equations was obtained by taking moments about H and is an expression of the fact that the zero frequency components of the forces acting on the vibrating rotor are in a state of static equilibrium, as discussed in Chapter 5 (end of section 5.3). In eqs. (6.8), $\alpha_{JJ}(\omega)$ and $\beta_{JJ}(\omega)$ are the point receptance functions of the rotor at J at frequency ω rad/s, relating the forces at J in the x and y directions respectively with the displacement responses there in the corresponding directions. Similarly, $\alpha_{BB}(\omega)$ and $\beta_{BB}(\omega)$ are the point receptances of the support structure at B in the x and y directions respectively. The receptances are given by:

$$\alpha_{JJ}(\omega) = \beta_{JJ}(\omega) = -\frac{1}{M_{R,J}\omega^2} \tag{6.9}$$

$$\alpha_{BB}(\omega) = \beta_{BB}(\omega) = \frac{1}{K_B - M_B\omega^2} \tag{6.10}$$

For solution, eqs. (6.8) are expressed in the form $\mathbf{p}(\hat{\mathbf{v}}, \hat{\Omega}) = \mathbf{0}$ of eq. (5.18) by bringing all the terms to one side of the equality signs. $\hat{\mathbf{v}} = \mathbf{v}/c$ where $\mathbf{v}$ is the $4(2m+1)\times 1$ vector of the unknown Fourier coefficients of the SFD displacements $\overline{X}_J$, $a_{XJ}^{(s)}$, $b_{XJ}^{(s)}$, $\overline{Y}_J$, $a_{YJ}^{(s)}$, $b_{YJ}^{(s)}$, $\overline{X}_B$, $a_{XB}^{(s)}$, $b_{XB}^{(s)}$, $\overline{Y}_B$, $a_{YB}^{(s)}$, $b_{YB}^{(s)}$ for $s = 1\ldots m$. $\hat{\Omega} = \Omega/\omega_0$ where ω_0 rad/s is taken as the rotor-support structure critical speed with the SFD locked (i.e. the bounce critical speed), given by:

$$\omega_0 = \sqrt{K_B/(M_{R,J} + M_B)} \tag{6.11}$$

The resulting system is then solved using the arc-length continuation method (section 5.3, pages 63-64), using the iterative algorithm in Appendix A1 to trace out a speed response curve of NT - periodic solutions, where N is of fixed value.

For stability and bifurcation analysis of the RHB-computed periodic response, the matrices $\mathbf{D}$, $\mathbf{H}_N$, $\partial \mathbf{f}_N/\partial \mathbf{u}_N$, $\partial \mathbf{f}_N/\partial \mathbf{u}'_N$ in the expression for the perturbation matrix $\mathbf{W}(\tau)$, eqs. (5.44), (5.45) are required. The system of Figure 6.1 has a total $H = 4$ modes: (a) one mode of the rigid pinned-free rotor in each plane xz, yz; (b) one mode of the support structure alone in each plane xz, yz. For (a), the natural frequencies in each plane are equal to zero, since they define pure rotation of the rigid rotor about H. For (b), the natural frequencies in each plane are $\omega_B = \sqrt{K_B/M_B}$ rad/s. Hence, the diagonal matrix $\mathbf{D}$ of eq. (5.31) is given by:

$$\mathbf{D} = \mathbf{diag}[0 \quad 0 \quad K_B/M_B \quad K_B/M_B] \tag{6.12}$$

The reduced modal matrix $\mathbf{H}_N$ of eq. (5.33) is given by the 4×4 matrix:

$$\mathbf{H}_N = \begin{bmatrix} \begin{bmatrix} \phi_J^{(Rx)} & 0 \\ 0 & \phi_J^{(Ry)} \end{bmatrix} & \mathbf{0}_{2\times2} \\ \mathbf{0}_{2\times2} & \mathbf{diag}\left[\phi_B^{(Sx)} \quad \phi_B^{(Sy)}\right] \end{bmatrix} \tag{6.13}$$

$\mathbf{0}_{i\times j}$ is defined as a zero matrix of size $i\times j$. $\phi_J^{(Rx)}$, $\phi_J^{(Ry)}$ are the mass-normalised mode shapes of the pinned-free rigid rotor, evaluated at J in the x and y directions. $\phi_B^{(Sx)}$, $\phi_B^{(Sy)}$ are the mass-normalised mode shapes of the support structure at B in the x and y directions. The first two columns of $\mathbf{H}_N$ pertain to the modes of the rotor, alternately in the xz and yz planes. The last two rows of these columns correspond to the values of the non-linear degrees of freedom at B in these modes and so are all zero. The remaining two columns of $\mathbf{H}_N$ pertain to the modes of the support structure at B, alternately in the xz and yz planes. The first two rows of these columns correspond to the values of the non-linear degrees of freedom at J in these modes and so are all zero. By comparing the receptance expressions of eqs. (6.9), (6.10) to the modal series expansion of the receptance function in eq. (A3.1) (Appendix A3):

$$\phi_J^{(Rx)} = \phi_J^{(Ry)} = 1/\sqrt{M_{R,J}} \ , \quad \phi_B^{(Sx)} = \phi_B^{(Sy)} = 1/\sqrt{M_B} \tag{6.14a,b}$$

From eqs. (6.1) and (6.2):

$$\frac{\partial \mathbf{f}_N}{\partial \mathbf{u}_N} = \begin{bmatrix} \dfrac{\partial Q_x}{\partial X_J} & \dfrac{\partial Q_x}{\partial Y_J} & \dfrac{\partial Q_x}{\partial X_B} & \dfrac{\partial Q_x}{\partial Y_B} \\ \dfrac{\partial Q_y}{\partial X_J} & \dfrac{\partial Q_y}{\partial Y_J} & \dfrac{\partial Q_y}{\partial X_B} & \dfrac{\partial Q_y}{\partial Y_B} \\ -\dfrac{\partial Q_x}{\partial X_J} & -\dfrac{\partial Q_x}{\partial Y_J} & -\dfrac{\partial Q_x}{\partial X_B} & -\dfrac{\partial Q_x}{\partial Y_B} \\ -\dfrac{\partial Q_y}{\partial X_J} & -\dfrac{\partial Q_y}{\partial Y_J} & -\dfrac{\partial Q_y}{\partial X_B} & -\dfrac{\partial Q_y}{\partial Y_B} \end{bmatrix}$$

From eqs. (4.6a,b), $Q_{x,y} = Q_{x,y}\left(X_{rel}, Y_{rel}, \dot{X}_{rel}, \dot{Y}_{rel}\right)$, where $X_{rel} = X_J - X_B$, ... etc. Hence, $\partial Q_{x,y}/\partial X_J = \partial Q_{x,y}/\partial X_{rel}$, $\partial Q_{x,y}/\partial Y_J = \partial Q_{x,y}/\partial Y_{rel}$, $\partial Q_{x,y}/\partial X_B = -\partial Q_{x,y}/\partial X_{rel}$, $\partial Q_{x,y}/\partial Y_B = -\partial Q_{x,y}/\partial Y_{rel}$. A similar process applies for $\partial \mathbf{f}_N/\partial \mathbf{u}'_N$. Hence,

$$\frac{\partial \mathbf{f}_N}{\partial \mathbf{u}_N} = \begin{bmatrix} \mathbf{J}_Q & -\mathbf{J}_Q \\ -\mathbf{J}_Q & \mathbf{J}_Q \end{bmatrix}, \qquad \frac{\partial \mathbf{f}_N}{\partial \mathbf{u}'_N} = \begin{bmatrix} \breve{\mathbf{J}}_Q & -\breve{\mathbf{J}}_Q \\ -\breve{\mathbf{J}}_Q & \breve{\mathbf{J}}_Q \end{bmatrix} \tag{6.15a,b}$$

where

$$\mathbf{J}_Q = \begin{bmatrix} \dfrac{\partial Q_x}{\partial X_{rel}} & \dfrac{\partial Q_x}{\partial Y_{rel}} \\ \dfrac{\partial Q_y}{\partial X_{rel}} & \dfrac{\partial Q_y}{\partial Y_{rel}} \end{bmatrix}, \ \breve{\mathbf{J}}_Q = \begin{bmatrix} \dfrac{\partial Q_x}{\partial X'_{rel}} & \dfrac{\partial Q_x}{\partial Y'_{rel}} \\ \dfrac{\partial Q_y}{\partial X'_{rel}} & \dfrac{\partial Q_y}{\partial Y'_{rel}} \end{bmatrix} \tag{6.16a,b}$$

and $(\,)'$ is $d(\,)/d\tau$, $\tau = \varpi t$ (ϖ rad/s being the fundamental frequency of the periodic solution). The partial derivatives in eqs. (6.16) are evaluated numerically at the RHB-computed periodic solution from the expressions for $Q_{x,y}$ in eqs. (4.6a,b). The above expressions for $\mathbf{D}$, $\mathbf{H}_N$, $\partial \mathbf{f}_N/\partial \mathbf{u}_N$, $\partial \mathbf{f}_N/\partial \mathbf{u}'_N$ determine the expression for $\mathbf{W}(\tau)$ in eqs. (5.44), (5.45). The monodromy matrix $\mathbf{G}$ of the periodic solution is computed from $\mathbf{W}(\tau)$ using either eq. (3.20) ("slow" method) or eq. (3.22) ("fast" method).

For the time domain solution (numerical integration), the equations used are an extension of eqs. (4.19) (Chapter 4):

$$\hat{X}_J'' = \hat{Q}_x + \hat{U}\sin\varsigma \tag{6.17a}$$

$$\hat{Y}_J'' = \hat{Q}_y - \hat{U}\cos\varsigma - \hat{W} \tag{6.17b}$$

$$\hat{X}_B'' = -\left(\frac{M_{R,J}}{M_B}\right)\hat{Q}_x - \left(\frac{\omega_B}{\Omega}\right)^2 \hat{X}_B \tag{6.17c}$$

$$\hat{Y}_B'' = -\left(\frac{M_{R,J}}{M_B}\right)\hat{Q}_y - \left(\frac{\omega_B}{\Omega}\right)^2 \hat{Y}_B \tag{6.17d}$$

where $(\,)'$ now denotes differentiation with respect to ς $(=\Omega t)$, $\hat{X}_J = X_J/c$, $\hat{Y}_J = Y_J/c$, $\hat{X}_B = X_B/c$, $\hat{Y}_B = Y_B/c$ are the non-dimensional displacements of J and B respectively and $\hat{Q}_{x,y}$ are the non-dimensional squeeze film forces:

$$\hat{Q}_{x,y} = Q_{x,y}\left(X_{rel}, Y_{rel}, \dot{X}_{rel}, \dot{Y}_{rel}\right)/\left(M_{R,J}c\Omega^2\right) \tag{6.18}$$

The non-dimensional dynamic load parameter $\hat{U}$ and the non-dimensional static load parameter $\hat{W}$ were defined in eqs. (4.21b,c). In this chapter, the integration of eqs. (6.17) was performed using a trapezoidal integration method [54], suitable for a system of stiff differential equations.

6.3 RESULTS OF SIMULATIONS AND DISCUSSION

The system parameters used here are taken from [8, 63]. $M_{R,J} = 24.5$ kg, $M_B = 3.5$ kg, $K_B = 6.21\times10^6$ N/m, $W = 294$ N. Hence the bounce critical speed is 75 rev/s. The SFD is short and unsealed, with two lands, as shown in Figure 4.1(a), with $c = 0.216\times10^{-3}$ m, $R = 68.216\times10^{-3}$ m, $L = 9\times10^{-3}$ m. The oil viscosity $\eta = 0.021$ Nsm^{-2} and the supply pressure $p_S = 34.5\times10^3$ Pa. In the simulations, the cavitation pressure p_c is fixed at -101.325×10^3 Pa (absolute zero). As in [8], all results refer to a non-dimensional dynamic load parameter of $\hat{U} = 0.229$.

Figure 6.2 shows the speed response curves of T-periodic solutions computed by RHB ($N=1$) with $m=5$ harmonics. Figures 6.2(a,b) refer to the amplitudes of the motion of the SFD journal J relative to the housing B in the x and y directions respectively, whereas Figures 6.2(c,d) refer to the amplitudes of the absolute motion of the housing B in the x and y directions respectively. The amplitudes are defined as half the peak-to-peak fluctuation in the displacement time history and are normalised with respect to the radial clearance c. The state of stability of each solution, according to the value of the leading eigenvalue λ_l (leading Floquet multiplier) of the monodromy matrix $\mathbf{G}$ is indicated according to the legend in the figure caption. In these figures, the matrix $\mathbf{G}$ is computed by the fast method of eq. (3.22) with $K=200$ subdivisions over one period of the RHB solution. Figures 6.3(a-c) compare the values of the leading Floquet multiplier λ_l obtained from this method for the computation of $\mathbf{G}$ with those obtained from the "slow" method for the computation of $\mathbf{G}$. The slow method used the 4th order Runge-Kutta method for the solution of the perturbation equation (3.12). In the solution of eq. (3.12), the use of the trapezoidal integration method instead of the Runge-Kutta method was found to result in negligible reduction of computation time. It is evident from Figure 6.3 that the results obtained by the fast and slow methods are virtually identical. The use of the fast method cut the computation time for the full set of results shown in Figure 6.3 from several hours to a few minutes (on a 333 MHz Pentium II computer). Additionally, the number of subdivisions K in the fast method could be doubled for an accuracy check, while still retaining a reasonable computation time. Hence, the fast method for the computation of $\mathbf{G}$, with $K=200$, is used throughout this thesis.

Attention is now focussed on the speed response curves of Figure 6.2, with particular interest in the motion of the journal J relative to the housing B. In this part of the discussion, reference is made to Figure 6.2(b) (without loss of generality, since all the graphs in Figure 6.2 express the same information regarding the stability of the T-periodic solutions). Multiple T-periodic solutions exist in the region $\hat{\Omega}=0.671$ to $\hat{\Omega}=0.752$ and the T-periodic solutions form a spring-softening characteristic for the y amplitude (i.e. jump-up in y amplitude on run-up in speed). This contrasts with the spring-hardening characteristic (i.e. jump-down in amplitude on run-up in speed) reported in "parallel" SFD configurations (in which the SFD is in parallel with the retainer spring or equivalent flexibility) [24, 30]. The stable solutions form three sections. The middle one, centred at G ($\hat{\Omega}=0.985$) is very short. Figures 6.4(a,b,c) show the T-periodic orbits at points B, G and L (on Figure 6.2(b)) which

lie close to bifurcation points. The stability of these orbits was confirmed by time-marching from equilibrium initial conditions (i.e. initial conditions on these orbits). The stable branch AB is characterised by distorted "figure-of-eight" orbits (Figure 6.4(a)).

Referring back to Figure 6.2(b), and moving along the curve, a bifurcation occurs beyond point B where λ_l escapes the unit circle in the complex plane along the positive real axis. This indicates that the T-periodic solutions become unstable and any disturbance causes the trajectory to jump to a periodic orbit of the same period (Chapter 3, section 3.2.3). As shown in Figure 6.5, which refers to point D (on Figure 6.2(b)), $\hat{\Omega} = 0.684$, time-marching from initial conditions on the unstable orbit causes the trajectory to collapse to a stable "figure-of-eight" T-periodic orbit residing along the lower branch AB of Figure 6.2(b).

Returning to Figure 6.2(b), as $\hat{\Omega}$ is decreased from the value at G (0.985), a period-doubling bifurcation occurs where λ_l escapes the unit circle in the complex plane along the negative real axis. A branch of $2T$-periodic solutions was traced out by RHB ($N = 2$) from $\hat{\Omega} = 0.951$ down to $\hat{\Omega} = 0.685$. Figures 6.6(a,b) show that two stable $2T$-periodic solutions are possible for $\hat{\Omega} = 0.951$, corresponding to point F on Figure 6.2(b). Figure 6.6(c) shows an unstable $2T$-periodic orbit at $\hat{\Omega} = 0.685$. This should be compared to the unstable T-periodic orbit obtained for around the same value of $\hat{\Omega}$ in Figure 6.5(a). The $2T$-periodic solutions lose their stability for $\hat{\Omega} < 0.72$ (approximately). This corresponds to point E′ in Figure 6.2(b). In fact, despite λ_l being real and negative along section E′E, the unstable T-periodic orbits along this short branch behaved as those along CD when disturbed (i.e. collapsed to stable T-periodic attractors along AB).

When $\hat{\Omega}$ is increased from the value at G (see Figure 6.2(b)), a secondary Hopf bifurcation occurs, where a pair of complex-conjugate eigenvalues λ_l, λ_l^* cross the unit circle simultaneously. This indicates the birth of stable 2-frequency quasi-periodic motion. This was verified in the Poincaré map of Figure 6.7 which refers to point H on Figure 6.2(b). Time-marching from unstable equilibrium initial conditions (on the T-periodic solution) caused the return points to spiral out from the first one (which lies on the unstable T-periodic orbit and is labelled "E" in Figure 6.7), successive points hopping from one spiral branch to the other. In the steady-state, the return points drift around a fixed closed curve, no point ever quite coinciding with another. This ring is the result of an additional fundamental frequency f_0 that is irrationally related to the original synchronous fundamental f_1. As

discussed in Chapter 3, section 3.2.3, the presence of two spiral branches in the transient phase of the map indicates that f_0 is approximately related to f_1 by the relation $f_0 = (\breve{k}/2)f_1$ where $\breve{k}$ is some positive integer and the ratio $\breve{k}/2$ is reduced to its lowest terms. The 2-frequency quasi-periodic attractor is shown in Figure 6.8(a). Unlike the $2T$-periodic orbits of Figure 6.6(a,b), consecutive pairs of "butterfly wings" do not coincide. Figure 6.8(b) shows the frequency spectrum of the y component of the motion in Figure 6.8(a). The horizontal axis in Figure 6.8(b) is the frequency normalised by the synchronous frequency component. The spectrum is seen to have two strong sub-synchronous frequency components offset on either side of $f/f_1 = 0.5$. The frequency components are combinations $k_0 f_0 + k_1 f_1$ where k_0 and k_1 are integers. This result applies with f_0 being taken as either one of the pair straddling $f/f_1 = 0.5$ (in Figure 6.8(b) it was taken as the lower frequency of the pair). If 1EO ("engine order") is the synchronous component (f_1), it is seen that those salient combination frequencies that are not equal to integers multiples of 1EO occur in pairs that are symmetrically disposed about 1EO/2, 3EO/2, 5EO/2, 7EO/2, ... etc., respectively.

Referring back to Figure 6.2(b), the quasi-periodic motion persists over a short regime. Along the branch J-K the stable motion has reverted back to $2T$-periodic motion, as seen in Figure 6.9. Shortly before point L is reached (Figure 6.2(b)), the two loops of the stable $2T$-periodic orbital motion coalesce into one and T-periodic motion finally becomes stable again.

Limited experimental results for the motion of the journal relative to the housing [8] are reproduced in Figures 6.10(a1-d1). These orbits are seen to evolve roughly as predicted: distorted "figure-of-eight" orbits, followed by an apparent jump-up in amplitude on run-up in speed, and period-doubling (evident by the double-looping in the orbits of Figures 6.10(c1,d1)). In the measurements, the period-doubling occurs somewhat later than predicted and is less pronounced. In fact, in Figure 6.10(b2), the predicted unstable T-periodic orbit is closer to the measurement than the stable ($2T$-periodic) one. This is attributed to additional damping provided by the SFD that is not taken into account in the SFD model used. In fact, the computational work in [8, 63] employed the same SFD model used here except that the value of the film rupture pressure p_c used at each speed was based on the corresponding measurements of the dynamic pressure in the oil-film, and this value was mostly below absolute zero to allow for the presence of a "tension spike" (as discussed in Chapter 4, section 4.4). For the present purposes of *predicting* overall trends in vibration, a fixed cavitation pressure of absolute zero is the best available option, as was shown in Chapter 4.

The occurrence of quasi-periodic motion was not reported in [8, 63]. However, this type of motion has been predicted here only for narrow range of speeds. Moreover, the investigation in [8, 63] was only carried out for the four speeds shown in Figures 6.10(a1-d1). 2-frequency quasi-periodic spectra similar to the one in Figure 6.8(b) are verified in experimental work in Chapter 8.

It is seen from Figure 6.2 that the unsupported SFD is particularly effective at providing a safe passage through the bounce critical speed. The relative motion results in Figure 6.2(a,b) indicate that for speeds well removed from the bounce critical speed, particularly for the y direction outside the region $0.6 < \hat{\Omega} < 1.8$, the damper practically acts as a rigid link. In fact, as seen in Figure 6.11, which refers to the mean y component of the T-periodic solutions for the displacement of the journal J relative to the housing B, there is very little lift of the journal from the base of the clearance outside the region $0.6 < \hat{\Omega} < 1.8$. However, Figure 6.2(d) shows that there is a sub-critical resonance of the T-periodic absolute housing vibration in the y direction at $\hat{\Omega} = 0.5$. Figures 6.12(a,b) respectively show the variation of the amplitude of the 1EO and 2EO harmonic components of the T-periodic solutions for the absolute housing vibration in the y direction. It is seen from Figure 6.12(b) that the sub-critical resonance in the y amplitude of the absolute housing motion in Figure 6.2(d) is due to a resonance in its 2EO harmonic component. Hence, this phenomenon is referred to as *sub-critical super-harmonic resonance*. This term was used by Ehrich [41], who obtained a similar effect with the contacting rotor-stator system in Figure 2.2 (Chapter 2). As discussed in Chapter 2, Ehrich cited a SFD journal bottomed in its clearance as an example, and modelled the rotor-stator interaction by a non-linear, but piecewise-linear, spring, ignoring the SFD forces. In the present case, a similar effect was obtained with an unsupported SFD, in which the housing and the bottomed journal interact through the oil film. To the author's knowledge, this is the first time that the sub-critical super-harmonic resonance phenomenon has been directly related to SFDs, without recourse to piecewise-linear spring models. From Figures 6.2, 6.11 and 6.12 it is seen that, for an unsupported SFD in this condition: (a) the SFD journal J lies at the base of the clearance circle (of centre B); (b) there is only a slight relative vibration between J and B; and (c) the absolute vibration of B (or J) in the y direction has a significant 2EO frequency component where 2EO is approximately equal to the bounce critical speed (i.e. the undamped critical speed with the SFD locked). Figure 6.13 shows the absolute orbital motion of the SFD housing at $\hat{\Omega} = 0.500$, computed by both RHB ($N = 1$, $m = 5$) and numerical integration. It is noted that, since X_B, $Y_B \approx X_J$, Y_J in this condition,

the problem is ill conditioned, particularly with respect to the computation of the SFD forces. Hence, very fine arc-length resolution had to be used in the RHB procedure. Similarly, fine tolerances for the numerical integration error had to be used for time-marching solutions in this region. It is noted that the absolute motion of the housing B in Figure 6.1 is directly proportional to the force transmitted to the foundation (engine frame). Hence, sub-critical super-harmonic resonance results in a sudden surge in the force transmitted to the engine frame in the vertical direction. This regime of operation was not investigated in [8, 63]. However, ample experimental evidence of sub-critical super-harmonic resonance in unsupported SFDs is provided in the subsequent chapters.

Like Ehrich's case [41], it was found that the above statements concerning sub-critical super-harmonic resonance could be generalised to resonance in the kEO frequency component, where k is a positive integer, when the rotational speed is approximately $1/k$ times the bounce critical speed. However, for the case of the unsupported SFD, super-harmonic resonances for $k \geq 3$ were found to insignificant and required very fine resolution to be located, even with the arc-length continuation procedure. Ehrich's bilinear oscillator model also exhibited a mirror-image effect i.e. the generation of *super-critical sub-harmonic resonance* in the $1\text{EO}/k$ frequency component when the rotational speed was close to k times the natural frequency. For the present case of the unsupported SFD, it is seen from Figure 6.3 that, in the region of $\hat{\Omega} = 2$, the imaginary part of the leading Floquet multiplier λ_l of the T-periodic solutions plunges towards zero, and the real part is negative (i.e. λ_l tends to be real and negative in the immediate vicinity of $\hat{\Omega} = 2$). Moreover, the absolute value of λ_l in this region is close to 1. Hence, a tendency towards period-doubling exists in the region of $\hat{\Omega} = 2$. However, by repeating the analysis in this region with finer arc-length increments, it was verified that, for the case studied, the modulus of λ_l does not become greater than 1 in the vicinity of $\hat{\Omega} = 2$ i.e. no period-doubling bifurcation occurs. This is likely to be due to the fact that the lift of the journal from the clearance circle base (Figure 6.11) is still sufficient at around $\hat{\Omega} = 2$ to prevent bilinear oscillator effects. However, the possibility of super-critical sub-harmonic resonance in unsupported SFDs with bottomed journals is noted.

6.4 CONCLUSIONS

In this chapter, the integrated modelling approach developed in Chapter 5 was applied to a simple example taken from the literature, consisting of a rigid rotor running in an unsupported, flexibly housed squeeze film damper. This configuration represented, to a limited extent, the essential features of the vibration of a small gas turbine near its anti-symmetric bounce mode. The conclusions are summarised as follows:

- The advantages of using Hsu's fast approximate method for the computation of the monodromy matrix $\mathbf{G}$ were clearly demonstrated. This method is hence used in the subsequent chapters, where, in combination with the modal approach introduced in Chapter 5 for the reduction in size of the matrix $\mathbf{W}(\tau)$, it is used to efficiently evaluate the stability of periodic motion in more complex systems.
- The dynamics were found to be particularly rich around the bounce critical speed, with a spring-softening characteristic for the T-periodic solutions, period-doubling, and 2-frequency quasi-periodicity. However, the attenuation in amplitude provided by the unsupported damper allowed a safe transition through the bounce critical speed.
- For regimes well removed from the critical speed region, the SFD virtually acted like a rigid link, but with one important difference – the generation of sub-critical super-harmonic resonance in the 2EO frequency component of the y component of the absolute housing (and journal) motion when the rotational speed was approximately equal to half the bounce critical speed. The sub-critical super-harmonic resonance resulted in a sudden surge in the vertical force transmitted to the foundation. This effect was associated with piecewise-linear (bilinear) oscillator effects reported elsewhere in the literature.

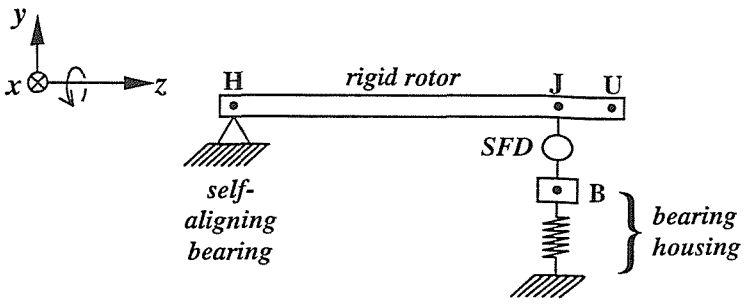

Figure 6.1: *Schematic diagram of configuration A*

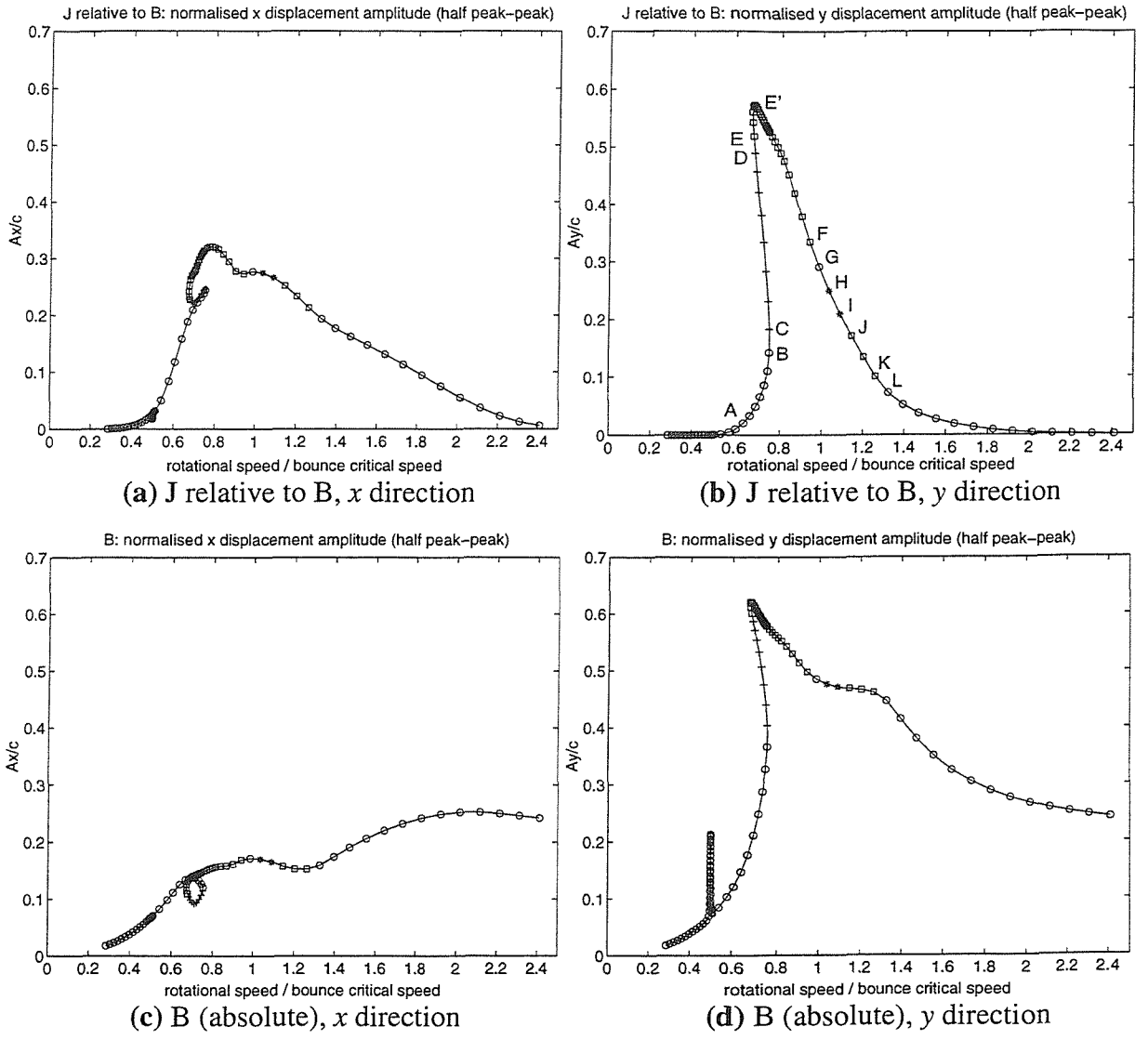

(a) J relative to B, x direction

(b) J relative to B, y direction

(c) B (absolute), x direction

(d) B (absolute), y direction

Figure 6.2: *Variation of amplitude of T-periodic solution with non-dimensional speed* $\hat{\Omega}$
($\hat{U} = 0.229$, vertical axes show half peak-to-peak displacement divided by c)
RHB $N = 1$, $m = 5$: "o" stable, "+" unstable (λ_l real, positive), "□" unstable (λ_l real, negative), "*" unstable (λ_l complex)

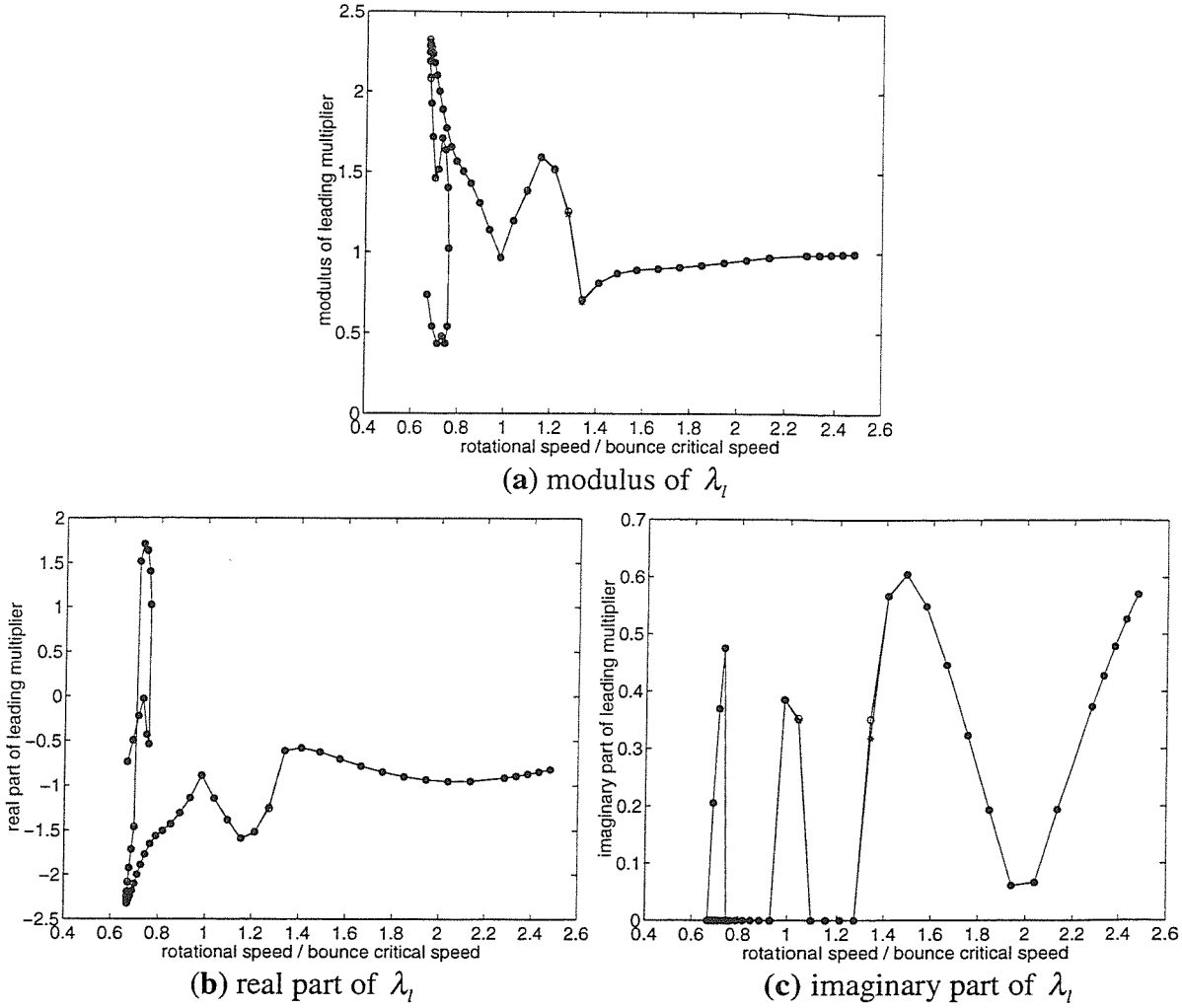

(a) modulus of λ_l

(b) real part of λ_l

(c) imaginary part of λ_l

Figure 6.3: *Variation of leading Floquet multiplier of T-periodic solution* (RHB $N=1$, $m=5$) *with* $\hat{\Omega}$ *: comparison of "fast"* (—o—) *and "slow"* (—*—) *methods for the computation of* $\boldsymbol{G}$

($\hat{U}=0.229$)

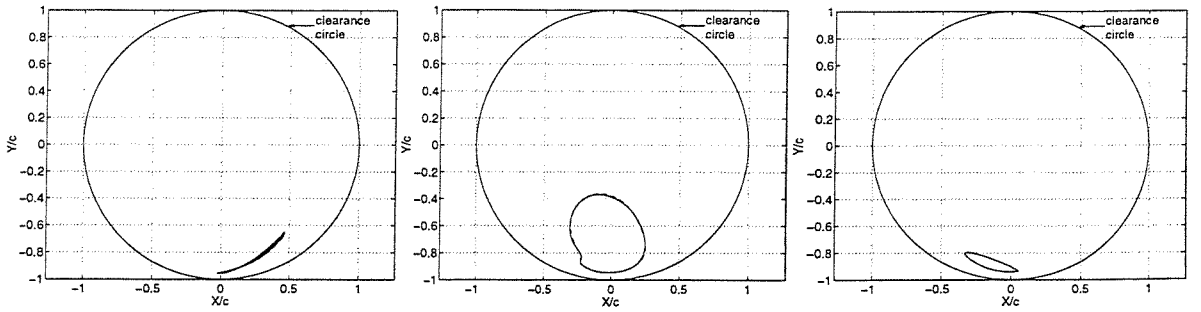

(a) B, $\hat{\Omega}=0.752$ (b) G, $\hat{\Omega}=0.985$ (c) L, $\hat{\Omega}=1.326$

Figure 6.4: *Stable T-periodic orbital motion of journal* J *relative to the housing centre* B *at points* B, G *and* L *in Figure 6.2(b)*

($\hat{U}=0.229$)

RHB $N=1$, $m=5$ (– – –), numerical integration (——)

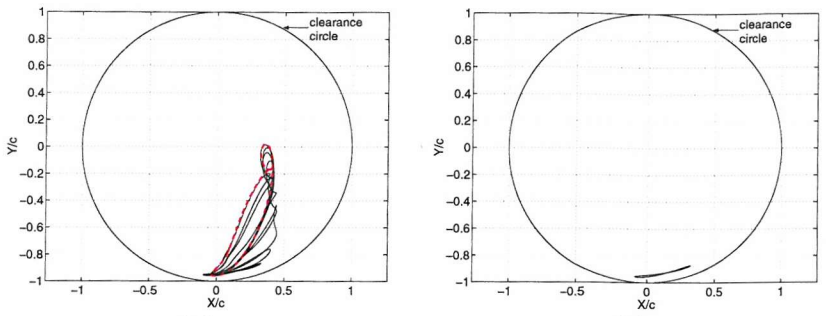

(a) **(b)**

Figure 6.5: *Numerical integration from initial conditions on unstable T-periodic orbit at* $\hat{\Omega} = 0.684$ $(\hat{U} = 0.229)$

(a) RHB $N = 1$, $m = 5$ (– – –); numerical integration, first 10 shaft revs. (——)

(b) numerical integration, further 5 shaft revs. (——)

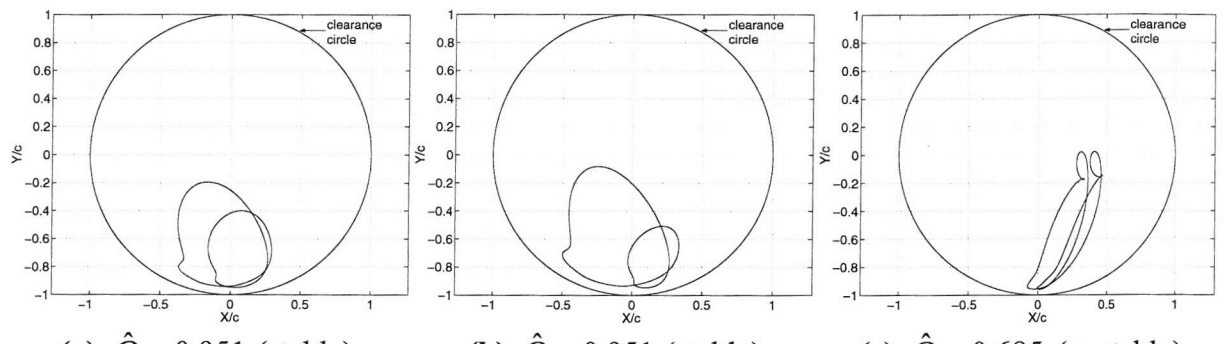

(a) $\hat{\Omega} = 0.951$ (stable) **(b)** $\hat{\Omega} = 0.951$ (stable) **(c)** $\hat{\Omega} = 0.685$ (unstable)

Figure 6.6: *2T-periodic orbits of journal relative to housing* (RHB $N = 1$, $m = 10$) $(\hat{U} = 0.229)$

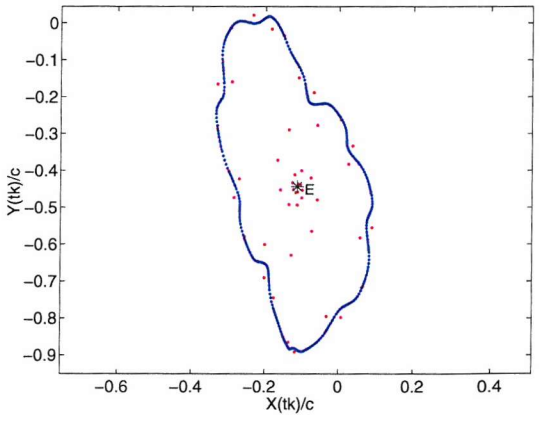

Figure 6.7: *Poincaré map of numerical integration solution for orbital motion of the journal relative to the housing at* $\hat{\Omega} = 1.035$, *starting from conditions on the unstable T-periodic orbit* $(\hat{U} = 0.229)$

$\Omega t_k = k2\pi$; first 80 shaft revs. – red; further 485 revs. – blue;

first point E (on unstable equilibrium solution) indicated by "*"

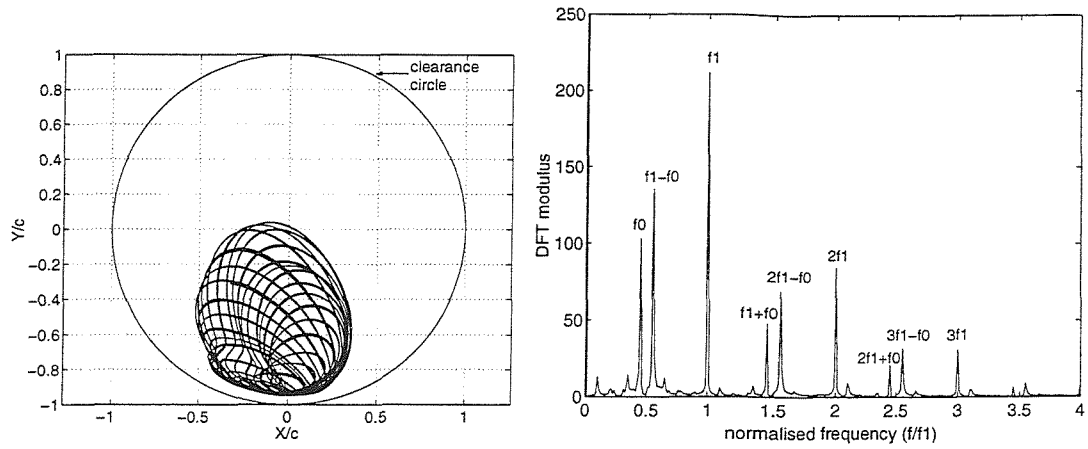

Figure 6.8: *Steady-state quasi-periodic motion of journal relative to housing at* $\hat{\Omega} = 1.035$ *over* 80 *shaft revolutions* ((**a**)) *and frequency spectrum of its y component* ((**b**)) ($\hat{U} = 0.229$)

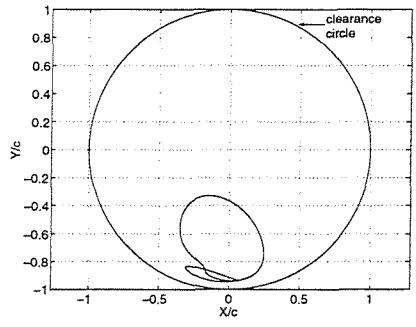

Figure 6.9: *Stable* 2*T-periodic orbit of journal relative to housing for* $\hat{\Omega} = 1.145$ ($\hat{U} = 0.229$)
(steady-state numerical integration solution)

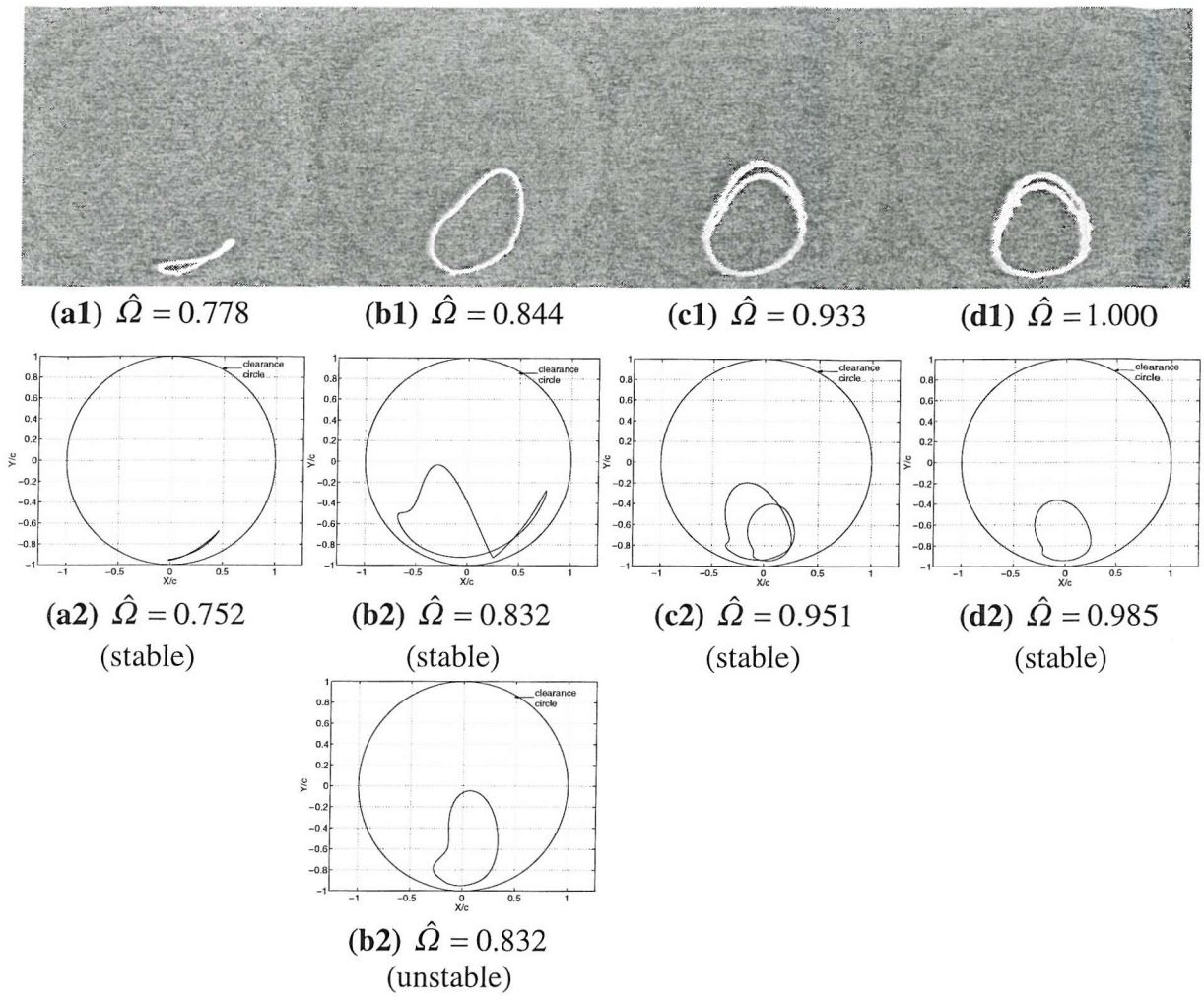

Figure 6.10: *Evolution of measured* (**(a1)-(d1)**) *and predicted* (**(a2)-(d2)**) *orbits of journal relative to housing* ($\hat{U} = 0.229$, measurements reproduced from [8])

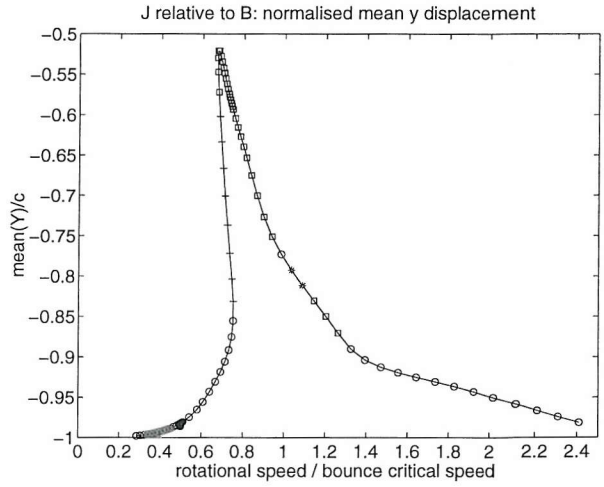

Figure 6.11: *Mean y component of T-periodic solution for the displacement of the journal relative to the bearing housing* ($\hat{U} = 0.229$). RHB $N = 1$, $m = 5$: "o" stable, "+" unstable (λ_l real, positive), "□" unstable (λ_l real, negative), "*" unstable (λ_l complex)

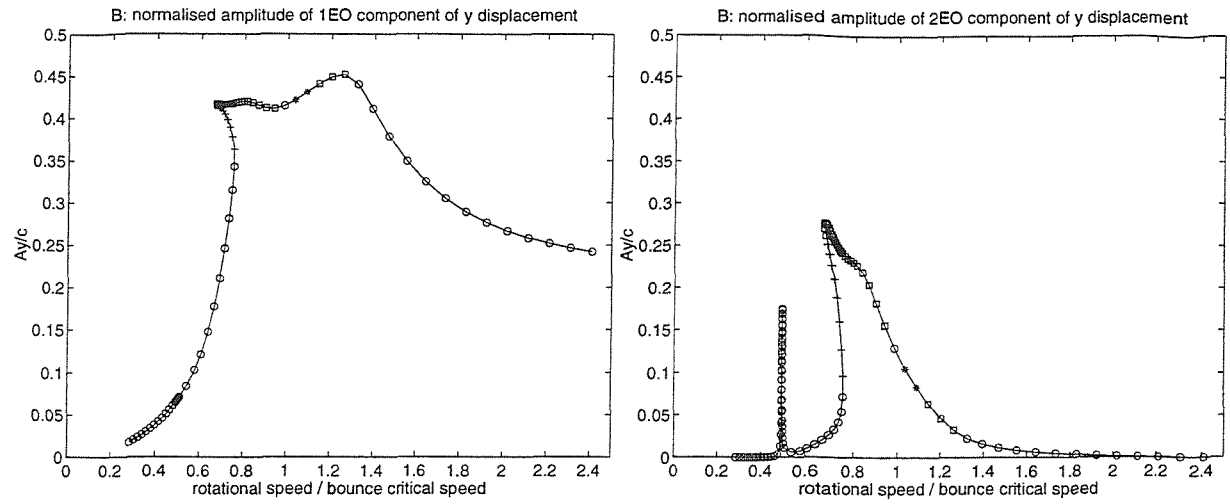

(a) 1EO harmonic component (b) 2EO harmonic component

Figure 6.12: *Variation with non-dimensional speed* $\hat{\Omega}$ *of the amplitude of the* 1*EO and* 2*EO harmonic components of the T-periodic solution for the absolute housing vibration in the y direction* ($\hat{U} = 0.229$, vertical axes show amplitude divided by c)
RHB $N = 1$, $m = 5$: "o" stable, "+" unstable (λ_l real, positive), "□" unstable (λ_l real, negative), "*" unstable (λ_l complex)

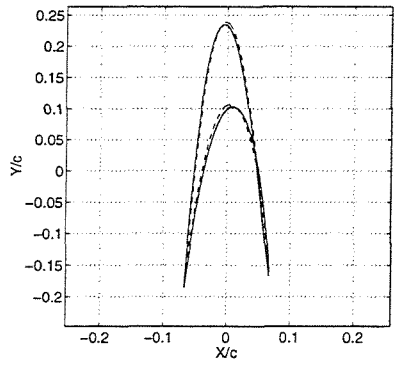

Figure 6.13: *Absolute orbital motion of bearing housing at sub-critical super-harmonic resonance of* 2*EO harmonic component,* $\hat{\Omega} = 0.500$ ($\hat{U} = 0.229$)
RHB $N = 1$, $m = 5$ (– – –),
steady-state numerical integration solution over 50 shaft revs. (——)

7 MODEL APPLICATION B: FLEXIBLE ROTOR IN ONE RIGIDLY HOUSED SFD

7.1 INTRODUCTION

In this chapter, the integrated model developed in Chapter 5 is used to analyse a flexible rotor with one rigidly housed squeeze film damper (SFD). Two variations of configuration B are considered. In one configuration (B1) the SFD is sprung and statically offset in its housing, and in the other configuration (B2) the retainer spring is removed so that the SFD is unsupported. The primary objectives of this work are three-fold: (a) the verification of the correlation between the three modelling blocks (i.e. receptance harmonic balance, modal Floquet stability analysis, and modal numerical integration) under conditions of multi-modal vibration of the rotor; (b) to predict and explain experimentally observed non-linear phenomena from a test rig; and, to a limited extent, (c) to provide additional validation to the model used for the computation of the SFD forces (discussed in Chapter 4). As discussed in Chapter 2, the simplified 3-mass model used for configuration B in [21] did not allow an adequate analysis of non-linear phenomena. The analytical and experimental information gained in this chapter enables, for the first time, a relatively accurate assessment of the non-linear performance of both sprung and unsupported SFDs when used in a bearing of a statically determinate flexible rotor system. A brief description of the test facility is given in the following section. The non-linear model equations are then presented. This is followed by a brief account of the experimental procedure. The analytical and experimental results are then presented and discussed, and conclusions drawn.

7.2 DESCRIPTION OF THE TEST FACILITY

Figure 7.1 shows a schematic diagram of the test rig. This flexible rotor-rigid pedestal (bearing housing) system is typical of a small centrifugal pump. Photographs of this rig are found in Appendix A5, section A5.4 (page 246). With reference to Figure 7.1, the mild steel stepped shaft (4) runs in self-aligning ball bearings (3) and (6) at H and J respectively. The ball bearing at H is rigidly supported. The ball bearing (6) has a ring fixed to its outer race

and is free to orbit in the oil-filled annular clearance within the bearing housing (7), forming the SFD (8). In Figure 7.1, J refers to the centre of the SFD journal (the "journal" being the ring fixed to the outer race of (6)), and B refers to the centre of the bearing housing (7). In configuration B1, four flexible bars (labelled (5) in Figure 7.1), forming a retainer spring, connect the damper journal to the frame. This arrangement is elucidated in Figure 7.2. If the pedestals E and F in Figure 7.1 are considered rigid and the bearing housing (7) is rigidly bolted to F, then the retainer spring formed by the flexible bars is effectively in parallel with the SFD. The retainer spring has equal stiffness values of 123.4 kN/m in both the x and y directions. The static eccentricity of J from B can be varied by adjusting the position of the housing (7). In configuration B2, the retainer spring is removed and the journal rests on the bottom of the annular clearance in the static condition. In this configuration, anti-rotation bolts are used to prevent the journal from rotating relative to the shaft axis, while allowing sufficient clearance for the movement of J in the x and y directions. This arrangement is elucidated in Figure 7.3. Referring back to Figure 7.1, unbalance masses are attached to the overhung disc (9) at U. The vibration is monitored at three locations J, U and M along the shaft. The point M is referred to here as the "mid-shaft" position, although the distance HM is actually 0.4 times the span HJ. The vibration in the x and y directions at each location is measured by a pair of orthogonal displacement transducers ("probes"). Those at J are aimed at projections on the damper journal (as shown in Figures 7.2, 7.3) while those at M and U are aimed directly at the shaft and disc respectively. The frame ((10) in Figure 7.1) is extremely rigid relative to the shaft and the bedplate is bolted down to a massive, isolated concrete block. The first two undamped modes of the rig with the retainer spring fitted and no oil in the damper clearance were calculated by the mechanical impedance (MI) technique [19] to occur at 13.7 Hz and 40.4 Hz (the MI model of the rig is described in the next section). The corresponding calculated mode shapes are shown in Figure 7.4. The natural frequencies compare favourably with the experimentally determined values in [21] (14 Hz, 41 Hz). The undamped natural frequencies of the rig with the SFD locked by inserting shims into the annular clearance are also of interest. These were calculated at 31.2 Hz and 91.1 Hz by the MI technique and the corresponding mode shapes (i.e. pin-pin modes) are shown in Figure 7.5. The pin-pin frequencies compare favourably with experimentally determined values in [21] (31.2 Hz, 88 Hz). The discrepancy in the latter frequency is attributed in part to the neglect of the flexibility of the ball bearings in the calculation. In fact, if stiffness

values of 10^8 N/m are assumed for both ball bearings at H and J, the first pin-pin resonance frequency remains virtually unaltered at 31.2 Hz, while the second one decreases to 89.8 Hz.

The SFD is unsealed, as shown schematically in Figure 7.6 and has a central circumferential groove. The oil groove depth is 5.25 mm. For configuration B2, some experimental results are quoted from [64] for which the groove depth is 2.00 mm. In both cases, the ratio d_{groove}/c is considered sufficiently large for the two-land model of the SFD to be applicable. Oil is supplied through 3 holes, spaced at 120° around the groove. The outlet oil temperature is monitored by a thermometer located below the SFD in the oil-collecting tray. The oils used are *Shell calibration fluid C* (viscosity of 0.0045 Nsm^{-2} at an average operating temperature of 34° C) and *Shell Tellus R*10 (viscosity of 0.0115 Nsm^{-2} at an average operating temperature of 32° C). Since the rig is run up to a top speed of 100 rev/s, the maximum gap Reynolds number (eq. (4.16)) for the thinner oil is 2 (taking the density to be 841 kg/m^3). Using eq. (4.15) with $C_1 = 0.287$ (for moderate *Re*) [60], an upper limit for the fluid inertia effect for both oils is estimated as $M_{fluid} = 0.17$ kg. This amounts to just 13 % of the combined mass of the ball bearing, damper journal and the equivalent retainer spring mass, justifying the neglect of fluid inertia in the simulations.

7.3 MODEL APPLICATION

7.3.1 Introduction

In this section, the equations of Chapter 5 are applied to configuration B. In Figure 7.1, the frame (10), bearing housing (7) and the self-aligning ball bearings are taken to be rigid, so that the linear subsystem will be the shaft pinned at H and either sprung or unsprung (i.e. free) at J (i.e. configurations B1 and B2 respectively). The polar moment of inertia of the disc is sufficiently small for gyroscopic effects to be negligible over the operational range of the rotational speed. Hence, in the linear subsystem the *xz* and *yz* planes are uncoupled. The SFD is assumed to be the only source of damping. As a result of the latter two simplifying assumptions, the $P_N \times 1$ vector $\mathbf{f_N}$ ((eq. (5.3)) is identical for both the frequency domain (receptance harmonic balance (RHB)) and the time domain (modal analysis) equations. Since the bearing housing is rigid, $P_N = 2$ and

$$\mathbf{f_N} = \begin{bmatrix} Q_x \\ Q_y \end{bmatrix} \tag{7.1}$$

Q_x, Q_y are the SFD forces on J, calculated from eqs. (4.6a,b) with $X_{rel}, Y_{rel} = X_J, Y_J$ where X_J, Y_J are the displacements of J from the (fixed) centre B of the rigid bearing housing. The unbalance forces P_x, P_y at U are given by eqs. (5.1a,b) with $\gamma_k = 0$ and the subscript k removed.

7.3.2 Configuration B1 (retainer spring fitted)

In this case, the linear subsystem is the rotor pinned at H and sprung at J and $\mathbf{u}_N$ is given by eq. (5.11a):

$$\mathbf{u}_N = \begin{bmatrix} X_J \\ Y_J \end{bmatrix} - \begin{bmatrix} e_{0x} \\ e_{0y} \end{bmatrix} \tag{7.2}$$

where e_{0x}, e_{0y} are the static eccentricities of J from the housing centre B in the x and y directions respectively. In the RHB approach:

$$X_J = \overline{X}_J + \sum_{s=1}^{m} \left(a_{XJ}^{(s)} \cos s\varpi t + b_{XJ}^{(s)} \sin s\varpi t \right), \; Y_J = \overline{Y}_J + \sum_{s=1}^{m} \left(a_{YJ}^{(s)} \cos s\varpi t + b_{YJ}^{(s)} \sin s\varpi t \right) \tag{7.3a,b}$$

and

$$Q_x = \overline{Q}_x + \sum_{s=1}^{m} \left(p_x^{(s)} \cos s\varpi t + q_x^{(s)} \sin s\varpi t \right), \; Q_y = \overline{Q}_y + \sum_{s=1}^{m} \left(p_y^{(s)} \cos s\varpi t + q_y^{(s)} \sin s\varpi t \right) \tag{7.4a,b}$$

where

$$\begin{bmatrix} \overline{Q}_x \\ \overline{Q}_y \end{bmatrix} = \frac{1}{\Gamma} \int_0^{\Gamma} \begin{bmatrix} Q_x \\ Q_y \end{bmatrix} dt, \; \begin{bmatrix} p_x^{(s)} \\ p_y^{(s)} \end{bmatrix} = \frac{2}{\Gamma} \int_0^{\Gamma} \begin{bmatrix} Q_x \\ Q_y \end{bmatrix} \cos s\varpi t \; dt, \; \begin{bmatrix} q_x^{(s)} \\ q_y^{(s)} \end{bmatrix} = \frac{2}{\Gamma} \int_0^{\Gamma} \begin{bmatrix} Q_x \\ Q_y \end{bmatrix} \sin s\varpi t \; dt \tag{7.5a-c}$$

In the above equations, $\Gamma = 2\pi/\varpi = NT$ (eq. (5.8b)). Hence, defining

$$\delta_{Ns} = \begin{cases} 0 & s \neq N \\ 1 & s = N \end{cases} \tag{7.6}$$

the complete set of RHB equations (5.14) can be written as:

$$\overline{X}_J - e_{0x} = \alpha_{JJ}(0)\overline{Q}_x$$

$$\overline{Y}_J - e_{0y} = \beta_{JJ}(0)\overline{Q}_y \qquad (7.7a1,a2)$$

$$a_{XJ}^{(s)} = \alpha_{JJ}(s\varpi)p_x^{(s)}$$

$$a_{YJ}^{(s)} = \beta_{JJ}(s\varpi)p_y^{(s)} - \delta_{Ns}\beta_{JU}(s\varpi)U\Omega^2, \quad s = 1\ldots m \qquad (7.7b1,b2)$$

$$b_{XJ}^{(s)} = \alpha_{JJ}(s\varpi)q_x^{(s)} + \delta_{Ns}\alpha_{JU}(s\varpi)U\Omega^2$$

$$b_{YJ}^{(s)} = \beta_{JJ}(s\varpi)q_y^{(s)}, \qquad s = 1\ldots m \qquad (7.7c1,c2)$$

In the above equations, $\alpha_{PQ}(\omega)$ and $\beta_{PQ}(\omega)$ are the receptance functions at frequency ω rad/s of the linear subsystem, relating the forces at position Q in the x and y directions respectively with the displacement responses in the corresponding directions at position P. All receptance functions are real and independent of rotational speed due to the neglect of linear damping and gyroscopic effects. Also, $\alpha_{PQ}(\omega) = \beta_{PQ}(\omega)$ (rotor isotropic). The rotor receptances are evaluated using the mechanical impendance (MI) technique [19] and the MI model used for the rotor is described in Appendix A2, section A2.2. An overview of the MI method is given in section A2.1. It suffices to say here that only the attachments to the shaft (e.g. the disc at U, the ball bearing and damper journal at J, ... etc.) were considered as lumped inertias. The impedance matrices of the shaft elements for each plane xz, yz were based on the exact solution of the plane harmonic bending wave equation of a uniform section beam of distributed inertia. Hence, these matrices were exact, irrespective of element length, and only 8 such elements needed to be used in the MI model of the rotor. For solution, eqs. (7.7) are expressed in the form $\mathbf{p}(\hat{\mathbf{v}}, \hat{\Omega}) = \mathbf{0}$ of eq. (5.18) by bringing all the terms to one side of the equality signs. $\hat{\mathbf{v}} = \mathbf{v}/c$ where $\mathbf{v}$ is the $2(2m+1)\times 1$ vector of the unknown Fourier coefficients of the SFD displacements $\overline{X}_J$, $a_{XJ}^{(s)}$, $b_{XJ}^{(s)}$, $\overline{Y}_J$, $a_{YJ}^{(s)}$, $b_{YJ}^{(s)}$ for $s = 1\ldots m$. $\hat{\Omega} = \Omega/\omega_0$, where ω_0 (rad/s) is arbitrarily chosen as the first pin-pin critical speed, $2\pi \times 31.2$ The resulting system is then solved using the arc-length continuation method (section 5.3, pages 63-64), using the iterative algorithm in Appendix A1 to trace out a speed response curve of NT - periodic solutions, where N is of fixed value. For each such solution, the Fourier coefficients of the SFD forces are known. The Fourier coefficients of the response at an arbitrary position P on the rotor:

$$X_P = \overline{X}_P + \sum_{s=1}^{m}\left(a_{XP}^{(s)}\cos s\varpi t + b_{XP}^{(s)}\sin s\varpi t\right),\ Y_P = \overline{Y}_P + \sum_{s=1}^{m}\left(a_{YP}^{(s)}\cos s\varpi t + b_{YP}^{(s)}\sin s\varpi t\right) \quad (7.8a,b)$$

are determined from eqs. (7.7) by omitting the terms e_{0x}, e_{0y}, replacing the subscript J by P in the displacement Fourier coefficients on the left hand side of eqs. (7.7) and replacing the first subscript J by P in the receptance terms on the right hand side of eqs. (7.7). The right hand sides of the modified equations can then be evaluated to yield the Fourier coefficients in eqs. (7.8).

For the time domain equations of motion, 4 modes of vibration of the undamped pinned-sprung rotor in each of the *xz* and *yz* planes are considered, giving a total of $H = 8$ modes. Hence, the modal coordinate vector $\mathbf{q}$ (eq. (5.29)) and matrix $\mathbf{D}$ (eq. (5.31)) are written as

$$\mathbf{q} = \begin{bmatrix} q_{x1} & q_{y1} & \cdots & q_{x4} & q_{y4} \end{bmatrix}^{\mathrm{T}} \quad (7.9)$$

$$\mathbf{D} = \mathbf{diag}\begin{bmatrix} \omega_{x1}^2 & \omega_{y1}^2 & \cdots & \omega_{x4}^2 & \omega_{y4}^2 \end{bmatrix} \quad (7.10)$$

The modal equations (5.32) hence reduce to

$$\ddot{q}_{xr} + \omega_{xr}^2 q_{xr} = \phi_J^{(xr)} Q_x + \phi_U^{(xr)} P_x \quad (7.11a)$$

$$\ddot{q}_{yr} + \omega_{yr}^2 q_{yr} = \phi_J^{(yr)} Q_y + \phi_U^{(yr)} P_y, \quad \text{where } r = 1\ldots4 \quad (7.11b)$$

In the above equations, ω_{xr}, ω_{yr}, $r = 1\ldots4$ are the natural frequencies in the *xz* and *yz* planes respectively and $\phi_P^{(xr)}$, $\phi_P^{(yr)}$ are the corresponding mass-normalised mode shapes, evaluated at position P in the *x* and *y* directions respectively. Note that $\omega_{xr} = \omega_{yr}$ and $\phi_P^{(xr)} = \phi_P^{(yr)}$. The first two mode shapes in each plane have already been illustrated in Figure 7.4. For the computation of the instantaneous SFD forces Q_x, Q_y, the instantaneous non-linear degrees of freedom, measured from the housing centre B (i.e. X_J, Y_J in eq. (7.2)) are required. The vector $\mathbf{u}_N$ of eq. (7.2) is expressed in terms of the modal coordinate vector $\mathbf{q}$ of eq. (7.9) by the reduced transformation $\mathbf{u}_N = \mathbf{H}_N\mathbf{q}$ (eq. (5.34)). The reduced modal matrix $\mathbf{H}_N$ (eq. (5.33)) is given by the 2×8 matrix:

$$\mathbf{H}_{\mathrm{N}} = \begin{bmatrix} \phi_J^{(x1)} & 0 & \cdots & \phi_J^{(x4)} & 0 \\ 0 & \phi_J^{(y1)} & \cdots & 0 & \phi_J^{(y4)} \end{bmatrix} \tag{7.12}$$

where the columns define the modes of the rotor, alternately in the xz and yz planes.

The evaluation of the modal parameters of the rotor is described in Appendix A3, sections A3.1, A3.2. The natural frequencies are determined from the mechanical impedance frequency response functions. The required mode shapes are then determined by fitting 4 modes to the exact receptance function $\alpha_{PQ}(\omega)$ (computed by MI) using a truncated modal series expansion for $\alpha_{PQ}(\omega)$ [47]. In Figure 7.7 the exact receptances $\alpha_{JJ}(\omega)$, $\alpha_{JU}(\omega)$, computed by MI, are compared with approximate ones, reconstructed from the first 4 modal terms in their series expansions. It is evident that excellent agreement prevails over a frequency range of 0-500 Hz, covering 5 harmonics of the top rotational speed of the rig (100 rev/s).

Equations (7.11) are ready for numerical integration from given initial conditions for the time domain response. Prior to integration, these equations are non-dimensionalised and expressed as a set of first order differential equations, as illustrated in Appendix A4, section A4.1. The instantaneous x and y response at an arbitrary position P on the rotor is given in terms of the modal coordinates by the appropriate pair of rows of the full transformation $\mathbf{u} = \mathbf{Hq}$ (eq. (5.28)), and thus necessitates the computation of $\phi_P^{(xr)}$, $\phi_P^{(yr)}$, $r = 1 \ldots 4$.

For stability and bifurcation analysis of the RHB response, the matrices $\partial \mathbf{f}_{\mathrm{N}} / \partial \mathbf{u}_{\mathrm{N}}$, $\partial \mathbf{f}_{\mathrm{N}} / \partial \mathbf{u}'_{\mathrm{N}}$ in the expression for $\mathbf{W}(\tau)$ (eqs. (5.44), (5.45)) are required. From eqs. (7.1) and (7.2) these are given by

$$\frac{\partial \mathbf{f}_{\mathrm{N}}}{\partial \mathbf{u}_{\mathrm{N}}} = \begin{bmatrix} \dfrac{\partial Q_x}{\partial X_J} & \dfrac{\partial Q_x}{\partial Y_J} \\ \dfrac{\partial Q_y}{\partial X_J} & \dfrac{\partial Q_y}{\partial Y_J} \end{bmatrix}, \quad \frac{\partial \mathbf{f}_{\mathrm{N}}}{\partial \mathbf{u}'_{\mathrm{N}}} = \begin{bmatrix} \dfrac{\partial Q_x}{\partial X'_J} & \dfrac{\partial Q_x}{\partial Y'_J} \\ \dfrac{\partial Q_y}{\partial X'_J} & \dfrac{\partial Q_y}{\partial Y'_J} \end{bmatrix} \tag{7.13a,b}$$

where $(\,)'$ is $d(\,)/d\tau$, $\tau = \varpi t$ (ϖ rad/s being the fundamental frequency of the periodic solution). The partial derivatives in eqs. (7.13) are evaluated numerically at the RHB-computed periodic solution from the expressions for $Q_{x,y}$ in eqs. (4.6a,b). The above expressions, along with the expressions for $\mathbf{H}_{\mathrm{N}}$ (eq. (7.12)) and $\mathbf{D}$ (eq. (7.10)) determine the

expression for $\mathbf{W}(\tau)$ in eqs. (5.44), (5.45), from which the monodromy matrix **G** of the periodic solution is computed, using eq. (3.22).

The equations presented in this section are processed as discussed in section 5.7 of Chapter 5.

7.3.3 Configuration B2 (no retainer spring)

In this case, the linear subsystem is the rotor pinned at H and free at J. The pinned-free rotor is degenerate, having in each plane *xz*, *yz*, one mode defining (non-oscillatory) pure rigid body rotation about the pivot H. In this situation, the static load of the rotor needs to be taken into account. The zero frequency components of the forces on the vibrating rotor are in a state of static equilibrium, as explained in Chapter 5 (end of section 5.3). Since this zero frequency equilibrium problem is statically determinate, the distributed rotor weight can be replaced by an equivalent concentrated load at J, equal to *W*, where

$$W = W_R l_{GH} / l_{HJ} \tag{7.14}$$

where W_R is the total rotor weight, l_{GH} is the distance of the rotor mass centre G from the pivot H, and l_{HJ} is the distance between H and J. Accordingly, the equations in the previous section 7.3.2 are modified as follows:

- The vector $[e_{0x} \quad e_{0y}]^T$ is omitted.
- The zero frequency RHB equations (7.7a1,a2) are replaced by the following static equilibrium equations at zero frequency (obtained by taking moments about H):

$$\overline{Q}_x = 0, \quad \overline{Q}_y - W = 0 \tag{7.15a1,a2}$$

- If required, the zero frequency Fourier coefficients in eqs. (7.8) can be found by considering the straight line joining the pivot H to the mean position of J, $\overline{X}_J$, $\overline{Y}_J$. The reason for this is that, with the equivalent static load system, the only zero frequency forces acting on the rotor are concentrated at H and J, producing no deformation. To obtain the precise zero frequency shape of the rotor in the *yz* plane, one needs to superimpose (on this undeformed straight line) the static deflection curve of the rotor supported at H and at the mean position of J, due to the distributed weight. However, this

refinement is unnecessary since it has no effect on the mean position of J, which is the only zero frequency component of vibration that is of interest.

- An additional term, equal to $-\phi_J^{(yr)}W$, is added to the right hand side of eq. (7.11b) to account for the static load.

For the time domain equations of motion, 4 modes of the pinned-free rotor are taken in each of the *xz* and *yz* planes. This number includes the rigid body mode i.e. $\omega_{x1}, \omega_{y1} = 0$. The modal parameters are given in Appendix A3, section A3.2. Figures 7.8(a,b) compare the exact receptances $\alpha_{JJ}(\omega)$, $\alpha_{JU}(\omega)$, computed by MI, with approximate ones, reconstructed from the first 4 modal terms in their series expansions. As for configuration B1, excellent agreement prevails over a frequency range of 0-500 Hz, covering 5 harmonics of the top rotational speed of the rig (100 rev/s).

7.4 EXPERIMENTAL WORK

For configuration B1 (retainer spring fitted), the static eccentricity $\varepsilon_{0x} = e_{0x}/c$, $\varepsilon_{0y} = e_{0y}/c$, of the journal centre J from the bearing housing centre B was set by loosening the screws bolting the housing (7) (Figure 7.1) to the frame. A small clearance in the screw holes of the housing allowed its position to be adjusted prior to retightening. The static eccentricity adjustment was complicated by a static run-out of the shaft. By rotating the shaft slowly by hand and using a micrometer dial indicator with its stem pressed to the shaft at M, and at locations as close as possible to J and U, it was found that the amplitude of the fluctuation in the reading was 0.015, 0.022 and 0.05 mm respectively, for the *y* direction. The run-out in the *x* direction was considerably less. The run-out at J was confirmed by the readings of the displacement transducers (see Figure 7.2). This meant that the run-out was not due to lack of roundness of the shaft surface since the displacement transducers at J were aimed at projections on the journal rather than at the shaft. This also meant that the static eccentricity of J was different for different angular positions of the shaft. At first this appeared unusual since the shaft was pivoted at H and, regardless of whether the shaft was distorted (due to the machining process, gravity, and temperature), the restoring force from the retainer spring should have maintained J at a fixed position within the clearance. The most likely explanation is that the distortion of the shaft resulted in angular misalignment of the hubs at the flexible drive coupling, resulting in a slight restraining torque that varied with the angular position of the shaft. This slight restraint was thought to affect the position of J, considering

the low stiffness of the retainer spring (123.4 kN/m). In view of this problem, the eccentricity was adjusted in the vertical and horizontal directions for each of four angular positions (0°, 90°, 180°, 270°) of the shaft. For each direction x, y, the average eccentricity over the four angular positions was brought as close as possible to the desired eccentricity in that direction. The static eccentricity was rechecked after each experiment, when the rig was hot. Details of the static eccentricity adjustment are found in Appendix A5, section A5.2. In the investigations carried out, the static eccentricity was entirely in the y direction.

In the experiments for configuration B2, the retainer spring was removed and the arrangement in Figure 7.3 was used.

The displacement transducers at J, U and M were connected through voltage amplifiers to a PC-operated *Hewlett Packard HP* 35650® spectrum analyser, which was set to acquire data in the form of a time history. The vibration data in the x and y directions were obtained for a given unbalance at U and fixed oil supply pressure over a range of speeds (10-100 rev/s) in steps of 2 rev/s. The rotor speed was measured using an optical sensor and the observed fluctuation in speed over each acquisition was within ± 0.5 rev/s. Instrumentation details are found in Appendix A5, section A5.1. For the SFD location (J), the mean component of the displacement response relative to the static position was of interest. In view of the variable nature of the static position in configuration B1, the method described in Appendix A5, section A5.3, was used. The time capture length of the vibration data was usually 0.5 s, but was increased to 2 s as required. The data were converted from standard format to *MATLAB*® format for time and frequency domain analysis.

7.5 RESULTS AND DISCUSSION

In this section, theoretical and experimental results are presented and discussed. In the theoretical treatment no attempt is made to compensate for the small residual unbalance left after the rig was balanced when first commissioned. The residual unbalance response was investigated experimentally in [64] and found to be adequately small. In the theoretical treatment, unless otherwise stated, the cavitation pressure $p_c = -101.325 \times 10^3$ Pa.

7.5.1 Configuration B1 (retainer spring fitted)

The oil used in this configuration is the thinner oil (*Shell calibration fluid C*) and the supply pressure is fixed at 1 bar. As mentioned in the previous section, the static eccentricity is entirely in the y direction.

The choice of the number of harmonics m to use in the T-periodic RHB solution (i.e. $N=1$ in eq. (5.8b)) is first considered. Figure 7.9 shows an example of how the RHB solution converges to the time-marching (modal numerical integration) result as m is increased from 1 to 5. It is seen that the inclusion of further harmonics in the RHB solution is unnecessary. It is worth mentioning that the RHB solution uses exact receptances (no modal truncation). Hence, the agreement between the RHB and modal numerical integration results is also a check on the adequacy of the number of modes used in the latter method. The example in Figure 7.9 illustrates the varying influence of the harmonics (which in this case are integer EOs, where 1EO ("engine order") represents the synchronous frequency component) on the orbital distortion at the three locations J, U and M. It is seen that, while the presence of these integer EOs is a symptom of the non-linearity of the system, the orbital distortion they produce does not necessarily manifest itself significantly at the actual source of the non-linearity (i.e. at J). In the example shown, the transfer receptance function linking M to J amplifies the responses at M to the individual harmonic components of the SFD forces at J. The high degree of correlation between the T-periodic RHB solutions with $m=5$ and the numerical integration results over the entire operating speed range is illustrated in the speed response curves of Figure 7.10 for $\varepsilon_{0y}=-0.8$ and $U=5.1\times10^{-4}$ kgm. The vertical axes show the displacement amplitude normalised with respect to the radial clearance c. In this thesis, the displacement amplitudes in the x and y directions are invariably defined as half the peak-to-peak fluctuation in the respective displacement time history. The state of stability of each RHB solution, computed by Floquet analysis, is indicated according to the legend in the figure caption. Arc-length continuation is used to trace out the RHB solution curve, so the rotational speed corresponding to each solution is not pre-selected, but comes out as part of the solution process. On the other hand, the time-marching results are performed at discrete pre-selected speeds, in steps of 2 rev/s, and the corresponding solution points are not joined in Figure 7.10 for emphasis. For each speed, the initial conditions for the time-marching solution were equilibrium conditions on the corresponding T-periodic solution, obtained by modal decomposition of the RHB $N=1$, $m=5$ solution at that speed (see eqs. (5.47a,b)). The time domain solution was then continued well into the steady-state

phase. In Figure 7.10 it is seen that excellent agreement is achieved between the stable RHB solutions and the time-marching results. According to the Floquet analysis results, in the range 32-35 rev/s, the T-periodic RHB solutions are unstable as a result of a secondary Hopf bifurcation, so the (stable) time-marching result at 34 rev/s does not agree with the (unstable) RHB $N=1$ result at this speed. Figure 7.11 shows the evolution of the time-marching solution at 30 rev/s, for which the RHB T-periodic solution is stable. The slight initial perturbations in Figures 7.11(a1-a3) are attributed to slight errors in the initial conditions. These perturbations rapidly die down and the time-marching trajectory remains closely matched with the T-periodic RHB solution, verifying that it is indeed an attractor. Figure 7.12 considers the evolution of the time-marching solution at 34 rev/s, where the T-periodic RHB solution is unstable. As can be seen, the time-marching result evolves into quasi-periodic motion, confirming the Floquet stability result. Figure 7.13 shows the Poincaré map of the time-marching solution at the SFD. It is seen that, in the transient phase, the return points (in red) spiral out from the first one (the unstable equilibrium point E), consecutive points hopping from one spiral branch to the next. In the steady-state, the return points (in blue) drift around a fixed closed curve, no point ever quite coinciding with another. This indicates 2-frequency quasi-periodic motion. From the discussion in Chapter 3 (section 3.2.3), the presence of 4 spiral branches in the transient phase indicates that the non-synchronous fundamental f_0 is related to the original (synchronous) fundamental f_1 (= 1EO) by the relation $f_0 = (\breve{k}/4)f_1$ where $\breve{k}$ is some positive integer and the ratio $\breve{k}/4$ is reduced to its lowest terms. In fact, as shown in the frequency spectra of the steady-state quasi-periodic motion of J at 34 rev/s (Figure 7.14), $f_0 = 9$ Hz (i.e. $f_0 \approx f_1/4$). It is also seen from these spectra that all frequency components can be expressed as combinations $k_0 f_0 + k_1 f_1$ where k_0, k_1 are integers.

Figure 7.15 shows the variation of the modulus of the leading Floquet multiplier for the T-periodic RHB solution for the static eccentricity and unbalance conditions considered in this discussion. It is evident that, as static eccentricity and/or unbalance is increased, there is a tendency for the T-periodic response to develop a region of instability. As shown in Figure 7.16, this instability is the result of a secondary Hopf bifurcation (λ_l complex). The region of instability of the T-periodic solutions lies between the first pin-pin critical speed (~31 rev/s) and the second undamped critical speed of the test rig (SFD unlocked, ~40 rev/s), and

is closer to the former speed than the latter. This region is also particularly sensitive in that it is the zone of maximum amplitude, as shall be seen later in the amplitude-speed plots.

In view of the results of Figure 7.15, the measured orbital motions (over 0.5 s) are investigated for the range 26-38 rev/s and compared with the T-periodic predictions. Figure 7.17 refers to $\varepsilon_{0y} = -0.6$ and $U = 2.59\times10^{-4}$ kgm and it can be seen that the measured orbits are periodic throughout the speed range under these conditions. Notice that, since the displacement probes at U were aimed at the disc rim, slight machining irregularities of the rim profile resulted in slight glitches in the elliptical orbit measured at U. In Figure 7.18, which refers to the same static eccentricity value ($\varepsilon_{0y} = -0.6$) but twice the previous unbalance, aperiodic motion was measured for 32 and 34 rev/s. This is contrary to the stability prediction (Figure 7.15(b)) but is understandable, given the proximity of the peak in Figure 7.15(b) to the instability threshold and, more importantly, the difficulty in obtaining precise static eccentricity conditions due to the static run-out. As expected, the measured aperiodic motion becomes more widespread as the static eccentricity is increased to $\varepsilon_{0y} = -0.8$ at the same unbalance level (see Figure 7.19). The aperiodicity appears at around 30 rev/s and stability of T-periodic motion is not restored until 38 rev/s. The region of instability is somewhat wider than predicted (32-35 rev/s). It is noted from the periodic orbits in Figure 7.18 at 26 and 30 rev/s, and those in Figure 7.19 at 26 and 28 rev/s, that the varying influence of the harmonics on the orbital distortion at the three locations J, U and M, predicted earlier in Figure 7.9, was indeed verified in the measurements. The outlines of the highly distorted measured orbits at M in Figure 7.18 for 30 rev/s and Figure 7.19 for 28 rev/s were correctly predicted with $m = 5$ harmonics in the RHB $N = 1$ solution. Moreover, the RHB $N = 1$ solution still gives a good prediction of the peak-to-peak displacement at those speeds for which the measured motion was aperiodic.

The frequency content of the measured aperiodic motion for $\varepsilon_{0y} = -0.8$ is next studied. For this purpose, the data length is increased from 0.5 s to 2 s. Figure 7.20 shows the orbital motion at J, U and M over 2 s for two speeds, 30 and 34 rev/s. The ones for 34 rev/s are comparable to the time-marching prediction for the same speed (Figures 7.12(b1-b3)). The frequency spectra of the y component of the measured SFD motion at 30 and 34 rev/s are shown in Figure 7.21. In these spectra, the Hanning window [47] is used to mitigate the leakage effect from adjacent frequency spikes. It is found that the salient peaks in the spectra of Figure 7.21 occur at combinations $k_0 f_0 + k_1 f_1$ where k_0, k_1 are integers. For 30 rev/s

(Figure 7.21(a)), $f_0 = 11\,\text{Hz}$ and $f_1 = 30\,\text{Hz}$ (synchronous). For 34 rev/s (Figure 7.21(b)), $f_0 = 12.5\,\text{Hz}$ and $f_1 = 34\,\text{Hz}$ (synchronous). The 9 Hz frequency component predicted in Figure 7.14 appears in the measured spectrum of Figure 7.21(b) as $f_1 - 2f_0$ rather than f_0. In fact, with reference to Figure 7.21(b): $9 = f_1 - 2f_0$, $12.5 = f_0$, $21.5 = f_1 - f_0$, $25 = 2f_0$, $34 = f_1$, $43 = 2(f_1 - f_0)$, $46 \approx f_1 + f_0$, $50 = 4f_0$, $68 = 2f_1$, $102 = 3f_1$. The lobe at ~17 Hz $(= f_1/2)$ is actually composed of a double peak, where each peak is a combination frequency. A double-peaked lobe centred at the $1EO/2$ location is also evident in Figure 7.21(a) (30 rev/s) and in the predicted spectrum of Figure 7.14(b) (34 rev/s). In fact, due to the sum and difference nature of the frequencies, the sub-synchronous frequencies are symmetrically arranged around the $1EO/2$ location (i.e. the mean of f_0 and $f_1 - f_0$ is $f_1/2$, and so is the mean of $f_1 - 2f_0$ and $2f_0$). The measured spectra of Figure 7.21 provide evidence that the measured T-periodic motion for $\varepsilon_{0y} = -0.8$, $U = 5.1\times10^{-4}\,\text{kgm}$ underwent a secondary Hopf bifurcation at some speed between 28 and 30 rev/s.

Attention is now focussed on the predicted and measured amplitudes in the x and y directions. The static eccentricity and unbalance conditions considered are those indicated in Figure 7.15. For the condition $\varepsilon_{0y} = -0.8$, $U = 5.1\times10^{-4}\,\text{kgm}$, the maximum change in amplitude, as a result of the instability of the T-periodic RHB solutions in the range 32-35 rev/s, is at 34 rev/s, and, as seen in Figure 7.10, this change is not that great. Hence, for the purposes of this part of the discussion, the issue of stability is ignored and the RHB $N = 1$ predictions are used throughout.

The predicted and measured amplitude-speed plots are shown in Figures 7.22-7.25. In addition to the lower pressure limit of $p_c = -101.325\times10^3$ Pa, another set of T-periodic RHB solutions was generated by taking $p_c = -\infty$ (no lower pressure limit imposed i.e. a full film at the SFD under all conditions). The predictions obtained with $p_c = -101.325\times10^3\,\text{Pa}$ are referred to here as the "absolute zero cavitation" results, while those obtained with $p_c = -\infty$ are referred to as the "full film" results. Those regimes of operation for which cavitation occurs are identified by those regimes for which divergence occurs between the speed response curves obtained by the two different values of p_c. The reason for this is that the divergence would be the result of the minimum oil film pressure in the full film model going below absolute zero. In this way, one can study the influence of static eccentricity and

unbalance on cavitation within the SFD at a fixed supply pressure (1 bar) and observe how the cavitation affects the predicted vibration levels.

Figures 7.22(a,b) show the vibration levels at the SFD for the static eccentricity of $\varepsilon_{0y} = -0.6$ and the lower unbalance ($U = 2.59\times10^{-4}$ kgm). It is clear that both the absolute zero pressure cavitation model and the full film model yield virtually identical results, indicating that negligible cavitation is predicted under such conditions. The predictions for the vibration levels at the other locations of the rotor are consequently very close for both models (Figures 7.22(c-f)), with maximum divergence being registered at the disc position (U) in the y direction (Figure 7.22(d)). Note that in Figures 7.22(a,c), which refer to the x direction (for which the SFD is centralised), two maxima are observed in both measurement and prediction. The lower predicted maximum is less defined, especially for the SFD x vibration, Figure 7.22(a). These maxima may be related to the undamped natural frequencies of the test rig (14, 40 rev/s). In the y direction (for which the SFD is offset), Figures 7.22(b,d,f), the first maximum is entirely absent from the prediction, while the second one is predicted at a lower speed (around 32 rev/s). Hence, the predicted behavior in the y direction is more akin to the pin-pin configuration of the test rig (i.e. with SFD locked, where the first critical speed is 31 rev/s). Figure 7.23 shows the effect of doubling the previous unbalance to $U = 5.1\times10^{-4}$ kgm for the same static eccentricity condition of $\varepsilon_{0y} = -0.6$. Large discrepancies emerge between the cavitated and uncavitated model predictions within the range 28-36 rev/s. As previously discussed, this means that within this speed range, in the full film model, the oil film supports a region below absolute zero pressure (i.e. absolute tension) and hence cavitation occurs in the absolute zero cavitation model. Within the zone of maximum amplitude, 30-34 rev/s, the full film model predicts extremely high vibration in the y direction at positions other than the SFD (i.e. at U and M), which were not verified in the measurement. In the x direction, the uncavitated predictions for the vibration at U and M are extremely large in the immediate vicinity of 31 rev/s. Figure 7.24 shows the vibration levels for the higher static eccentricity of $\varepsilon_{0y} = -0.8$ and the lower unbalance ($U = 2.59\times10^{-4}$ kgm). This figure is included for completeness. Of more interest is Figure 7.25, which shows the effect of employing a static offset of $\varepsilon_{0y} = -0.8$ at the higher unbalance ($U = 5.1\times10^{-4}$ kgm). Large differences between the two SFD models now emerge not just in the 27-37 rev/s zone, but for the y direction especially, above 70 rev/s (Figures 7.25(b,d,f)). This implies an additional predicted cavitation regime.

From the full film unbalance response predictions in Figures 7.23-7.25, it is evident that as the static eccentricity and/or unbalance is increased, an uncavitated SFD (i.e. a full film) would cause the rotor to behave in certain speed ranges as though it were pinned at the SFD journal J. This tendency is especially strong in the y direction at the higher offset of $\varepsilon_{0y} = -0.8$: the critical speeds tend to 31 rev/s for $\varepsilon_{0y} = -0.6$, and 31 rev/s and 91 rev/s for $\varepsilon_{0y} = -0.8$. However, cavitation in the SFD around these speeds mitigates this effect and maintains the predicted vibration within acceptable limits at all positions along the rotor. In the case of the offset condition $\varepsilon_{0y} = -0.8$, cavitation completely attenuates the predicted peak at the second pin-pin critical speed of 91 rev/s (Figure 7.25(f)), which agrees more closely with measurement. The reason for this striking difference in vibration amplitudes predicted by the two SFD models is a direct consequence of the centralising effect cavitation has on the SFD journal. A direct consequence of cavitation in an eccentric damper is the steady component of displacement it produces counter to the direction of the static offset. The example of Figure 4.4 (Chapter 4) indicates that an uncavitated squeeze film that is unsupported by a parallel retainer spring cannot produce a sustained lift to counter the gravity load. In the present case, the full film model does not produce any lift (of the mean position of vibration) from the statically offset position of J. Hence, as the static eccentricity and/or unbalance are increased, the vibration is limited by the clearance circle (i.e. there is less room for vibration) and the SFD forces become very large, especially in the y direction (the direction of the offset), but also at the limits of the x vibration. These large SFD forces would render the SFD ineffective, and the resulting effect at the other locations M and U would approach that obtained by locking the SFD. However, in the present case, this adverse effect is prevented by the centralising effect of cavitation. Figure 7.26 shows the variation of the mean y displacement at the SFD (i.e. $\bar{Y}_J/c$ in eq. (7.3b)) with rotational speed for four different conditions. It is clear that, under all conditions, the full film model produces no lift from the static position. On the other hand, the cavitation regimes are clearly defined by those speed ranges where the absolute zero pressure cavitation prediction rises from the static position. The measurements in Figure 7.26 follow the trend predicted by the absolute zero pressure cavitation model. In fact, approximately over the cavitation regimes predicted in Figure 7.26, pinhole bubbles were observed within the oil flowing out of the damper, indicating cavitation, and these observations tend to agree with those made in a previous investigation [64].

It is noted that Figures 7.23(a,b), 7.24(a,b), and Figure 7.25(a) indicate that the amplitude at the SFD in the immediate vicinity of 31 rev/s (first pin-pin critical speed) is greater with the full film than with the cavitated film. This may at first appear to contradict previous studies [11]. However, it is important to note that studies like [11] were restricted to rigid rotors. To the author's knowledge, this is the first time that comparisons have been made between cavitated and uncavitated SFDs interacting non-linearly with a flexible rotor. However, it is noted that this effect is restricted to an extremely narrow speed range centred at 31 rev/s. In fact, a similar effect would be obtained if the SFD and retainer spring were replaced by a very large but still finite stiffness: since the stiffness is finite, the node will not be located exactly at J and, in the absence of any other damping in the system, a spike at 31 Hz would appear in the transfer receptance function linking J to U. It is also worth mentioning here that all the full film RHB $N=1$ results shown in Figures 7.22-7.26 tested positive for stability (with the Floquet test). However, it is noted that those solutions at the very tip of the spikes at 31 rev/s in Figures 7.23(a,b)-7.25(a,b) were on the verge of instability.

In Figures 7.22-7.25, the very low level in the SFD vibration at 50-52 rev/s corresponds to the anti-resonance at 52 Hz in the calculated transfer receptance function between J and U for the linear subsystem (i.e. $\alpha_{JU}(\omega)$ in Figure 7.7(b)). At 50-52 rev/s, the measured orbit at J is practically a "dot" of amplitude that is much less than the static run-out there. This indicates that the run-out at J has little or no effect on the alternating part of the displacement i.e. the run-out is a purely static or, at worst, a low frequency (quasi-static) phenomenon. The position of this dot within the clearance circle corresponds to the static eccentricity setting (which was averaged over four angular positions of the shaft in cold and hot conditions), as seen in Figure 7.26.

The results in Figures 7.22-7.26 show that, overall, the assumption of film rupture at absolute zero pressure gives satisfactory predictions for the vibration levels. Unfortunately, the limitations of the test facility did not allow the tests to be repeated at higher supply pressures. However, the present theoretical study highlights the beneficial effect of cavitation in maintaining the critical vibration amplitudes at U and M at a safe level for a supply pressure of 1 bar under conditions of high static eccentricity and unbalance. Hence, it is not advisable to increase the supply pressure and consequently, suppress cavitation, under such conditions.

7.5.2 Configuration B2 (no retainer spring)

In the first part of this section, the same oil used in configuration B1 (i.e. *Shell calibration fluid C*) is used. The experimental results are obtained from [64] and the supply pressure is slightly higher (1.2 bar).

Figure 7.27 shows the amplitude-speed plots obtained with the higher unbalance ($U = 5.1\times10^{-4}$ kgm), upon removing the retainer spring. The predictions are RHB $N = 1$, $m = 5$. The state of stability of each such T-periodic solution, evaluated by Floquet analysis, is indicated in the figure caption. Beyond ~82 rev/s, the T-periodic solutions become unstable as a result of a secondary Hopf bifurcation. Hence, the steady-state time-marching solutions for 82-100 rev/s are also included in blue in Figure 7.27, for discrete speeds, in steps of 2 rev/s. The initial conditions for each time-marching solution were obtained from the final ones of the solution at the previous speed and the integration was continued well into the steady-state phase. The following observations can be made of the results in Figure 7.27:

(a) At the SFD, in the y direction especially, there is hardly any vibration except in the regions around 31 and 90 rev/s. These speeds correspond to the first two undamped pin-pin critical speeds. The measured values for the half peak-to-peak displacement at J in the y direction around both pin-pin critical speeds, and in the x direction, around the first, are actually greater than the radial clearance. In [64], this was attributed to the anti-rotation mechanism for the journal not functioning properly. In fact, only one of the two anti-rotation bolts shown in Figure 7.3 had been used in [64]. Figure 7.28 shows that the mean position of the T-periodic solutions only lifts off from the base of the clearance in the vicinity of the pin-pin critical speeds. The lift-off at the first critical speed is sudden. The lift-off of the T-periodic solutions around the second critical speed is more restrained. However, it should be noted that beyond ~82 rev/s these T-periodic solutions are unstable. The stable motion in this region is discussed later. The amplitude measurements in Figure 7.27 indicate that the actual lift at the SFD was as predicted. However, the mean ("dc") component of the SFD vibration was not acquired in [64].

(b) Around the first pin-pin critical speed (31 rev/s), the predicted speed response curve of T-periodic solutions is very complicated, with a multiplicity of solutions, some of which are stable, some unstable. This is also seen in Figure 7.29(a), which shows the corresponding variation of the modulus of the leading Floquet multiplier with rotational speed. In Figure 7.30, a T-periodic RHB solution at 31 rev/s that was found to be stable by Floquet

analysis is checked by time-marching from initial conditions on it. For accuracy, the number of harmonics m of the RHB solution is increased to 8. In Figure 7.30(a) it is seen that considerable initial perturbations are obtained. However, these are not attributed to instability of the orbit, but to errors in the initial conditions, that were obtained by modal decomposition of the RHB solution (eqs. (5.47a,b)). In fact, these perturbations disappear in Figures 7.30(b1-b3).

(c) The RHB-computed T-periodic solutions outside the critical speed regions are marked as stable in Figure 7.27. Actually however, they are mainly on the verge of instability, as seen in Figure 7.29(a), and, as seen in Figure 7.29(c), λ_l is complex in these regions. The reason for this is that the SFD journal J is at the bottom of the clearance in these regimes and so, the damper is ineffective. Since the SFD is the only source of damping in the model, any perturbation of the T-periodic solutions would lead to a practically non-decaying transient at one or more of the pin-pin natural frequencies, which combines with the T-periodic motion to form quasi-periodic motion.

(d) The overall trend in the measured amplitude-speed plots of Figure 7.27 is correctly predicted. However, speed-for-speed agreement in amplitude is unattainable for the SFD, and, beyond 82 rev/s, for all locations J, U, and M. This is due to the uncertainty in the oil film conditions that is inherent in unsupported dampers, especially when no dynamic oil film pressure measurements are made. Nonetheless, in the following discussion it is seen that the predicted stable motion beyond 82 rev/s has an orbital structure and frequency content that is similar to the measurement

As mentioned earlier, the T-periodic RHB solutions become unstable at some speed between 82 and 84 rev/s as a result of a complex-conjugate pair of leading Floquet multipliers λ_l, λ_l^* escaping the unit circle simultaneously (Figure 7.29). However, beyond this bifurcation point, there exists a small segment of unstable T-periodic solutions in the range 85-87 rev/s (segment AB in Figure 7.27(b)) for which λ_l is real and negative, as seen in Figures 7.29(b,c). In Figure 7.31, by time-marching from initial conditions on the unstable T-periodic solution at 86 rev/s, it is verified that there is no error in the associated value of λ_l. In the *initial* stages of the time-marching solution (Figure 7.31(a)), the transient trajectory does indeed show a tendency to period-double, as can be seen from the corresponding Poincaré map of Figure 7.31(b) where successive return points diverge from the first one E (E lies on the unstable T-periodic orbit) by flipping on either side of it, approximately along a straight line (as in Figure 3.2(b) of Chapter 3). However, this

behaviour is only local to the vicinity of the unstable T-periodic orbit and no stable $2T$-periodic orbit develops in the steady state (Figure 7.31(c)).

The predicted transition from T-periodic to aperiodic motion over the sensitive range 82-84 rev/s is quite sudden, as can be seen in Figure 7.32(a), which shows the steady-state time-marching solution at the SFD at 84 rev/s. The measured orbit, Figure 7.32(b), is remarkably similar in structure. This similarity also extends to the frequency spectra in Figure 7.33. These spectra show combination frequencies $k_0 f_0 + k_1 f_1$ where k_0, k_1 are integers, f_1 is the 1EO frequency component and f_0 is approximately the first (pin-pin) critical speed (31.2 rev/s). The predicted value of f_0 agrees with the measured value to within the frequency resolution of the spectrum (2 Hz). Figures 7.34(a,b) show the Poincaré maps of the steady-state predicted SFD orbit at 84 rev/s over consecutive intervals of 80 and 160 shaft revolutions. It is seen that the general form of the map is repeatable, but it is not the usual simple closed curve one expects from a 2-frequency quasi-periodic solution. The question of whether the predicted motion at 84 rev/s (Figure 7.32(a)) is indeed pure 2-frequency quasi-periodic motion or has already descended into a mild form of chaos is purely academic. In the spectra of Figure 7.33, the frequency components f_0, $f_1 - f_0$, $f_1 + f_0$, and $2f_1 - f_0$ loosely approximate to 1EO/3, 2EO/3, 4EO/3, and 5EO/3 respectively. These frequency components give the Poincaré maps of Figure 7.34 the approximate triangular shape. At 86 rev/s, the predicted orbital motion locks into $3T$-periodic motion, as shown in Figure 7.35. Also included in this figure is the $3T$-periodic RHB solution. It is seen that satisfactory correlation is maintained between the RHB and modal numerical integration results. In Figure 7.36, the Poincaré map of the predicted SFD orbital motion at 86 rev/s is seen to have degenerated into three points, situated approximately at the vertices of the Poincaré map at 84 rev/s (Figure 7.34(b)).

Figure 7.37 shows predicted and measured waterfall diagrams of the frequency spectra of the x and y vibrations at the three locations J, U, and M. The predicted diagrams were constructed entirely from steady-state time-marching solutions. No solutions were performed below a speed of 24 rev/s due to the insufficient lift at the damper. It is seen that overall correlation with experiment is good. In particular, frequency components that either equal or approximate to integer multiples of 1EO/3 are prominent in both measured and predicted spectra of the y component of the motion at J (Figures 7.37(b1,b2)). From Figure 7.29(a) it is

predicted that stability of T-periodic motion is restored at some speed beyond 100 rev/s. However the study was only performed up to 100 rev/s.

It is evident from the above that the performance of the unsupported SFD when used in this flexible rotor system is much worse than that of a badly centralised sprung SFD. In the following part of the discussion, the performance of the unsupported SFD with a thicker lubricant is investigated for the same unbalance $U = 5.1\times10^{-4}$ kgm. The lubricant (*Shell Tellus R*10) has an average viscosity of around 2.6 times that of the previous oil. The supply pressure remains approximately the same at 1 bar. The aims of this investigation are to note any improvements in performance, and to confirm any of the interesting non-linear features previously observed with the thinner oil that recur with the thicker oil. The time record length of the experimental data acquisition is increased from 0.5 s to 2 s for a more in-depth analysis. An improved anti-rotation device is used for the journal, with two anti-rotation bolts instead of one (Figure 7.3).

Figure 7.38 shows the predicted and measured speed response curves for the amplitudes at the SFD (J) and mid-shaft (M). As before, the time-marching solutions for 82-100 rev/s are included (in blue). No measurements were performed at the disc position to avoid potential damage to the transducers. It is seen that the overall performance is still essentially the same, although the performance at the SFD around the pin-pin critical speeds is marginally improved. In the first pin-pin critical speed region, the multiplicity of T-periodic RHB solutions obtained with the thinner oil has been totally eliminated and the only region of instability there is a narrow quasi-periodic zone. Figure 7.39 shows the orbital motion at the sensitive speed of 32 rev/s: it is seen that the predicted (numerical integration, steady-state) and measured orbits are similar. Referring back to Figure 7.38, it is seen that, in the second pin-pin critical speed region, the secondary Hopf bifurcation of the T-periodic solutions still occurs between 82 and 84 rev/s, but the stability of T-periodic motion is predicted to be restored by 100 rev/s. This is illustrated in Figure 7.40, which shows predicted (stable) and measured orbits in the sensitive range 76–100 rev/s over an interval of 2 s. The predicted orbits show that the transition from T-periodic to 2-frequency quasi-periodic motion between 82 and 84 rev/s is smoother with the thicker oil than with the thinner oil (compare the predicted SFD orbit at 84 rev/s in Figure 7.40 to the one in Figure 7.32(a)). In Figure 7.40 it is seen that the predicted motion still locks into $3T$-periodic motion at 86 rev/s and remains so locked until some speed between 92 and 94 rev/s. The predicted orbits at 94 rev/s appear to be chaotic. Stable T-periodic motion is predicted to be

restored by 100 rev/s. The measured orbits evolve in a similar manner. However, the bifurcation of the T-periodic motion into quasi-periodic motion occurs somewhat earlier (between 76 and 78 rev/s). In Figure 7.40, the measured orbits for 90-94 rev/s are locked into $3T$-periodic motion over most of the acquisition time. The $3T$-periodicity is evident by the triple-looping of the measured orbits at M. Particularly at the SFD, the measured motion at these speeds unlocks from the $3T$-periodic orbit for short parts of the acquisition time. This is likely to be the result of slight jolts from the anti-rotation bolts (Figure 7.3). The "periodic part" of the measured orbits at the SFD for 90-94 rev/s is similar to the predicted $3T$-periodic SFD orbits at 86 and 90 rev/s. As predicted, the measured orbits at 100 rev/s are seen to be approximately T-periodic.

Figure 7.41 shows the evolution of the Poincaré maps of the predicted stable SFD orbits. The map in Figure 7.41(d) shows that the predicted orbits at 94 rev/s are indeed chaotic. Figure 7.41 indicates that this type of motion was arrived at through the quasi-periodic frequency-locking route. That the secondary Hopf bifurcation (between 82 and 84 rev/s) is smoother with the thicker oil is highlighted in Figures 7.41(a,b): the single dot at 82 rev/s evolves into the simple triangular closed curve at 84 rev/s. The map in Figure 7.41(b) contrasts with that in Figure 7.34(b). Despite the difference in Poincaré maps, the structure of the frequency spectrum of the predicted stable SFD orbital motion at 84 rev/s is essentially the same for both oils, as can be seen by comparing Figure 7.42(a1) with Figure 7.33(b1). The same can be said of the frequency spectrum of the measured SFD orbital motion in Figure 7.42(a2) (which is similar to that in Figure 7.33(b2)). In Figures 7.42(a1,a2) it is again seen that f_0 is close to the first pin-pin critical speed and the difference in the predicted and measured value of f_0 is within the frequency resolution (0.5 Hz). Frequency-locking into $3T$-periodic motion is clearly evident in the predicted and measured spectra of Figure 7.42(b1,b2) (for 90 rev/s).

Figure 7.43 shows predicted and measured waterfall diagrams for the x and y vibration at J and M. The predicted diagrams were efficiently constructed from the RHB $N=1$, $m=5$ solutions for those speed regimes for which T-periodic motion was predicted to be stable, and from the steady-state time-marching solutions for the remaining speed regimes. The correlation with measurement is good and frequency components that either equal or approximate to integer multiples of 1EO/3 are evident in the region of the second pin-pin critical speed. As can be seen in Figure 7.44, the non-integer EOs are mostly eliminated

upon halving the unbalance (note that the predictions in Figures 7.44(a1,b1) are only performed for 84 to 100 rev/s). This feature was also observed with the thinner oil [64].

In the measured waterfall diagram of Figure 7.43(d2), it is noted that there exists a strong 2EO frequency component in the y vibration at M at a speed of 44 rev/s. This 2EO component corresponds to the second pin-pin critical speed, measured at 88 rev/s [21]. Hence a sub-critical super-harmonic resonance occurs at 44 rev/s. This resonance is absent from the corresponding prediction, Figure 7.43(d1). The phenomenon of sub-critical super-harmonic resonance in an unsupported SFD was introduced in the preceding chapter, where the phenomenon was associated with bilinear oscillator effects in a contacting rotor-stator system, studied by Ehrich [40, 41] using a piecewise-linear spring model. In Chapter 6, it was shown that, for the case of an unsupported SFD in this condition: (a) the SFD journal J lies at the base of the clearance circle (centre B); (b) there is a slight relative vibration between J and B; and (c) the absolute vibration of B (or J) in the y direction has a significant kEO frequency component, where k is a positive integer and kEO is approximately equal to the undamped critical speed with the SFD locked. For the present study, $k = 2$ and it was postulated that slight absolute vibration of the bearing housing B (and J, since the relative vibration between J and B is minimal at 44 rev/s, especially in the y direction) with a significant 2EO frequency component was inducing a strong component of vibration of the shaft in the second pin-pin mode (i.e. slight excitation of the pinned support at J in Figure 7.5(b) at around the second pin-pin frequency). Since the model used so far in this chapter assumes a rigid bearing housing, this effect could not be predicted in the waterfall diagram of Figure 7.43(d1). This hypothesis was tested by repeating the RHB $N = 1$ calculations for the range 40-50 rev/s, taking into account an assumed flexibility of the bearing housing. This involved the addition of the following extra set of equations to the existing set (which is defined by eqs. (7.15a1,a2), (7.7b1,b2), (7.7c1,c2)):

$$\overline{X}_B = -\alpha_{BB}(0)\overline{Q}_x, \quad \overline{Y}_B = -\beta_{BB}(0)\overline{Q}_y \tag{7.16a1,a2}$$

$$a_{XB}^{(s)} = -\alpha_{BB}(s\varpi)p_x^{(s)}, \quad a_{YB}^{(s)} = -\beta_{BB}(s\varpi)p_y^{(s)}, \quad s = 1\ldots m \tag{7.16b1,b2}$$

$$b_{XB}^{(s)} = -\alpha_{BB}(s\varpi)q_x^{(s)}, \quad b_{YB}^{(s)} = -\beta_{BB}(s\varpi)q_y^{(s)}, \quad s = 1\ldots m \tag{7.16c1,c2}$$

The above equations are taken from Chapter 6 (eqs. (6.8d1,d2-f1,f2)). In these equations $\overline{X}_B$, $a_{XB}^{(s)}$, ... etc. are the Fourier coefficients of the absolute displacements of B, X_B, Y_B .

As in Chapter 6, the SFD forces (which, under such conditions, very nearly reduce to contact forces) were calculated from eqs. (4.6a,b) with $X_{rel} = X_J - X_B$, $Y_{rel} = Y_J - Y_B$. Since the significant harmonics involved in the RHB solution were well below the first natural frequency of the support structure, the support structure receptances at B, $\alpha_{BB}(\omega)$, $\beta_{BB}(\omega) \approx 1/K_{xB}$, $1/K_{yB}$ respectively, where K_{xB}, K_{yB} are the equivalent stiffness values at the bearing housing in the x and y directions respectively. It was assumed that $K_{xB} = K_{yB} = 10^8$ N/m. This stiffness value was sufficiently low to avoid aggravating the ill conditioned nature of this problem (since $X_J, Y_J \approx X_B, Y_B$ in this problem). It was also sufficiently high to have little effect on the second pin-pin mode. In fact, the predicted second pin-pin frequency changed to 90.1 Hz (from 91.1 Hz) and there was practically no change in the mode shape of Figure 7.5(b) (other than the slight repositioning of the right hand nodes). Figure 7.45 shows the RHB $N = 1$, $m = 5$ speed response curves for the y amplitude. It should be noted that, since $X_J, Y_J \approx X_B, Y_B$, very small arc-length increments had to be used to avoid failure in the iteration (the arc-length increment used in this case was typically 10^{-4}, as opposed to the normal value of 10^{-1}). The effect of the inclusion of the flexibility of B is the appearance of spikes at 45 rev/s in Figures 7.45(a-c). It is seen that resonant amplitude in the y direction at B of less than 1 % of the radial clearance induces a corresponding peak in the y displacement at M but not at U. In fact, in the measurements of Figure 7.38(d), the peak in the y amplitude at M at 44 rev/s is observed, and in Figure 7.27 this peak is again observed at M (Figure 7.27(f)) but not at U (Figure 7.27(d)). The most likely reason for this is that, in the second pin-pin mode, the vibration at M is twice that at U (Figure 7.5(b)). The predicted and measured orbits at M at the super-harmonic resonance are remarkably similar (Figures 7.46(b1,b2)) and have a shape that is similar to (though less "sharp" than) the sub-critical super-harmonic resonance orbit shown in Figure 6.13 (Chapter 6). In Figures 7.47(a,b), the frequency spectra of the y components of the predicted and measured orbital motions at M reveal that, at super-harmonic resonance, the 2EO frequency component is practically of the same strength as the 1EO component.

A feature that is also observed in the following chapter is that a sub-critical super-harmonic resonance in an unsupported SFD becomes more prominent at lower levels of unbalance, standing out as a distinctive peak from the otherwise low level of the amplitude-speed curve. Indeed, as long as the lift of the journal from the base of the clearance is minimal and provided the unbalance excitation can still maintain a slight wobble of the

journal relative to the housing, the piecewise-linear spring-like behaviour of the SFD appears to be independent of the unbalance level. The measurements of Figure 7.48 show the effect of halving the unbalance. It is seen that a distinctive spike at 44 rev/s is obtained in the y amplitude at M (Figure 7.48(a)). Again, no corresponding spike is observed at U (Figure 7.48(b)). The results in Figure 7.48 provide additional validation to the results in Figure 7.45(c,d). Note that the results in Figure 7.48 are for the thinner oil. However, the value of the oil viscosity is most likely to be immaterial in this regime of operation.

7.6 CONCLUSIONS

In this chapter, the integrated model developed in Chapter 5 was applied to a test rig having a flexible rotor and one rigidly housed squeeze film damper (SFD). Two variations of the rig were considered. In one configuration (B1) the SFD had a parallel retainer spring and the journal was statically offset in the housing, and in the other configuration (B2) the SFD was unsupported. In either case, the correlation between the three modelling blocks (i.e. receptance harmonic balance, modal Floquet stability analysis, and modal numerical integration) under conditions of multi-modal rotor vibration was found to be highly satisfactory. The integrated modelling approach was also generally successful in predicting and explaining the observed highly non-linear performance of the experimental rig.

With reference to configuration B1 (retainer spring fitted):

- Under conditions of high static eccentricity and unbalance, the T-periodic motion was found to become unstable for a range of speeds between the first pin-pin critical speed and the second undamped critical speed of the rig (with retainer spring). The frequency spectrum of the resulting stable motion was composed of combinations of two fundamental frequencies: one synchronous, and the other sub-synchronous.
- For a fixed supply pressure, cavitation was promoted by increased static eccentricity and/or unbalance. For the configuration studied, the centralising effect of cavitation was seen to be beneficial in that it prevented excessive vibration along the shaft. Hence, for a statically determinate flexible rotor-rigid pedestal system with a SFD in one of its bearings it is not recommended to suppress cavitation by increasing supply pressure or removing dissolved air in the sump, under conditions of high static eccentricity and unbalance

With reference to configuration B2 (retainer spring removed):

- Lift-off at the damper was only achieved around the pin-pin critical speeds.

- The T-periodic motion around the second pin-pin critical speed became unstable as a result of the emergence of a second fundamental frequency that approximates to the first pin-pin critical speed. Since the rotational speed approached three times this frequency, the salient frequency components approximated to integer multiples of 1EO/3 and frequency-locking into $3T$-periodic motion occurred over a range of speeds. The likelihood that frequency-locking lead to the mild chaotic motion that was predicted at certain speeds was not formally investigated.
- The lack of lift at the SFD results in sub-critical super-harmonic resonance of the flexible rotor induced by slight vibration of the bearing housing. In such a condition, if the rotational speed is approximately equal to $1/k$ times a pin-pin critical speed (k being a positive integer) a relatively strong kEO frequency component develops in the slight vibration of the housing. This slight vibration then induces kEO frequency components at locations P along the rotor, the strength of which depends on the amplitude at P in the excited pin-pin mode shape. In this work, this phenomenon has been verified for the case $k = 2$ and the second pin-pin critical speed.
- The main effect of increasing the oil viscosity by a factor of 2.6 on the predicted vibration was to eliminate the complicated behaviour around the first critical speed. The thicker oil also smoothed the secondary Hopf bifurcation in the second critical speed region and restored the stability of T-periodic motion at an earlier speed. However, the performance was still much worse than that of the badly centralised sprung SFD with the thinner oil.
- It is therefore not recommended to use an unsupported SFD in a bearing of a statically determinate flexible rotor-rigid pedestal system. In a statically indeterminate system (with three bearings), an unsprung SFD in one of these bearings would perform much better since it would be off-loaded by the other two bearings i.e. would not need to generate lift to support the static load in order to function. In such a case, with the terminology used in this thesis, the SFD would still be "unsprung" (i.e. has no parallel retainer spring) although it would not be "unsupported".

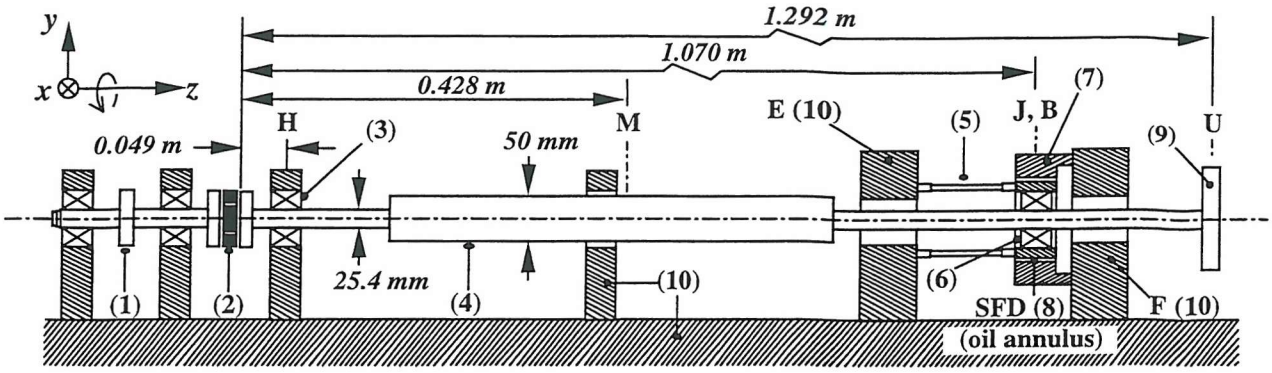

(1) Motor driven pulley
(2) Flexible coupling
(3) Self-aligning ball bearing
(4) Shaft
(5) Flexible bar × 4 (retainer spring)
(6) Self-aligning ball bearing and damper journal (centre J)
(7) Bearing housing (centre B)
(8) Oil annulus (SFD)
(9) Unbalance disc
(10) Frame and bedplate

Figure 7.1: *Test rig for configuration B*

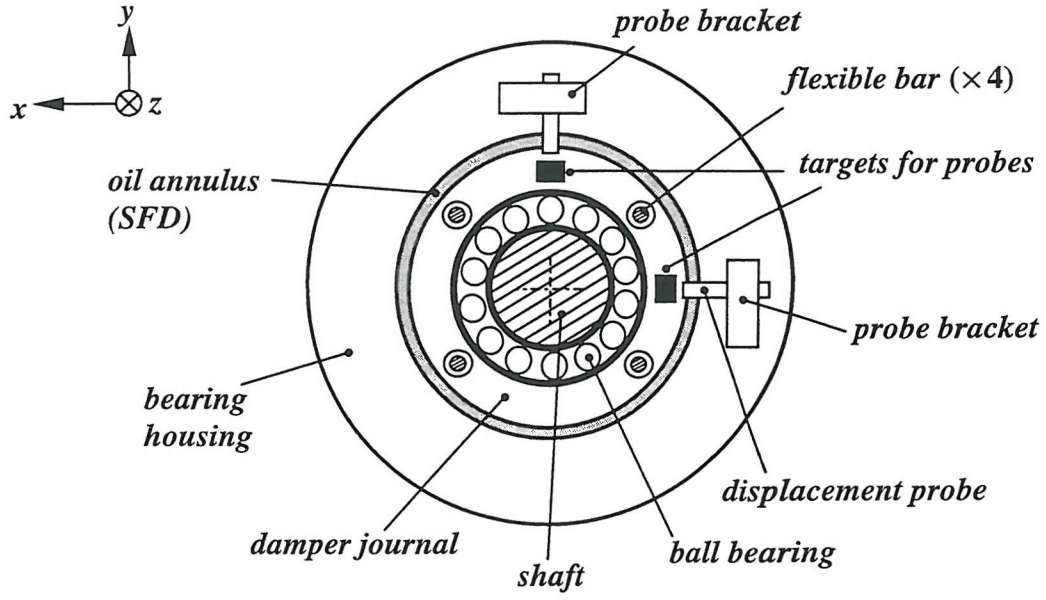

Figure 7.2: *Damper arrangement for configuration B1 (retainer spring fitted)*

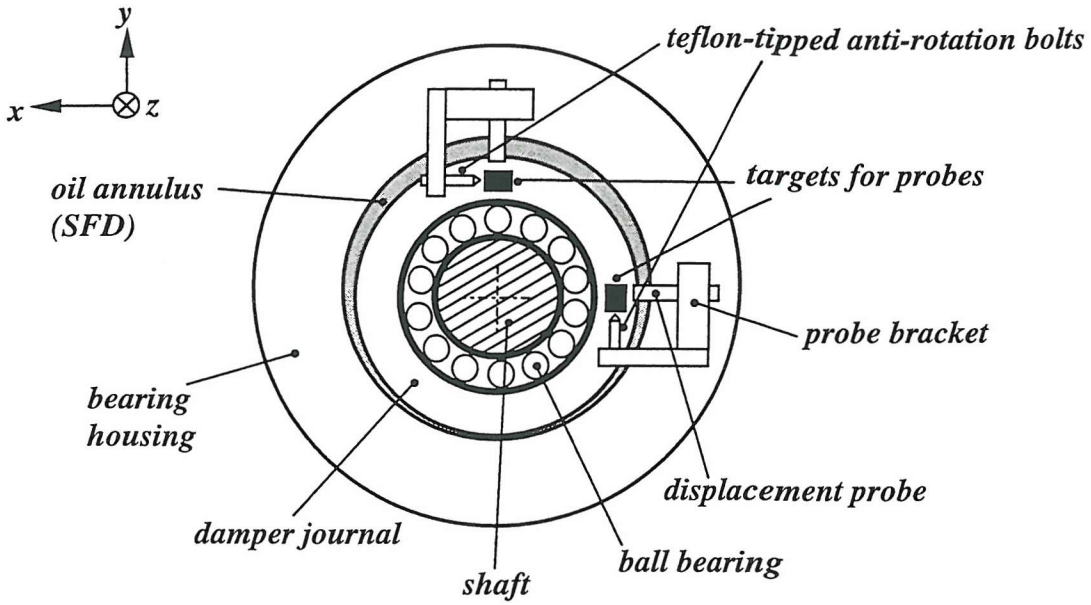

Figure 7.3: *Damper arrangement for configuration B2 (no retainer spring)*

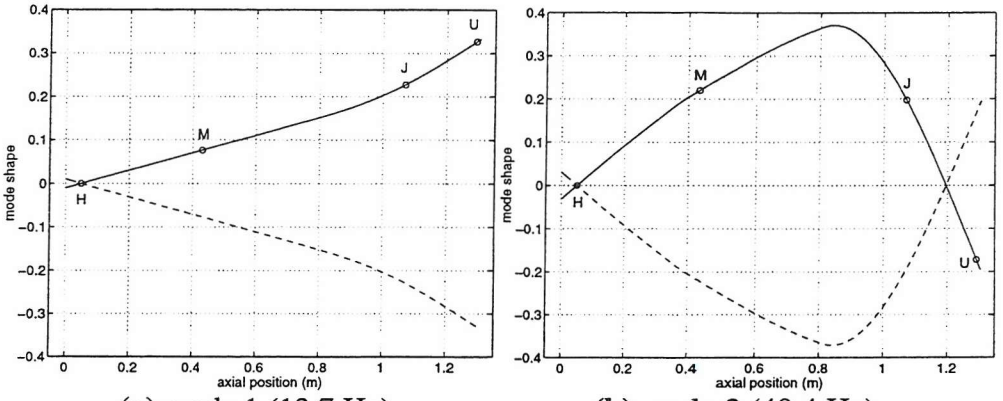

(a) mode 1 (13.7 Hz) **(b)** mode 2 (40.4 Hz)

Figure 7.4: *First two calculated undamped modes for rig with retainer spring*

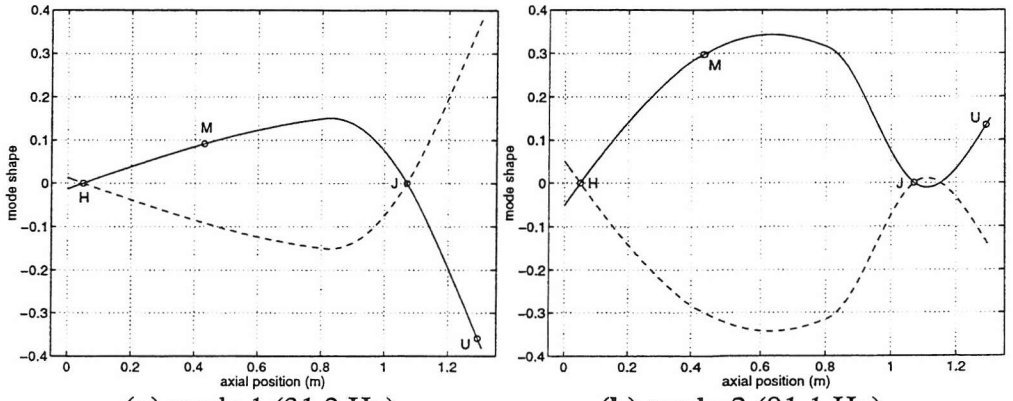

(a) mode 1 (31.2 Hz) **(b)** mode 2 (91.1 Hz)

Figure 7.5: *First two calculated undamped modes for rig with SFD locked (pin-pin modes)*

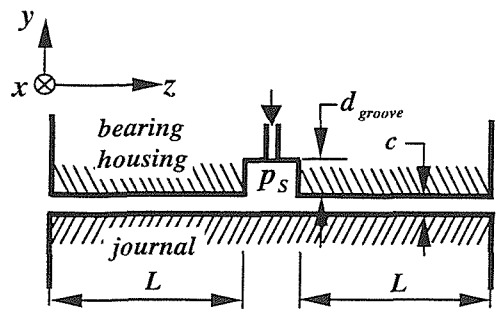

$c = 0.132\times10^{-3}$ m $\quad L = 9.72\times10^{-3}$ m

$d_{groove} = 5.25\times10^{-3}$ m and 2.00×10^{-3} m

housing bore radius $R = 50.022\times10^{-3}$ m

Figure 7.6: *SFD dimensions for configuration B*

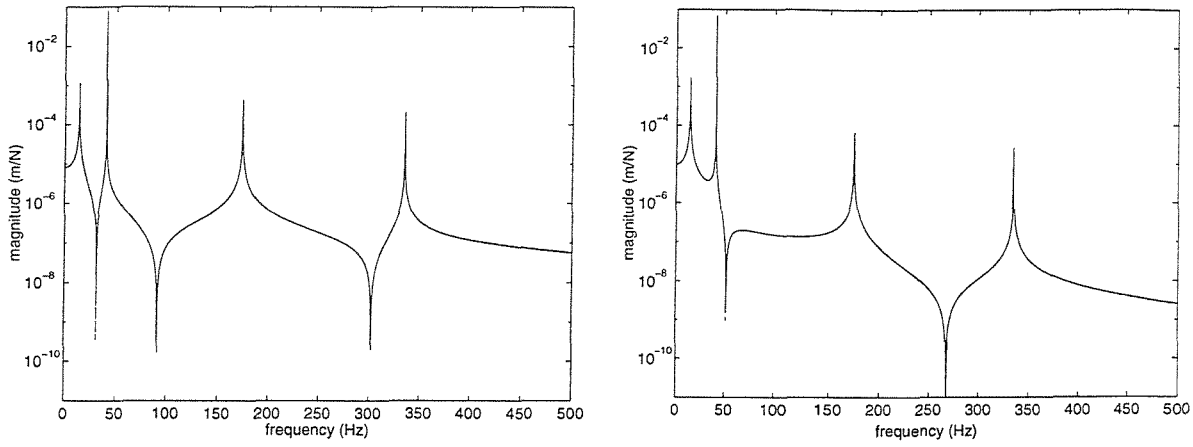

(a) α_{JJ} (b) α_{JU}

Figure 7.7: *Comparison of exact rotor receptance functions computed by MI* (——) *with approximations reconstructed from* 4 *modes* (– – –) *for linear subsystem of conf. B1* (pinned-sprung shaft)

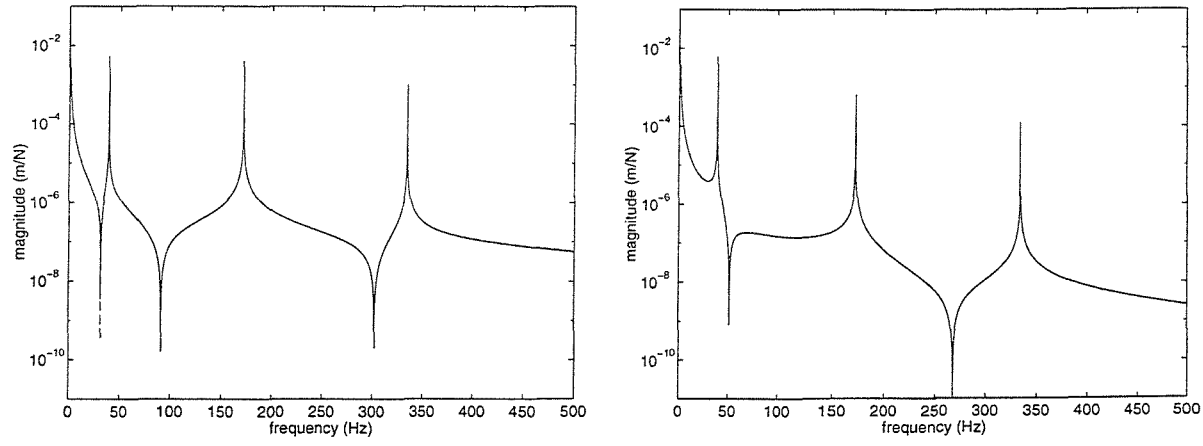

(a) α_{JJ} (b) α_{JU}

Figure 7.8: *Comparison of exact rotor receptance functions computed by MI* (——) *with approximations reconstructed from* 4 *modes* (– – –) *for linear subsystem of conf. B2* (pinned-free shaft)

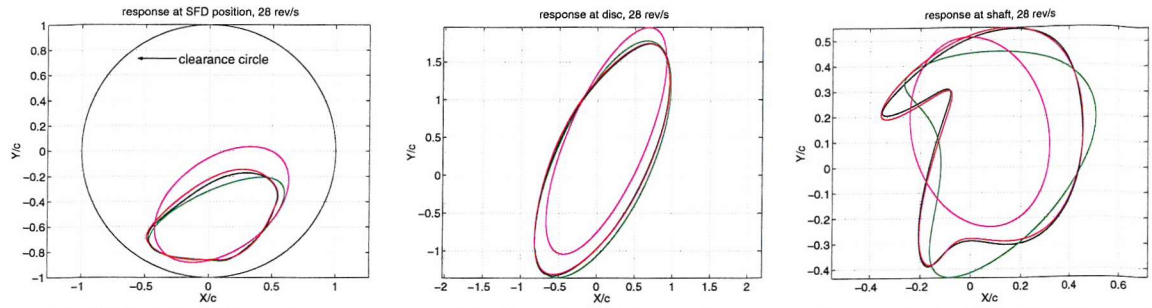

(a) SFD (J), 28 rev/s **(b)** disc (U), 28 rev/s **(c)** mid-shaft (M), 28 rev/s

Figure 7.9: *Convergence of RHB* $N=1$ *as the number of harmonics m is increased*
$m=1$ (——), $m=2$ (——), $m=5$ (——); modal numerical integration (——)
Conf. B1, $\varepsilon_{0y}=-0.8$, $U=5.1\times10^{-4}$ kgm, $\eta=0.0045$ Nsm^{-2}, p_S, $p_c=100,-101.3$ kPa

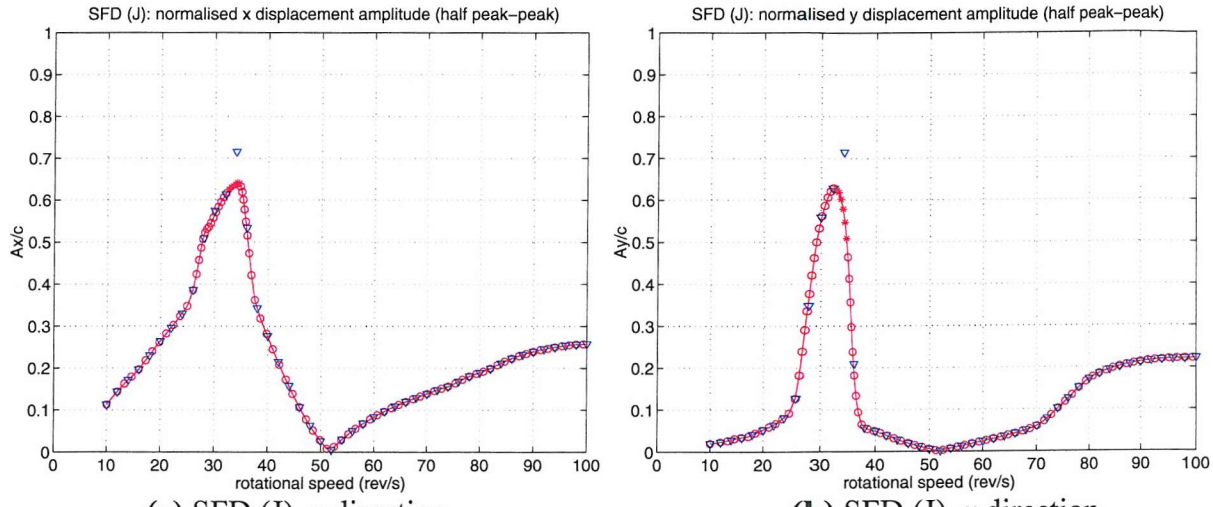

(a) SFD (J), x direction **(b)** SFD (J), y direction

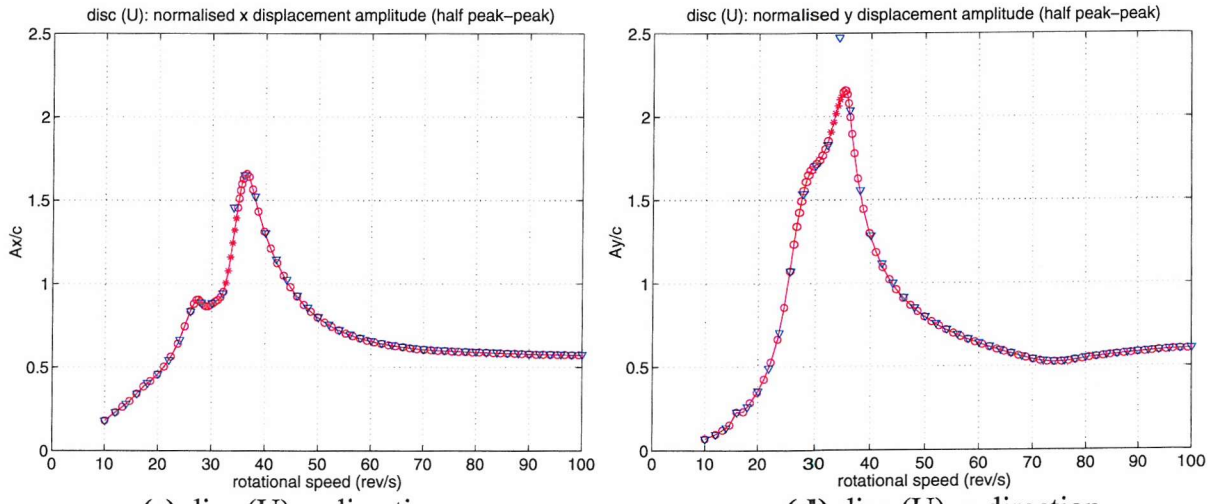

(c) disc (U), x direction **(d)** disc (U), y direction

Figure 7.10: *Correlation between RHB and time-marching predictions for amplitude*
(half peak-to-peak displacement divided by c) (continues on next page)
RHB $N=1$, $m=5$ – red: "o" stable, "*" unstable (λ_I complex);
numerical integration – blue
Conf. B1, $\varepsilon_{0y}=-0.8$, $U=5.1\times10^{-4}$ kgm, $\eta=0.0045$ Nsm^{-2}, p_S, $p_c=100,-101.3$ kPa

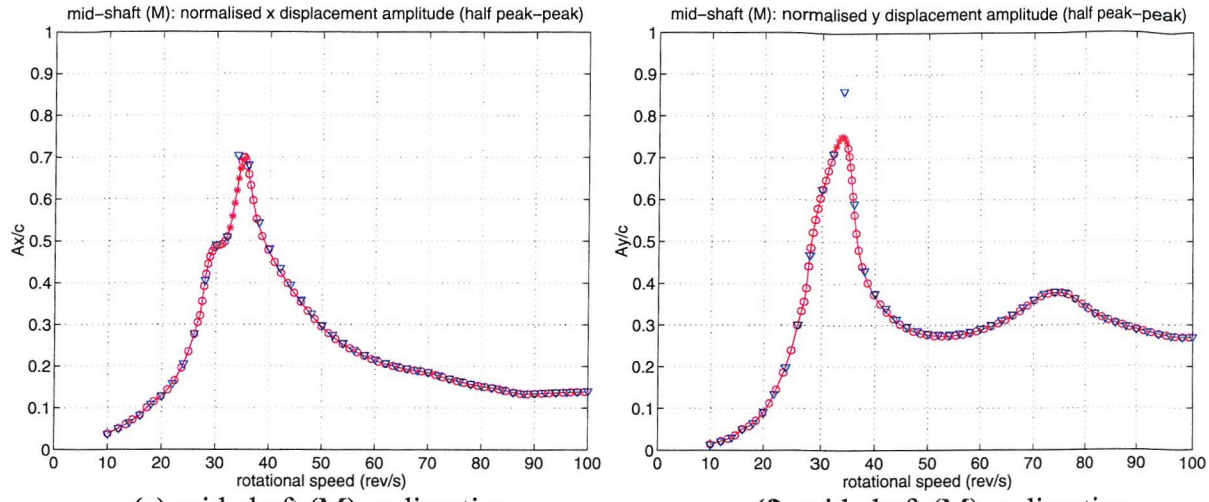

(e) mid-shaft (M), x direction **(f)** mid-shaft (M), y direction

Figure 7.10 (continued): *Correlation between RHB and time-marching predictions for amplitude* (half peak-to-peak displacement divided by c)
RHB $N=1$, $m=5$ – red: "o" stable, "*" unstable (λ_1 complex);
numerical integration – blue
Conf. B1, $\varepsilon_{0y}=-0.8$, $U=5.1\times10^{-4}$ kgm, $\eta=0.0045$ Nsm^{-2}, p_S, $p_c=100,-101.3$ kPa

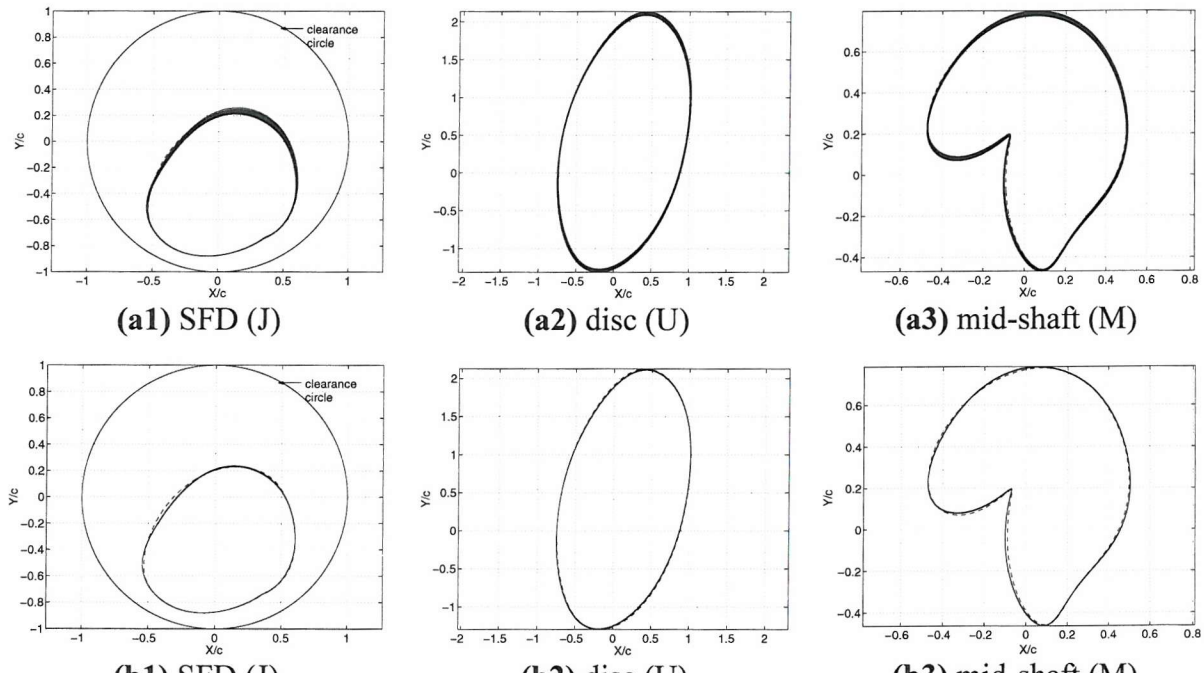

(a1) SFD (J) **(a2)** disc (U) **(a3)** mid-shaft (M)

(b1) SFD (J) **(b2)** disc (U) **(b3)** mid-shaft (M)

Figure 7.11: *Verification of Floquet stability result for T-periodic RHB solution at* 30 *rev/s by time-marching from initial conditions on the T-periodic cycle* **(a1)-(a3)** first 30 shaft revs.; **(b1)-(b3)** further 30 revs. RHB $N=1$, $m=5$ (– – –); numerical integration (——)
Conf. B1, $\varepsilon_{0y}=-0.8$, $U=5.1\times10^{-4}$ kgm, $\eta=0.0045$ Nsm^{-2}, p_S, $p_c=100,-101.3$ kPa

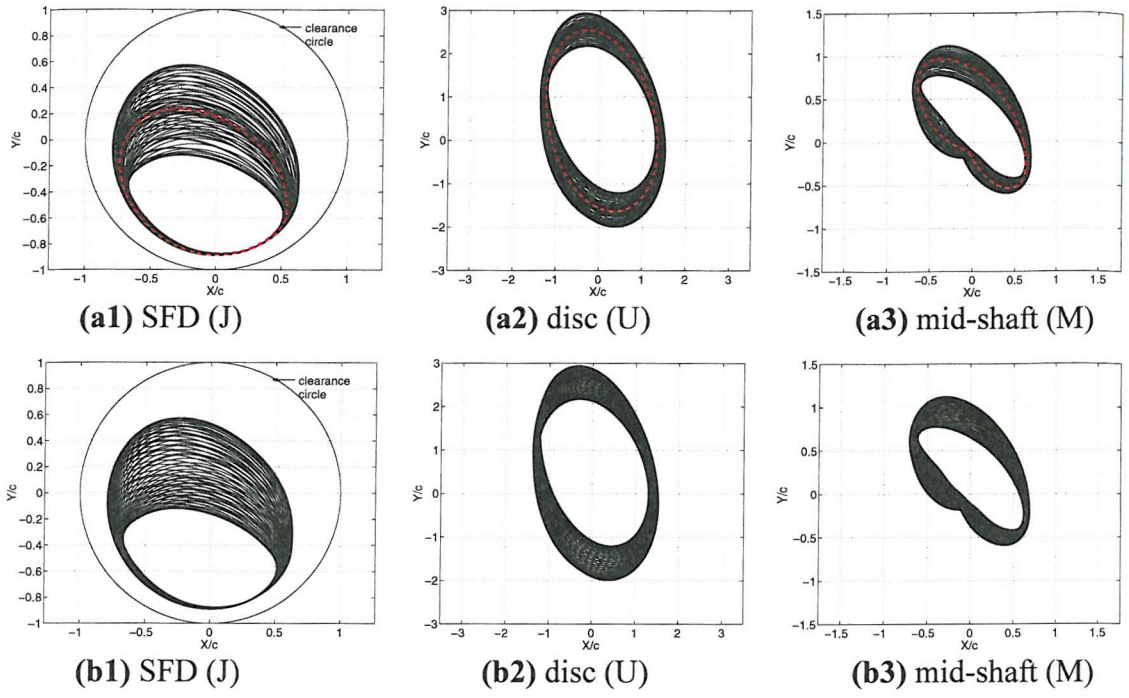

Figure 7.12: *Verification of Floquet stability result for T-periodic RHB solution at* 34 *rev/s by time-marching from initial conditions on the T-periodic cycle*
(a1)-(a3) RHB $N=1$, $m=5$ (– – –); numerical integration, first 80 shaft revs. (——);
(b1)-(b3) numerical integration solution over further 80 revs. (steady-state)
Conf. B1, $\varepsilon_{0y}=-0.8$, $U=5.1\times10^{-4}$ kgm, $\eta=0.0045$ Nsm^{-2}, p_S, $p_c=100,-101.3$ kPa

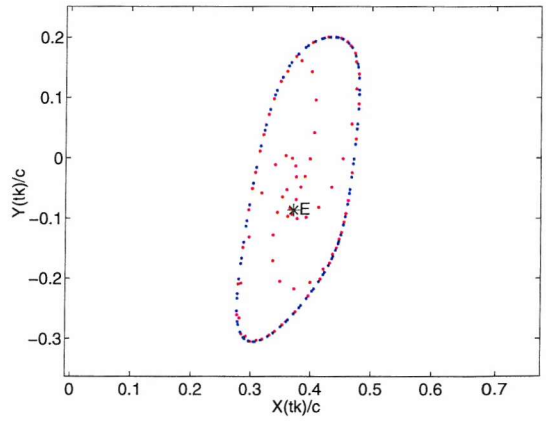

Figure 7.13: *Poincaré map of numerical integration solution at* J *in Figures 7.12(a1,b1)* ($\Omega t_k = k2\pi$). First 80 shaft revs. (i.e. Figure 7.12(a1)) – red; further 80 revs. (i.e. Figure 7.12(b1)) – blue; first point E (on unstable equilibrium solution) indicated by "*"
Conf. B1, $\varepsilon_{0y}=-0.8$, $U=5.1\times10^{-4}$ kgm, $\eta=0.0045$ Nsm^{-2}, p_S, $p_c=100,-101.3$ kPa

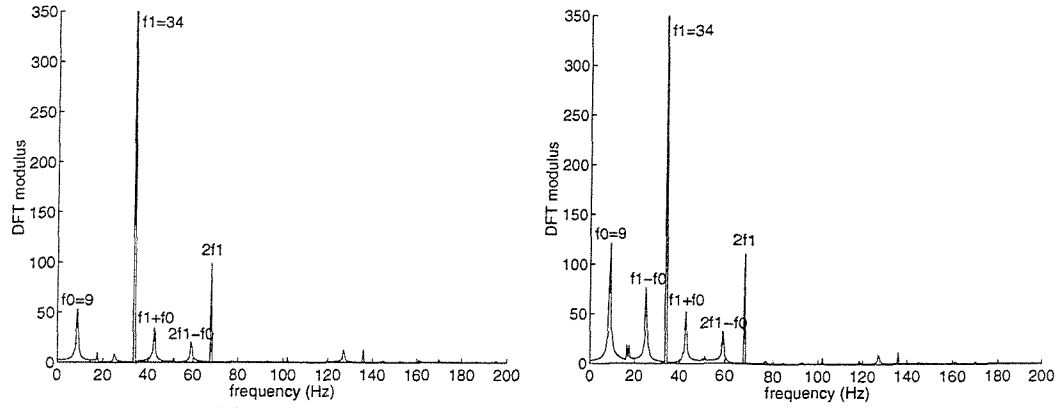

(a) x direction (b) y direction

Figure 7.14: *Frequency spectra of quasi-periodic solution at* J *at* 34 *rev/s* (data length 2 s) Conf. B1, $\varepsilon_{0y}=-0.8$, $U=5.1\times10^{-4}$ kgm, $\eta=0.0045$ Nsm^{-2}, p_s, $p_c=100,-101.3$ kPa

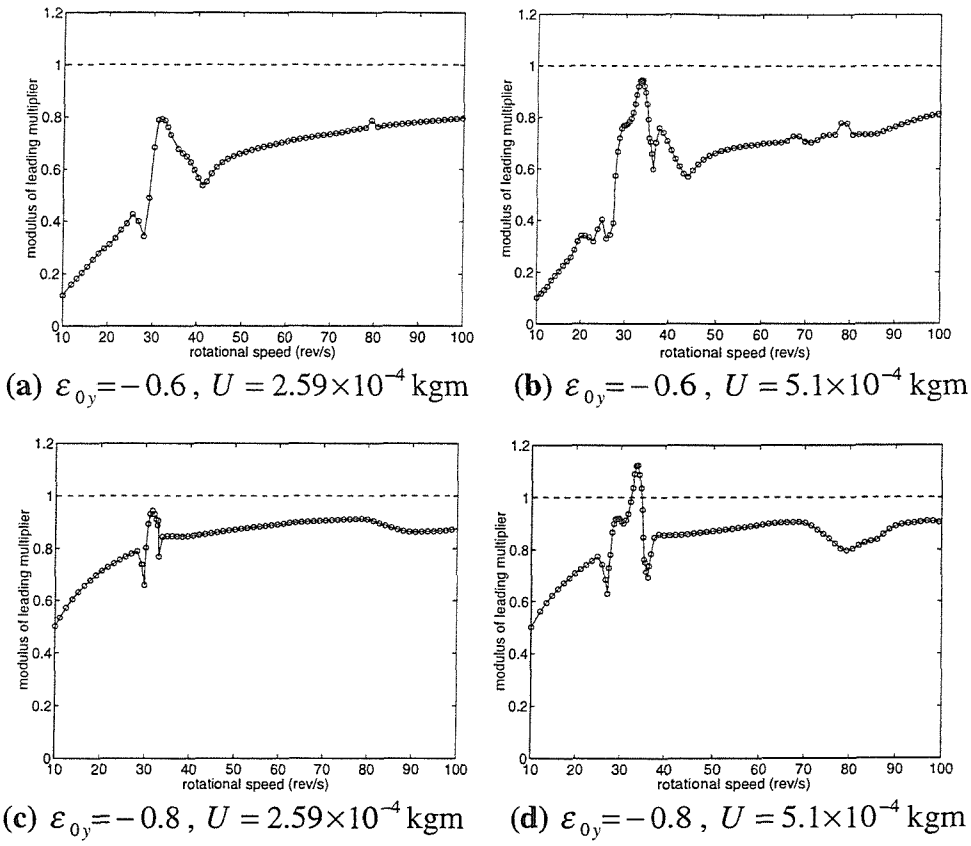

(a) $\varepsilon_{0y}=-0.6$, $U=2.59\times10^{-4}$ kgm (b) $\varepsilon_{0y}=-0.6$, $U=5.1\times10^{-4}$ kgm

(c) $\varepsilon_{0y}=-0.8$, $U=2.59\times10^{-4}$ kgm (d) $\varepsilon_{0y}=-0.8$, $U=5.1\times10^{-4}$ kgm

Figure 7.15: *Variation of modulus of leading Floquet multiplier for T-periodic solutions* (RHB $N=1$, $m=5$) *with rotational speed for various static offset and unbalance conditions* Conf. B1, $\eta=0.0045$ Nsm^{-2}, p_s, $p_c=100,-101.3$ kPa

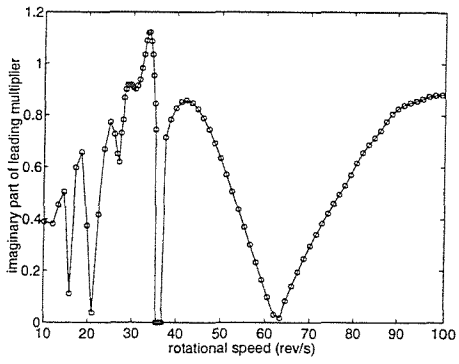

Figure 7.16: *Variation of imaginary part of leading Floquet multiplier for T-periodic solutions* (RHB $N=1$, $m=5$) *with rotational speed for* $\varepsilon_{0y}=-0.8$, $U=5.1\times10^{-4}\,kgm$ Conf. B1, $\eta=0.0045$ Nsm^{-2}, p_S, $p_c=100,-101.3$ kPa

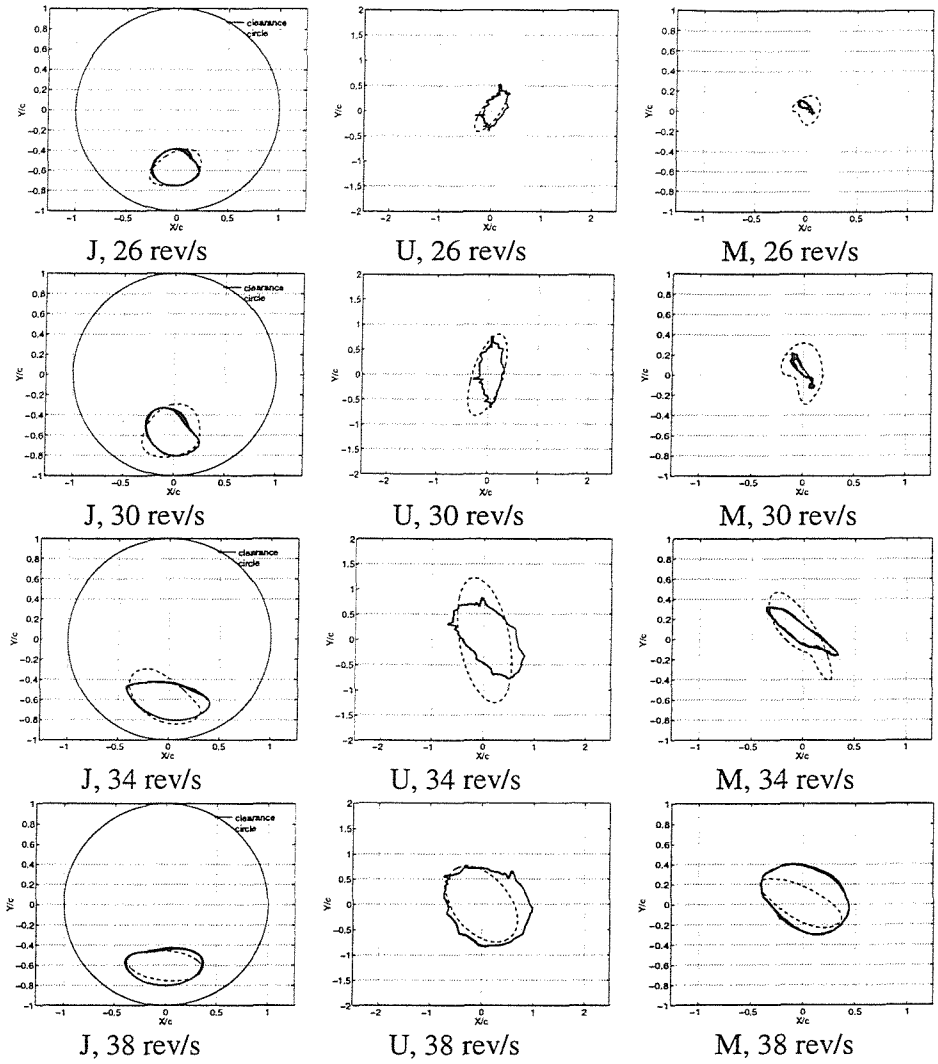

Figure 7.17: *Orbital motion for* $\varepsilon_{0y}=-0.6$, $U=2.59\times10^{-4}\,kgm$ Measured, over 0.5 s (——); RHB $N=1$, $m=5$ (– – –) with $p_c=-101.3$ kPa Conf. B1, $\eta=0.0045$ Nsm^{-2}, $p_S=100$ kPa

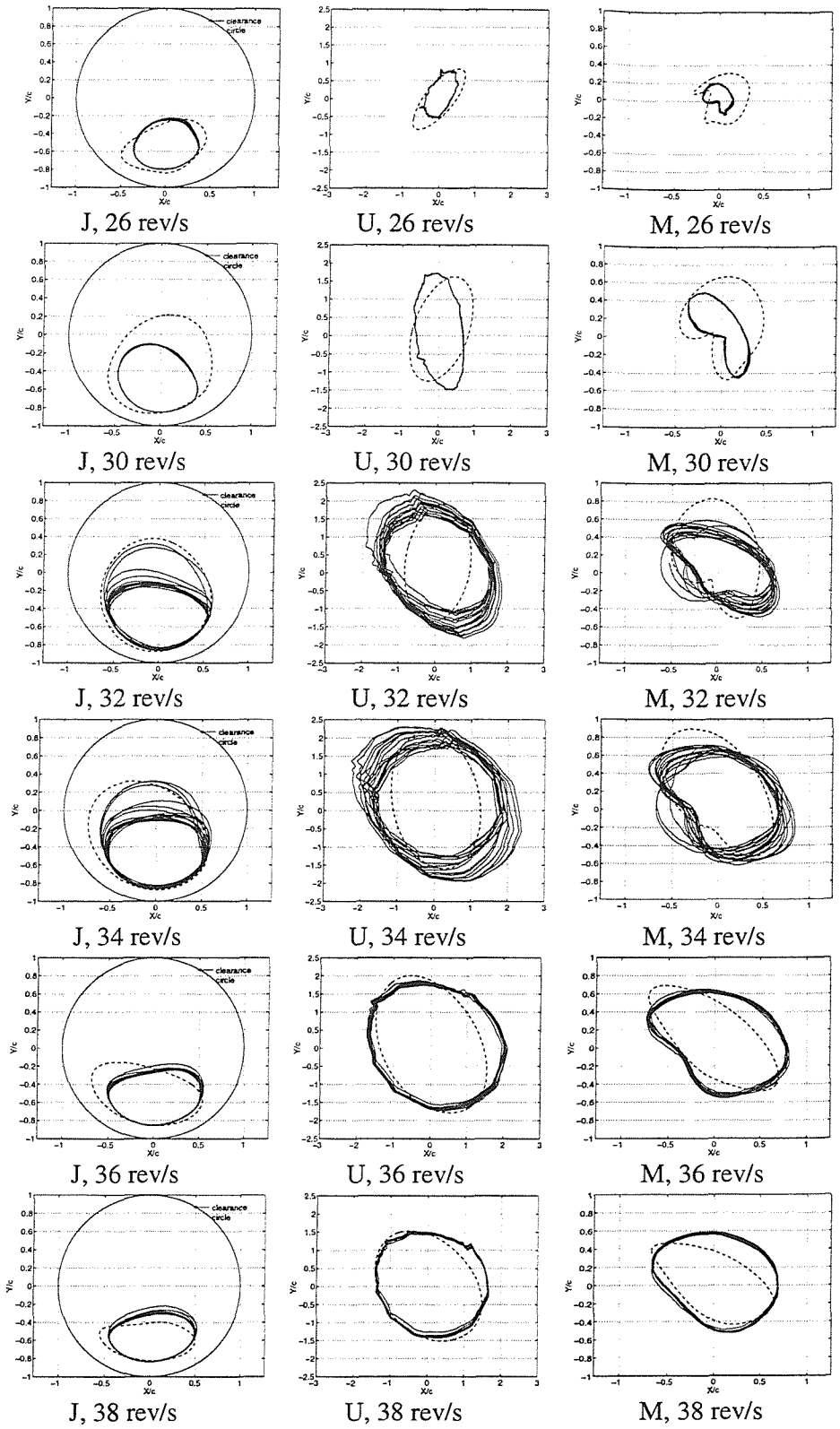

Figure 7.18: *Orbital motion for* $\varepsilon_{0y}=-0.6$, $U=5.1\times10^{-4}\,kgm$

Measured, over 0.5 s (——); RHB $N=1$, $m=5$ (– – –) with $p_c=-101.3$ kPa

Conf. B1, $\eta=0.0045$ Nsm^{-2}, $p_S=100$ kPa

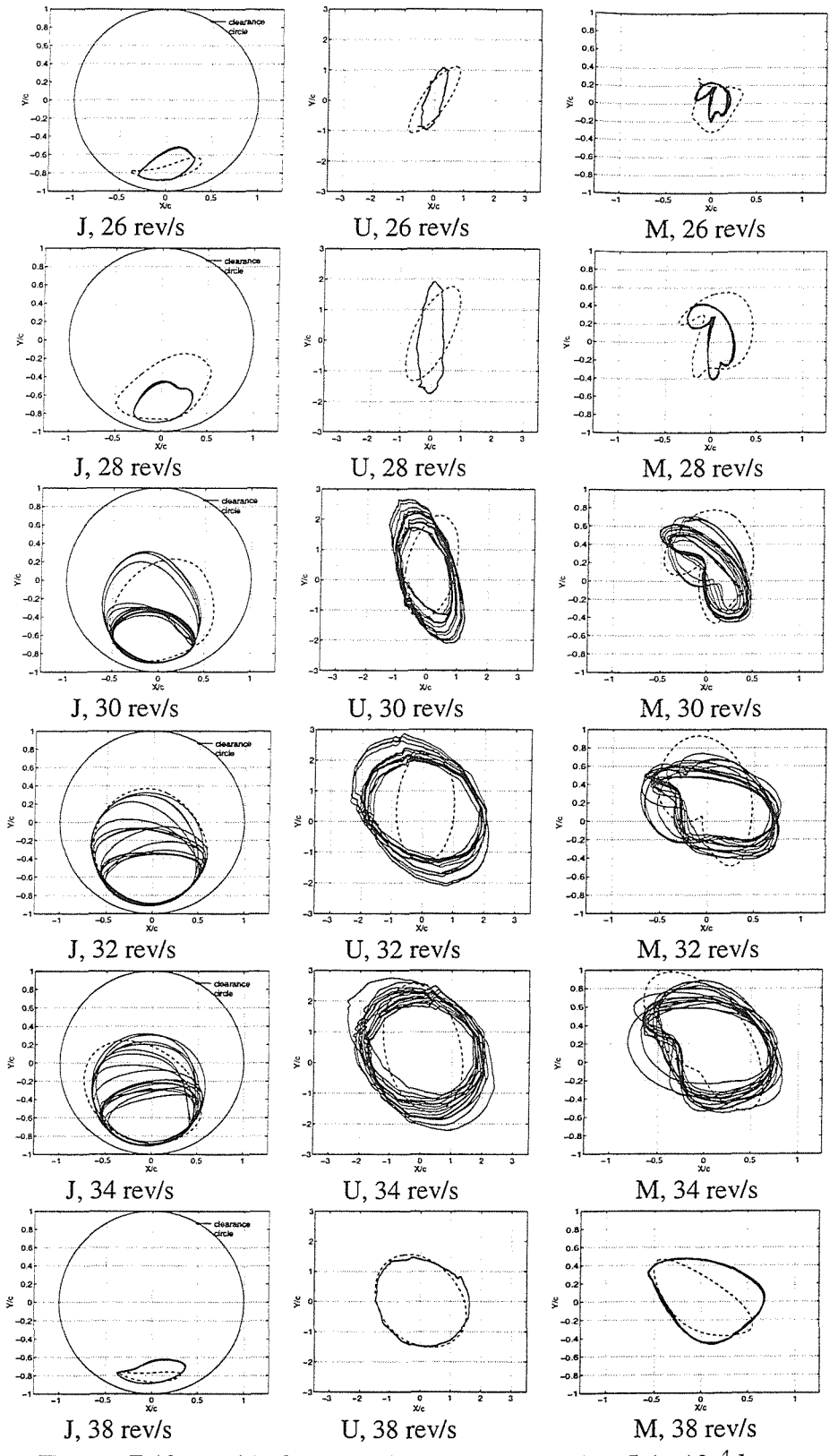

Figure 7.19: *Orbital motion for* $\varepsilon_{0y}=-0.8$, $U=5.1\times10^{-4}\,kgm$

Measured, over 0.5 s (——); RHB $N=1$, $m=5$ (– – –) with $p_c=-101.3$ kPa

Conf. B1, $\eta=0.0045$ Nsm^{-2}, $p_S=100$ kPa

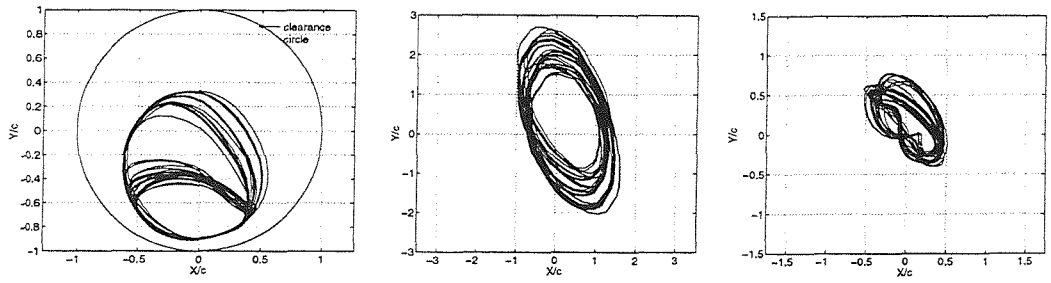

(**a1**) SFD (J), 30 rev/s (**a2**) disc (U), 30 rev/s (**a3**) mid-shaft (M), 30 rev/s

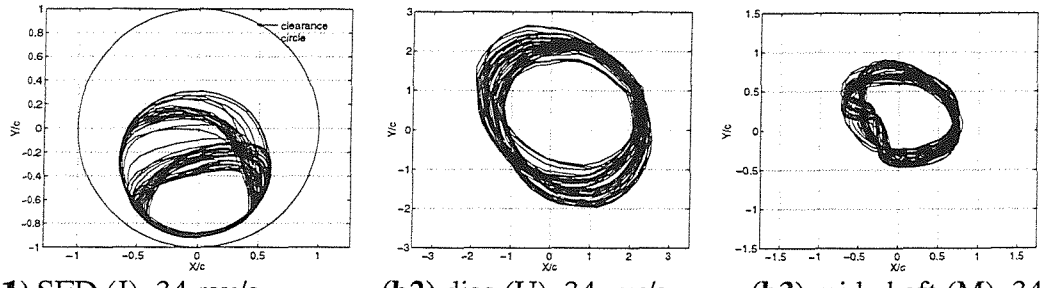

(**b1**) SFD (J), 34 rev/s (**b2**) disc (U), 34 rev/s (**b3**) mid-shaft (M), 34 rev/s

Figure 7.20: *Measured aperiodic orbital motion over* 2 *s for* $\varepsilon_{0y}=-0.8$, $U=5.1\times10^{-4}$ *kgm* Conf. B1, $\eta=0.0045$ Nsm^{-2}, $p_S=100$ kPa

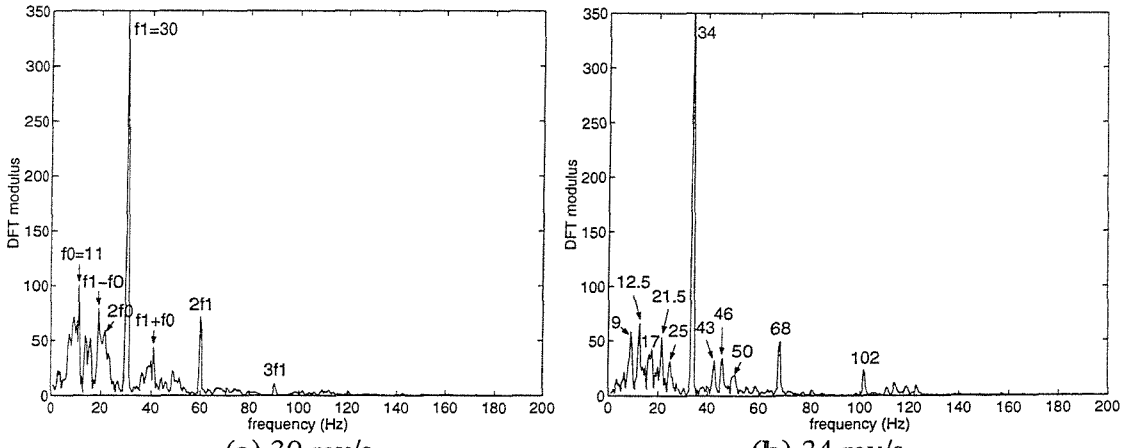

(**a**) 30 rev/s (**b**) 34 rev/s

Figure 7.21: *Frequency spectra of y component of measured aperiodic motion* at *SFD* (J) *for* $\varepsilon_{0y}=-0.8$, $U=5.1\times10^{-4}$ *kgm* (data length 2 s). Conf. B1, $\eta=0.0045$ Nsm^{-2}, $p_S=100$ kPa

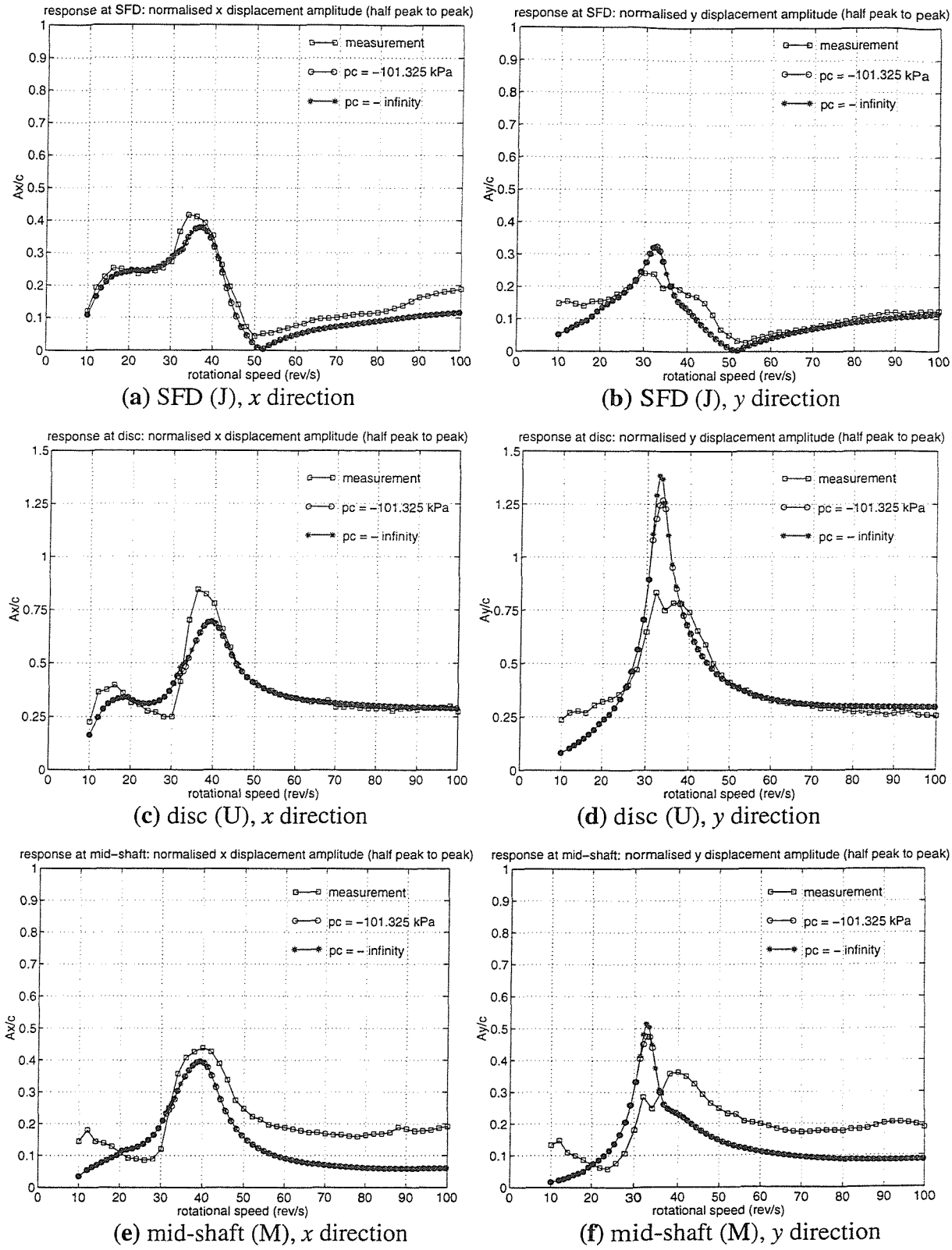

(a) SFD (J), x direction

(b) SFD (J), y direction

(c) disc (U), x direction

(d) disc (U), y direction

(e) mid-shaft (M), x direction

(f) mid-shaft (M), y direction

Figure 7.22: *Unbalance response for* $\varepsilon_{0y} = -0.6$, $U = 2.59 \times 10^{-4}\, kgm$. All predictions are RHB $N = 1$, $m = 5$. Vertical axes show ratio of half peak-to-peak displacement to c. Conf. B1, $\eta = 0.0045$ Nsm^{-2}, $p_s = 100$ kPa

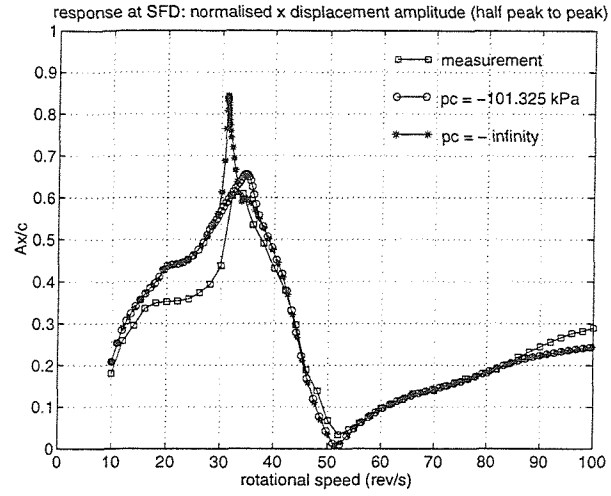

(a) SFD (J), x direction

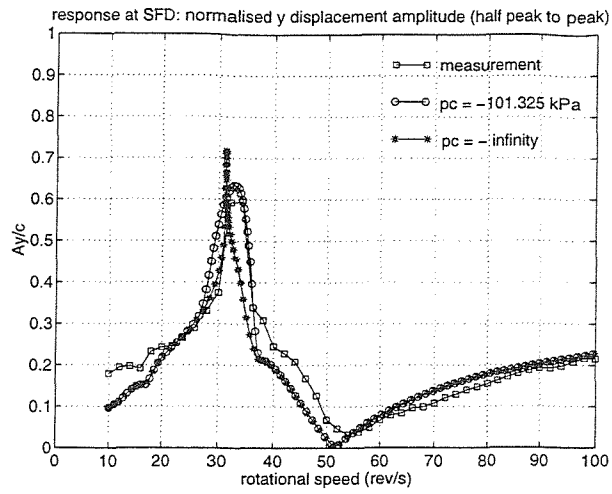

(b) SFD (J), y direction

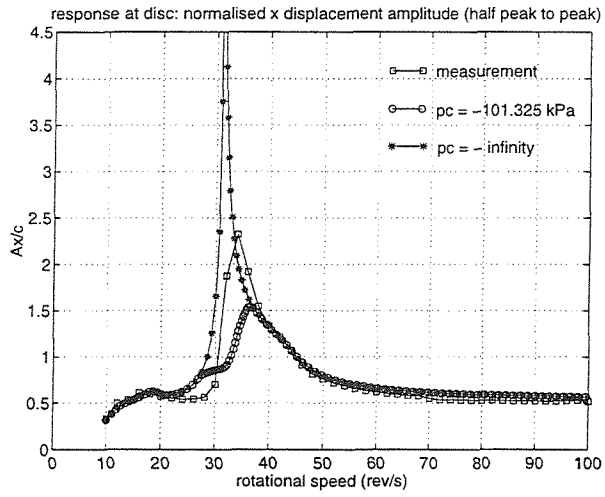

(c) disc (U), x direction

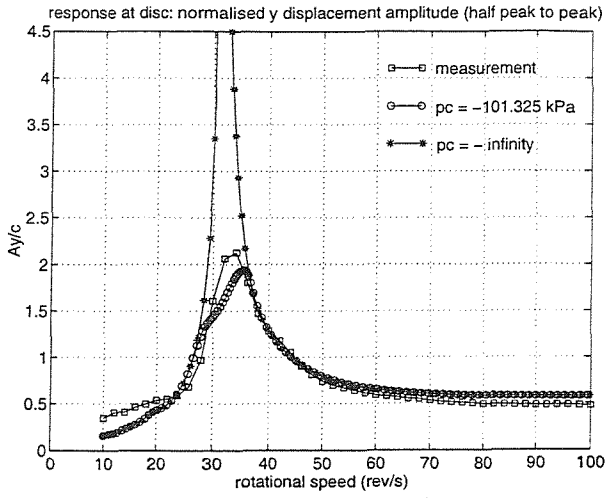

(d) disc (U), y direction

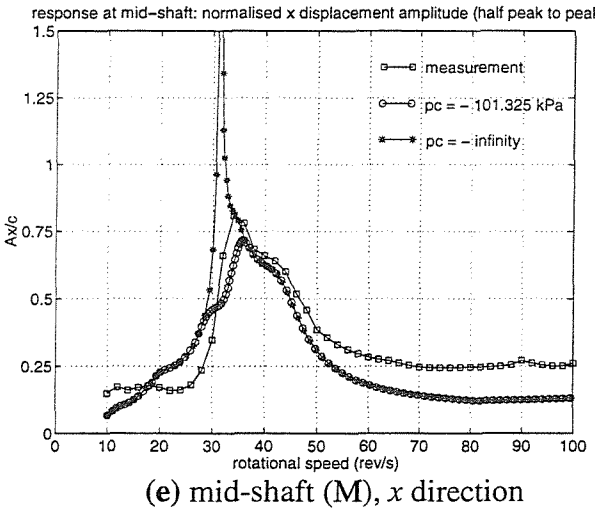

(e) mid-shaft (M), x direction

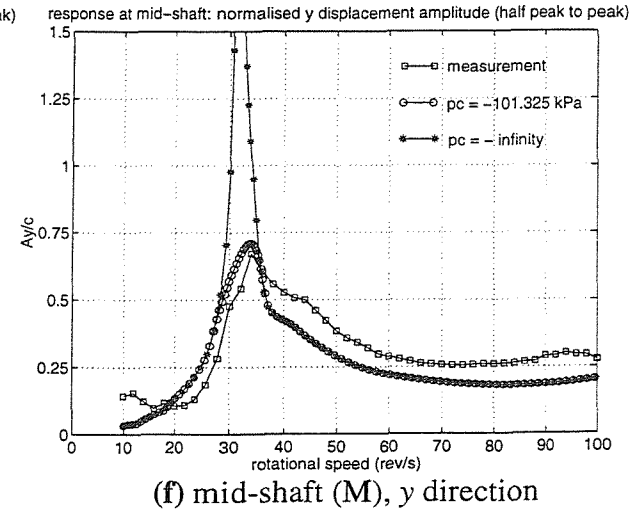

(f) mid-shaft (M), y direction

Figure 7.23: *Unbalance response for* $\varepsilon_{0y} = -0.6$, $U = 5.1\times10^{-4}$ *kgm.* All predictions are RHB $N = 1$, $m = 5$. Vertical axes show ratio of half peak-to-peak displacement to c. Conf. B1, $\eta = 0.0045$ Nsm^{-2}, $p_s = 100$ kPa

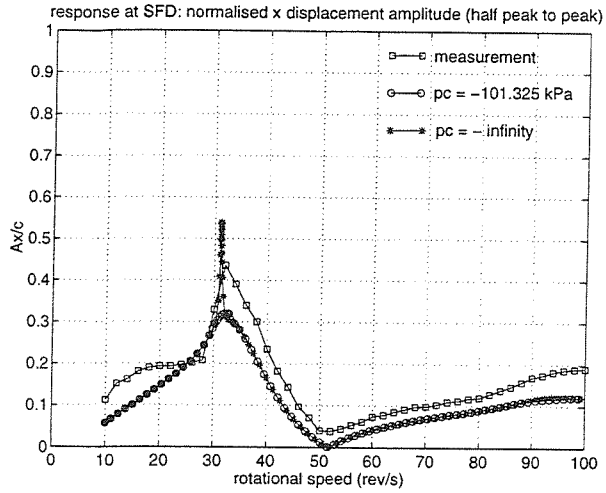

(a) SFD (J), x direction

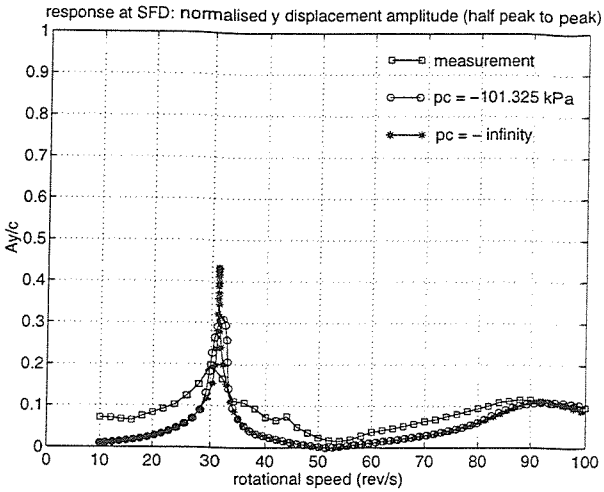

(b) SFD (J), y direction

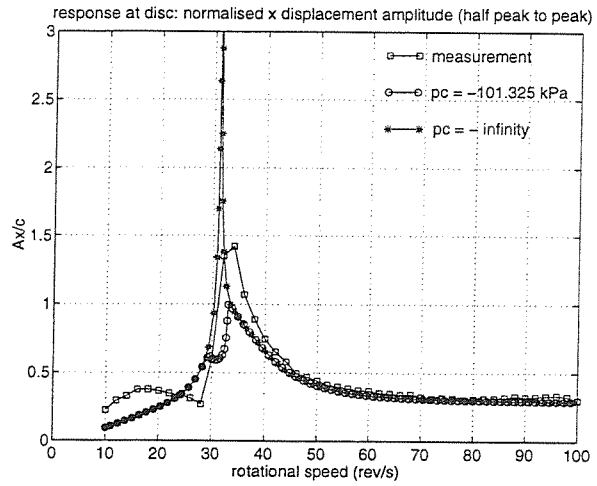

(c) disc (U), x direction

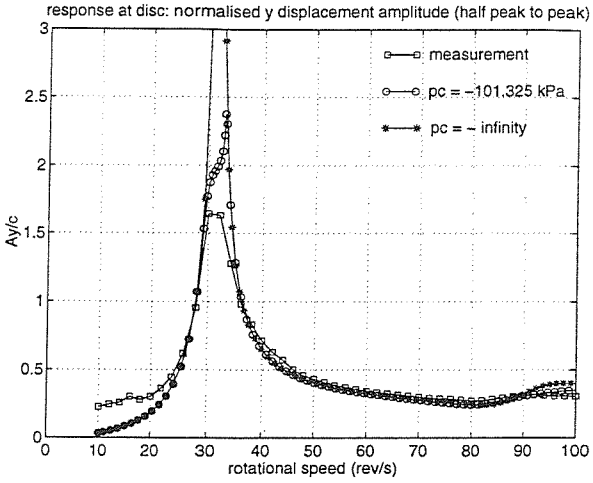

(d) disc (U), y direction

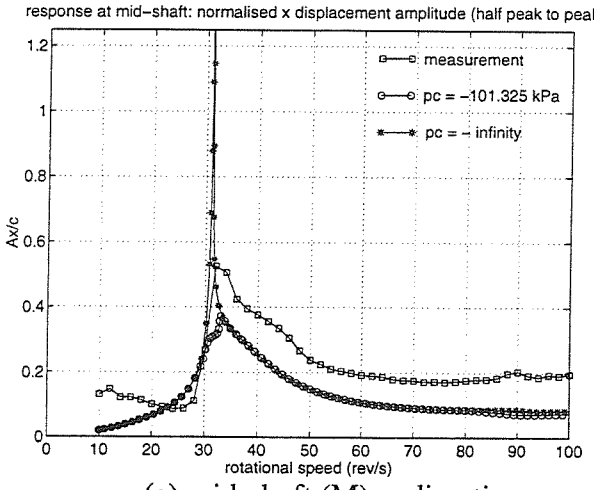

(e) mid-shaft (M), x direction

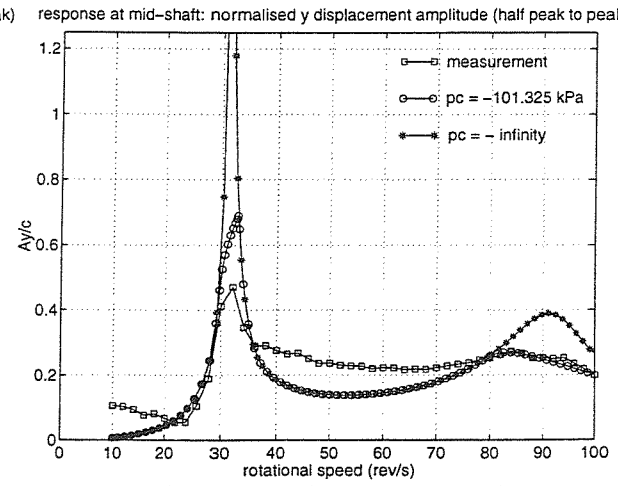

(f) mid-shaft (M), y direction

Figure 7.24: *Unbalance response for* $\varepsilon_{0y} = -0.8$, $U = 2.59 \times 10^{-4}\ kgm$. All predictions are RHB $N = 1$, $m = 5$. Vertical axes show ratio of half peak-to-peak displacement to c. Conf. B1, $\eta = 0.0045$ Nsm^{-2}, $p_s = 100$ kPa

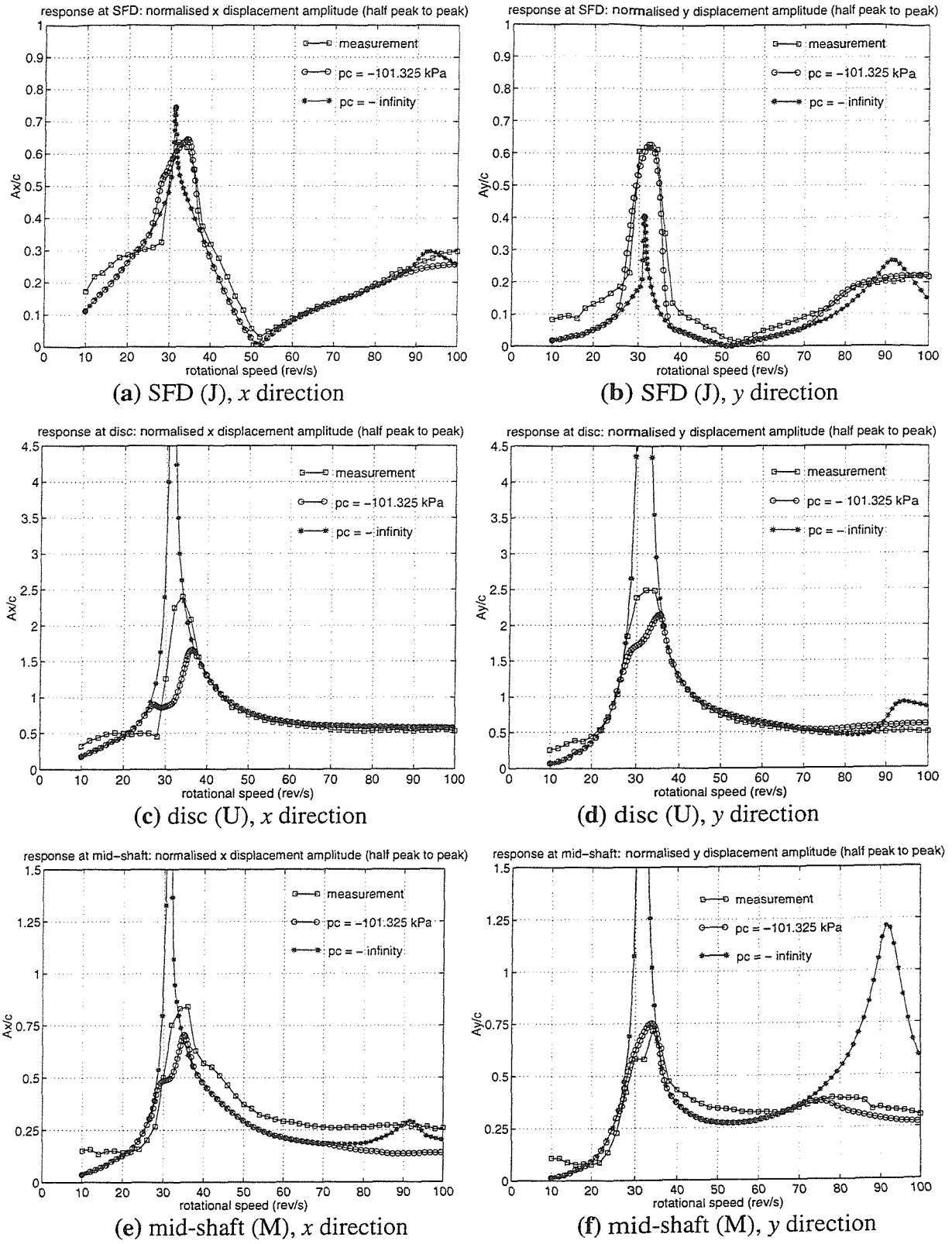

(a) SFD (J), x direction

(b) SFD (J), y direction

(c) disc (U), x direction

(d) disc (U), y direction

(e) mid-shaft (M), x direction

(f) mid-shaft (M), y direction

Figure 7.25: *Unbalance response for* $\varepsilon_{0y} = -0.8$, $U = 5.1\times10^{-4}$ *kgm.* All predictions are RHB $N = 1$, $m = 5$. Vertical axes show ratio of half peak-to-peak displacement to c. Conf. B1, $\eta = 0.0045$ Nsm^{-2}, $p_S = 100$ kPa

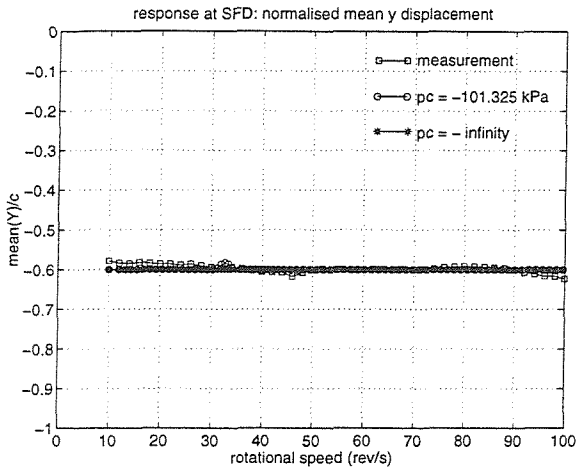

(a) $\varepsilon_{0y}=-0.6$, $U=2.59\times10^{-4}$ kgm

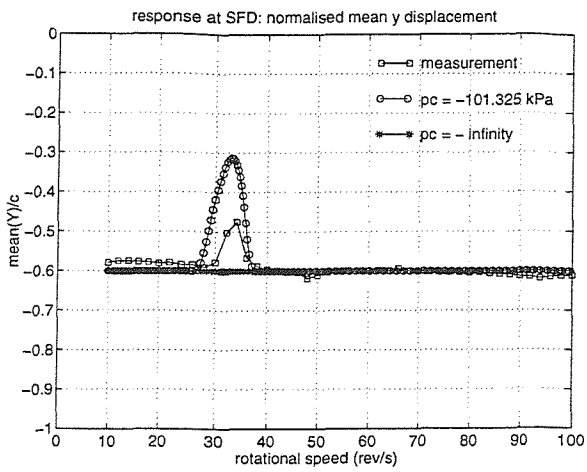

(b) $\varepsilon_{0y}=-0.6$, $U=5.1\times10^{-4}$ kgm

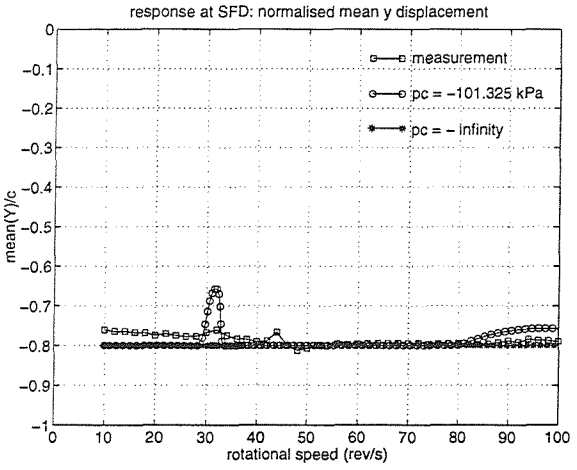

(c) $\varepsilon_{0y}=-0.8$, $U=2.59\times10^{-4}$ kgm

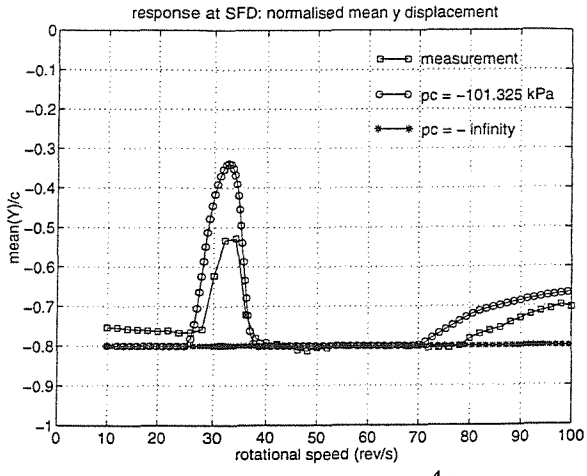

(d) $\varepsilon_{0y}=-0.8$, $U=5.1\times10^{-4}$ kgm

Figure 7.26: *Variation of normalised mean y displacement of* J *relative to housing centre with rotational speed.* All predictions are RHB $N=1$, $m=5$.
Conf. B1, $\eta=0.0045$ Nsm^{-2}, $p_s=100$ kPa

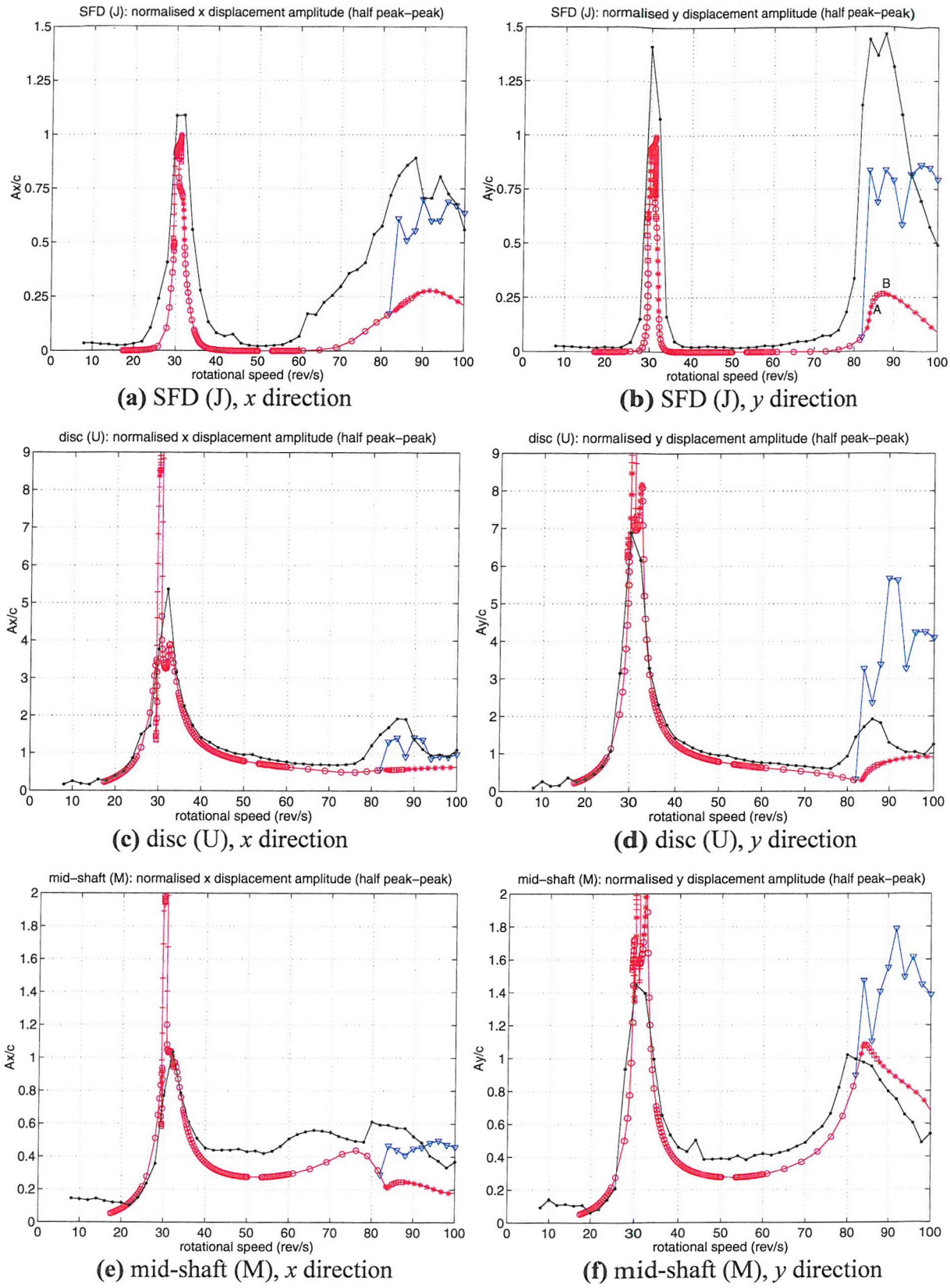

(a) SFD (J), x direction **(b)** SFD (J), y direction

(c) disc (U), x direction **(d)** disc (U), y direction

(e) mid-shaft (M), x direction **(f)** mid-shaft (M), y direction

Figure 7.27: *Response of conf. B2* (no retainer spring) *for* $U = 5.1\times10^{-4}\ kgm$, $\eta = 0.0045\ Nsm^{-2}$, $p_S = 120\ kPa$. Vertical axes show ratio of half peak-to-peak displacement to c. RHB $N = 1$, $m = 5$ – red: "o" stable, "+" unstable (λ_1 real, positive), "□" unstable (λ_1 real, negative), "*" unstable (λ_1 complex); numerical integration – blue; measured [64] – black.

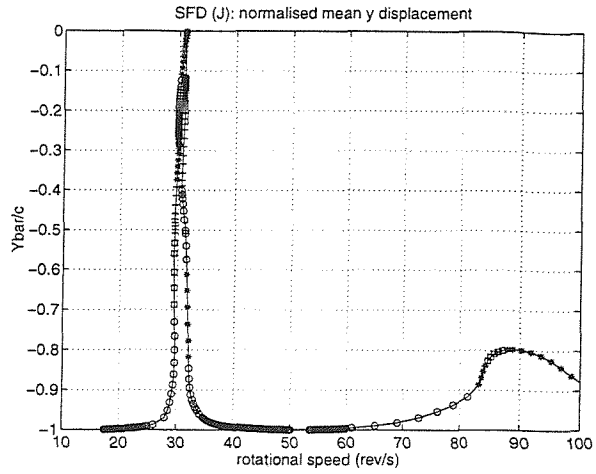

Figure 7.28: *Variation with rotational speed of the mean y component of the T-periodic solution for the displacement of* J *relative to housing centre* (RHB $N=1$, $m=5$)
"o" stable, "+" unstable (λ_l real, positive), "□" unstable (λ_l real, negative),
"*" unstable (λ_l complex). Conf. B2, $U=5.1\times10^{-4}$ kgm, $\eta=0.0045$ Nsm^{-2}, $p_S=120$ kPa

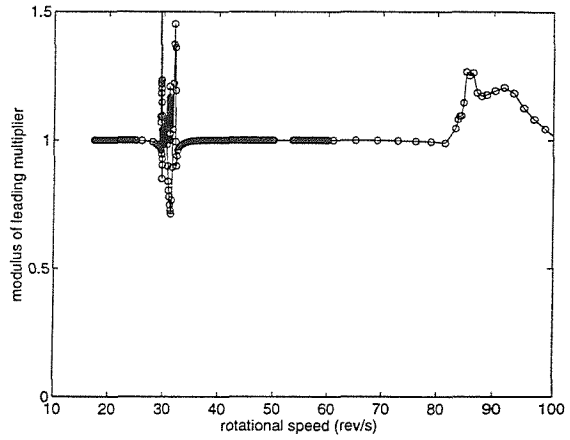

(**a**) modulus of λ_l

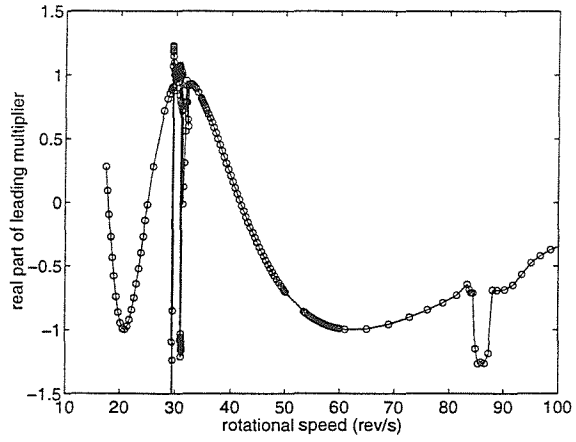

(**b**) real part of λ_l

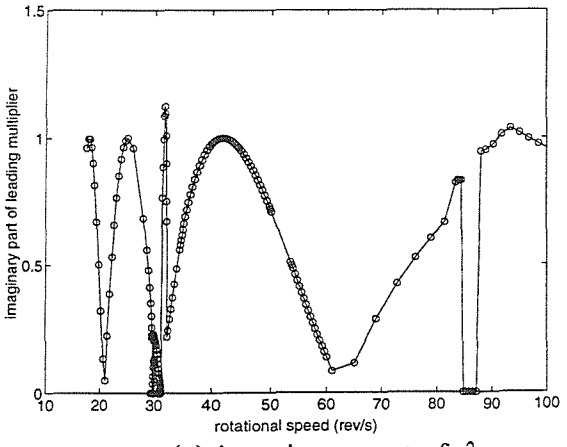

(**c**) imaginary part of λ_l

Figure 7.29: *Variation of leading Floquet multiplier of T-periodic solution* (RHB $N=1$, $m=5$) *with rotational speed*
Conf. B2, $U=5.1\times10^{-4}$ kgm, $\eta=0.0045$ Nsm^{-2}, $p_S=120$ kPa

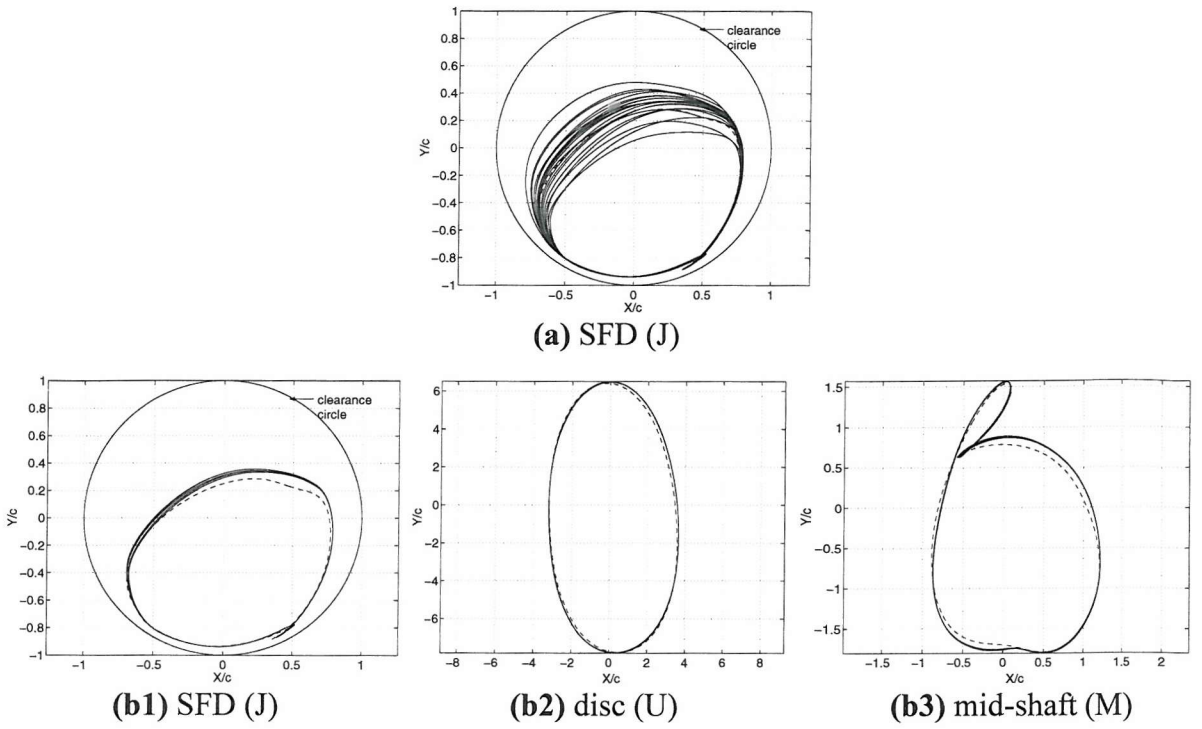

(a) SFD (J)

(b1) SFD (J) **(b2)** disc (U) **(b3)** mid-shaft (M)

Figure 7.30: *Stability verification for T-periodic RHB solution at* 31 *rev/s by time-marching from initial conditions on the T-periodic cycle* **(a)** first 20 shaft revs.; **(b1)-(b3)** further 5 revs.
RHB $N=1$, $m=8$ (– – –); numerical integration (——)
Conf. B2, $U=5.1\times10^{-4}$ kgm, $\eta=0.0045$ Nsm^{-2}, $p_S=120$ kPa

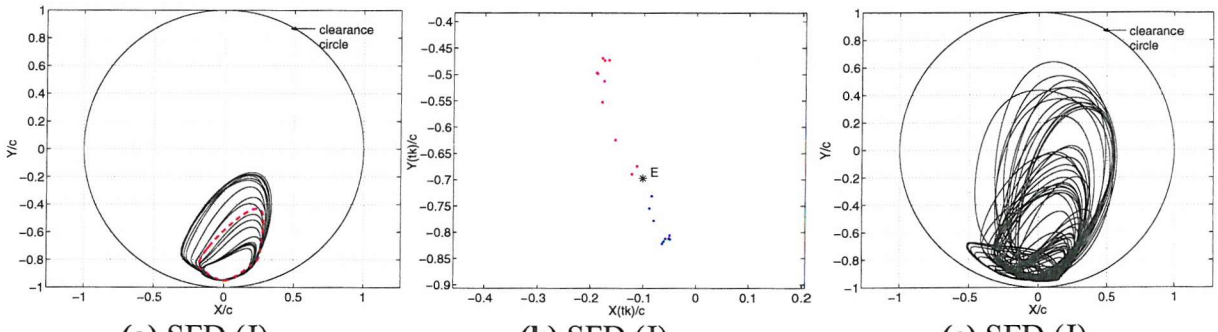

(a) SFD (J) **(b)** SFD (J) **(c)** SFD (J)

Figure 7.31: *Verification of Floquet stability result for T-periodic RHB solution at* 86 *rev/s by time-marching from initial conditions on the T-periodic cycle* **(a)** RHB $N=1$, $m=5$ – red; numerical integration, first 20 shaft revs. – black; **(b)** Poincaré map of transient orbit in **(a)** with $\Omega t_k = k2\pi$, consecutive return points in blue and red and first point E (unstable equilibrium) indicated by "*"; **(c)** numerical integration solution over further 80 shaft revs.
Conf. B2, $U=5.1\times10^{-4}$ kgm, $\eta=0.0045$ Nsm^{-2}, $p_S=120$ kPa

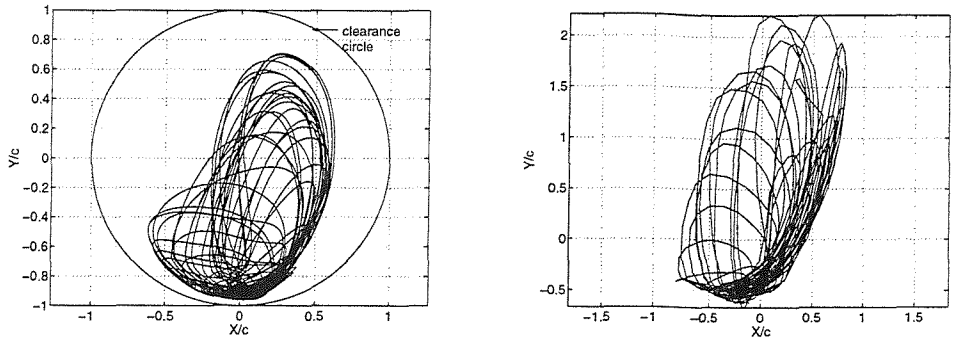

(a) predicted (b) measured [64] ("ac" component only)

Figure 7.32: *Predicted* (numerical integration) *and measured orbits at SFD* (J) *for* 84 *rev/s* Conf. B2, $U = 5.1\times10^{-4}$ kgm, $\eta = 0.0045$ Nsm^{-2}, $p_S = 120$ kPa

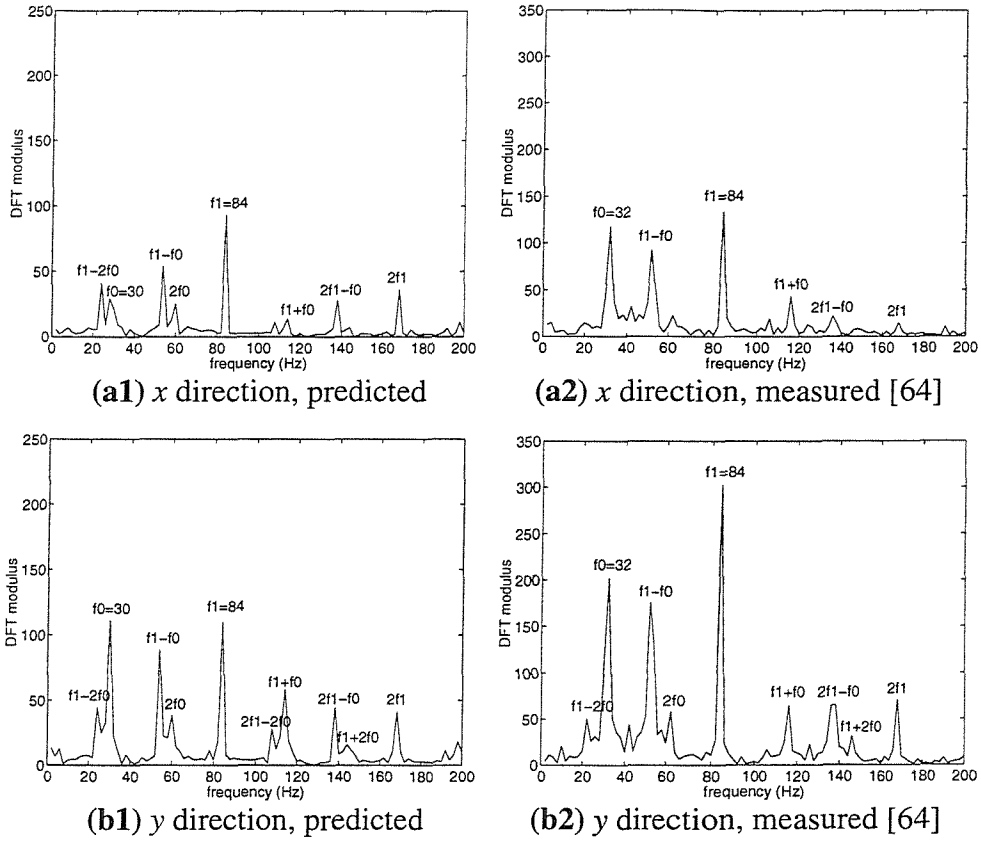

(a1) x direction, predicted (a2) x direction, measured [64]

(b1) y direction, predicted (b2) y direction, measured [64]

Figure 7.33: *Predicted and measured frequency spectra of displacement of* J *for* 84 *rev/s* (data length 0.5 s). Conf. B2, $U = 5.1\times10^{-4}$ kgm, $\eta = 0.0045$ Nsm^{-2}, $p_S = 120$ kPa

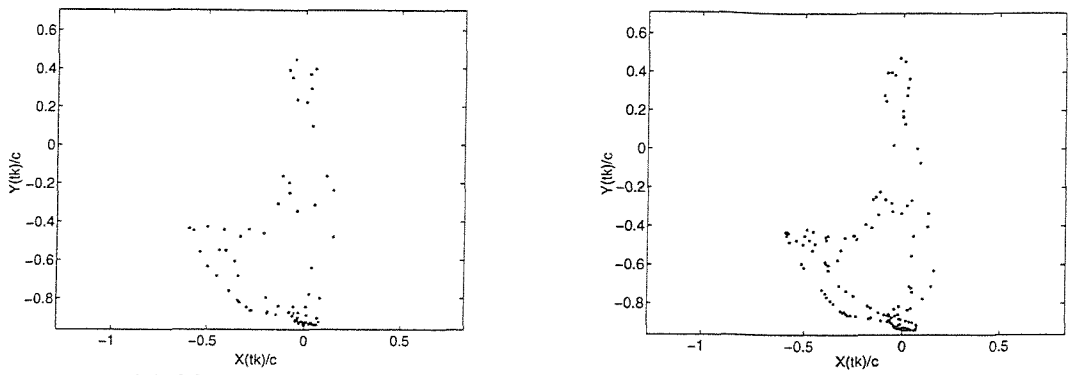

(**a**) 80 samples (**b**) further 160 samples

Figure 7.34: *Poincaré maps of predicted orbital motion at* J *for* 84 *rev/s* ($\Omega t_k = k2\pi$)
Conf. B2, $U = 5.1\times10^{-4}$ kgm, $\eta = 0.0045$ Nsm^{-2}, $p_S = 120$ kPa

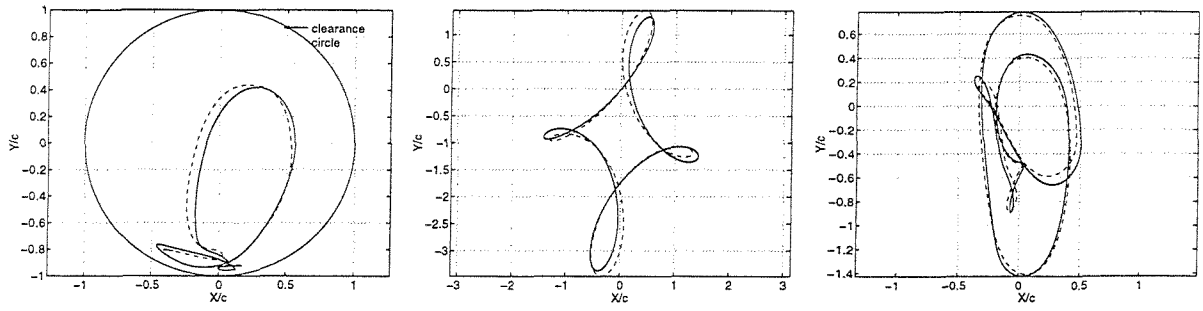

(**a**) SFD (J) (**b**) disc (U) (**c**) mid-shaft (M)

Figure 7.35: *Predicted frequency-locking into* 3*T-periodic motion at* 86 *rev/s*
numerical integration, steady-state (——); RHB $N = 3$, $m = 20$ (– – –)
Conf. B2, $U = 5.1\times10^{-4}$ kgm, $\eta = 0.0045$ Nsm^{-2}, $p_S = 120$ kPa

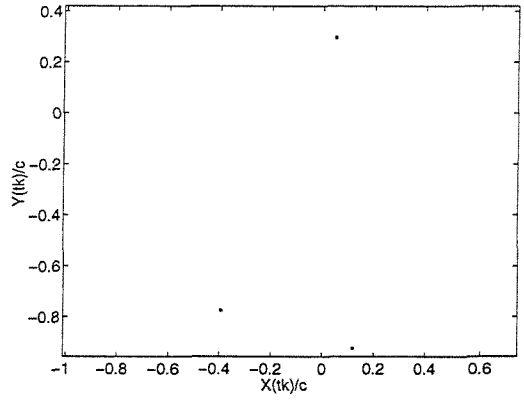

Figure 7.36: *Poincaré map of predicted orbital motion at* J *for* 86 rev/s ($\Omega t_k = k2\pi$)
Conf. B2, $U = 5.1\times10^{-4}$ kgm, $\eta = 0.0045$ Nsm^{-2}, $p_S = 120$ kPa

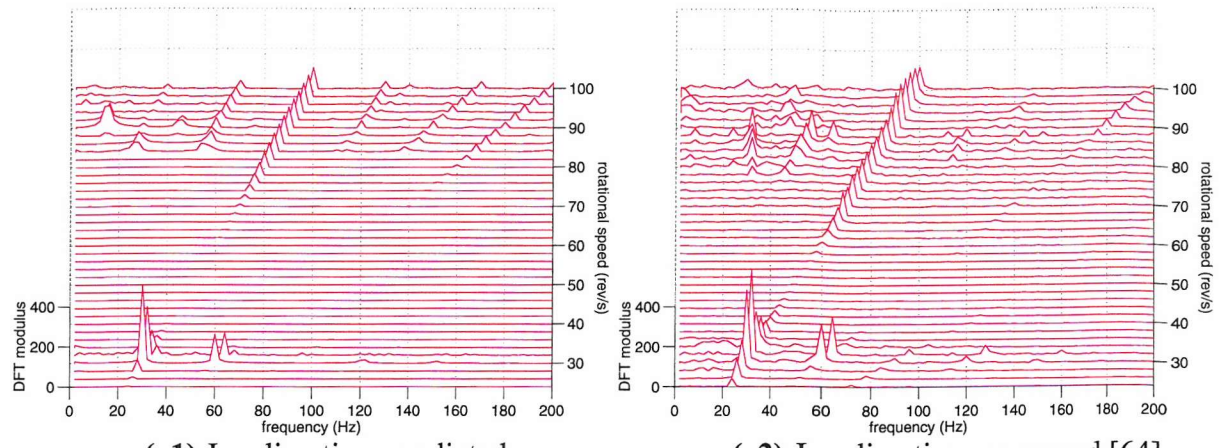

(a1) J, x direction, predicted

(a2) J, x direction, measured [64]

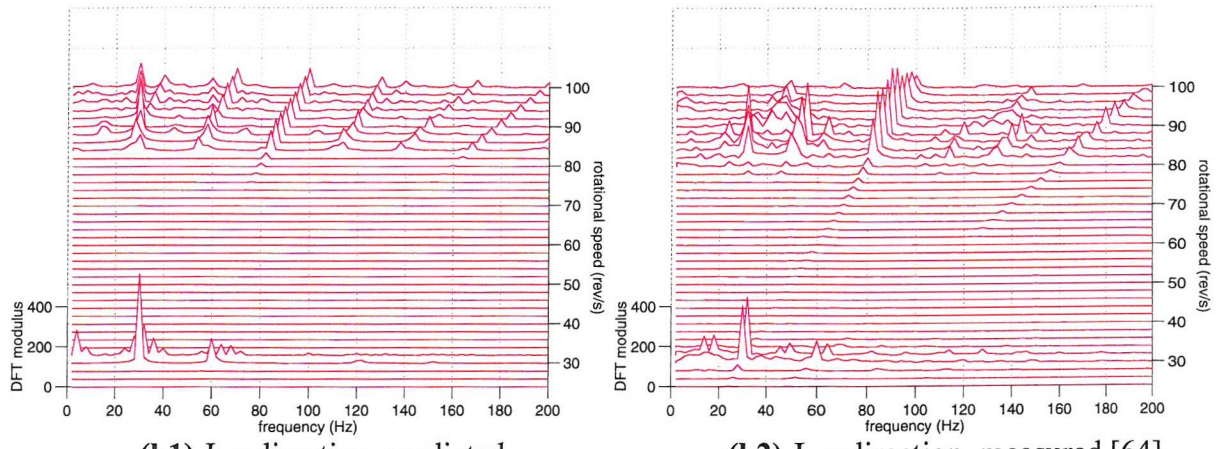

(b1) J, y direction, predicted

(b2) J, y direction, measured [64]

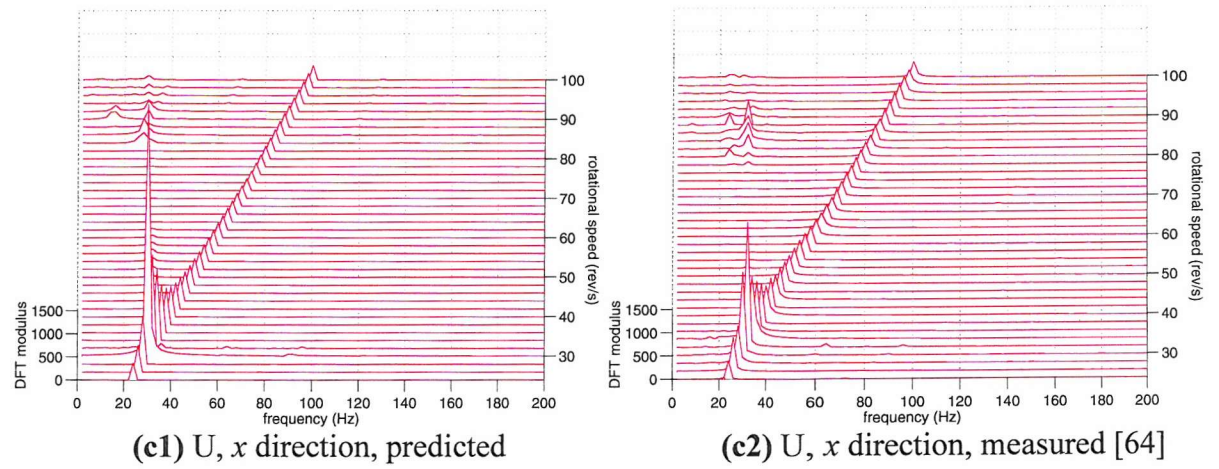

(c1) U, x direction, predicted

(c2) U, x direction, measured [64]

Figure 7.37: *Waterfall diagrams of the frequency spectra of the displacement response for conf. B2* (no retainer spring), $U = 5.1\times10^{-4}\ kgm$, $\eta = 0.0045\ Nsm^{-2}$, $p_S = 120\ kPa$ (data length 0.5 s)

(Figure continues on the following page)

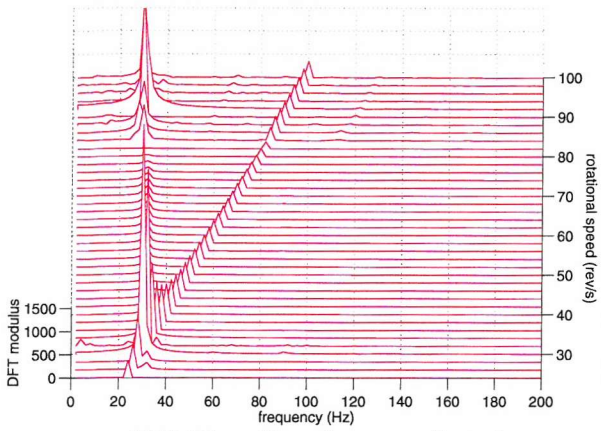

(d1) U, *y* direction, predicted

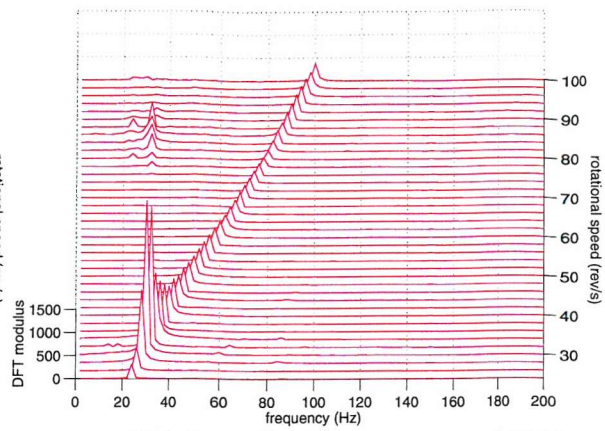

(d2) U, *y* direction, measured [64]

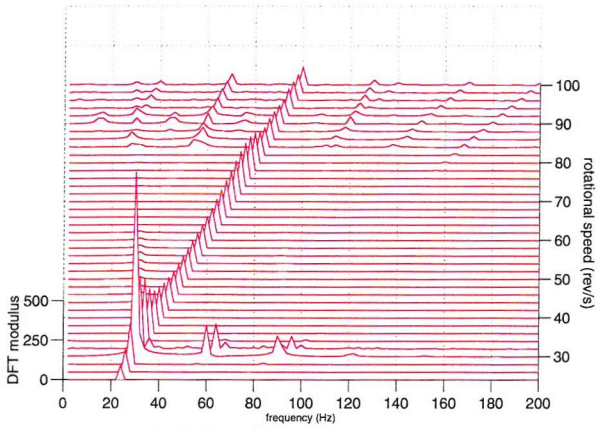

(e1) M, *x* direction, predicted

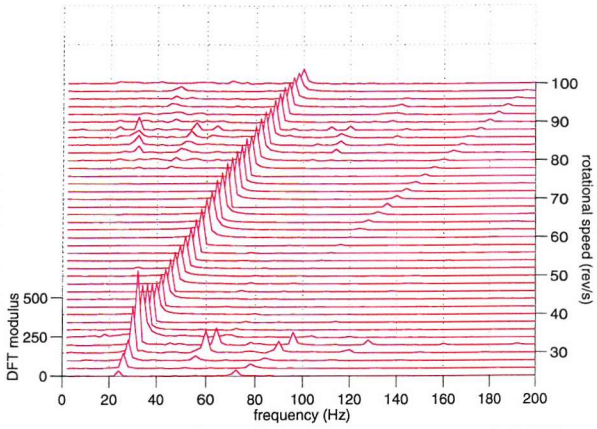

(e2) M, *x* direction, measured [64]

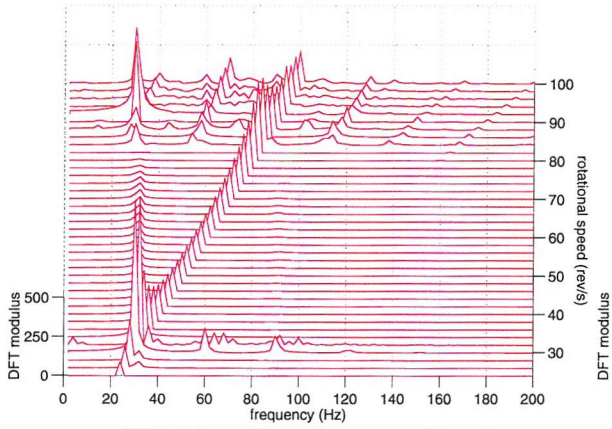

(f1) M, *y* direction, predicted

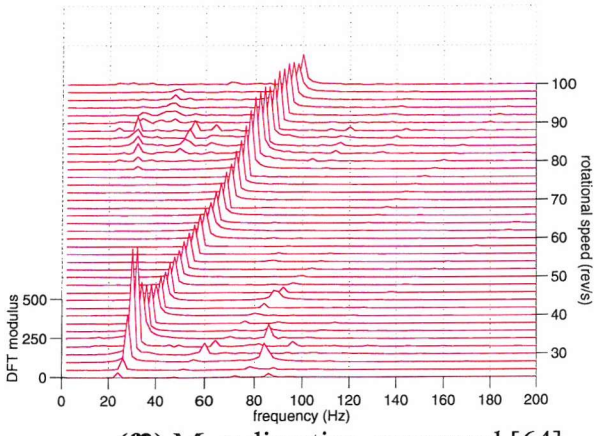

(f2) M, *y* direction, measured [64]

Figure 7.37 (continued): *Waterfall diagrams of the frequency spectra of the displacement response for conf. B2,* $U = 5.1\times10^{-4}\ kgm$, $\eta = 0.0045\ Nsm^{-2}$, $p_S = 120\ kPa$ (data length 0.5 s)

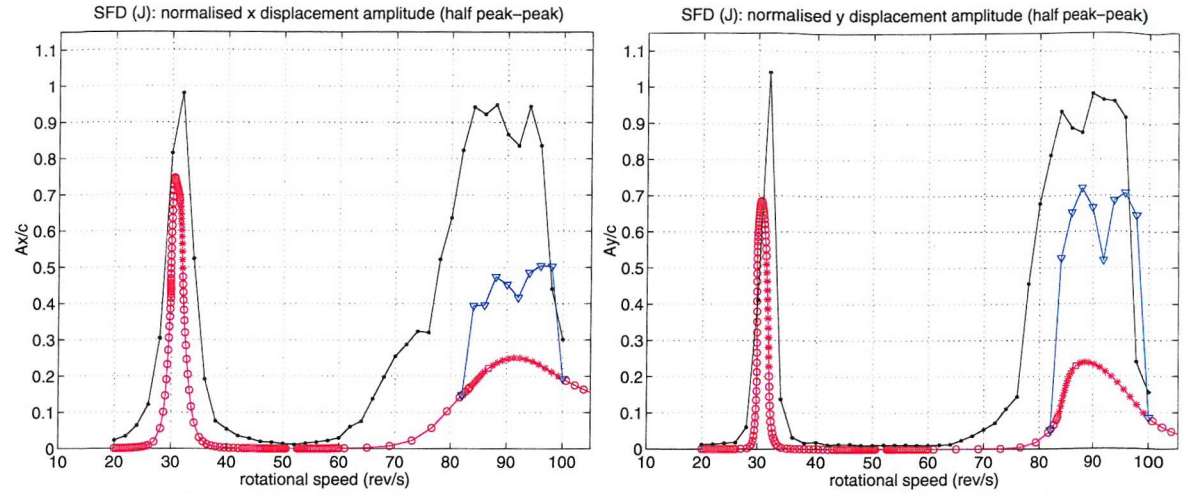

(a) SFD (J), x direction

(b) SFD (J), y direction

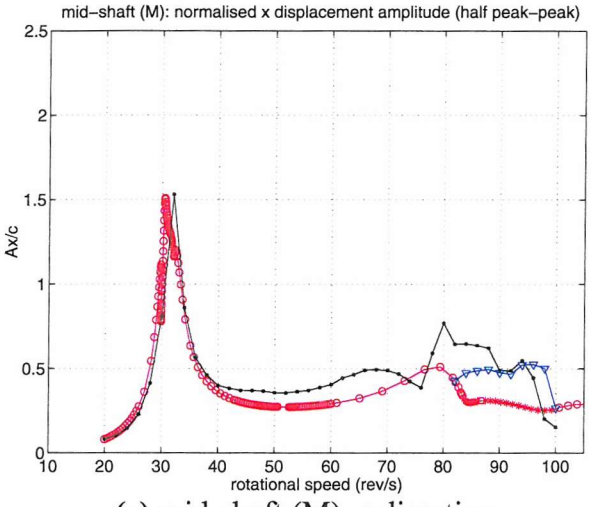

(c) mid-shaft (M), x direction

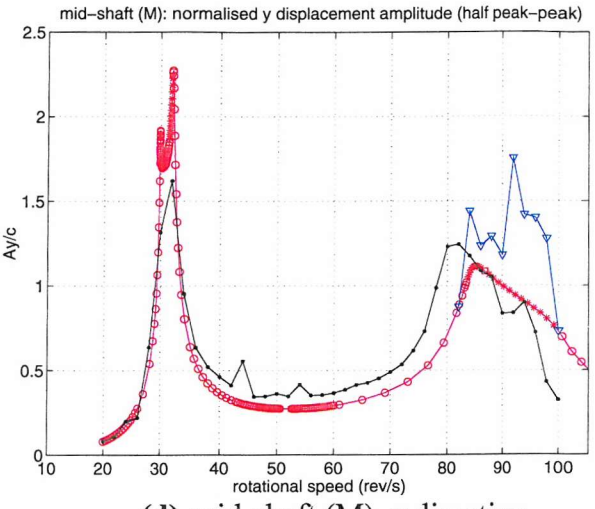

(d) mid-shaft (M), y direction

Figure 7.38: *Response of conf. B2* (no retainer spring) *for* $U = 5.1\times10^{-4}\ kgm$, $\eta = 0.0115\ Nsm^{-2}$, $p_S = 100\ kPa$. Vertical axes show ratio of half peak-to-peak displacement to c. RHB $N = 1$, $m = 5$ – red: "o" stable, "+" unstable (λ_1 real, positive), "□" unstable (λ_1 real, negative), "*" unstable (λ_1 complex); numerical integration – blue; measured – black.

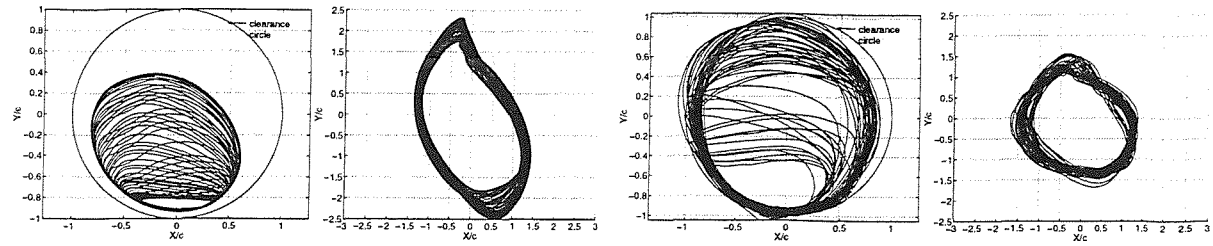

J, 32 rev/s (pred.) M, 32 rev/s (pred.) J, 32 rev/s (meas.) M, 32 rev/s (meas.)

Figure 7.39: *Predicted (stable) and measured orbits* (over 2 s) *at the first pin-pin critical speed*

Conf. B2, $U = 5.1\times10^{-4}$ kgm, $\eta = 0.0115$ Nsm^{-2}, $p_S = 100$ kPa

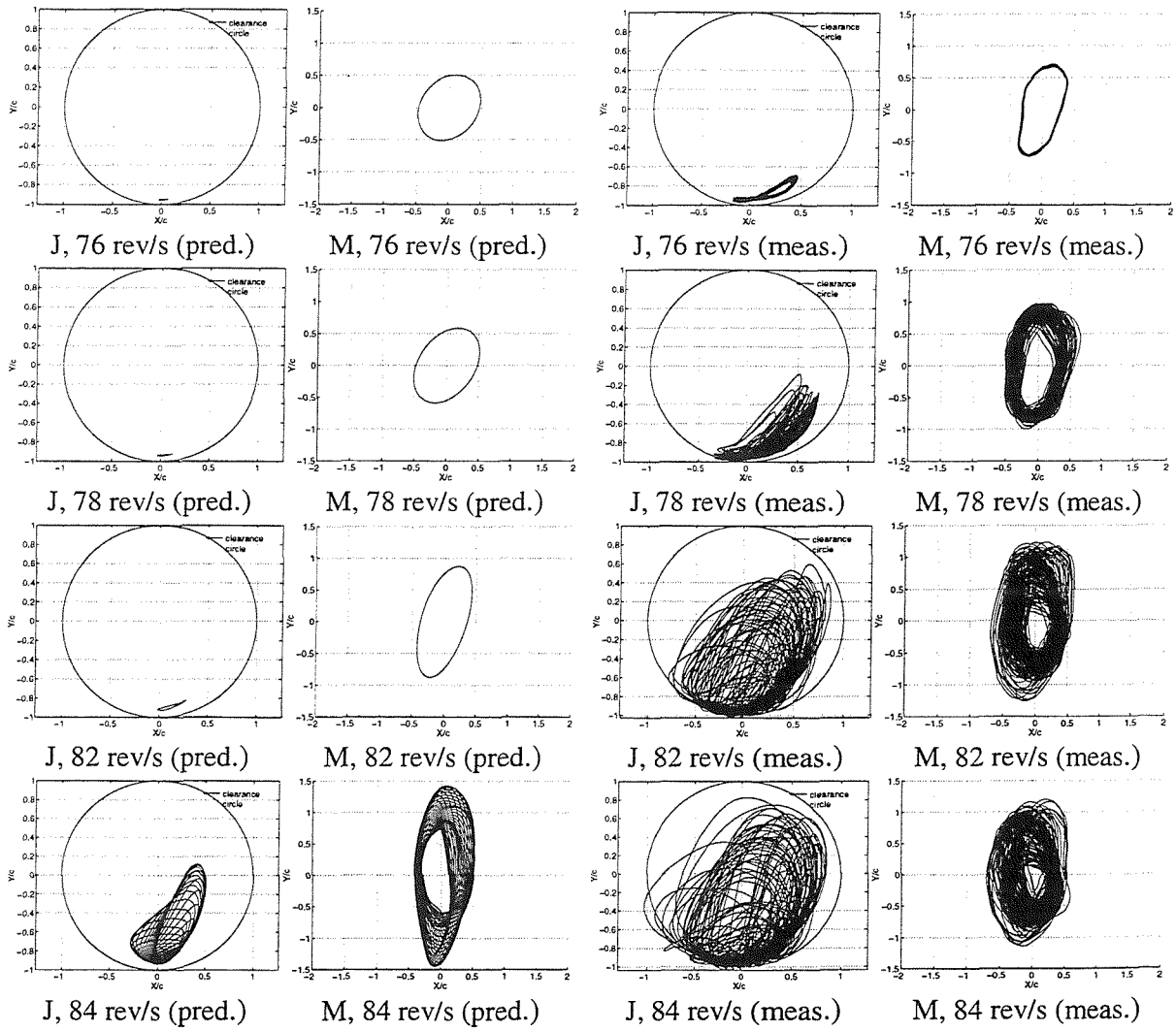

J, 76 rev/s (pred.) M, 76 rev/s (pred.) J, 76 rev/s (meas.) M, 76 rev/s (meas.)

J, 78 rev/s (pred.) M, 78 rev/s (pred.) J, 78 rev/s (meas.) M, 78 rev/s (meas.)

J, 82 rev/s (pred.) M, 82 rev/s (pred.) J, 82 rev/s (meas.) M, 82 rev/s (meas.)

J, 84 rev/s (pred.) M, 84 rev/s (pred.) J, 84 rev/s (meas.) M, 84 rev/s (meas.)

Figure 7.40: *Predicted (stable) and measured orbits* (over 2 s) *in the region of the second pin-pin critical speed*

Conf. B2, $U = 5.1\times10^{-4}$ kgm, $\eta = 0.0115$ Nsm^{-2}, $p_S = 100$ kPa

(Figure continues on the following page)

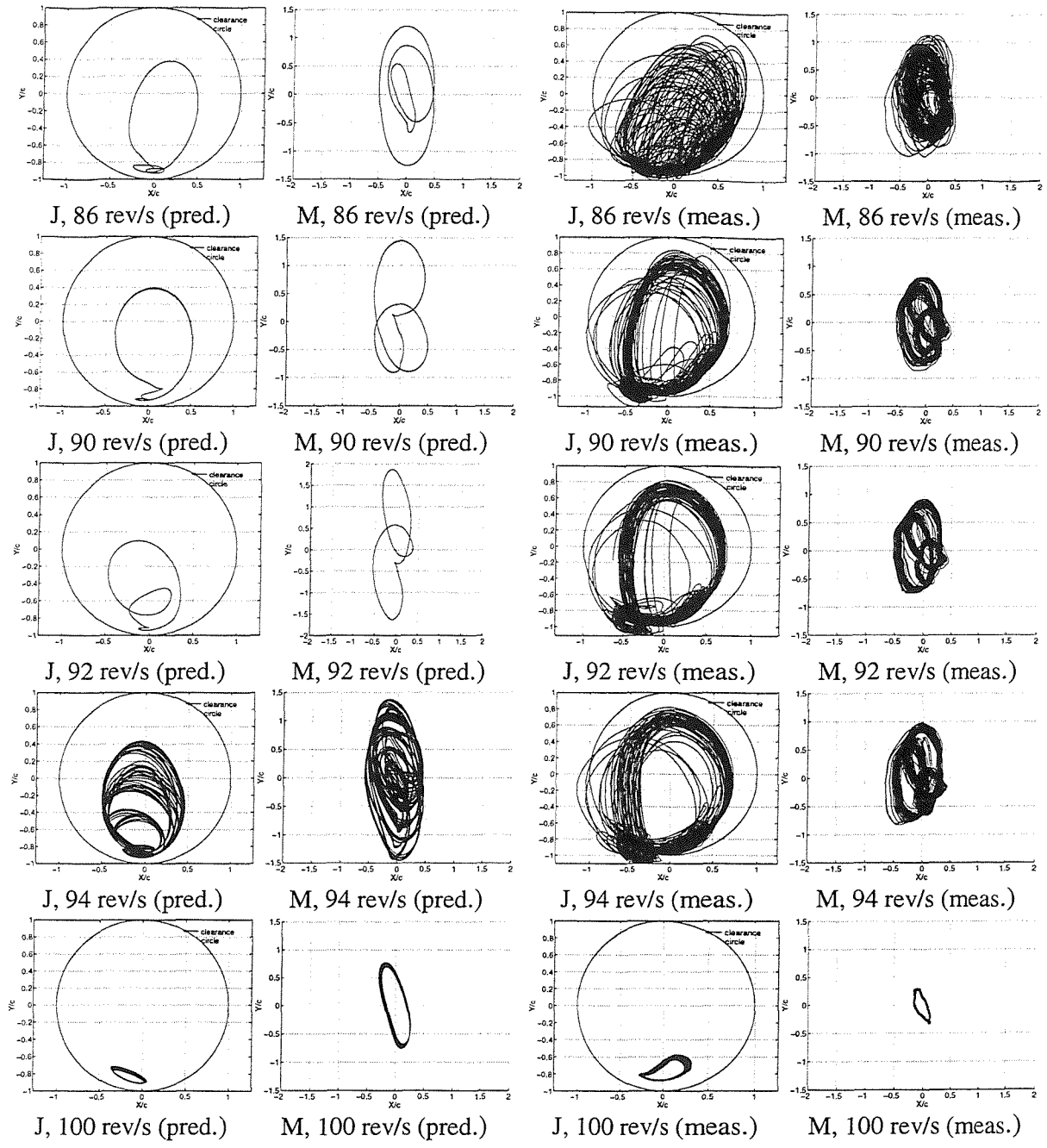

Figure 7.40 (continued): *Predicted (stable) and measured orbits* (over 2 s) *in the region of the second pin-pin critical speed*

Conf. B2, $U = 5.1\times10^{-4}$ kgm, $\eta = 0.0115$ Nsm^{-2}, $p_S = 100$ kPa

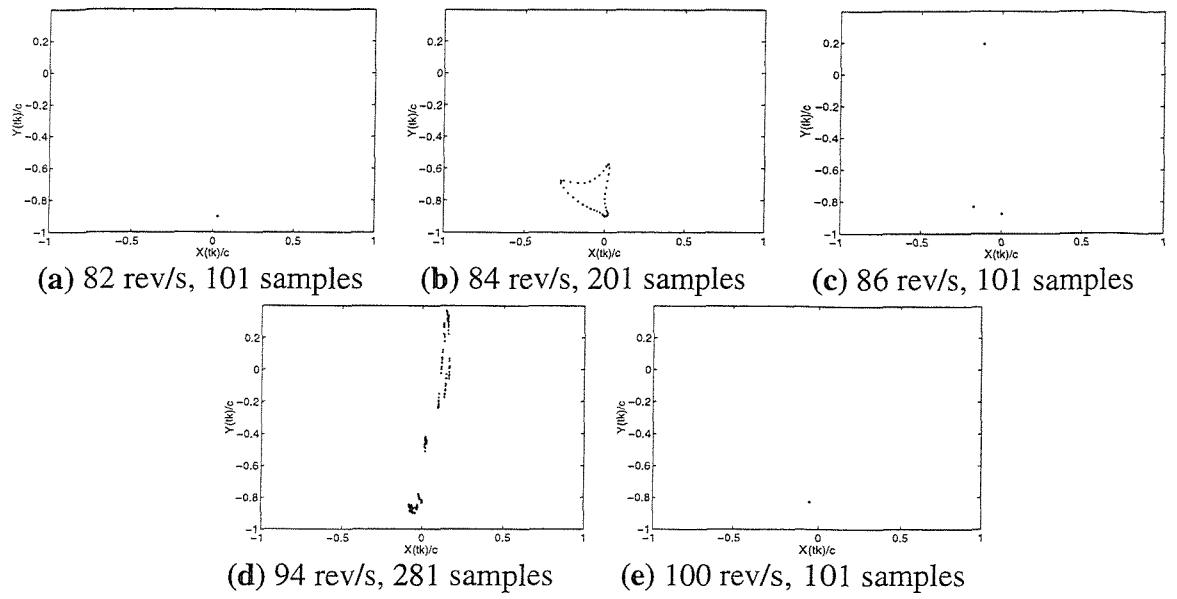

(a) 82 rev/s, 101 samples **(b)** 84 rev/s, 201 samples **(c)** 86 rev/s, 101 samples

(d) 94 rev/s, 281 samples **(e)** 100 rev/s, 101 samples

Figure 7.41: *Predicted Poincaré maps of motion of* J *around second pin-pin critical speed* ($\Omega t_k = k2\pi$). Conf. B2, $U = 5.1\times10^{-4}$ kgm, $\eta = 0.0115$ Nsm^{-2}, $p_S = 100$ kPa

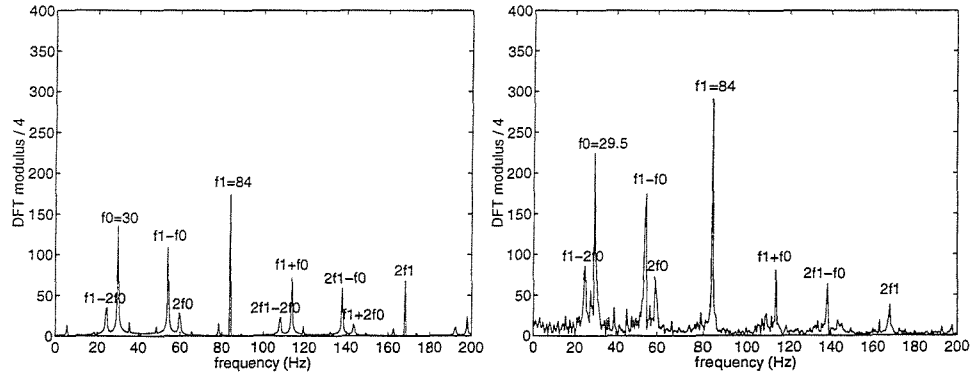

(a1) 84 rev/s, predicted **(a2)** 84 rev/s, measured

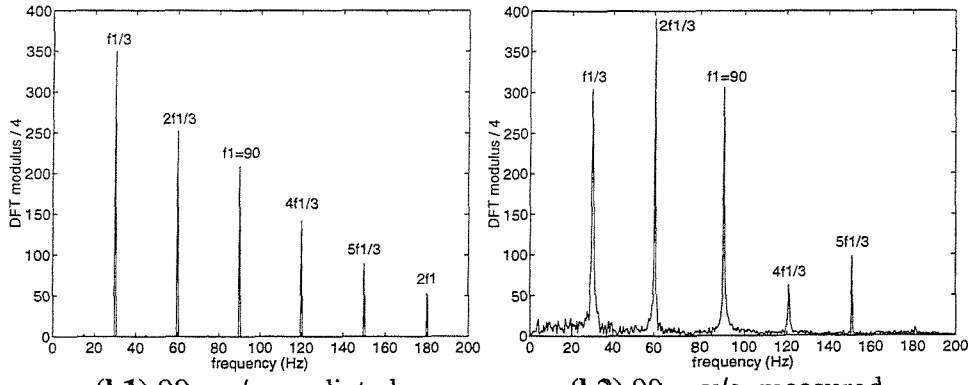

(b1) 90 rev/s, predicted **(b2)** 90 rev/s, measured

Figure 7.42: *Predicted and measured frequency spectra of y displacement of* J (data length 2 s). Conf. B2, $U = 5.1\times10^{-4}$ kgm, $\eta = 0.0115$ Nsm^{-2}, $p_S = 100$ kPa

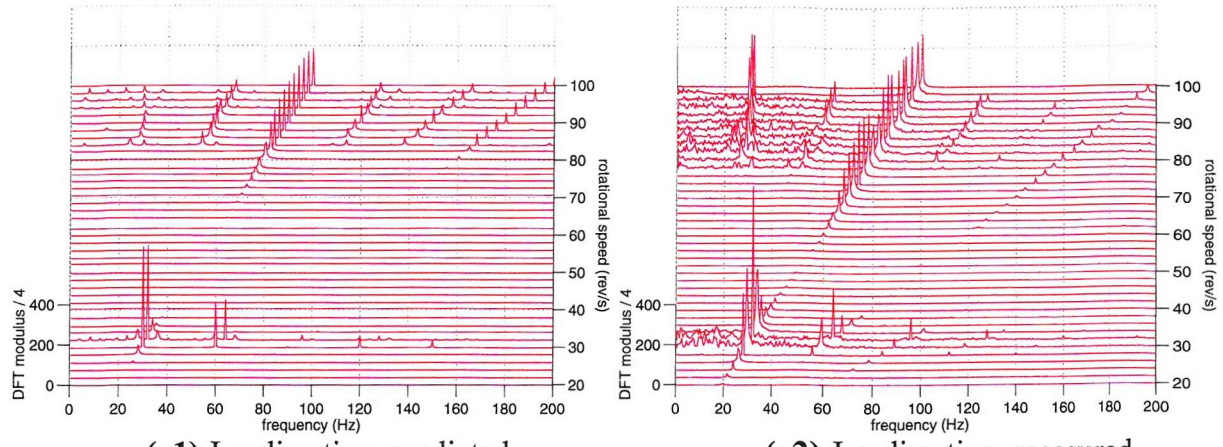

(a1) J, x direction, predicted **(a2)** J, x direction, measured

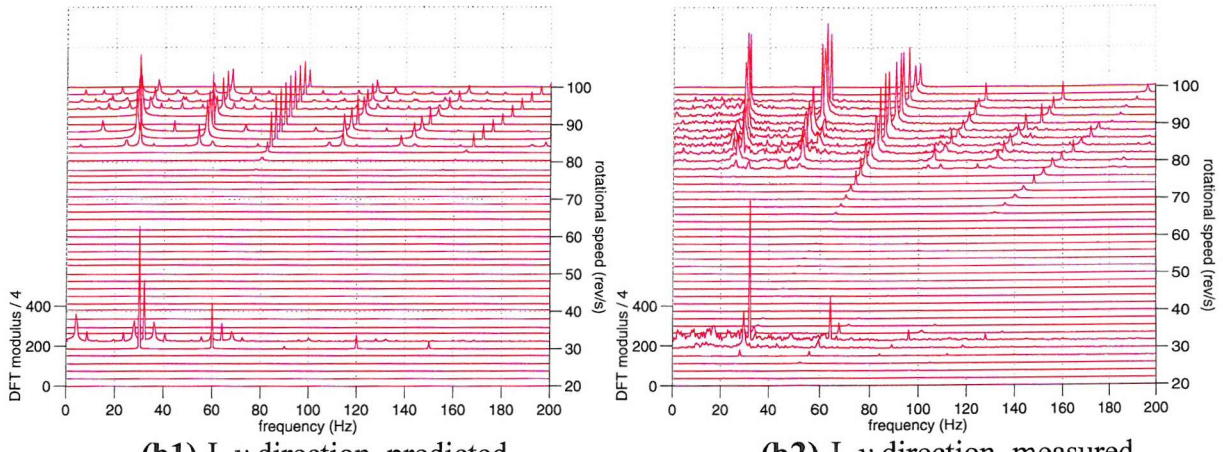

(b1) J, y direction, predicted **(b2)** J, y direction, measured

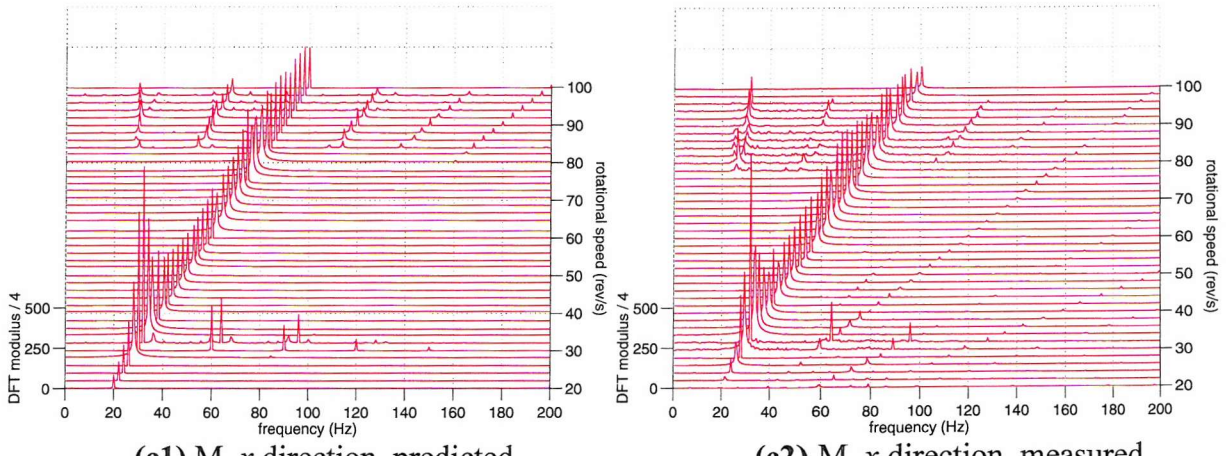

(c1) M, x direction, predicted **(c2)** M, x direction, measured

Figure 7.43: *Waterfall diagrams of the frequency spectra of the displacement response for conf. B2* (no retainer spring), $U = 5.1\times10^{-4}\ kgm$, $\eta = 0.0115\ Nsm^{-2}$, $p_S = 100\ kPa$ (data length 2 s)

(Figure continues on the following page)

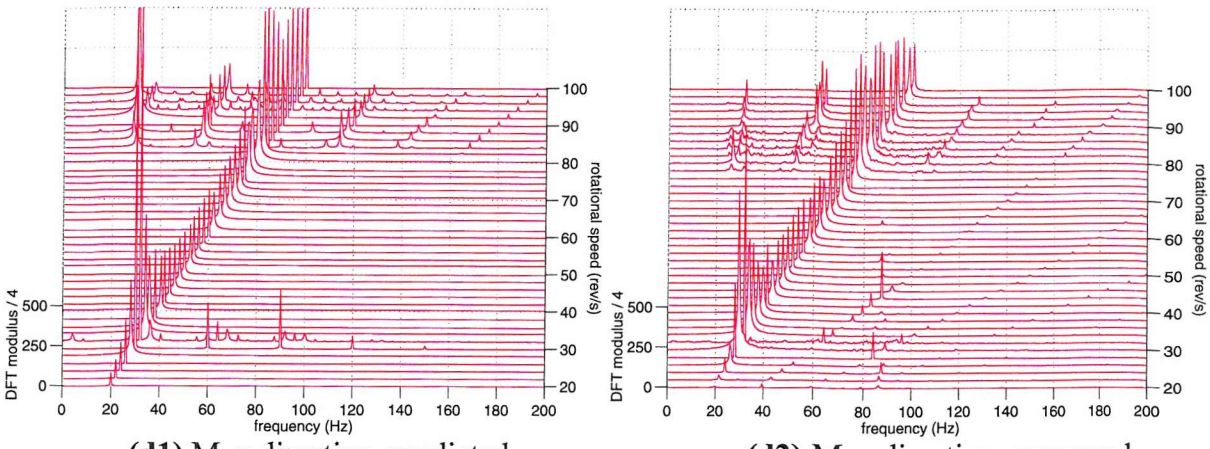

(d1) M, *y* direction, predicted **(d2)** M, *y* direction, measured

Figure 7.43 (continued): *Waterfall diagrams of the frequency spectra of the displacement response for conf. B2,* $U = 5.1\times10^{-4}\ kgm$, $\eta = 0.0115\ Nsm^{-2}$, $p_S = 100\ kPa$ (data length 2 s)

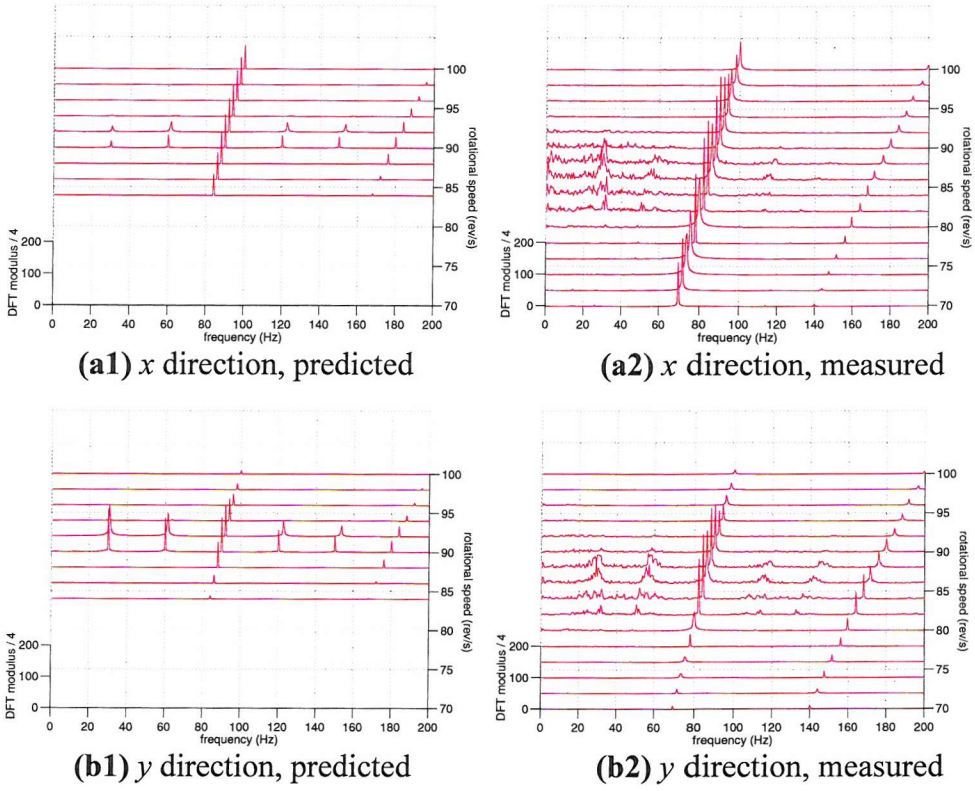

(a1) *x* direction, predicted **(a2)** *x* direction, measured

(b1) *y* direction, predicted **(b2)** *y* direction, measured

Figure 7.44: *Waterfall diagrams of the frequency spectra of the displacement of* J *for conf. B2,* $U = 2.59\times10^{-4}\ kgm$, $\eta = 0.0115\ Nsm^{-2}$, $p_S = 100\ kPa$ (data length 2 s)

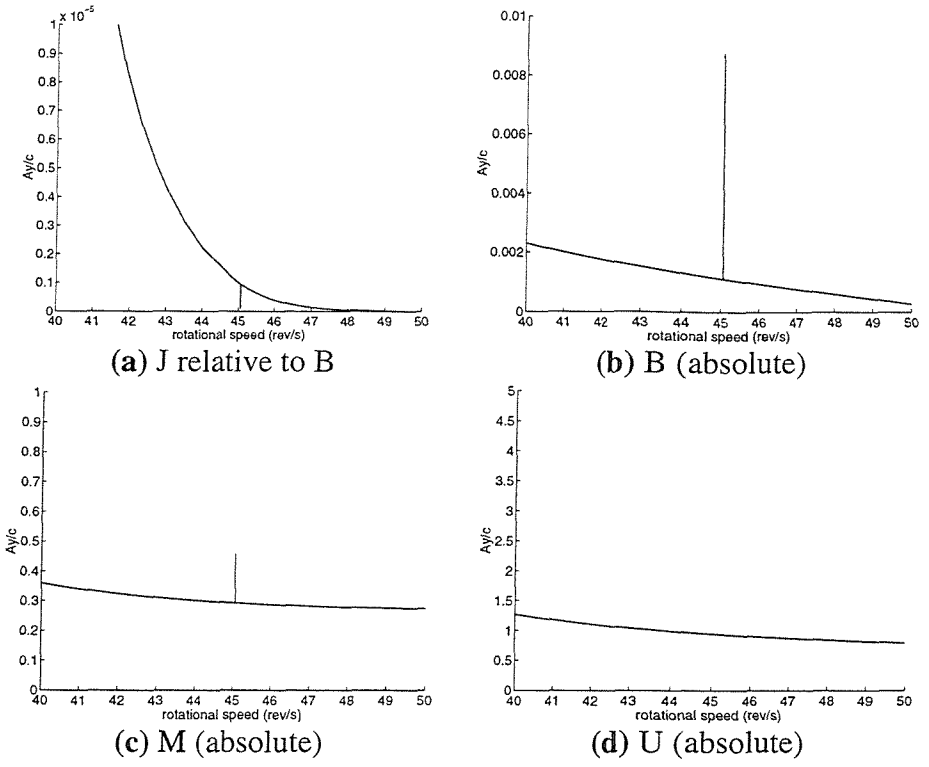

Figure 7.45: *Predicted response in y direction around super-harmonic resonance, taking into account the SFD bearing housing flexibility*

RHB $N=1$, $m=5$. Vertical axes show ratio of half peak-to-peak displacement to *c*.
Conf. B2, $U=5.1\times10^{-4}$ kgm, $\eta=0.0115$ Nsm^{-2}, $p_S=100$ kPa

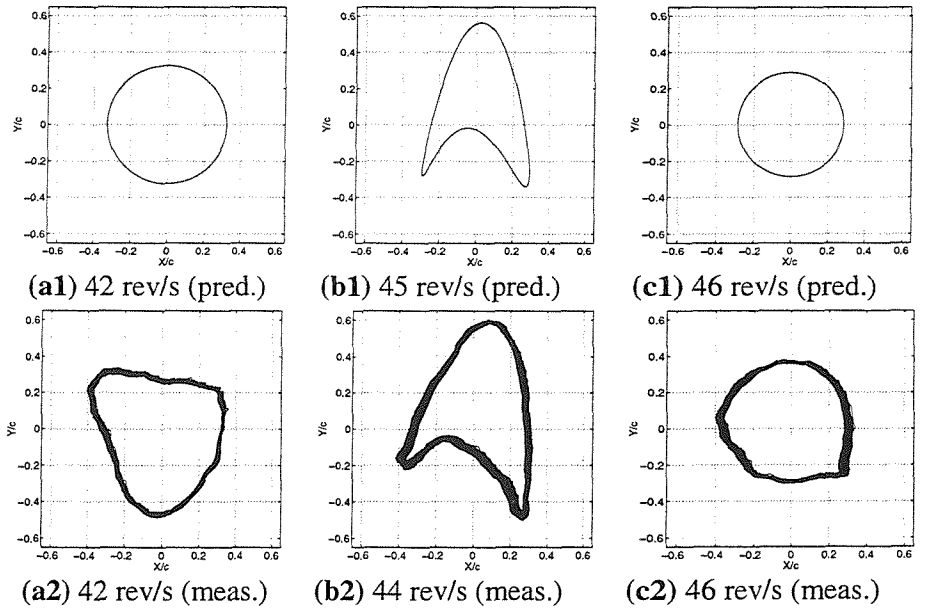

Figure 7.46: *Orbital motion* (over 2 s) *at mid-shaft* (M) *around super-harmonic resonance,* 44-45 *rev/s* (predictions take into account the flexibility of the SFD bearing housing)
Conf. B2, $U=5.1\times10^{-4}$ kgm, $\eta=0.0115$ Nsm^{-2}, $p_S=100$ kPa

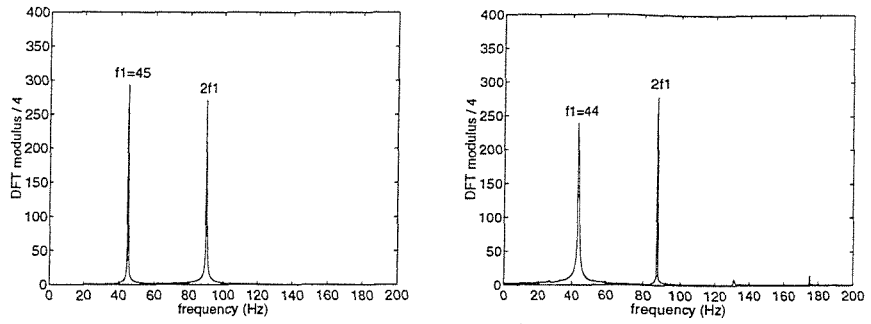

(**a**) predicted (at 45 rev/s) (**b**) measured (at 44 rev/s)

Figure 7.47: *Frequency spectra of y component of predicted and measured orbital motion at* M *in Figures 7.46(b1,b2) respectively* (data length 2 s)
Conf. B2, $U = 5.1\times10^{-4}$ kgm, $\eta = 0.0115$ Nsm^{-2}, $p_s = 100$ kPa

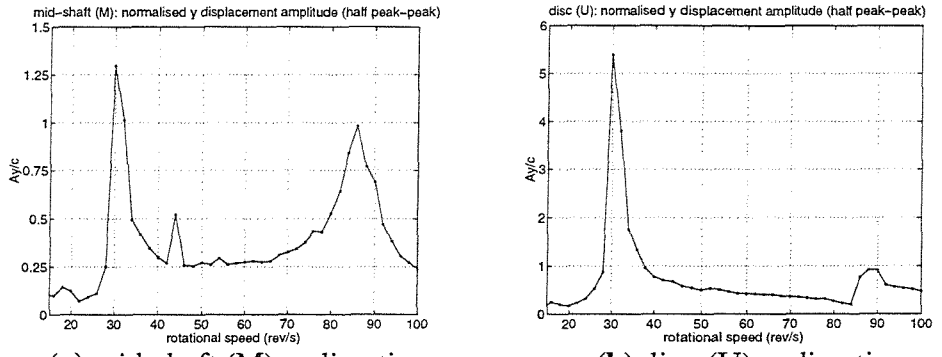

(**a**) mid-shaft (M), *y* direction (**b**) disc (U), *y* direction

Figure 7.48: *Measured normalised half peak-to-peak displacement for conf. B2,* $U = 2.59\times10^{-4}$ *kgm,* $\eta = 0.0045$ *Nsm*$^{-2}$, $p_s = 120$ *kPa* [64]

8 MODEL APPLICATION C: FLEXIBLE ROTOR IN TWO FLEXIBLY HOUSED UNSUPPORTED SFDs

8.1 INTRODUCTION

The rigid rotor-flexible housing configuration of Chapter 6 and the flexible rotor-rigid housing configuration of Chapter 7 are idealisations. In this chapter the integrated model is used to analyse a more realistic system in which both rotor and support structure are considered flexible. Moreover, practical systems have more than one squeeze film damper (SFD). Hence, the use of two SFDs in configuration C. In configuration C, both "symmetric" and "anti-symmetric" bounce modes are present, unlike the simplified system in Chapter 6. It will be seen in this chapter that, despite the first two rotor-support structure critical speeds with the SFDs locked (i.e. their radial clearances shimmed) still being essentially "bounce modes" (i.e. the rotor showing much less deflection than the housings), the presence of harmonics of the rotational speed in the non-linear response of the unbalanced squeeze film damped system necessitates the consideration of the flexibility of the rotor. A description of the test facility is given in the following section, together with a description of impact tests on the support structure alone, and on the complete non-rotating rig with the SFDs locked. The non-linear model equations are then presented. This is followed by an account of the experimental procedure for vibration acquisition for the rotating rig. The correlation between the predicted results from the three modelling blocks (i.e. receptance harmonic balance, modal Floquet stability analysis, and modal numerical integration) is then assessed and the results compared with measurements. The aim of the latter comparison is limited to the assessment of the ability to predict and explain observed non-linear phenomena.

8.2 DESCRIPTION OF THE TEST FACILITY

The test rig for configuration C is illustrated in Figure 8.1. Photographs of the rig are found in Appendix A6, section A6.6 (page 259). This rig was originally built in 1984 under a

research contract with *Rolls-Royce plc* to represent, to a limited extent, the essential features of the RB401 aero-engine. Since then, it has been modified to include two SFDs and recommissioned in 2001, as part of this Ph.D. project, in the rotor dynamics laboratory of the Institute of Sound and Vibration Research (ISVR), University of Southampton. In its most general form, the test rig has two independently driven shafts, labelled (7) and (14) in Figure 8.1, which respectively represent the low pressure (LP) and high pressure (HP) rotors of an aero-engine. In one modification, described in [31], a bell housing (not shown in Figure 8.1) connects the bearing housing (5) at the right hand end of the LP shaft (7) to the left hand bearing housing of the HP shaft (14) (the latter bearing housing is also not shown in Figure 8.1). In this thesis, the LP and HP assemblies are disengaged, as shown in Figure 8.1, and attention is placed entirely on the LP assembly. The HP shaft (14) is kept fixed and non-rotating.

The mild steel shaft (7) runs in two roller bearings (3) at its ends J_1, J_2. Oil is pumped into the annular clearance between each bearing housing (5) and the ring (4) fixed to the outer race of each roller bearing, forming the SFD (6). Each SFD journal (4) is prevented from rotating relative to the shaft axis by dogs on the outer end-plate of the bearing housing, which engage with dogs projecting from the outer end of the journal. Each of the bearing housings B_1, B_2 is flexibly mounted on the engine frame (10) by four mild steel bars (8). The frame is bolted down to a cast iron bedplate (11) that is bonded by a thin layer of adhesive to a massive concrete block mounted on isolators. Torque is transmitted to the shaft at (2) via two pins covered in *nitrile* that contact opposite faces of a rectangular steel bar bolted to the left hand end of the shaft. This ensures torque transmission with no flexural restraint in either plane *xz*, *yz*. The drive shaft (1) is belt-driven by an electric motor (belt drive and motor not shown). The motor is bolted to the ground rather than the bedplate and concrete block to avoid spurious vibration transmission to the rig. Axial location of the shaft (7) is maintained by *teflon* (*PTFE*) buttons at its ends: one at the centre of the driven bar at (2) and the other at the end of the HP shaft (14). Impact tests on the non-rotating rig with the SFDs locked by inserting shims into their radial clearances indicate that the first two rotor-support structure critical speeds are around 66 rev/s and 100 rev/s, corresponding respectively to the symmetric and anti-symmetric bounce modes. With the dampers operational, the rig is driven up to a maximum speed of 110 rev/s.

The SFDs are end-plated, of the type shown in Figure 4.1(b). Both left hand and right hand SFDs (SFD 1, SFD 2 respectively) are nominally identical, with the dimensions shown

in Figure 8.2. The radial clearance $c = 0.11\times10^{-3}$ m and the groove depth $d_{groove} = 2.03\times10^{-3}$ m, satisfying the two-land criterion, eq. (4.1). The lengths of the two lands of each SFD are slightly unequal and the value in Figure 8.2 ($L = 6.26\times10^{-3}$ m) is an average. The axial location of the journal within the housing is maintained by small and smooth *tufnol* spacers 0.5 mm thick (see Figure 8.2), three such spacers being glued to each end-plate at positions spaced by 120°. This ensures a fixed end-plate gap of $d_{gap} = 0.50\times10^{-3}$ m, which is over four times the radial clearance c. Hence, the SFDs are short unsealed dampers. Note that there is a lower limit to the circumferential extent of the glued *tufnol* spacers in order to ensure adequate bonding. Hence, the outlet flow is blocked over portions of the circumference in Figure 8.2. However, the total circumferential extent of the three spacers at each outlet should be around 10% and so, this sealing effect is considered negligible. Oil is supplied to each SFD through three holes, spaced at 120° around the groove. The oil used is *Shell Morlina* 10 (formerly known as *Shell Tellus R*10) with a viscosity of 15×10^{-3} Nsm^{-2} and density 866.8 kg/m^3 at 25°C. The oil pressure supply to both dampers is monitored by a single common pressure gauge (not shown in Figure 8.1). The oil exit temperature from each SFD is measured by a thermocouple located underneath each housing. The oil from both dampers collects in a tray fixed to the bedplate (not shown in Figure 8.1) and is recirculated into the hydraulic system. Since the oil also acts as a coolant for the roller bearings, its equilibrium temperature increases with speed. However, this temperature never exceeds 44°C. At this temperature, the oil has a viscosity of 8.84×10^{-3} Nsm^{-2} and density 854.4 kg/m^3. Since the top speed is 110 rev/s, the maximum value of the gap Reynolds number (eq. (4.16)) is 0.8. Using eq. (4.15) with $C_I = 0.287$ (for moderate *Re*) [60], an upper limit for the fluid inertia effect is estimated as $M_{fluid} = 76.4\times10^{-3}$ kg. This amounts to merely 6% of the combined mass of the roller bearing and damper journal. Considering also that the total rotor mass is 55.4 kg, it is ascertained that the fluid inertia effects are negligible.

Referring back to Figure 8.1, unbalance masses m_{U_1}, m_{U_2} can be attached to the rotor at axial positions U_1, U_2 respectively and can be either in anti-phase (180° out of phase) or in phase. The displacement response to rotating out-of-balance is measured by four transducers (proximity probes) at each SFD location: one pair of orthogonal probes, with brackets marked (13), measure the x, y displacements of the bearing housing relative to the engine frame (10), and the other pair, with brackets marked (12), measure the x, y displacements of

the rotor relative to the housing. As shown in Figure 8.1, the rotor vibration measurements are taken at positions J_{1m}, J_{2m}, as close as practically possible to the respective SFD positions J_1, J_2. Hence, these measurements are compared with the corresponding theoretical predictions for the rotor vibration at J_{1m}, J_{2m} rather than J_1, J_2. The displacement response of each housing relative to the frame is directly proportional to the corresponding force transmitted to the frame. Impact tests on the support structure, discussed in the following subsection, indicate that the absolute vibration of the frame is normally negligible when compared to the absolute vibration of the bearing housings B_1, B_2. Hence, measured responses relative to the frame can be regarded as "absolute", allowing them to be compared with the theoretical predictions for the absolute response.

The following two subsections respectively describe impact tests on the support structure alone (to determine its modal parameters) and on the complete non-rotating rig with the SFDs locked (to estimate the bounce resonance frequencies i.e. the bounce critical speeds).

8.2.1 Impact Tests on Support Structure

In these tests, the oil supply was disconnected and the end-plates of the housings (5) (see Figure 8.1) were removed. The roller bearings (3) were then removed and the rotor was suspended from an overhead girder, well clear from the inner surface of each housing. The proximity probe brackets were also removed. Preliminary impact tests verified that there was virtually no dynamic cross-coupling between the *xz* and *yz* planes so that the dynamics in each plane could be studied separately as follows. For each housing B_i ($i = 1, 2$) in turn, an impact was applied in the *y* direction with an instrumented hammer[1] connected through a voltage amplifier to a *Hewlett Packard* 35650® multi-channel spectrum analyser operated by a personal computer (PC). The following accelerance frequency response functions $\breve{\beta}_{PQ}(\omega)$, ($\omega$ is the frequency in rad/s, see eq. (5.27)) relating the applied force at position Q in the *y* direction to the acceleration response in the same direction at position P, were then measured: the point accelerance $\breve{\beta}_{B_iB_i}$ at B_i; the transfer accelerance $\breve{\beta}_{B_jB_i}$ between the other housing B_j and B_i; and the transfer accelerance $\breve{\beta}_{F_iB_i}$ between F_i and B_i, where F_i corresponds to the axial position on the frame where the bracket (13) for the probe measuring the unbalance response of B_i in the *y* direction is fixed (see Figure 8.1). For this set of measurements, piezoelectric accelerometers were attached at B_i, F_i and B_j with their axes in the *y* direction

[1] i.e. a hammer with a force gauge at its tip.

and connected through charge amplifiers to the spectrum analyser. The process was repeated in the x direction for the accelerances $\breve{\alpha}_{B_iB_i}$, $\breve{\alpha}_{B_jB_i}$, $\breve{\alpha}_{F_iB_i}$. The instrumentation details are given in Appendix A6 (section A6.1). The results are shown in Figures 8.3(a,b,c,d) which refer respectively to the magnitudes of the accelerance measurements of the four impact tests: ($\breve{\alpha}_{B_1B_1}$, $\breve{\alpha}_{B_2B_1}$, $\breve{\alpha}_{F_1B_1}$), ($\breve{\alpha}_{B_2B_2}$, $\breve{\alpha}_{B_1B_2}$, $\breve{\alpha}_{F_2B_2}$), ($\breve{\beta}_{B_1B_1}$, $\breve{\beta}_{B_2B_1}$, $\breve{\beta}_{F_1B_1}$), ($\breve{\beta}_{B_2B_2}$, $\breve{\beta}_{B_1B_2}$, $\breve{\beta}_{F_2B_2}$). Since piezoelectric accelerometers were used, the low frequency data were susceptible to noise contamination. However, this was not important for the purposes of these tests since they focused on the resonance region. It is evident that the (absolute) vibration transmitted to F_i, indicated by the magnitudes of $\breve{\alpha}_{F_iB_i}$, $\breve{\beta}_{F_iB_i}$, was, in the main, negligible with respect to the vibration at B_i, indicated by the magnitudes of $\breve{\alpha}_{B_iB_i}$, $\breve{\beta}_{B_iB_i}$. The dynamic cross-coupling between B_1 and B_2, indicated by the magnitudes of $\breve{\alpha}_{B_jB_i}$, $\breve{\beta}_{B_jB_i}$, was only significant in the immediate vicinity of resonance.

In order to facilitate the experimental modal analysis, the cross-coupling between B_1 and B_2 was neglected and so, the required modal parameters of the support structure were determined by fitting a single mode to each point receptance function $\alpha_{B_iB_i}(\omega)$, $\beta_{B_iB_i}(\omega)$, ($= -\breve{\alpha}_{B_iB_i}/\omega^2$, $-\breve{\beta}_{B_iB_i}/\omega^2$) [47]:

$$\alpha_{B_1B_1}(\omega) \approx \frac{A_{B_1B_1}^{(Sx1)}}{\omega_{Sx1}^2 - \omega^2 + j\hat{\eta}_{Sx1}\omega_{Sx1}^2}, \qquad \alpha_{B_2B_2}(\omega) \approx \frac{A_{B_2B_2}^{(Sx2)}}{\omega_{Sx2}^2 - \omega^2 + j\hat{\eta}_{Sx2}\omega_{Sx2}^2} \tag{8.1a,b}$$

$$\beta_{B_1B_1}(\omega) \approx \frac{A_{B_1B_1}^{(Sy1)}}{\omega_{Sy1}^2 - \omega^2 + j\hat{\eta}_{Sy1}\omega_{Sy1}^2}, \qquad \beta_{B_2B_2}(\omega) \approx \frac{A_{B_2B_2}^{(Sy2)}}{\omega_{Sy2}^2 - \omega^2 + j\hat{\eta}_{Sy2}\omega_{Sy2}^2} \tag{8.1c,d}$$

In eqs. (8.1), ω_{Sxr}, ω_{Syr} ($r = 1, 2$) are the undamped natural frequencies of the support structure in the xz and yz planes respectively and $A_{B_iB_i}^{(Sxr)}$, $A_{B_iB_i}^{(Syr)}$ are the corresponding modal constants of the receptance functions $\alpha_{B_iB_i}(\omega)$, $\beta_{B_iB_i}(\omega)$ respectively, where:

$$A_{B_iB_i}^{(Sxr)} = \phi_{B_i}^{(Sxr)}\phi_{B_i}^{(Sxr)}, \quad A_{B_iB_i}^{(Syr)} = \phi_{B_i}^{(Syr)}\phi_{B_i}^{(Syr)} \tag{8.2a,b}$$

$\phi_{B_i}^{(Sxr)}$, $\phi_{B_i}^{(Syr)}$ being the undamped mass-normalised mode shapes of the support structure in the xz and yz planes respectively, evaluated at position B_i in the x and y directions respectively. $\hat{\eta}_{Sxr}$, $\hat{\eta}_{Syr}$ are the modal loss factors for the structural (hysteretic) damping. The approximations of eqs. (8.1) mean that in the first mode of the support structure in the xz plane (natural frequency ω_{Sx1}), B_1 vibrates and B_2 is stationary ($A_{B_2B_2}^{(Sx1)} = 0$), and in the second mode of the support structure (natural frequency ω_{Sx2}), B_2 vibrates and B_1 is stationary ($A_{B_1B_1}^{(Sx2)} = 0$). The same applies for the yz plane. The modal fitting procedure is described in Appendix A6, section A6.1. The technique used the Nyquist plot [47] to determine the natural frequencies and loss factors, and the dynamic stiffness method [47] to determine the modal constants. The computed modal parameters ω_{Sxr}, ω_{Syr}, $A_{B_iB_i}^{(Sxr)}$, $A_{B_iB_i}^{(Syr)}$, $\hat{\eta}_{Sxr}$, $\hat{\eta}_{Syr}$ ($i = 1, 2$ and $r = 1, 2$) are given in Table 8.1. As it turns out from Table 8.1, with the notation used, in either plane xz, yz, the first mode is at a higher frequency than the second. In view of the fact that modal analysis does not actually require that the modes be ordered according to the relative magnitudes of the corresponding natural frequencies, the notation for the modal parameters is left unaltered.

xz plane			yz plane		
mode no. r	1	2	mode no. r	1	2
$\omega_{Sxr}/(2\pi)$ (Hz)	209.125	201.375	$\omega_{Syr}/(2\pi)$ (Hz)	210.875	202.625
$A_{B_1B_1}^{(Sxr)}$ ($\times 10^{-1}$ kg^{-1})	2.7619	0	$A_{B_1B_1}^{(Syr)}$ ($\times 10^{-1}$ kg^{-1})	2.8304	0
$A_{B_2B_2}^{(Sxr)}$ ($\times 10^{-1}$ kg^{-1})	0	2.8196	$A_{B_2B_2}^{(Syr)}$ ($\times 10^{-1}$ kg^{-1})	0	2.7715
$\hat{\eta}_{Sxr}$ (%)	0.48	0.87	$\hat{\eta}_{Syr}$ (%)	1.66	0.49

Table 8.1: *Computed modal parameters of support structure*

The quality of fit is shown in Figures 8.4(a1-d1) and 8.4(a2-d2) which respectively compare the magnitudes and phases of the measured point receptances with those of the receptances reconstructed from one mode (i.e. the right hand sides of eqs. (8.1a-d)). It is evident that the correlation is satisfactory over the entire measurement frequency range.

In view of the single mode approximations of eqs. (8.1), one can compute the "effective masses" M_{xB_i}, M_{yB_i} and the "effective stiffnesses" K_{xB_i}, K_{yB_i} at B_i $(i=1,2)$ in the x and y directions respectively, from the modal parameters of Table 8.1 by using the relations:

$$M_{xB_1} = 1/A_{B_1B_1}^{(Sx1)},\ M_{xB_2} = 1/A_{B_2B_2}^{(Sx2)},\ M_{yB_1} = 1/A_{B_1B_1}^{(Sy1)},\ M_{yB_2} = 1/A_{B_2B_2}^{(Sy2)} \qquad (8.3a\text{-}d)$$

$$K_{xB_1} = \omega_{Sx1}^2 M_{xB_1},\ K_{xB_2} = \omega_{Sx2}^2 M_{xB_2},\ K_{yB_1} = \omega_{Sy1}^2 M_{yB_1},\ K_{yB_2} = \omega_{Sy2}^2 M_{yB_2} \qquad (8.4a\text{-}d)$$

The values of these parameters are given in Table 8.2.

Housing 1		Housing 2	
M_{xB_1} (kg)	3.6207	M_{xB_2} (kg)	3.5466
K_{xB_1} ($\times 10^6$ N/m)	6.25	K_{xB_2} ($\times 10^6$ N/m)	5.68
$\hat{\eta}_{xB_1} = \hat{\eta}_{Sx1}$ (%)	0.48	$\hat{\eta}_{xB_2} = \hat{\eta}_{Sx2}$ (%)	0.87
M_{yB_1} (kg)	3.5331	M_{yB_2} (kg)	3.6081
K_{yB_1} ($\times 10^6$ N/m)	6.20	K_{yB_2} ($\times 10^6$ N/m)	5.85
$\hat{\eta}_{yB_1} = \hat{\eta}_{Sy1}$ (%)	1.66	$\hat{\eta}_{yB_2} = \hat{\eta}_{Sy2}$ (%)	0.49

Table 8.2: *Alternative expression of support structure parameters*

It should be noted from Tables 8.1 and 8.2 that the estimated loss factors were not that insignificant since they ranged from 0.48 % to 1.66 %. These values correspond to equivalent viscous damping ratios of 0.24 % to 0.83 % at the corresponding resonance frequencies, which are comparable to the equivalent ratio of 1.35 % measured by Dogan [63] for the rig of Chapter 6. As in [63], this damping is deemed negligible when analysing the complete rig with the SFDs operational (section 8.3).

8.2.2 Impact Tests on Non-Rotating Rig with SFDs Locked

The aim of these tests was to estimate the bounce resonance frequencies, which are the first two resonance frequencies in each plane *xz*, *yz*. For these tests, the rotor was remounted on the support structure with the roller bearings (3) in their housings (5), as in Figure 8.1. Shims were inserted in the radial clearances (6) of the dampers. The point accelerances at the bearing housings and the transfer accelerances between them were then measured in each of

the *xz* and *yz* planes, using the same impact test technique as in section 8.2.1. The results are shown in Figures 8.5(a1,b1,c1), (a2,b2,c2) where the former refer to the *xz* plane and the latter to the *yz* plane. Each set respectively shows the measured point accelerance at B_1, point accelerance at B_2 and the transfer accelerance between B_1 and B_2. Overlaid on the same axes are the predictions using the mechanical impedance (MI) model. The model made use of the support structure parameters in Table 8.2 (see Appendix A6, section A6.2 for details). The structural damping had virtually no effect on the predicted values of the first two resonance frequencies. In Table 8.3, these frequencies are compared with the measured ones, as well as the predicted resonances with the rotor assumed to be rigid.

xz plane			*yz* plane		
mode no.	1	2	mode no.	1	2
measured (Hz)	64.0*	100.7	measured (Hz)	66.0	99.7
predicted – flex. rotor (Hz)	66.2	98.5	predicted – flex. rotor (Hz)	66.6	99.0
predicted – rigid rotor (Hz)	68.7	98.8	predicted – rigid rotor (Hz)	69.1	99.3

Table 8.3: *The first two rotor-support structure resonance frequencies with SFDs locked*
(* average of resonance frequencies of the two peaks in Figures 8.4(a1,b1,c1)

The undamped mass-normalised mode shapes of the first two rotor-support structure modes were predicted for each plane from the MI model by the modal method illustrated in Appendix A3, section A3.1. Figure 8.6(a) shows the predicted mode shapes for the vertical plane (which were similar to the ones in the horizontal plane). As can be seen, the modes were essentially bounce modes and there was virtually no flexure of the rotor in the anti-symmetric bounce mode (this latter effect was also reflected by the corresponding resonance values of Table 8.3). It is also seen that the rig is approximately symmetrical in construction.

It is noticed from Figure 8.5 that: (a) the measured symmetric bounce resonance frequency in the horizontal plane (*xz*) was not well defined, consisting of two peaks (Figures 8.5(a1,b1,c1)); in fact, the measured estimate for this frequency quoted in Table 8.3 was the average of the frequencies at the two peaks; (b) in both the *xz* and *yz* planes the value of the third resonance frequency was under-predicted and the corresponding amplitude peak was over-estimated. The fact that effect (a) was not observed in the vertical (*yz*) plane led to the conclusion that it was the result of slight "play": either between the inner and outer races of

the roller bearings, or between the damper journal and the housing, the latter play being due to imperfect shimming. In the *yz* plane, this effect must have been eliminated by the dead weight of the rotor. In the horizontal plane there is no static load to counter the play, so the micro relative movement adds an extra degree of freedom to the symmetric bounce mode, splitting the otherwise single peak into two. The effect in (b) was most probably due to the fact that the roller bearings were not self-aligning, thus resulting in flexural restraint from the suspension bars being transmitted to the rotor. This effect was not considered in the prediction. Moreover, since the third mode predominantly involved the flexural vibration of the rotor, the associated amplitude peak was overestimated due to the neglect of structural damping in the rotor. It is important to observe that these two effects (a), (b) are either insignificant, or not relevant at all when the SFDs are operational since the linear subsystem then consists of the *free-free* rotor and the *uncoupled* support structure.

8.3 MODEL APPLICATION

In this section, the equations of Chapter 5 are applied to configuration C with the SFDs operational. In this case, the linear subsystem consists of two uncoupled sub-subsystems: the free-free rotor and the support structure. In this rig, the polar moment of inertia of the rotor is sufficiently small for gyroscopic effects to be negligible over the operational range of the rotational speed. Hence, in the linear subsystem, the *xz* and *yz* planes are uncoupled for the rotor, as well as the support structure. The SFDs are assumed to be the only sources of damping. As a result of the above simplifying assumptions, the $P_N \times 1$ vector $\mathbf{f}_N$ (eq. (5.3)) is identical for both the frequency domain (receptance harmonic balance (RHB)) and the time domain (modal analysis) approaches:

$$\mathbf{f}_N = \begin{bmatrix} Q_{x1} & Q_{y1} & Q_{x2} & Q_{y2} & -Q_{x1} & -Q_{y1} & -Q_{x2} & -Q_{y2} \end{bmatrix}^T \tag{8.5}$$

where $P_N = 8$. $Q_{x1,y1}$ are the SFD forces on J_1 and $Q_{x2,y2}$ are those on J_2. $-Q_{x1,y1}$, $-Q_{x2,y2}$ are the SFD forces on B_1 and B_2 respectively. The SFD forces are calculated from equations (5.2a,b). The unbalance forces $P_{x1,y1}$ and $P_{x2,y2}$ at U_1 and U_2 are given by eqs. (5.1a,b) with γ_1 set to zero. The true sense of the rig rotation is shown in the upper left hand corner of Figure 8.1, and is opposite to that in Figure 5.1(b). Since the rotational speed Ω is always taken as positive, the *x* component of the final results for the computed vibration is reversed,

in accordance to the frame of reference in Figure 8.1. The free-free rotor is degenerate, having in each plane *xz*, *yz* two modes defining non-oscillatory rigid body motion: pure translation at the speed of the mass centre G and pure rotation about G (see Figure 8.6(b)). Hence, the static load of the rotor needs to be taken into account. The vector $\mathbf{u}_N$ of degrees of freedom associated with $\mathbf{f}_N$ is then given by eq. (5.12).

$$\mathbf{u}_N = \mathbf{h} = \left[X_{J_1} \quad Y_{J_1} \quad X_{J_2} \quad Y_{J_2} \quad X_{B_1} \quad Y_{B_1} \quad X_{B_2} \quad Y_{B_2}\right]^T \tag{8.6}$$

where each displacement is measured from the static position of the corresponding housing centre without the rotor weight applied. The distributed rotor load can be replaced by two loads W_1 and W_2 concentrated at J_1 and J_2 where:

$$W_1 = W_R l_{GJ_2} / l_{J_1J_2}, \quad W_2 = W_R l_{GJ_1} / l_{J_1J_2} \tag{8.7a,b}$$

W_R is the total rotor weight, l_{GJ_1} and l_{GJ_2} are the distances of the mass centre G from J_1 and J_2 respectively, and $l_{J_1J_2}$ is the distance between J_1 and J_2. The zero frequency components of the forces on the vibrating rotor are in a state of static equilibrium, as explained in Chapter 5 (end of section 5.3). Since this zero frequency equilibrium problem is statically determinate, the equivalent load system of eqs. (8.7) is exact. However, with this load system, the resulting zero frequency shape of the vibrating rotor will be a straight (undeformed) line joining the mean positions of J_1 and J_2 for the *yz* plane, as well as the *xz* plane, since the zero frequency forces are all concentrated at J_1 and J_2. The superposition on this line of the static deflection curve of the rotor supported at the mean positions of J_1 and J_2, due to the distributed weight, yields the precise zero frequency shape for the *yz* plane. However, this refinement is unnecessary since it has no effect on the mean positions of J_1 and J_2, which are the only zero frequency components of rotor vibration that are of interest.

In the RHB approach

$$X_{J_i} = \overline{X}_{J_i} + \sum_{s=1}^{m}\left(a_{XJ_i}^{(s)} \cos s\varpi t + b_{XJ_i}^{(s)} \sin s\varpi t\right), \; Y_{J_i} = \overline{Y}_{J_i} + \sum_{s=1}^{m}\left(a_{YJ_i}^{(s)} \cos s\varpi t + b_{YJ_i}^{(s)} \sin s\varpi t\right) \tag{8.8a,b}$$

$$X_{B_i} = \overline{X}_{B_i} + \sum_{s=1}^{m}\left(a_{XB_i}^{(s)} \cos s\varpi t + b_{XB_i}^{(s)} \sin s\varpi t\right), \; Y_{B_i} = \overline{Y}_{B_i} + \sum_{s=1}^{m}\left(a_{YB_i}^{(s)} \cos s\varpi t + b_{YB_i}^{(s)} \sin s\varpi t\right) \tag{8.8c,d}$$

and

$$Q_{xi} = \overline{Q}_{xi} + \sum_{s=1}^{m} \left(p_{xi}^{(s)} \cos s\varpi t + q_{xi}^{(s)} \sin s\varpi t \right),\ Q_{yi} = \overline{Q}_{yi} + \sum_{s=1}^{m} \left(p_{yi}^{(s)} \cos s\varpi t + q_{yi}^{(s)} \sin s\varpi t \right) \quad (8.9a,b)$$

where

$$\begin{bmatrix} \overline{Q}_{xi} \\ \overline{Q}_{yi} \end{bmatrix} = \frac{1}{\Gamma} \int_0^{\Gamma} \begin{bmatrix} Q_{xi} \\ Q_{yi} \end{bmatrix} dt\,,\ \begin{bmatrix} p_{xi}^{(s)} \\ p_{yi}^{(s)} \end{bmatrix} = \frac{2}{\Gamma} \int_0^{\Gamma} \begin{bmatrix} Q_{xi} \\ Q_{yi} \end{bmatrix} \cos s\varpi t\ dt\,,\ \begin{bmatrix} q_{xi}^{(s)} \\ q_{yi}^{(s)} \end{bmatrix} = \frac{2}{\Gamma} \int_0^{\Gamma} \begin{bmatrix} Q_{xi} \\ Q_{yi} \end{bmatrix} \sin s\varpi t\ dt \quad (8.10a\text{-}c)$$

In the above equations, $\Gamma = 2\pi/\varpi = NT$ (eq. (5.8b)) and $i = 1, 2$. For the degenerate rotor, 4 zero frequency static equilibrium equations can be written (Chapter 5, end of section 5.3):

$$0 = \breve{\alpha}_{J_1J_1}(0)\overline{Q}_{x1} + \breve{\alpha}_{J_1J_2}(0)\overline{Q}_{x2},\ 0 = \breve{\beta}_{J_1J_1}(0)(\overline{Q}_{y1} - W_1) + \breve{\beta}_{J_1J_2}(0)(\overline{Q}_{y2} - W_2) \quad (8.11a,b)$$

$$0 = \breve{\alpha}_{J_2J_1}(0)\overline{Q}_{x1} + \breve{\alpha}_{J_2J_2}(0)\overline{Q}_{x2},\ 0 = \breve{\beta}_{J_2J_1}(0)(\overline{Q}_{y1} - W_1) + \breve{\beta}_{J_2J_2}(0)(\overline{Q}_{y2} - W_2) \quad (8.11c,d)$$

where $\breve{\alpha}_{J_iJ_j}(0) = \breve{\beta}_{J_iJ_j}(0)$ are the zero frequency values of the accelerance functions of the linear subsystem, relating the forces at J_j ($j = 1, 2$) in the x and y directions respectively with the acceleration response in the corresponding directions at J_i ($i = 1, 2$). Since the inverse of the matrix $\begin{bmatrix} \breve{\alpha}_{J_1J_1}(0) & \breve{\alpha}_{J_1J_2}(0) \\ \breve{\alpha}_{J_2J_1}(0) & \breve{\alpha}_{J_2J_2}(0) \end{bmatrix}$ exists, eqs. (8.11) are seen to reduce to $\overline{Q}_{x1} = 0$, $\overline{Q}_{x2} = 0$, $\overline{Q}_{y1} - W_1 = 0$, $\overline{Q}_{y2} - W_2 = 0$. Hence, defining

$$\delta_{Ns} = \begin{cases} 0 & s \neq N \\ 1 & s = N \end{cases} \quad (8.12)$$

the complete set of RHB equations (5.14) can be written as:

$$\overline{Q}_{x1}=0,\quad \overline{Q}_{y1}-W_1=0,\quad \overline{Q}_{x2}=0,\quad \overline{Q}_{y2}-W_2=0$$

$$\overline{X}_{B_1}=-\alpha_{B_1B_1}(0)\overline{Q}_{x1},\quad \overline{Y}_{B_1}=-\beta_{B_1B_1}(0)\overline{Q}_{y1},\quad \overline{X}_{B_2}=-\alpha_{B_2B_2}(0)\overline{Q}_{x2},\quad \overline{Y}_{B_2}=-\beta_{B_2B_2}(0)\overline{Q}_{y2}$$

(8.13a1-a8)

$$a_{XJ_1}^{(s)}=\alpha_{J_1J_1}(s\varpi)p_{x1}^{(s)}+\alpha_{J_1J_2}(s\varpi)p_{x2}^{(s)}+\delta_{Ns}\alpha_{J_1U_2}(s\varpi)U_2\Omega^2\sin\gamma_2$$

$$a_{YJ_1}^{(s)}=\beta_{J_1J_1}(s\varpi)p_{y1}^{(s)}+\beta_{J_1J_2}(s\varpi)p_{y2}^{(s)}-\delta_{Ns}\beta_{J_1U_1}(s\varpi)U_1\Omega^2-\delta_{Ns}\beta_{J_1U_2}(s\varpi)U_2\Omega^2\cos\gamma_2$$

$$a_{XJ_2}^{(s)}=\alpha_{J_2J_1}(s\varpi)p_{x1}^{(s)}+\alpha_{J_2J_2}(s\varpi)p_{x2}^{(s)}+\delta_{Ns}\alpha_{J_2U_2}(s\varpi)U_2\Omega^2\sin\gamma_2$$

$$a_{YJ_2}^{(s)}=\beta_{J_2J_1}(s\varpi)p_{y1}^{(s)}+\beta_{J_2J_2}(s\varpi)p_{y2}^{(s)}-\delta_{Ns}\beta_{J_2U_1}(s\varpi)U_1\Omega^2-\delta_{Ns}\beta_{J_2U_2}(s\varpi)U_2\Omega^2\cos\gamma_2$$

$$a_{XB_1}^{(s)}=-\alpha_{B_1B_1}(s\varpi)p_{x1}^{(s)},\quad a_{YB_1}^{(s)}=-\beta_{B_1B_1}(s\varpi)p_{y1}^{(s)},$$

$$a_{XB_2}^{(s)}=-\alpha_{B_2B_2}(s\varpi)p_{x2}^{(s)},\quad a_{YB_2}^{(s)}=-\beta_{B_2B_2}(s\varpi)p_{y2}^{(s)}$$

where $s=1\ldots m$ (8.13b1-b8)

$$b_{XJ_1}^{(s)}=\alpha_{J_1J_1}(s\varpi)q_{x1}^{(s)}+\alpha_{J_1J_2}(s\varpi)q_{x2}^{(s)}+\delta_{Ns}\alpha_{J_1U_1}(s\varpi)U_1\Omega^2+\delta_{Ns}\alpha_{J_1U_2}(s\varpi)U_2\Omega^2\cos\gamma_2$$

$$b_{YJ_1}^{(s)}=\beta_{J_1J_1}(s\varpi)q_{y1}^{(s)}+\beta_{J_1J_2}(s\varpi)q_{y2}^{(s)}+\delta_{Ns}\beta_{J_1U_2}(s\varpi)U_2\Omega^2\sin\gamma_2$$

$$b_{XJ_2}^{(s)}=\alpha_{J_2J_1}(s\varpi)q_{x1}^{(s)}+\alpha_{J_2J_2}(s\varpi)q_{x2}^{(s)}+\delta_{Ns}\alpha_{J_2U_1}(s\varpi)U_1\Omega^2+\delta_{Ns}\alpha_{J_2U_2}(s\varpi)U_2\Omega^2\cos\gamma_2$$

$$b_{YJ_2}^{(s)}=\beta_{J_2J_1}(s\varpi)q_{y1}^{(s)}+\beta_{J_2J_2}(s\varpi)q_{y2}^{(s)}+\delta_{Ns}\beta_{J_2U_2}(s\varpi)U_2\Omega^2\sin\gamma_2$$

$$b_{XB_1}^{(s)}=-\alpha_{B_1B_1}(s\varpi)q_{x1}^{(s)},\quad b_{YB_1}^{(s)}=-\beta_{B_1B_1}(s\varpi)q_{y1}^{(s)},$$

$$b_{XB_2}^{(s)}=-\alpha_{B_2B_2}(s\varpi)q_{x2}^{(s)},\quad b_{YB_2}^{(s)}=-\beta_{B_2B_2}(s\varpi)q_{y2}^{(s)}$$

where $s=1\ldots m$ (8.13c1-c8)

In the above equations, $\alpha_{PQ}(\omega)$, $\beta_{PQ}(\omega)$ are the receptance functions at frequency ω rad/s of the linear subsystem, relating the forces at position Q in the x and y directions respectively with the displacement responses in the corresponding directions at position P. Note that for points P and Q situated on the rotor and support structure respectively or vice versa, $\alpha_{PQ}(\omega)$, $\beta_{PQ}(\omega)=0$. Also, eqs. (8.13a5-a8), (8.13b5-b8), (8.13c5-c8) neglect the cross-coupling between B_1 and B_2 i.e. $\alpha_{B_iB_j}(\omega)$, $\beta_{B_iB_j}(\omega)=0$ for $i\neq j$ $(i,j=1,2)$. All receptance functions are real and independent of rotational speed due to the neglect of linear damping and gyroscopic effects. Also, for points P_R, Q_R on the rotor, $\alpha_{P_RQ_R}(\omega)=\beta_{P_RQ_R}(\omega)$ (rotor isotropic). From eqs. (8.1), (8.3) and (8.4), the (undamped) support receptances are given by:

$$\alpha_{B_iB_i}(\omega)=1/\left(K_{xB_i}-M_{xB_i}\omega^2\right),\quad \beta_{B_iB_i}(\omega)=1/\left(K_{yB_i}-M_{yB_i}\omega^2\right) \tag{8.14a,b}$$

The values of M_{xB_i}, M_{yB_i} used in eqs. (8.14) are higher than those quoted in Table 8.2 due to the additional mass of the housing end-plates, rotor probe brackets (marked (12) in Figure 8.1), and their probes (the revised values of the masses are found in Appendix A6, section A6.3). The rotor receptances are evaluated using the mechanical impedance (MI) technique [19], and the MI model for the rotor is described in Appendix A2, section A2.3. For solution, eqs. (8.13) are expressed in the form $\mathbf{p}\left(\hat{\mathbf{v}},\hat{\Omega}\right)=\mathbf{0}$ of eq. (5.18) by bringing all the terms to one side of the equality signs. $\hat{\mathbf{v}}=\mathbf{v}/c$ where $\mathbf{v}$ is the $8(2m+1)\times 1$ vector of the unknown Fourier coefficients of the SFD displacements $\overline{X}_{J_i}$, $a_{XJ_i}^{(s)}$, $b_{XJ_i}^{(s)}$, $\overline{Y}_{J_i}$, $a_{YJ_i}^{(s)}$, $b_{YJ_i}^{(s)}$, $\overline{X}_{B_i}$, $a_{XB_i}^{(s)}$, $b_{XB_i}^{(s)}$, $\overline{Y}_{B_i}$, $a_{YB_i}^{(s)}$, $b_{YB_i}^{(s)}$ for $i=1,2$ and $s=1\ldots m$. $\hat{\Omega}=\Omega/\omega_0$ where ω_0 is arbitrarily chosen as the symmetric bounce mode frequency, $2\pi\times 66$ rad/s. The resulting system is then solved using the arc-length continuation method (section 5.3, pages 63-64), using the iterative algorithm in Appendix A1 to trace out a speed response curve of NT - periodic solutions, where N is of fixed value. For each such solution, the Fourier coefficients of the SFD forces are known. The Fourier coefficients of the response at an arbitrary position P_R on the rotor

$$X_{P_R}=\overline{X}_{P_R}+\sum_{s=1}^{m}\left(a_{XP_R}^{(s)}\cos s\varpi t+b_{XP_R}^{(s)}\sin s\varpi t\right),\ Y_{P_R}=\overline{Y}_{P_R}+\sum_{s=1}^{m}\left(a_{YP_R}^{(s)}\cos s\varpi t+b_{YP_R}^{(s)}\sin s\varpi t\right) \tag{8.15a,b}$$

can be determined as follows:

(a) In each of eqs. (8.13b1,b2) and (8.13c1,c2) replace the subscript J_1 by P_R on the left hand side and replace the first subscript J_1 by P_R in the receptance terms of the right hand side. The right hand sides of the modified equations can then be evaluated to yield the dynamic Fourier coefficients in eqs. (8.15).

(b) The mean terms $\overline{X}_{P_R}$, $\overline{Y}_{P_R}$ in eqs. (8.15) can be found by considering the straight line joining the mean positions $\left(\overline{X}_{J_1},\overline{Y}_{J_1}\right)$, $\left(\overline{X}_{J_2},\overline{Y}_{J_2}\right)$ at the SFDs, as explained previously:

$$\overline{X}_{P_R}=\overline{X}_{J_1}+\left(\frac{\overline{X}_{J_2}-\overline{X}_{J_1}}{l_{J_1J_2}}\right)l_{P_RJ_1},\ \overline{Y}_{P_R}=\overline{Y}_{J_1}+\left(\frac{\overline{Y}_{J_2}-\overline{Y}_{J_1}}{l_{J_1J_2}}\right)l_{P_RJ_1} \tag{8.16a,b}$$

where $l_{P_R J_1}$ is the displacement of P_R from J_1 in the positive z direction.

For this application, P_R corresponds to J_{1m} or J_{2m} (Figure 8.1), and the mean terms there are calculated since, for measurement purposes, these locations are substitutes for the actual SFD positions.

For the time domain equations of motion, a total of $H = 10$ modes of the undamped non-rotating linear subsystem are considered. These comprise:

(a) 3 modes of the free-free rotor in each of the xz and yz planes with natural frequencies ω_{Rxr}, ω_{Ryr}, $r = 1...3$. $\phi_{P_R}^{(Rxr)}$, $\phi_{P_R}^{(Ryr)}$ are the corresponding mass-normalised mode shapes evaluated at position P_R in the x and y directions respectively. Since the rotor is isotropic, $\omega_{Rxr} = \omega_{Ryr}$ and $\phi_{P_R}^{(Rxr)} = \phi_{P_R}^{(Ryr)}$. As explained previously, for each plane, the first two modes define non-oscillatory rigid body motion, so that $\omega_{Rxr}, \omega_{Ryr} = 0$, $r = 1, 2$. The third mode is the first bending mode of the rotor (see Figure 8.6(b)).

(b) 2 modes of the support structure alone in each of the xz and yz planes, with natural frequencies ω_{Sxr}, ω_{Syr}, $r = 1, 2$, where, for each plane, the vibration of one housing is uncoupled from that of the other housing, as explained in section 8.2.1.

Hence, the modal coordinate vector $\mathbf{q}$ (eq. (5.29)) and the matrix $\mathbf{D}$ (eq. (5.31)) are written as

$$\mathbf{q} = \begin{bmatrix} q_{Rx1} & q_{Ry1} & q_{Rx2} & q_{Ry2} & q_{Rx3} & q_{Ry3} & q_{Sx1} & q_{Sy1} & q_{Sx2} & q_{Sy2} \end{bmatrix}^T \tag{8.17}$$

$$\mathbf{D} = \mathbf{diag}\begin{bmatrix} \omega_{Rx1}^2 & \omega_{Ry1}^2 & \omega_{Rx2}^2 & \omega_{Ry2}^2 & \omega_{Rx3}^2 & \omega_{Ry3}^2 & \omega_{Sx1}^2 & \omega_{Sy1}^2 & \omega_{Sx2}^2 & \omega_{Sy2}^2 \end{bmatrix}^T \tag{8.18}$$

The modal equations are then given by:

$$\ddot{q}_{Rxr} + \omega_{Rxr}^2 q_{Rxr} = \phi_{J_1}^{(Rxr)} Q_{x1} + \phi_{J_2}^{(Rxr)} Q_{x2} + \phi_{U_1}^{(Rxr)} P_{x1} + \phi_{U_2}^{(Rxr)} P_{x2}$$

$$\ddot{q}_{Ryr} + \omega_{Ryr}^2 q_{Ryr} = \phi_{J_1}^{(Ryr)} \left(Q_{y1} - W_1\right) + \phi_{J_2}^{(Ryr)} \left(Q_{y2} - W_2\right) + \phi_{U_1}^{(Ryr)} P_{y1} + \phi_{U_2}^{(Ryr)} P_{y2},$$

where $r = 1...3$ (8.19a,b)

$$\ddot{q}_{Sx1} + \omega_{Sx1}^2 q_{Sx1} = -\phi_{B_1}^{(Sx1)} Q_{x1} \tag{8.19c}$$

$$\ddot{q}_{Sy1} + \omega_{Sy1}^2 q_{Sy1} = -\phi_{B_1}^{(Sy1)} Q_{y1} \tag{8.19d}$$

$$\ddot{q}_{Sx2} + \omega_{Sx2}^2 q_{Sx2} = -\phi_{B_2}^{(Sx2)} Q_{x2} \tag{8.19e}$$

$$\ddot{q}_{Sy2} + \omega_{Sy2}^2 q_{Sy2} = -\phi_{B_2}^{(Sy2)} Q_{y2} \tag{8.19f}$$

For the computation of the instantaneous SFD forces Q_{xi}, Q_{yi} $(i=1,2)$ from eqs. 5.2(a,b), the instantaneous non-linear degrees of freedom $\mathbf{u}_N$ (eq. (8.6)) are required. These are expressed in terms of the modal coordinate vector $\mathbf{q}$ of eq. (8.17) by the reduced transformation $\mathbf{u}_N = \mathbf{H}_N\mathbf{q}$ (eq. (5.34)) where the reduced modal matrix $\mathbf{H}_N$ (eq. (5.33) is given by the 8×10 matrix:

$$\mathbf{H}_N = \begin{bmatrix} \begin{bmatrix} \phi_{J_1}^{(Rx1)} & 0 & \phi_{J_1}^{(Rx2)} & 0 & \phi_{J_1}^{(Rx3)} & 0 \\ 0 & \phi_{J_1}^{(Ry1)} & 0 & \phi_{J_1}^{(Ry2)} & 0 & \phi_{J_1}^{(Ry3)} \\ \phi_{J_2}^{(Rx1)} & 0 & \phi_{J_2}^{(Rx2)} & 0 & \phi_{J_2}^{(Rx3)} & 0 \\ 0 & \phi_{J_2}^{(Ry1)} & 0 & \phi_{J_2}^{(Ry2)} & 0 & \phi_{J_2}^{(Ry3)} \end{bmatrix} & \mathbf{0}_{4\times4} \\ \mathbf{0}_{4\times6} & \mathbf{diag}\left[\phi_{B_1}^{(Sx1)} \quad \phi_{B_1}^{(Sy1)} \quad \phi_{B_2}^{(Sx2)} \quad \phi_{B_2}^{(Sy2)}\right] \end{bmatrix} \tag{8.20}$$

where $\mathbf{0}_{i\times j}$ is defined as a zero matrix of size $i\times j$. The first six columns of $\mathbf{H}_N$ pertain to the modes of the rotor, alternately in the *xz* and *yz* planes. The last four rows of these columns correspond to the values of the non-linear degrees of freedom at the two housings in these modes and so are all zero. The remaining four columns of $\mathbf{H}_N$ pertain to the modes of the support structure, alternately in the *xz* and *yz* planes. The first four rows of these columns correspond to the values of the non-linear degrees of freedom at the two journals in these modes and so are all zero.

The evaluation of the modal parameters of the rotor is described in Appendix A3, sections A3.1, A3.3. The non-zero natural frequency ω_{Rx3} is determined from the mechanical impedance frequency response functions. The required mode shapes are then determined by fitting 3 modes to the exact receptance functions $\alpha_{P_RQ_R}(\omega)$ (computed by MI) [47]. A typical example of the quality of fit is given in Figures 8.7(a,b), which respectively compare the exact receptances $\alpha_{J_2J_2}(\omega)$, $\alpha_{J_1J_2}(\omega)$ with the approximate ones reconstructed from 3 modes. It is seen that satisfactory agreement prevails over a frequency range of 0 Hz to 500 Hz, covering nearly 5 harmonics of the top rotational speed. It is also evident that the flexure mode introduces an anti-resonance at the relatively low frequency of 280 Hz. The omission of this mode would result in serious error to the third and higher harmonics of the rotational speed around the anti-symmetric bounce critical speed of the complete rig (around 100 rev/s), despite the fact that the rotor has virtually no deformation in the anti-symmetric

bounce mode (Figure 8.6(a)). More illustrations on the quality of fit are given in Appendix A3, Figure A3.1. These illustrations, together with those of Figure 8.7, cover all the rotor receptance functions used in the RHB approach of equations (8.13).

The modal parameters used for the support structure are slightly different from those in Table 8.1 due to additional mass added to the housings. The final values of these parameters are found in Appendix A6, section A6.3.

Equations (8.19) are ready for numerical integration from given initial conditions for the time domain response. Prior to integration, these equations are non-dimensionalised and expressed as a set of first order differential equations, as illustrated in Appendix A4, section A4.2. The instantaneous x and y response at an arbitrary position P_R on the rotor is given in terms of the modal coordinates by the appropriate pair of rows of the transformation of eq. (5.28), $\mathbf{u} = \mathbf{Hq}$, and thus necessitates the knowledge of $\phi_{P_R}^{(Rxr)}$, $\phi_{P_R}^{(Ryr)}$, $r = 1 \ldots 3$.

For stability and bifurcation analysis of the RHB response, the matrices $\partial \mathbf{f}_N / \partial \mathbf{u}_N$, $\partial \mathbf{f}_N / \partial \mathbf{u}'_N$ in the expression for $\mathbf{W}(\tau)$ (eqs. (5.44), (5.45)) are required. From eqs. (8.5) and (8.6):

$$\frac{\partial \mathbf{f}_N}{\partial \mathbf{u}_N} = \begin{bmatrix} \frac{\partial Q_{x1}}{\partial X_{J_1}} & \frac{\partial Q_{x1}}{\partial Y_{J_1}} & \frac{\partial Q_{x1}}{\partial X_{J_2}} & \frac{\partial Q_{x1}}{\partial Y_{J_2}} & \frac{\partial Q_{x1}}{\partial X_{B_1}} & \frac{\partial Q_{x1}}{\partial Y_{B_1}} & \frac{\partial Q_{x1}}{\partial X_{B_2}} & \frac{\partial Q_{x1}}{\partial Y_{B_2}} \\ \vdots & \vdots & \vdots & \vdots & \vdots & \vdots & \vdots & \vdots \\ -\frac{\partial Q_{y2}}{\partial X_{J_1}} & -\frac{\partial Q_{y2}}{\partial Y_{J_1}} & -\frac{\partial Q_{y2}}{\partial X_{J_2}} & -\frac{\partial Q_{y2}}{\partial Y_{J_2}} & -\frac{\partial Q_{y2}}{\partial X_{B_1}} & -\frac{\partial Q_{y2}}{\partial Y_{B_1}} & -\frac{\partial Q_{y2}}{\partial X_{B_2}} & -\frac{\partial Q_{y2}}{\partial Y_{B_2}} \end{bmatrix}$$

Now $\partial Q_{xi,yi}/\partial X_{J_j}, \partial Q_{xi,yi}/\partial Y_{J_j}, \partial Q_{xi,yi}/\partial X_{B_j}, \partial Q_{xi,yi}/\partial Y_{B_j} = 0$ when $i \neq j$. Also, from eqs. (5.2a,b), $Q_{xi,yi} = Q_{x,y}\left(X_{rel_i}, Y_{rel_i}, \dot{X}_{rel_i}, \dot{Y}_{rel_i}\right)$, where $X_{rel_i} = X_{J_i} - X_{B_i}$, ... etc. Hence, $\partial Q_{xi,yi}/\partial X_{J_i} = \partial Q_{xi,yi}/\partial X_{rel_i}$, $\partial Q_{xi,yi}/\partial Y_{J_i} = \partial Q_{xi,yi}/\partial Y_{rel_i}$, $\partial Q_{xi,yi}/\partial X_{B_i} = -\partial Q_{xi,yi}/\partial X_{rel_i}$, $\partial Q_{xi,yi}/\partial Y_{B_i} = -\partial Q_{xi,yi}/\partial Y_{rel_i}$. A similar process applies for $\partial \mathbf{f}_N / \partial \mathbf{u}'_N$. Hence,

$$\frac{\partial \mathbf{f}_N}{\partial \mathbf{u}_N} = \begin{bmatrix} \mathbf{J}_{Q1} & \mathbf{0}_{2\times2} & -\mathbf{J}_{Q1} & \mathbf{0}_{2\times2} \\ \mathbf{0}_{2\times2} & \mathbf{J}_{Q2} & \mathbf{0}_{2\times2} & -\mathbf{J}_{Q2} \\ -\mathbf{J}_{Q1} & \mathbf{0}_{2\times2} & \mathbf{J}_{Q1} & \mathbf{0}_{2\times2} \\ \mathbf{0}_{2\times2} & -\mathbf{J}_{Q2} & \mathbf{0}_{2\times2} & \mathbf{J}_{Q2} \end{bmatrix}, \quad \frac{\partial \mathbf{f}_N}{\partial \mathbf{u}'_N} = \begin{bmatrix} \breve{\mathbf{J}}_{Q1} & \mathbf{0}_{2\times2} & -\breve{\mathbf{J}}_{Q1} & \mathbf{0}_{2\times2} \\ \mathbf{0}_{2\times2} & \breve{\mathbf{J}}_{Q2} & \mathbf{0}_{2\times2} & -\breve{\mathbf{J}}_{Q2} \\ -\breve{\mathbf{J}}_{Q1} & \mathbf{0}_{2\times2} & \breve{\mathbf{J}}_{Q1} & \mathbf{0}_{2\times2} \\ \mathbf{0}_{2\times2} & -\breve{\mathbf{J}}_{Q2} & \mathbf{0}_{2\times2} & \breve{\mathbf{J}}_{Q2} \end{bmatrix} \tag{8.21}$$

where

$$\mathbf{J}_{Qi} = \begin{bmatrix} \dfrac{\partial Q_{xi}}{\partial X_{rel_i}} & \dfrac{\partial Q_{xi}}{\partial Y_{rel_i}} \\ \dfrac{\partial Q_{yi}}{\partial X_{rel_i}} & \dfrac{\partial Q_{yi}}{\partial Y_{rel_i}} \end{bmatrix}, \quad \breve{\mathbf{J}}_{Qi} = \begin{bmatrix} \dfrac{\partial Q_{xi}}{\partial X'_{rel_i}} & \dfrac{\partial Q_{xi}}{\partial Y'_{rel_i}} \\ \dfrac{\partial Q_{yi}}{\partial X'_{rel_i}} & \dfrac{\partial Q_{yi}}{\partial Y'_{rel_i}} \end{bmatrix}, \quad i = 1,\ 2 \qquad (8.22a,b)$$

and $(\,)'$ is $d(\,)/d\tau$, $\tau = \varpi t$ (ϖ rad/s being the fundamental frequency of the periodic solution). The partial derivatives in eqs. (8.22) are evaluated numerically at the RHB-computed periodic solution from the expressions for $Q_{xi,yi}$ in eqs. (5.2) and (4.6). The above expressions, along with the expressions for $\mathbf{H}_N$ (eq. 8.20) and $\mathbf{D}$ (eq. (8.18)) determine the expression for $\mathbf{W}(\tau)$ in eqs. (5.44), (5.45), from which the monodromy matrix $\mathbf{G}$ of the periodic solution is computed, using eq. (3.22).

The equations presented in this section are processed as discussed in section 5.7 of Chapter 5.

8.4 EXPERIMENTAL WORK

For this work, the shims were removed from the radial clearances of the dampers and their oil supply restored. The rig was run under unbalance conditions in the speed range 20 rev/s to 110 rev/s and vibration data acquired at each speed in steps of 2 rev/s. The oil supply pressure p_S to both dampers was kept constant at 34.5×10^3 Pa. This pressure was sufficient to fill both clearances. Preliminary experiments were conducted without unbalance masses attached, in order to examine the influence of the small residual unbalance left after the rotor was balanced in the first commissioning period. Experiments were then conducted with unbalance masses attached at U_2 only (see Figure 8.1) and then with symmetrically disposed equal masses attached at both U_1 and U_2. In this thesis, emphasis is placed on the former case since this represents a general unbalance condition in which both symmetric and anti-symmetric bounce modes are excited. A summary of the experiments discussed in this thesis is given in Table 8.4.

Experiment No.	U_1 ($\times 10^{-4}$ kgm)	U_2 ($\times 10^{-4}$ kgm)	γ_2	$\overline{Temp_1}$ (° C)	$\overline{\mu}_1$ ($\times 10^{-3}$ Nsm^{-2})	$\overline{Temp_2}$ (° C)	$\overline{\mu}_2$ ($\times 10^{-3}$ Nsm^{-2})
1	0	7.065975	0	36	9.85	35	10.17
2	0	10.735900	0	37	9.53	34	10.57
3	0	13.146000	0	36	9.85	33	10.98
4	10.735900	10.735900	0	36	9.85	34	10.57

Table 8.4: *Summary of unbalance response experiments for test rig C*

With reference to this table:

- $\overline{Temp_i}$ and $\overline{\mu}_i$ $(i = 1, 2)$ are, respectively, the average oil temperature and the oil viscosity at that temperature for SFD no. i. The viscosity values $\overline{\mu}_i$ were used in the analytical treatment.
- The resultant unbalance mass attached at position U_k $(k = 1, 2)$ is given by U_k / r_U where the unbalance radius $r_U = 54.775 \times 10^{-3}$ m.
- γ_2 is the phase angle of unbalance U_2 relative to U_1 as described in Figure 5.1(b).
- The acquisitions were conducted both on run-up and run-down in rig speed.

Vibration in the x and y directions was measured by displacement probe pairs at J_{1m}, B_1, J_{2m} and B_2 (Figure 8.1). As explained in section 8.2, the probes at J_{1m} and J_{2m} measured displacements relative to B_1 and B_2 respectively, whereas those at B_1 and B_2 measured displacements relative to the machine frame, which were taken as absolute for the purpose of comparison with theory. The probes were connected through voltage amplifiers to a PC-operated *Hewlett Packard HP* 35650® spectrum analyser, which was set to acquire data in the form of a time history. The speed was measured using an optical sensor connected to a tachometer. The sensor was targeted at a section of the rotor close to F_1 (Figure 8.1), which was painted black all round except for two diametrically opposed white strips aligned with the unbalance. Hence, the output of the tachometer was two rectangular pulses per shaft revolution. This signal was fed to a digital frequency meter, its reading being divided by 2 to give the speed. The speed fluctuation was within ± 0.5 rev/s. Since the time capture length of the vibration was 2 s, the fluctuation was within the resolution of the frequency spectrum of the acquisition (i.e. 0.5 Hz). The tachometer pulse was also fed to the spectrum analyser for acquisition, in order to obtain knowledge of the phase of the vibration time histories

relative to the unbalance. Since the *HP* 35650® analyser had a maximum of 8 channels and 9 signals needed to be acquired, two such analysers, each with its own PC, had to be used. The analysers were linked together by a common input from an instrumented hammer. This is illustrated in the instrumentation diagram of Figure A6.3 in Appendix A6, section A6.4. At each speed, data were acquired by both analysers simultaneously upon being triggered by a light tap from the hammer applied by the experimenter to the desk. The frequency range was 0-1.6 kHz and the sampling rate of the analysers was thus $2.56 \times 1.6 = 4096$ samples/s, to avoid aliassing in subsequent spectral analysis. Further details of the instrumentation are given in Appendix A6, section A6.4. The data were converted from standard format to *MATLAB*® format and processed for frequency spectra, vibration orbits, and peak-to-peak displacements. Poincaré maps could also be constructed from the time records through the knowledge of the tachometer pulse signals. Since the time record length was 2 s, the number of samples in the map at a given speed S rev/s was limited to $2S \pm 1$.

The rotor probes at J_{1m} and J_{2m} (Figure 8.1) revealed a run-out when the shaft was rotated at very low speed. This was due to the non-uniformity of the shaft radius ("lack of roundness") and so, was termed "geometric run-out". The run-out was significant for the position J_{2m}, as can be seen from Figure 8.8(a). This figure shows the alternating ("ac") component of the y versus x "orbit" recorded by the probes at J_{2m} over 2 s at a speed of 3 rev/s. This "orbit" did not define vibration, but actually defined the fluctuation in the shaft profile at J_{2m}. The "ac" x and y signals are shown in Figure 8.8(b) with the tachometer pulse signal superimposed, the distance between the tachometer pulse edges UU, VV defining one shaft revolution. The x and y signals were periodic at the period of rotation and practically identical except for an offset of a quarter period (allowing for the sign convention used for the x and y fluctuations). From Figure 8.8(a), it is seen that the peak fluctuation in shaft radius at J_{2m} (taken as half the peak-to-peak fluctuation) amounted to 16 % of the radial clearance or 0.0007", which was comparable to the machining tolerance for the shaft. Knowing the x and y geometric run-outs at J_{1m} and J_{2m} at a reference speed (~3 rev/s), as well as the associated tachometer pulse signal, the x and y geometric run-outs at any speed S rev/s could be constructed from the tachometer pulse signal at S rev/s. This enabled a correction to be made to the vibration recordings at J_{1m} and J_{2m} at S rev/s. For each location J_{1m} and J_{2m}, a "reference" profile for the x run-out was formed by taking a portion of the profile of the corresponding x run-out at 3 rev/s between an arbitrarily chosen pair of tachometer pulse edges UU, VV, covering one shaft revolution (Figure 8.8(b)). This profile was then uniformly shrunk along its time base to fit the space between each consecutive pair of similar

edges UU, VV in the tachometer pulse signal at S rev/s, thus constructing the x run-out at this speed (see Figure 8.9 where $S = 60$ rev/s). Any remaining gaps at the beginning and end of the time history were filled by continuing the constructed periodic waveform backward and forward respectively. A similar process was followed for the y run-out. The x (y) run-outs at S rev/s at J_{1m}, J_{2m} were then subtracted from the corresponding x (y) displacement probe readings to obtain the true vibration signatures at J_{1m} and J_{2m}. The method described in Figure 8.9 did not depend on the knowledge of the values of the speed S and the reference speed (~3 rev/s) and thus avoided cumulative errors in phase that would otherwise occur due to inevitable uncertainty in the precise values of the speeds. Moreover, minor fluctuations in speed, which resulted in variations in T (Figure 8.9) from one pair of pulse edges UU, VV to the other, were accommodated by the method since the reference profile was "custom" fitted to each pair of pulse edges in turn. The method merely assumed that the speed was uniform over the short time interval separating each pair of edges UU, VV. Since the run-out at speed S was periodic with period $1/S$, the correction should affect the synchronous frequency component of the vibration and its super-harmonics, without affecting the other frequency components or introducing spurious frequencies. This is verified in the waterfall diagrams of Figure 8.10, which refer to the frequency spectra of the y vibration of J_{2m} relative to B_2 for the unbalance condition in the first row of Table 8.4. It is also clear that the corrected diagram is much more realistic than the uncorrected one, showing activity in the synchronous frequency component around the bounce critical speeds of ~66, ~100 rev/s, especially the latter mode (as is expected from the unbalance distribution). Also, a resonance in the second harmonic of the rotational speed appears in the corrected diagram at 32 rev/s, which is around half the first (i.e. symmetric) bounce critical speed. This sub-critical super-harmonic resonance cannot be identified from the uncorrected diagram.

8.5 RESULTS AND DISCUSSION

The first part of this section focuses exclusively on the quality of the correlation between the three modelling blocks i.e. RHB, modal Floquet stability analysis, and modal numerical integration (time-marching). The second part of this section deals with the ability of the model to predict observed non-linear phenomena. All simulations presented use the absolute zero cavitation model for the SFDs i.e. $p_c = -101.325 \times 10^3$ Pa.

8.5.1 Correlation Between Modelling Blocks

For the purposes of the discussion in this section, one can focus on the response at a particular position without loss of generality, since the nature of the vibration (i.e. whether it is periodic, quasi-periodic, ... etc.) is the same for all locations. Figures 8.11(a-f) present predicted speed response curves for the displacement amplitude of J_2 relative to B_2 for the three different unbalance conditions in the first three rows of Table 8.4 (for which $U_1 = 0$). The vertical axis shows the half peak-to-peak displacement (normalised with respect to c) in the x or y directions. The RHB predictions (red curve) are for T-periodic motion ($N = 1$) with $m = 10$ harmonics taken. These solutions are classified according to their state of stability, computed by the Floquet analysis block (see figure caption). The steady-state time-marching predictions (in blue) are in steps of 2 rev/s and are performed for the two speed regions, I and II, that contain regions of instability of T-periodic motion. The initial conditions for the first time-marching solution in each range were obtained from the RHB prediction at that speed and the initial conditions for the solution at a subsequent speed were obtained from the final conditions of the solution at the preceding speed. For each speed, the integration was carried out over at least 200 shaft revolutions and only the last 1 s analysed. The very good correlation between the three modelling blocks is illustrated by the fact that the time-marching solution curves part company from the RHB curves only in the regions of instability of T-periodic motion. Elsewhere, both methods give the same stable T-periodic motion, as seen in Figure 8.12. This correlation between the RHB and time-marching predictions for stable T-periodic motion was not always that good, as seen in Figure 8.13. The reason for this was an insufficient number of rotor modes in the time-marching solution rather than insufficiency in the number of harmonics in the RHB solution (which, at $m = 10$, was more than adequate). In fact, as seen in this figure, agreement was restored when the RHB solution was performed using rotor receptances reconstructed from the 3 modes considered in the time-marching solution (using eq. A3.9 of section A3.3, Appendix A3) rather than the exact ones (computed by MI). This example illustrates the "inter-checking" properties of the RHB and modal time-marching methods when "exact" receptances are used in the former method. Despite the occasional inadequacy in the number of rotor modes taken, the stability analysis block gave a consistent result every time. According to the Floquet test, the instability in speed range I is the result of a secondary Hopf bifurcation. This is consistent with the Poincaré map of the time-marching result at 60 rev/s for $U_2 = 7.07 \times 10^{-4}$ kgm (Figure 8.14(a)). For the highest and lowest values of U_2, the onset of

instability in speed range II, as the speed is increased, is also the result of a secondary Hopf bifurcation (points H on Figures 8.11(a,b,e,f)). This is consistent with the Poincaré map of the time-marching result at 88 rev/s for $U_2 = 7.07\times10^{-4}$ kgm (Figure 8.14(b)) and at 84 rev/s for $U_2 = 13.15\times10^{-4}$ kgm (Figure 8.14(c)). Notice that for the highest unbalance, a narrow region of instability of T-periodic solutions, the onset of which is marked by a period-doubling bifurcation, is also evident in Figures 8.11(e,f) for the range ~72 rev/s to ~74 rev/s. However, the resulting sub-harmonic motion is weak and stable T-periodic motion is restored by 74 rev/s. For the intermediate unbalance, $U_2 = 10.74\times10^{-4}$ kgm (Figures 8.11(c,d)), the onset of instability in the speed range II, as the speed is increased, is marked by a period-doubling bifurcation (point F in Figures 8.11(c,d)). This is confirmed by the time-marching solution of Figure 8.15 for 84 rev/s, which shows double-looping. The (stable) $2T$-periodic RHB solution ($N = 2$) with $m = 15$ harmonics taken is overlaid on the same axes. It is seen that correlation between both solutions is very good. Notice that, in Figures 8.11(c,d), the unstable T-periodic solution (close to F) marked "□" (where $\lambda_l = -1.0442$) is followed by an apparently stable one marked "o". However, this subsequent solution is actually at the threshold of instability ($\lambda_l = -0.9885$) and, given its isolation, stable T-periodic motion is not restored, the motion remaining locked in $2T$-periodic motion. For the lowest unbalance only (Figures 8.11(a,b)) stability of T-periodic motion is restored by 110 rev/s, where the time-marching and RHB curves rejoin. Moreover, at this unbalance, as the speed is decreased from 110 rev/s, a period-doubling bifurcation is predicted (point F, Figures 8.11(a,b)). This is confirmed by the time-marching solution in Figure 8.16 for 106 rev/s. Overlaid on the same axes is the (stable) $2T$-periodic RHB solution (i.e. $N = 2$) with $m = 15$ harmonics taken. It is seen that correlation between both solutions is very good.

Note that the restriction to just one flexural rotor mode in each plane was done to cut down on computing time in generating the time-marching response. The stability analysis block was found to accommodate an extra flexural rotor mode (in each plane) in the matrices $\mathbf{H}_N$ (eq. (8.20)) and $\mathbf{D}$ (eq. (8.18)) with negligible effect on computation time. However, as illustrated in this section, this was not necessary.

8.5.2 Correlation With Experiment

The residual unbalance is first discussed, since this is an inevitable source of error. Figure 8.17 shows the measured residual unbalance response of the rig (i.e. with no unbalance masses attached). The relative responses across the dampers in the x and y directions, as well as the housing vibration in the x direction, are minimal. However, the housing vibration in the y direction shows peaks at 32, 48, 64, and 95 rev/s (Figures 8.17(f,h)). This latter effect is to be expected since the level of relative vibration across the dampers is low and consequently, there is little lift of the mean position of the journal vibration from the base of the clearance under the gravity load, over the entire speed range. The latter two peaks in Figures 8.17(f,h) correspond approximately to the first (i.e. symmetric) and second (i.e. anti-symmetric) bounce modes respectively. It should be noted that if one takes into account the extra mass added to the housings due to the attached rotor displacement probes and their brackets, the predicted bounce critical speeds in the yz plane quoted in Table 8.3 reduce to 66.4 rev/s and 98.3 rev/s. Hence, it can be assumed that the measured value of the second bounce critical speed (99.7 rev/s) goes down, at most, to 99 rev/s. Still, the latter two peaks in Figures 8.17(f,h) occur at around 2-4 rev/s less than the bounce speeds. This difference from the condition with the SFDs locked is not unusual since there *is* some relative movement across the dampers in the y direction (Figures 8.17(b,d)), especially around the bounce speeds. The first pair of peaks in Figures 8.17(f,h) occur at speeds roughly equal to half the bounce critical speeds and are sub-critical super-harmonic resonances, introduced in Chapter 6. These correspond to the state where the SFDs are reduced to piecewise-linear springs in the y direction. The strength of these peaks is not indicative of the magnitude of the unbalance, since the 2EO frequency component is the main contributor to the vibration (as explained in Chapter 2, 1EO ("engine order") refers to the synchronous frequency component of the vibration). In fact, as will be seen in later results, the amplitude at these peaks is practically independent of the unbalance level while the lift at the dampers is negligible. The 1EO frequency component is the major contributor to the peaks at 64 rev/s and 95 rev/s in Figures 8.17(f,h). The amplitudes at these peaks are not insignificant when compared to the housing vibration in the y direction with unbalance masses attached to the rotor (to be shown later). However, the relatively high amplitudes at the bounce critical speeds in the residual unbalance response of the housings in the y direction are more likely to be the result of inadequate damping provided by the SFDs due to the small relative vibration across the dampers, rather than a significant residual unbalance.

Figures 8.18-8.21 compare predictions and measurements for the vibration of J_{1m} relative to B_1, J_{2m} relative to B_2, and the absolute vibrations of B_1 and B_2 for the three levels of unbalance in the first three rows of Table 8.4 (page 169). The theoretical results (RHB $N=1$, $m=10$ and numerical integration) are presented in a similar fashion to those in Figure 8.11. The following observations can be made.

- Fair correlation of the measurements with the relative vibration predictions at the SFDs (Figures 8.18, 8.19) is evident, although it is noted, particularly in the y direction, that the mismatch around the first bounce speed (60-70 rev/s) increases with unbalance level. The orbital motion at the dampers in this region for $U_1=0$, $U_2=10.74\times10^{-4}$ kgm is shown in Figure 8.22. Although speed-for-speed agreement is generally unattainable, the predicted and measured orbits evolve in a similar manner. It is outside the scope of the work in this chapter to investigate how oil film conditions affect the orbital motion, especially in the absence of measurements of the dynamic pressure within the oil film.
- The sub-critical super-harmonic resonances are clearly defined in the absolute displacements of B_1 and B_2 in the y direction, at around 32 and 48 rev/s, Figures 8.20(b,d,f)-8.21(b,d,f). The first super-harmonic resonance is practically independent of unbalance, whereas the second one tends to become less prominent with increasing unbalance due to the increased lift at the dampers causing them to behave less like piecewise-linear springs. The absolute response at B_2 in the y direction is characterised by a pronounced trough in the range 68 rev/s to 78 rev/s, unlike the absolute y response at B_1. This is probably due to the unbalance being concentrated at U_2 only: the trough in the absolute y response at B_2 loosely corresponding to the anti-resonance between the bounce mode resonances of the measured point accelerance at B_2 (which is close to U_2) for the system with SFDs locked (Figure 8.5(b2)). The absence of such a pronounced trough in the absolute y response at B_1 can be associated with the absence of an anti-resonance in the measured transfer accelerance between B_1 and B_2 (and hence U_2) for the system with SFDs locked (Figure 8.5(c2)). The absolute responses of B_1 and B_2 in the x direction do not exhibit such a relation to the case with the SFDs locked since the absence of a static load in that direction promotes relative motion across the dampers.
- The experimental results presented are for run-up in rig speed. Similar orbital motion was reproduced on run-down. The only exception was for the highest value of U_2 at 86 rev/s, where an unexpected jump-up in the x component of the motions of B_1 and B_2 relative to the engine frame was observed as the speed was increased from 86 rev/s to 88

rev/s as shown in Figures 8.20(e), 8.21(e). On run-down in speed, the amplitude jumped back down as the speed was decreased from 86 rev/s to 84 rev/s. This unique behaviour in the x component of the motion relative to the frame could not be predicted.

- The (stable) numerical integration result in regions of predicted instability of T-periodic motion generally results in an improvement in prediction for vibration amplitude. This is not always the case, as shown in Figure 8.23, where the predicted $2T$-periodic relative orbits at the SFDs overestimate the vibration amplitude. Nonetheless, the occurrence of $2T$-periodic motion is correctly predicted. That the measured motion in Figure 8.23 is indeed almost pure $2T$-periodic motion is not just evident from the double-looping of the absolute housing orbits (Figures 8.23(c1,c2)), but also from the measured Poincaré map of the relative motion at each damper (Figure 8.24). The sampling times t_k of the map are given by $\Omega t_k = 3\pi/4 + k2\pi$, $k = 0,1,\ldots$, where $\Omega t_0 = 3\pi/4$ corresponds to the angular position of the speed probe, according to the convention of Figure 5.1(b). It is seen that the return points of both measured orbital motions (in red) congregate roughly at two locations within the clearance, in a similar manner to the predicted return points (in blue).

Non-synchronous frequency components are clearly evident in the waterfall diagrams of the frequency spectra of the relative and absolute responses at the dampers and housings respectively in the y direction, Figures 8.25-8.28. The corresponding diagrams for the x direction are found in Figures A6.4-A6.7 in Appendix A6, section A6.5. The frequency resolution is 1 Hz for the predictions and 2 Hz for the measurements. The prediction diagrams were efficiently constructed from the RHB $N = 1$, $m = 10$ predictions for those ranges of rotational speed for which the predicted T-periodic motion is stable and from numerical integration solutions at the other speeds. The sub-critical super-harmonic resonance speeds at ~32 rev/s and ~48 rev/s are clearly evident by the strong 2EO frequency components in both measurements and predictions of the housing response in the y direction, Figures 8.27, 8.28. The predicted super-harmonic resonances occur at speeds exactly equal to one half the predicted bounce speeds (66 rev/s and 98 rev/s). The measured bearing housing spectra also reveal a sub-critical super-harmonic resonance at a speed of 22 rev/s $= 66/3$ rev/s, evident by the 3EO frequency component at this speed (Figures 8.27(b,d,f), 8.28(b,d,f)). This frequency component is hardly visible in the predictions, but slight peaks at 22 rev/s are evident in the predicted absolute housing vibration amplitude-speed plots (y direction) of Figures 8.20(d,f)-8.21(d,f), as in the measurements. It is also interesting to note

that for the lower speeds, the frequency spectra of the measured housing y vibration show a slight frequency component at 100 Hz, approximately equal to the second bounce resonance frequency, possibly due to the very low damping when the SFD journals are bottomed in their clearances. This was not obtained with the prediction since RHB was used for the low speeds. However, it is noted that the RHB solutions in the region of the sub-critical resonances are on the threshold of instability due to the ineffectiveness of the SFDs and the lack of other sources of damping in the model – moderate disturbances from the T-periodic motion would result in a practically non-decaying natural motion superposed on the T-periodic motion.

The frequency spectra at the higher speeds are now discussed. At the lowest unbalance, Figures 8.25(a,b)-8.28(a,b), sub-synchronous activity starts in earnest at speeds approaching the second (i.e. anti-symmetric) bounce critical speed. In the measurements (Figures 8.25(b)-8.28(b)), the sub-synchronous motion starts with the appearance of non-integer EO frequency components of the form $(2k-1)\mathrm{EO}/2$, where k is a positive integer, mostly equal to 1 or 2. For later speeds the non-integer EO frequencies "fan out": they are each replaced by pairs of frequencies that are centred on the respective $(2k-1)\mathrm{EO}/2$ frequency locations. The spacing of each pair increases with speed, but each pair remains centred on the corresponding $(2k-1)\mathrm{EO}/2$ location. The corresponding predictions for this unbalance (Figures 8.25(a)-8.28(a)) show a reverse forking effect: pairs of frequencies centred on the $(2k-1)\mathrm{EO}/2$ locations first appear and are then replaced by $(2k-1)\mathrm{EO}/2$ components. For both measurements and predictions, the non-integer EOs disappear by 110 rev/s, which is consistent with the restoration of stability of T-periodic motion predicted in Figures 8.18(a,b)-8.21(a,b). For the next higher unbalance, Figures 8.25(c,d)-8.28(c,d), the non-integer EOs develop at an earlier speed in both measurements and predictions. The observed forking effect of the non-integer EOs is not evident in the prediction until 104 rev/s. However, for the highest unbalance, Figures 8.25(e,f)-8.28(e,f), the experimentally observed development of non-integer EOs in the region of the second bounce speed is evident in the predictions. Two sections of the predicted and measured waterfall diagrams in Figures 8.25(e,f)-8.28(e,f) are taken at speeds of 94 rev/s and 104 rev/s, straddling the second bounce critical speed, and are compared in Figures 8.29 and 8.30. It is seen that the salient frequency components in these figures occur at combinations $k_0 f_0 + k_1 f_1$ of two fundamental frequencies f_1 and f_0 where k_0 and k_1 are integers, f_1 is the synchronous component and

f_0 is either one of the pair of frequencies straddling the 1EO/2 location on the frequency axis (in Figures 8.29, 8.30 f_0 was chosen as the lower frequency of the pair). For both speeds 94 rev/s and 104 rev/s, the predicted value of f_0 is very close to the measured value (practically equal for 104 rev/s). It is seen that the mean of f_0 and $f_1 - f_0$ is $f_1/2$ ($= 1\text{EO}/2$) and that of $f_1 + f_0$ and $2f_1 - f_0$ is $3f_1/2$ ($= 3\text{EO}/2$). Spectra of the type shown in Figures 8.29, 8.30 were predicted for the simple system of Chapter 6 (Figure 6.8(b)). It would appear that the motions in the region of the second bounce speed are 2-frequency quasi-periodic. Figure 8.31 shows the predicted and measured steady-state orbital motion at 94 rev/s over 2 s. For the prediction, the first 350 shaft revolutions were discarded to ensure steady-state conditions. The Poincaré maps of the orbital motions in Figure 8.31 are shown in Figure 8.32. These are sampled at two different phases: $\Omega t_0 = 3\pi/4$ (Figures 8.32(a1,b1) and $\Omega t_0 = 3\pi/4 + \pi$ (Figures 8.32(a2,b2)). It is seen that the predicted and measured maps show remarkable similarity with regard to position, orientation within the clearance, and overall shape, particularly the curvature of the maps in Figure 8.32(b2). The predicted maps *approximate* to closed curves, albeit much more complicated ones than that in Figure 8.14(c), for 84 rev/s, which is close to the secondary Hopf bifurcation point H in Figures 8.11(e,f). The measured maps do not reveal the detailed structure of some complex closed curve or other form, and it appears unlikely that increasing the relatively small number of samples would yield any additional information. However, the measured orbits in Figure 8.31 are actually more ordered than the predicted ones. Figure 8.33 shows the predicted and measured orbital motion at 104 rev/s over 2 s. The predicted motion appears to be approximately locked into NT-periodic motion, where N is very high. The predicted and measured Poincaré maps are shown in Figure 8.34. It is again seen that good agreement exists between predicted and measured maps with regard to position and orientation within the clearance. By counting the number of distinct points on the predicted maps it is estimated that $N \approx 33$. In fact, as the speed is increased, the predicted motion in the region of the second bounce critical speed alternates between motion of the type of Figures 8.31(a1,b1) and approximately NT-periodic motion of high N as in Figures 8.33(a1,b1). This, coupled with the fact that only two fundamental frequencies are evident in the predicted (and measured) spectra of Figures 8.29, 8.30, seems to suggest that the predicted 2-frequency quasi-periodic motion is following the frequency-locking quasi-periodic route to chaos (end of section 3.5). As mentioned in section 3.5, the question of whether the predicted motion in

Figures 8.31(a1,b1) is really quasi-periodic or actually mildly chaotic is purely academic. Moreover, this question could only be answered by a reliable estimate of the Lyapunov exponent, which, for complicated dynamical systems like the one under consideration, is still unavailable.

Attention is now focused on the case of symmetrically applied unbalance, as in the last row of Table 8.4 (page 169). The waterfall diagrams of the frequency spectra of the y displacement are shown in Figure 8.35. Those for the x displacement are in Figure A6.8 of Appendix A6, section A6.5. The results in Figures 8.35 and A6.8 are for run-up in rig speed. It is noted that only the first sub-critical super-harmonic resonance (i.e. the strong 2EO frequency at 32-33 rev/s) is present in the absolute housing y displacement spectra. The reason for this is that sufficient lift has been generated by 48 rev/s to eliminate the piecewise-linear spring behaviour of the SFDs. It is also evident from the diagrams in Figure 8.35 that non-integer EO activity (and the subsequent forking effect described above) around the second bounce critical speed is absent. Instead, $(2k-1)$EO/2 (k integer) activity is concentrated in the vicinity of the first bounce critical speed. This activity starts at a lower speed for the measurements than for the predictions. The absence of sub-synchronous activity around the second bounce critical speed is consistent with fact that the rig is nearly symmetrical in construction, the unbalance symmetrically applied, and the SFDs nominally identical except for a slight inequality in viscosity (see Table 8.4). However, the predicted relative motion spectra, Figures 8.35(a,c), show unusual, highly asymmetric behaviour of the 1EO frequency component. Firstly, a jump-up on run-up in the 1EO frequency component is predicted at ~51 rev/s and the jump is much more pronounced for SFD 1 than SFD 2. This effect is not that obvious in the corresponding measurements, Figures 8.35(b,d), but can be seen in the measured displacement amplitude (half peak-to-peak) response of Figure 8.36.

The asymmetry of the predicted results for the SFD relative motion is explained in Figure 8.37 using RHB $N=1$, $m=10$ and the Floquet stability test. In this figure one can identify two bistable regimes. The first one is between 47.2 rev/s and 50.6 rev/s, and is typical of a spring-softening characteristic (i.e. jump-up in amplitude on run-up in speed). Prior to the jump-up speed, the stable motion is practically the same for both SFDs ("symmetrical" motion, Figure 8.38(a)). Beyond the jump-up speed (i.e. upon exiting the first bistable region), in the region ~51 rev/s to ~78 rev/s, a closed curve of T-periodic solutions exists, in addition to the main ("open") curve (see Figure 8.37). This results in a second bistable region in which the stable motions at the two SFDs are highly dissimilar ("asymmetrical"

motion). In fact, in the region ~51 rev/s to ~65 rev/s, one can choose a stable solution on the main (open) curves of SFDs 1 and 2 of Figures 8.37(a,b), giving stable asymmetrical motion like that in Figure 8.38(b). Alternatively, in the region ~51 rev/s to ~65 rev/s, one can choose a stable solution on the closed curves of Figure 8.37. Such a solution will reside on the upper part of the loop for SFD1 (Figure 8.37(a)) and on the lower part of the loop for SFD 2 (Figure 8.37(b)). This results in stable asymmetrical motion like that of Figure 8.38(c). The unstable solutions marked "+" along the lower part of the loop for SFD 1 (Figure 8.37(a)) and along the upper part of the loop for SFD 2 (Figure 8.37(b)) define the unstable "symmetrical" T-periodic motion like that in Figure 8.38(d). It should be remembered that the rig model is not perfectly symmetrical. Hence, in the present context, the pair of orbits in Figure 8.38(d) is regarded as defining "symmetrical" motion when compared to those in Figures 8.38(b,c), especially with respect to orbit size and mean position within the clearance. The RHB-computed stable T-periodic orbits in Figures 8.38(b,c) were also obtained by time-marching, in which case the choice of initial conditions determined which orientation was assumed by the rotor in the steady-state (i.e. either Figure 8.38(b) or Figure 8.38(c)).

Stable, highly asymmetrical motion of the type in Figures 8.38(b,c) was still obtained when the rig model was slightly altered to make it *perfectly symmetrical in all its parameters* (including those of the SFDs, like the oil viscosity). In such a case, the unstable motions in Figure 8.38(d) became identical to each other (i.e. perfectly symmetrical motion) and the stable asymmetrical motion was perfectly interchangeable between the SFDs (i.e. the orbits of Figure 8.38(c) could be obtained by interchanging the orbits of Figure 8.38(b), and vice-versa). Hence, for a symmetrical unbalanced rotor running in (identical) unsupported SFDs at each end it is generally incorrect to reduce the number of degrees of freedom by half by assuming kinematic symmetry about the rotor midpoint, as in Figure 4.3(a) (Chapter 4). This assumption is tantamount to excluding the rigid rotation mode of the free-free rotor (mode 2 in Figure 8.6(b)). Such an assumption has frequently been made in the theoretical analysis of symmetrical unbalanced rotors running in unsupported SFDs in the literature e.g. [12, 15], without due consideration being given to the possibility that symmetric periodic motion can become unstable under certain operating conditions, such that the slightest disturbance of the state variables would cause the rotor to assume a conical mode of vibration in the steady-state. To the author's knowledge this the first time that such a possibility has been reported.

The orbits in Figures 8.38(b-d) show that, in the range ~51 rev/s to ~65 rev/s, each SFD has three different mean positions of vibration about which the static load transmitted by the respective journal is balanced. Two of these mean positions can be regarded as stable

(Figures 8.38(b,c)), while the other (Figure 8.38(d)) is unstable. Hence, just like the jump phenomenon of the first bistable region, the asymmetric vibration phenomenon in the second bistable region owes its existence to the non-linear spring-like characteristic of an unsupported damper.

Turning back to the first bistable region (47.2 to 50.6 rev/s), it is noted from Figure 8.37 that a hysterisis (i.e. a difference between the "jump-up on run-up" speed and the "jump-down on run-down" speed) of around 3 rev/s exists. Hysterisis was not evident in the corresponding measurement. Likewise, the predicted asymmetry beyond the jump speed was not evident in the measurement. However, when the unbalance level was increased by about 22 %, a hysterisis of 1 rev/s was observed in the measurement, as illustrated in Figure 8.39. It should be noted that, as in Chapter 6, the hysterisis effect was predicted using a uniform value of cavitation pressure throughout ($p_c = -101.325\times10^3$ Pa in this work). Hence, while it is likely that, in practice, air entrainment following a jump-up causes a change in cavitation pressure [28], a change in cavitation pressure is not necessary to produce a hysterisis effect as was implied in [28]. The striking difference in orbit size between the two SFDs (Figures 8.39(b,c)) appears to lend experimental validity to the predicted asymmetrical operation beyond the jump-up speed. However, it is noted that the predicted interchangeability of orbits between the SFDs (as in Figures 8.38(b,c)) was not observed.

The jump-up on run-up in SFD relative displacement amplitude (spring-softening) and period doubling (i.e. $(2k-1)$EO/2 frequency components) were also predicted by the simple 4 degree of freedom system in Chapter 6. Notice that if the rig of this chapter was taken as perfectly symmetrical in all respects and, additionally, modes 2 and 3 in Figure 8.6(b) were not considered (i.e. kinematic symmetry about the rotor midpoint is assumed and rotor flexibility is neglected), then the resulting dynamical system would have the same equations as that of Chapter 6.

A source of error that may have degraded correlation between experiments and predictions must have been the assumption of free conditions at the left hand (LH) end of the rotor. Figure 8.40 shows a schematic of the drive coupling at the LH end of the rotor. While it is true that there is no bending moment at the LH end in either plane *xz* and *yz*, the component of rotor velocity at the LH end normal to the drive bar causes an inequality in contact force, resulting in a net opposing force. This restraining force is thought to be influential at high amplitudes of absolute rotor vibration at the LH end.

The development of the sub-critical super-harmonic resonances is now discussed in more detail. Figure 8.41 shows the predicted and measured development of the first super-harmonic resonance. It is seen that the predicted results evolve in a similar manner to the measured ones but on a very much smaller bandwidth of speed. Moreover, when the measured loss factors in Table 8.1 were used in the (RHB) computation, the super-harmonic resonances were totally attenuated. While it is probable that the loss factors were overestimated, this is not likely to be the cause of the disappearance of the super-harmonic resonances, especially since attenuation of the predicted super-harmonic resonances was still severe even when the estimated loss factors were reduced by an order of magnitude. A more plausible explanation for this effect and the contrast in bandwidths in Figure 8.41 would be the unsuitability of the SFD model under such extreme conditions. The generation of the large amplitude of absolute bearing housing (and rotor) vibration in the y direction at the super-harmonic resonance depends on the existence of a large non-linear force at the interface between the housing and the journal. The journal is bottomed in the clearance and vibrating with minute amplitude relative to the housing. In the real system, the oil is likely to be squeezed out of the interface between the journal and the housing so that the interface force would be a pure contact force. However, the model always takes into consideration the oil film at the interface and the force transmission characteristics of the oil film under these extreme conditions are difficult to predict using the conventional SFD model. Figure 8.42(a) shows the typical predicted variation of lift in the damper in the region of a sub-critical super-harmonic resonance, with support structural damping excluded. It is clear from this figure that the SFD force comes close to a contact force only at the resonance. Elsewhere, in the region of resonance, the SFD force is an attenuated version of the contact force. Hence, it appears justifiable to exclude structural damping, even in the super-harmonic resonance region, in order to compensate for the attenuation in contact force. For the drop in lift (Figure 8.42(a)) to be possible, the amplitude of the relative vibration at the SFDs must dip as in Figure 8.42(b). This allows the gravity load to pull J_2 (and J_1) further to the bottom of the clearance. From the oil pressure equation (4.8), although $\dot{\varepsilon}$, $\psi \rightarrow 0$, the eccentricity $\varepsilon \rightarrow -1$, so the SFD force ($\approx$ contact force) is maintained. Paradoxically, the relative displacement amplitude at the SFDs can never be exactly zero since this would mean a perfectly rigid connection (resulting in a linear system) and hence there would be no 2EO frequency component and no super-harmonic resonance. It is interesting to note that, while the predicted amplitudes of the y displacements of J_2 and J_1 relative to B_2 and B_1 respectively

dip at the super-harmonic resonances (Figure 8.42(b)), the predicted amplitudes of the y displacements of J_{2m} and J_{1m} relative to B_2 and B_1 respectively actually peak at the resonances, as shown in Figure 8.42(c). This is consistent with the y relative displacement amplitude measurements in Figures 8.18(b,d,f)-8.19(b,d,f), which show small peaks at the super-harmonic resonances.

8.6 CONCLUSIONS

This chapter formed the final part of the validation of the general model developed in Chapter 5. In Chapters 6 and 7, the integrated model was tested on a rigid rotor-flexible housing assembly and a flexible rotor-rigid housing assembly respectively, both with a single SFD. In this chapter, the model was applied to a test rig that, to a limited extent, captured the essential features of the low pressure rotor assembly of a practical aero-engine in which the flexibilities of both the rotor and the support structure are relevant, and in which more than one SFD is used. The model was first "internally" validated by testing the correlation between the three modelling blocks (i.e. RHB, modal Floquet stability analysis, and modal numerical integration). The model was then used to predict and explain experimentally observed non-linear phenomena from the rig.

The following conclusions and comments can be made regarding the theoretical part of the work in this chapter:

- In general, no problems of computational efficiency were encountered when implementing the model on a 333 MHz Pentium II computer.
- The correlation between the three modelling blocks was highly satisfactory, validating the soundness and applicability of the model.
- The influence of the flexural modes of the rotor should not be disregarded simply because the rotor-support structure modes with the SFDs locked are very nearly "bounce" modes in which the housings show much more deflection than the rotor.
- Among other things, the RHB method was particularly useful in identifying sub-critical super-harmonic resonances and the complicated operation of the symmetrically unbalanced rig, where stable asymmetric motion at the SFDs was found to be theoretically possible.
- For a perfectly symmetrical unbalanced rotor running in identical unsupported SFDs at each end, it is generally incorrect to reduce the number of degrees of freedom by half by

pre-assuming kinematic symmetry, due to the non-linear spring-like characteristics of the SFDs.

As regards correlation with experimental observations, the following conclusions and comments can be made:

- Overall, correlation between measured and predicted displacement amplitude responses was acceptable, although speed-for-speed agreement was generally unattainable.
- Under conditions of general (asymmetrical) unbalance (at U_2 only), odd number multiples of 1EO/2 around the second bounce critical speed were found to fork out into combination frequencies composed of two fundamentals, one of which being the 1EO component. Predicted and measured Poincaré maps of the resulting 2-frequency motion showed good correlation. It was concluded that the motion was either quasi-periodic, or at worst, mildly chaotic. As in Chapter 7, frequency-locking of the 2-frequency quasi-periodic motion was identified as a potential route to chaos, although no formal investigations were carried out.
- For the symmetrically unbalanced rotor, odd number multiples of 1EO/2 were obtained in the vicinity of the first bounce critical speed and no such activity was observed in the region of the second bounce critical speed. A jump-up on run-up in SFD relative displacement amplitude (spring-softening), with hysterisis, was correctly predicted.
- In modelling the sub-critical super-harmonic resonance regime of operation, the attenuating effect of the oil film on the transmitted contact force between journal and housing justified the exclusion of structural damping for the purpose of predicting the super-harmonic resonances.
- Despite the highly non-linear performance, the unsupported SFDs fulfilled their intended function in this application i.e. to provide a safe transition through the bounce critical speeds (by attenuating the vibration amplitude).

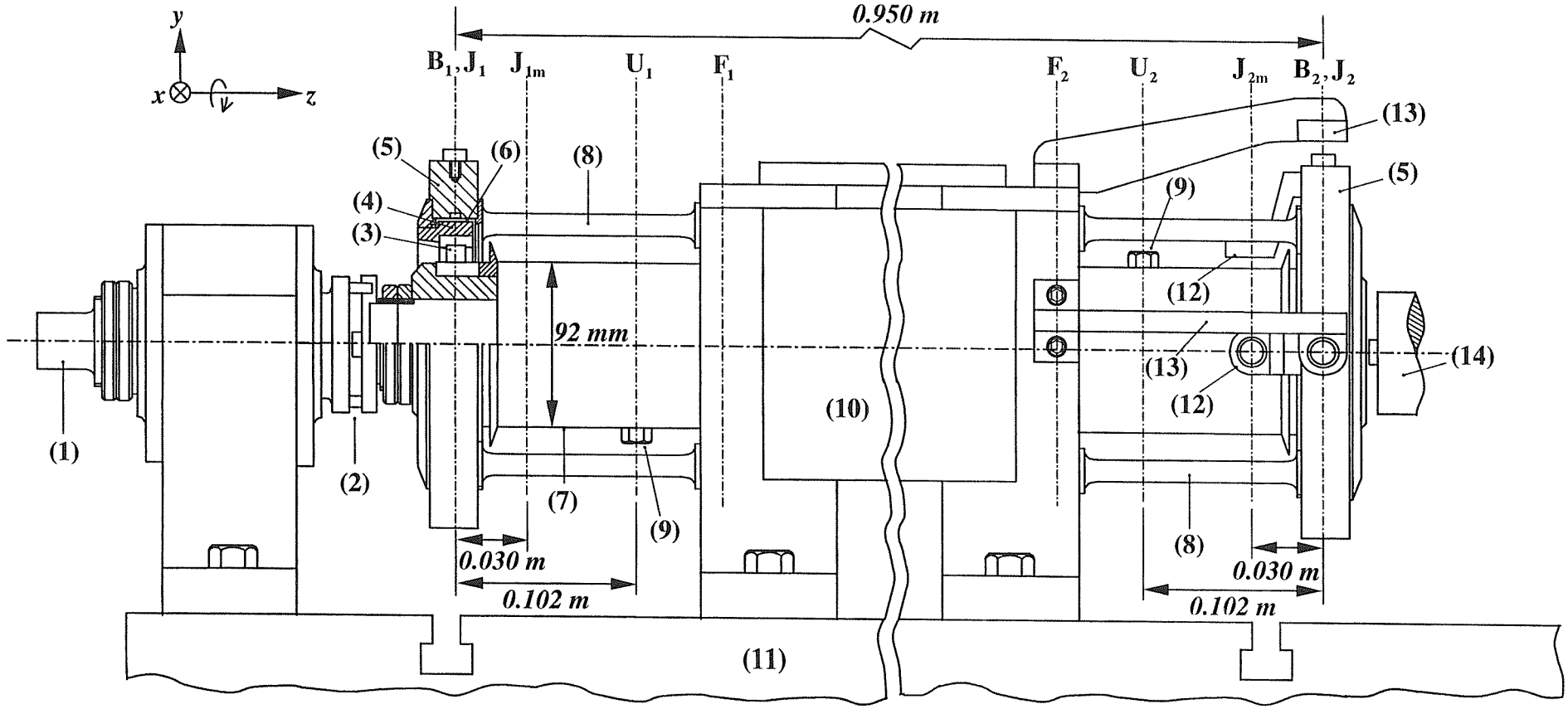

(1) Drive shaft
(2) Drive coupling
(3) Roller bearing
(4) SFD journal
(5) Bearing housing
(6) Oil annulus (SFD)
(7) Shaft ("LP rotor")
(8) Housing suspension bar (× 4)
(9) Unbalance mass
(10) Frame
(11) Bedplate
(12) Rotor probe bracket
(13) Housing probe bracket
(14) Shaft ("HP rotor")

Figure 8.1: *Test rig for configuration C*

(probe brackets for left hand SFD not shown in above figure)

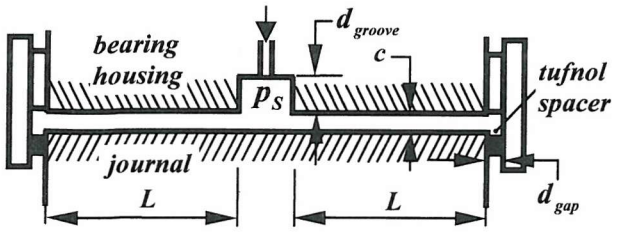

$c = 0.11\times10^{-3}$ m $\quad d_{groove} = 2.03\times10^{-3}$ m

$L = 6.26\times10^{-3}$ m $\quad d_{gap} = 0.50\times10^{-3}$ m

housing bore radius $R = 69.85\times10^{-3}$ m

Figure 8.2: *SFD dimensions for configuration C and axial location of journal*

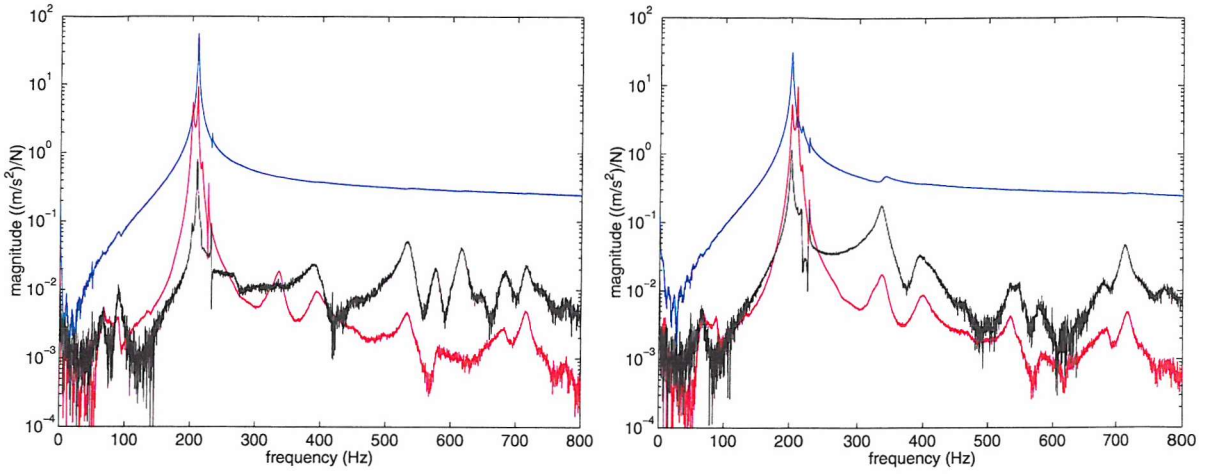

(a) $\breve{\alpha}_{B_1B_1}$ (blue), $\breve{\alpha}_{B_1B_2}$ (red), $\breve{\alpha}_{B_1F_1}$ (black) **(b)** $\breve{\alpha}_{B_2B_2}$ (blue), $\breve{\alpha}_{B_2B_1}$ (red), $\breve{\alpha}_{B_2F_2}$ (black)

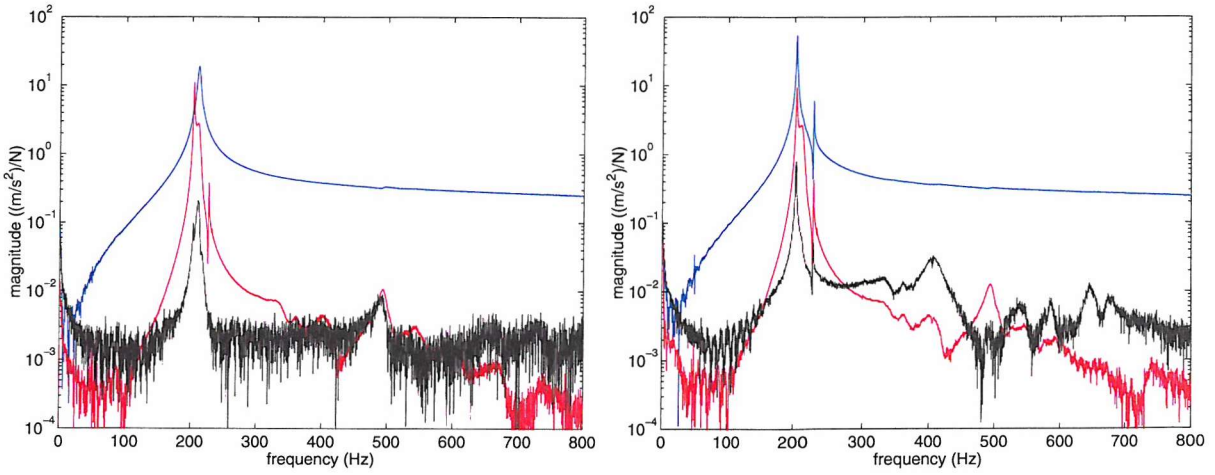

(c) $\breve{\beta}_{B_1B_1}$ (blue), $\breve{\beta}_{B_1B_2}$ (red), $\breve{\beta}_{B_1F_1}$ (black) **(d)** $\breve{\beta}_{B_2B_2}$ (blue), $\breve{\beta}_{B_2B_1}$ (red), $\breve{\beta}_{B_2F_2}$ (black)

Figure 8.3: *Accelerance measurements on support structure*

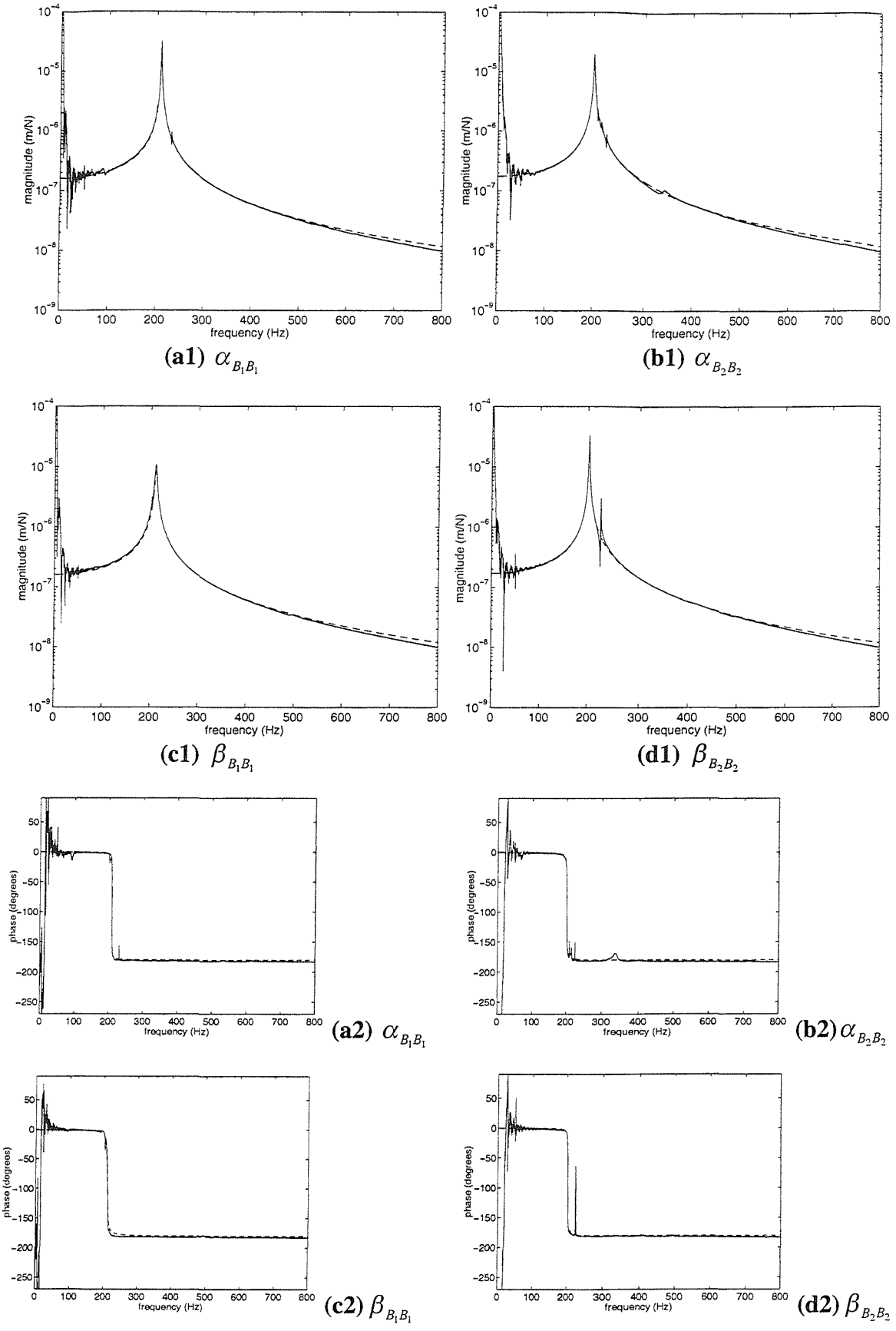

Figure 8.4: *Comparison of measured receptance* (——) *with modal approximation* (– – –)

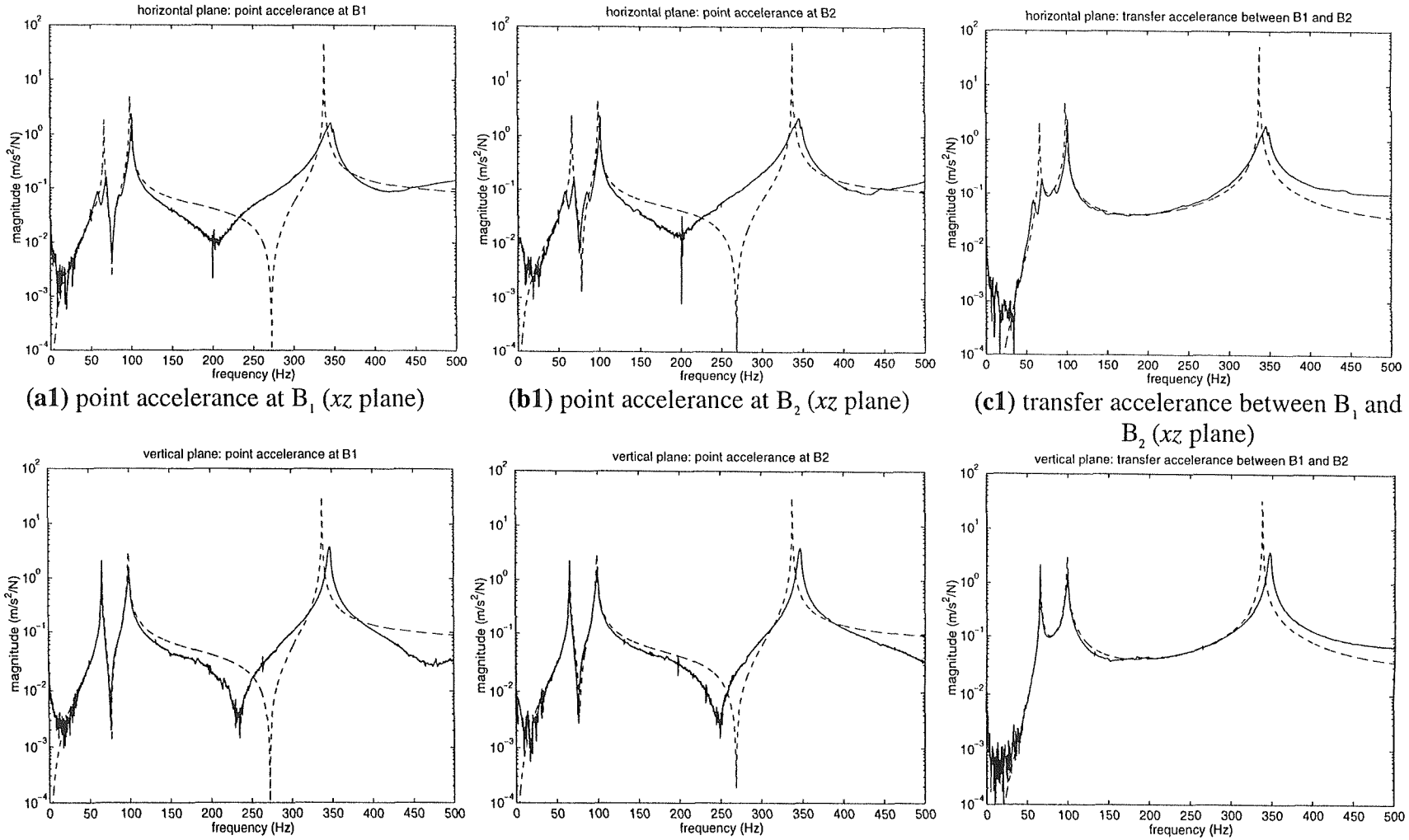

(a1) point accelerance at B_1 (*xz* plane)

(b1) point accelerance at B_2 (*xz* plane)

(c1) transfer accelerance between B_1 and B_2 (*xz* plane)

(a2) point accelerance at B_1 (*yz* plane)

(b2) point accelerance at B_2 (*yz* plane)

(c2) transfer accelerance between B_1 and B_2 (*yz* plane)

Figure 8.5: *Comparison of measurements* (——) *with MI predictions* (– – –), *for non-rotating rig with SFDs locked*

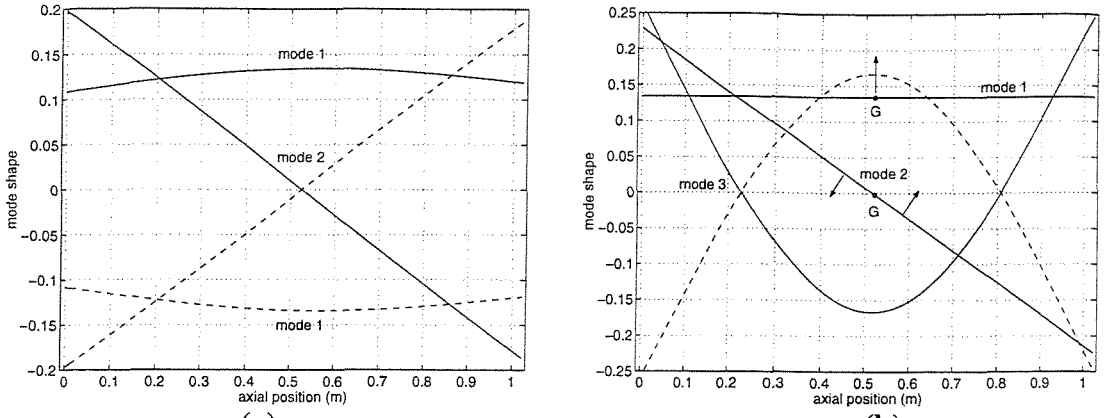

(a) (b)

Figure 8.6: *Mode shapes in one plane for* (**a**) *rotor-support structure combination (SFDs locked) and* (**b**) *free-free rotor of linear subsystem*

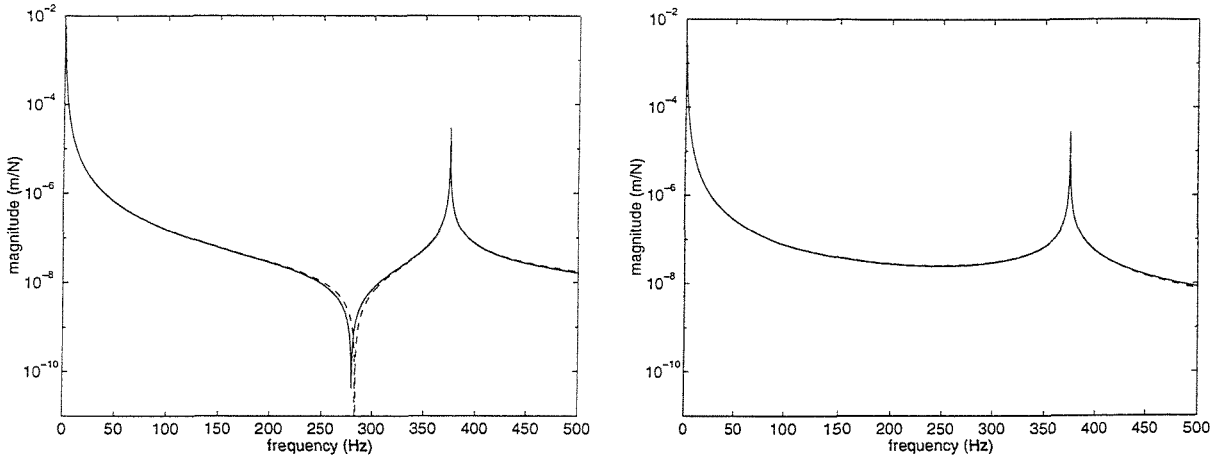

(a) $\alpha_{J_2J_2}$ (b) $\alpha_{J_1J_2}$

Figure 8.7: *Comparison of exact rotor receptances computed by MI* (——) *with approximations reconstructed from* 3 *modes in Figure 8.6(b)* (– – –)

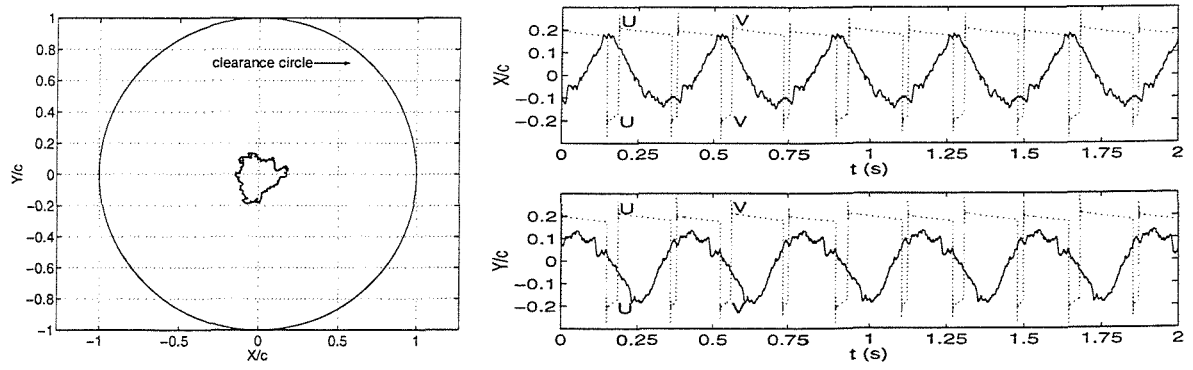

(**a**) orbit (**b**) run-out (——); tachometer pulse (·····)

Figure 8.8: *Geometric run-out at* J_{2m} (mean component of signals removed)

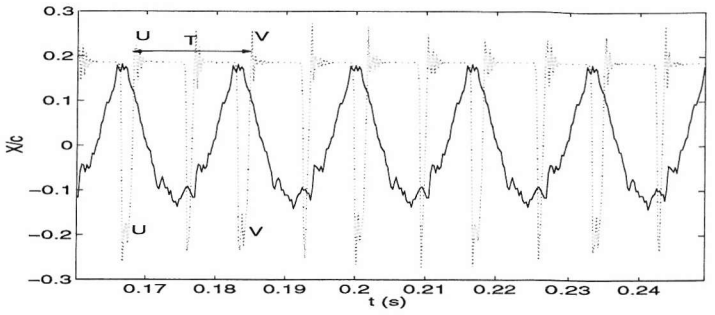

Figure 8.9: *Construction of geometric run-out profile at* J_{2m} *in x direction at* 60 *rev/s* run-out (——); tachometer pulse (·····) (mean component of signals removed)

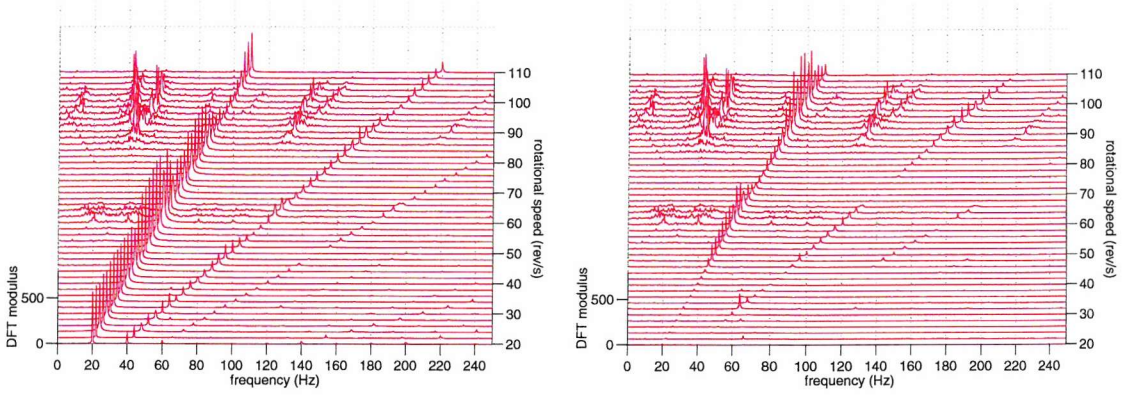

(a) uncorrected **(b)** corrected for geometric run-out

Figure 8.10: *Waterfall diagram of the frequency spectra of the measured y displacement of* J_{2m} *relative to* B_2 (unbalance as in first row of Table 8.4, data length 2 s)

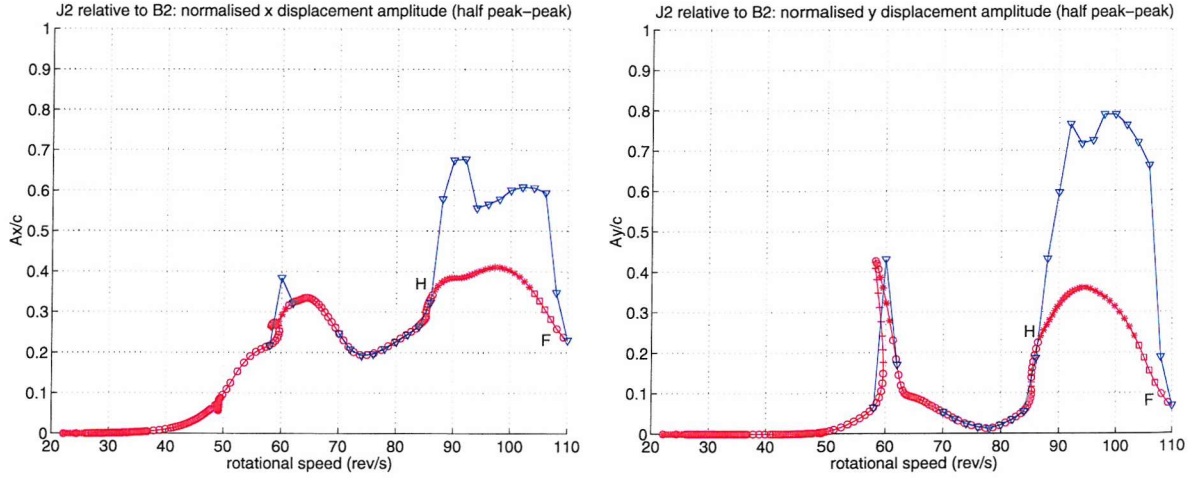

(a) *x* direction **(b)** *y* direction

Figure 8.11: *Predicted response of* J_2 *relative to* B_2 *for three states of unbalance* (first three rows of Table 8.4: **(a)**, **(b)** row 1; **(c)**, **(d)** row 2; **(e)**, **(f)** row 3). RHB $N = 1$, $m = 10 -$ red: "o" stable, "+" unstable (λ_l real, positive), "□" unstable (λ_l real, negative), "*" unstable (λ_l complex); numerical integration – blue. Vertical axes show ratio of half peak-to-peak displacement to *c*.

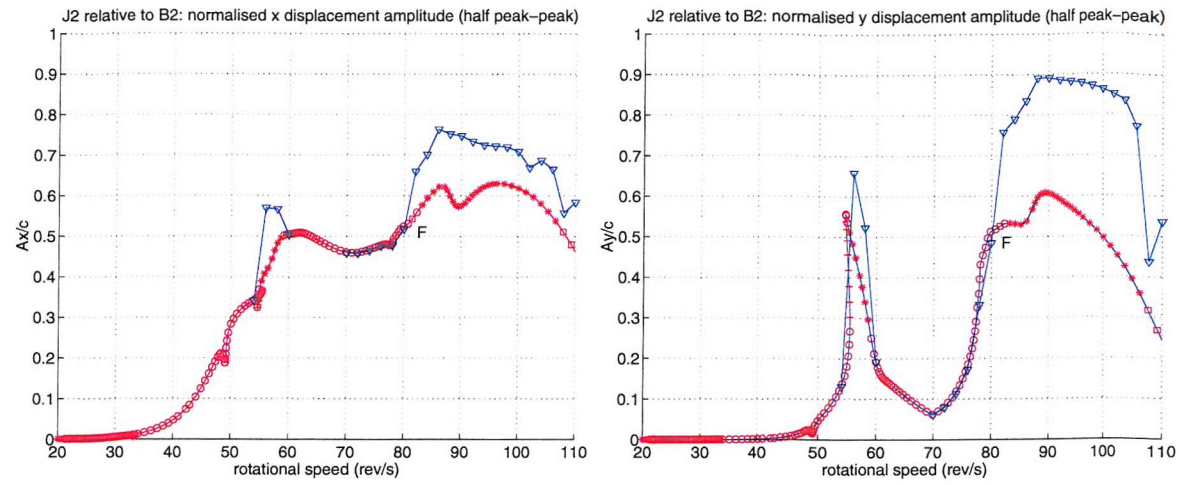

(c) x direction **(d)** y direction

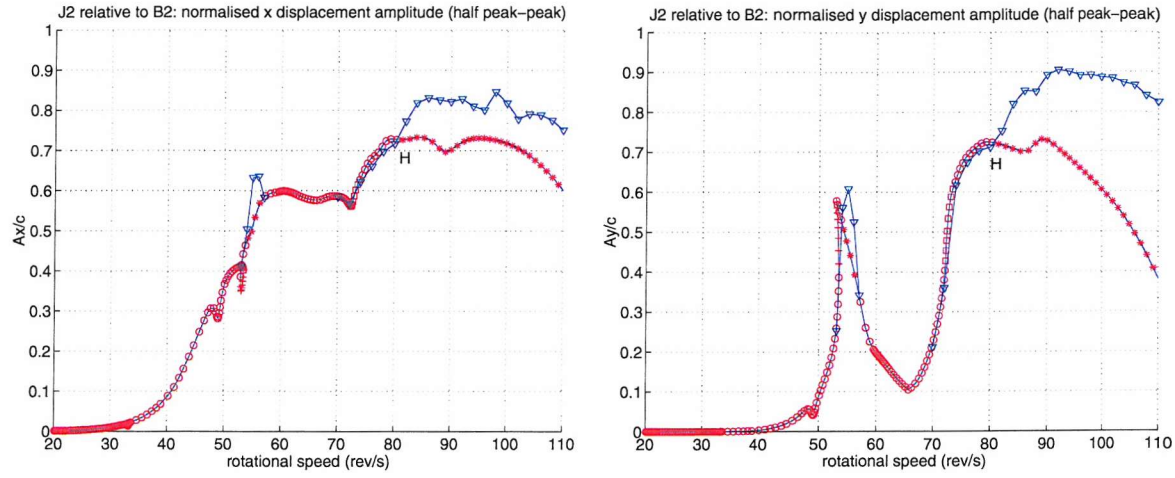

(e) x direction **(f)** y direction

Figure 8.11 (continued)**:** RHB $N=1$, $m=10-$ red: "o" stable, "+" unstable (λ_1 real, positive), "□" unstable (λ_1 real, negative), "*" unstable (λ_1 complex); numerical integration – blue. Vertical axes show ratio of half peak-to-peak displacement to c.

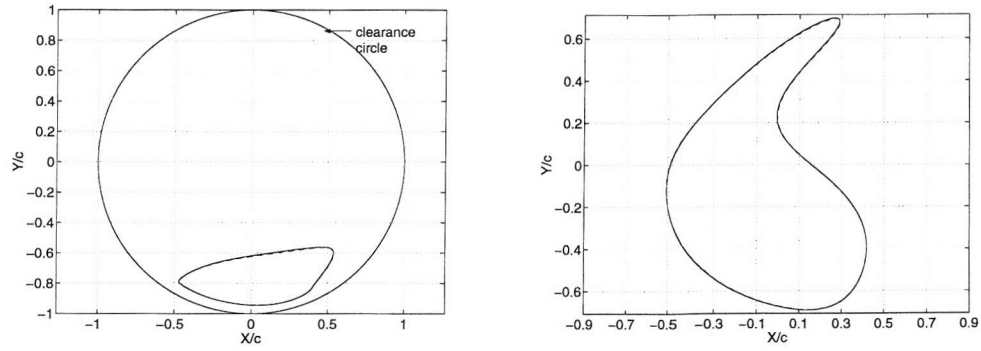

(a) J_2 relative to B_2 **(b)** B_2

Figure 8.12: *Predicted orbits at SFD 2 at 60 rev/s for* $U_1=0$, $U_2=10.74\times10^{-4}$ *kgm*
RHB $N=1$, $m=10$ (– – –); numerical integration (——)

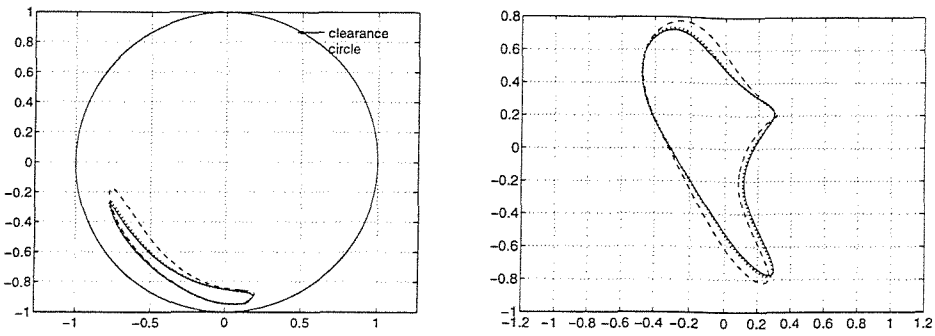

(a) J_2 relative to B_2 (b) B_2

Figure 8.13: *Predicted orbits at SFD* 2 *at* 78 *rev/s for* $U_1 = 0$, $U_2 = 10.74\times10^{-4}\,kgm$. RHB $N = 1$, $m = 10$ with exact receptances (– – –) and with receptances computed from modal approximation (·····); numerical integration (——)

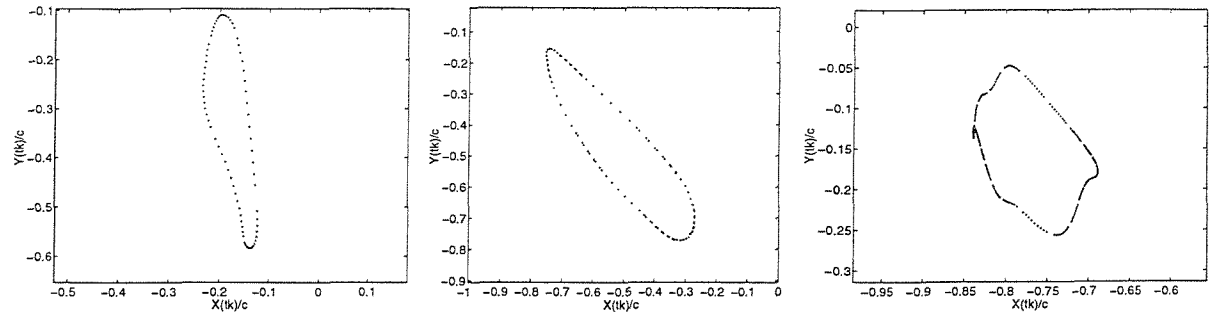

(a) (b) (c)

Figure 8.14: *Predicted Poincaré maps of the orbit of* J_2 *relative to* B_2 *for* $U_1 = 0$ *and* (**a**) $U_2 = 7.07\times10^{-4}\,kgm$, 60 *rev/s*; (**b**) $U_2 = 7.07\times10^{-4}\,kgm$, 88 *rev/s*; (**c**) $U_2 = 13.15\times10^{-4}\,kgm$, 84 *rev/s*. ($\Omega t_k = 3\pi/2 + k2\pi$)

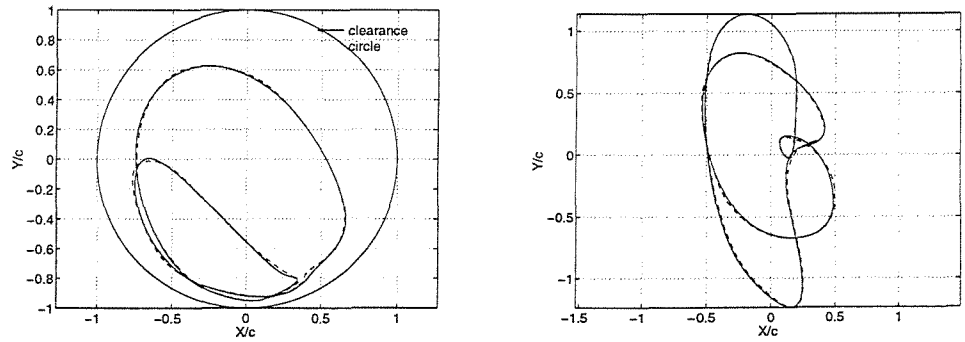

(a) J_2 relative to B_2 (b) B_2

Figure 8.15: *Predicted 2T-periodic orbits at SFD* 2 *at* 84 *rev/s for* $U_1 = 0$, $U_2 = 10.74\times10^{-4}\,kgm$. RHB $N = 2$, $m = 15$ (– – –); numerical integration (——)

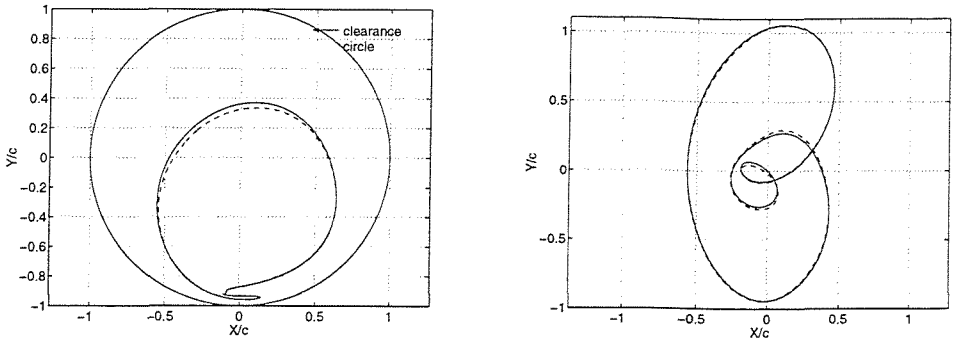

(a) J_2 relative to B_2 **(b)** B_2

Figure 8.16: *Predicted 2T-periodic orbits at SFD* 2 *at* 106 *rev/s for* $U_1 = 0$, $U_2 = 7.07\times10^{-4}\,kgm$. RHB $N = 2$, $m = 15$ (– – –); numerical integration (——)

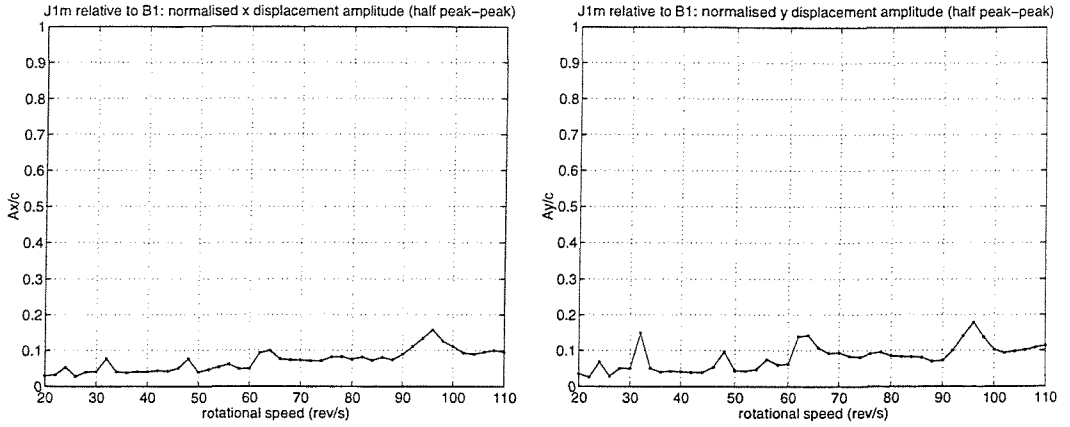

(a) J_{1m} relative to B_1, x direction **(b)** J_{1m} relative to B_1, y direction

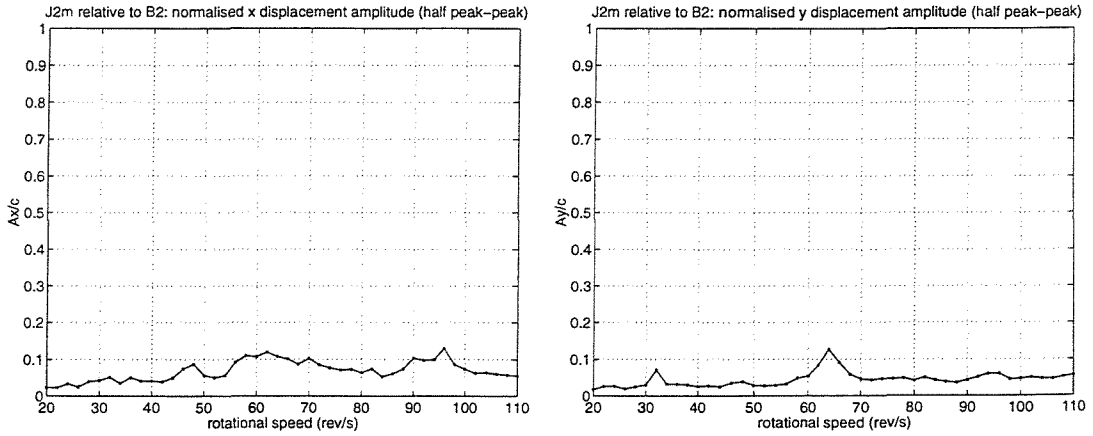

(c) J_{2m} relative to B_2, x direction **(d)** J_{2m} relative to B_2, y direction

Figure 8.17: *Residual unbalance response*
(half peak-to-peak displacement normalised with respect to c)
(Figure continues on the following page)

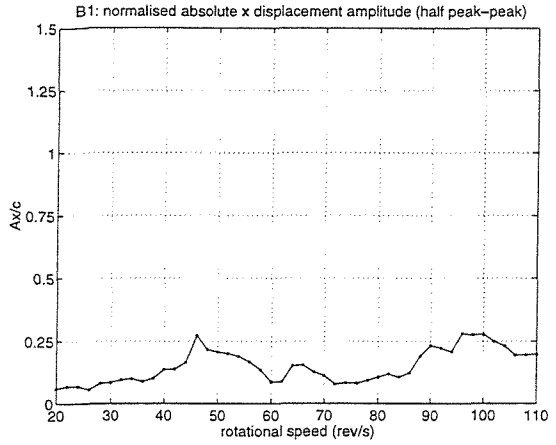

(e) B_1, x direction

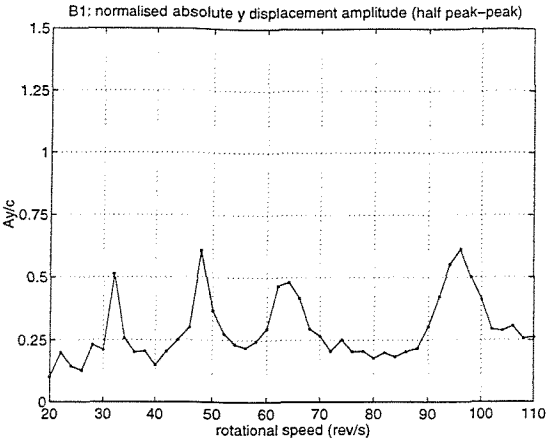

(f) B_1, y direction

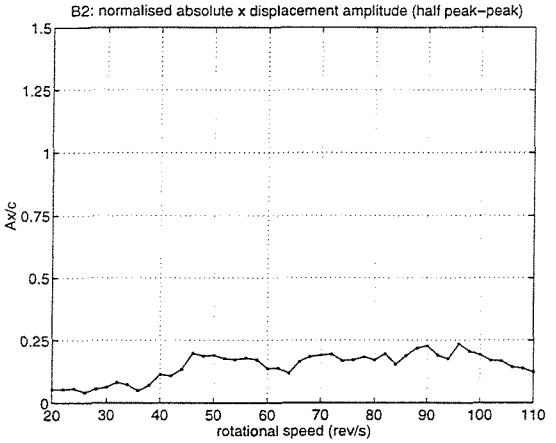

(g) B_2, x direction

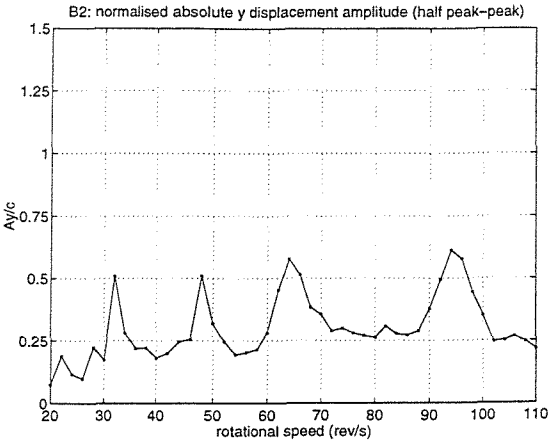

(h) B_2, y direction

Figure 8.17 (continued): *Residual unbalance response*
(half peak-to-peak displacement normalised with respect to c)

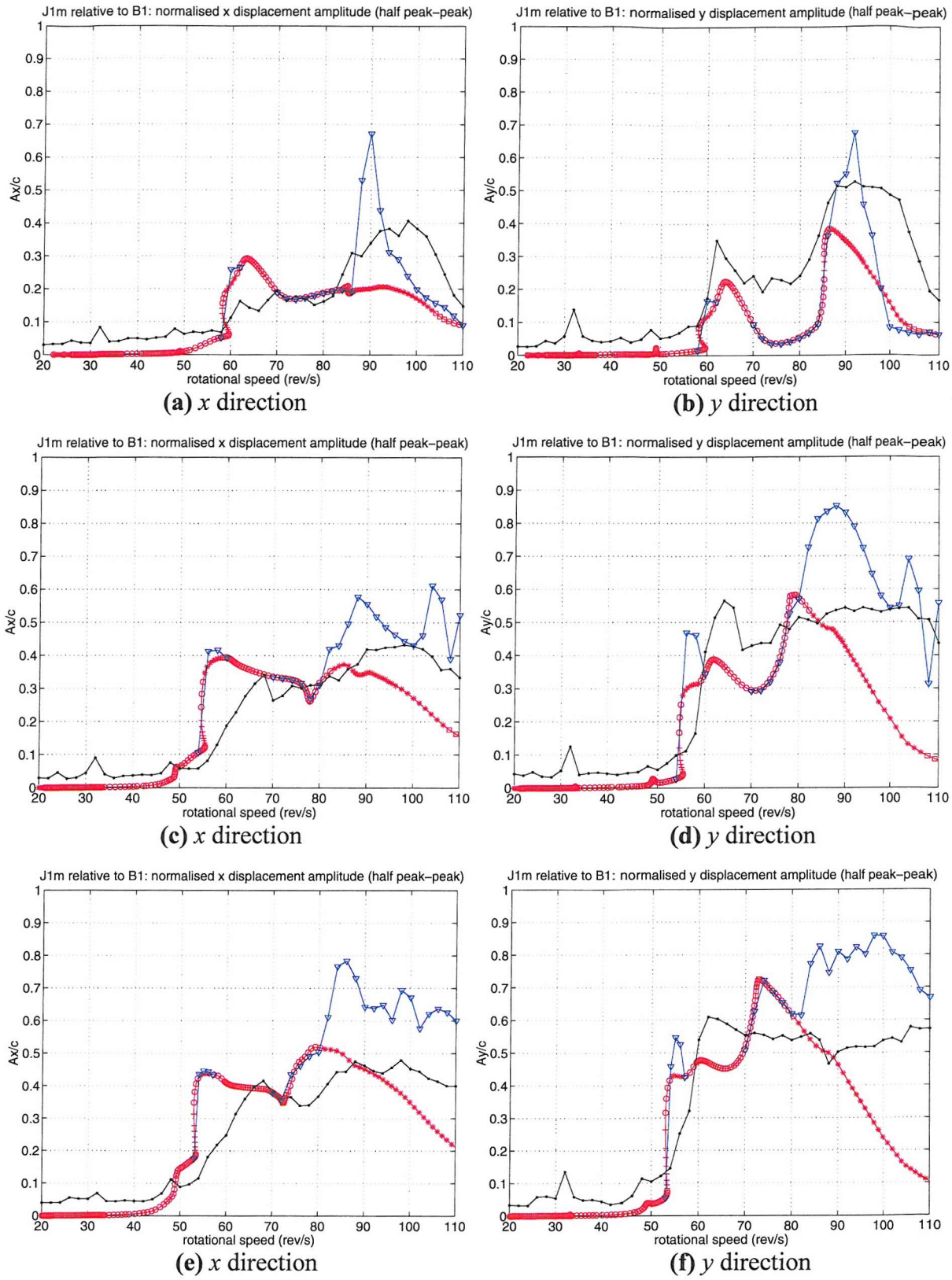

Figure 8.18: *Response of* J_{1m} *relative to* B_1 *for three states of unbalance* (first three rows of Table 8.4: **(a)**, **(b)** row 1; **(c)**, **(d)** row 2; **(e)**, **(f)** row 3). Measurements – black. RHB $N = 1$, $m = 10$ – red: "o" stable, "+" unstable (λ_1 real, positive), "□" unstable (λ_1 real, negative), "*" unstable (λ_1 complex); numerical integration – blue. Vertical axes show ratio of half peak-to-peak displacement to c.

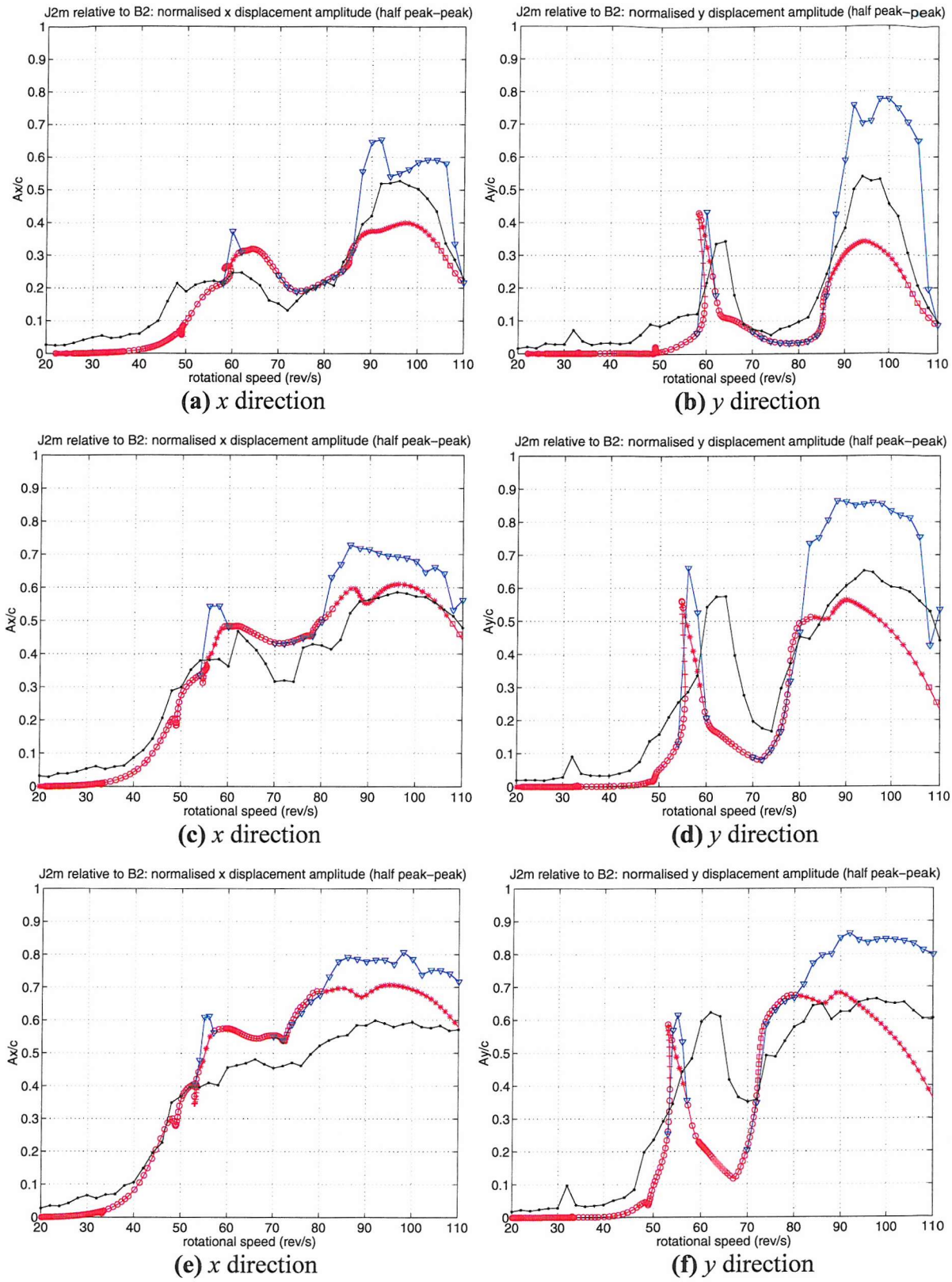

Figure 8.19: *Response of* J_{2m} *relative to* B_2 *for three states of unbalance* (first three rows of Table 8.4: **(a)**, **(b)** row 1; **(c)**, **(d)** row 2; **(e)**, **(f)** row 3). Measurements – black. RHB $N = 1$, $m = 10$ – red: "o" stable, "+" unstable (λ_1 real, positive), "□" unstable (λ_1 real, negative), "*" unstable (λ_1 complex); numerical integration – blue. Vertical axes show ratio of half peak-to-peak displacement to c.

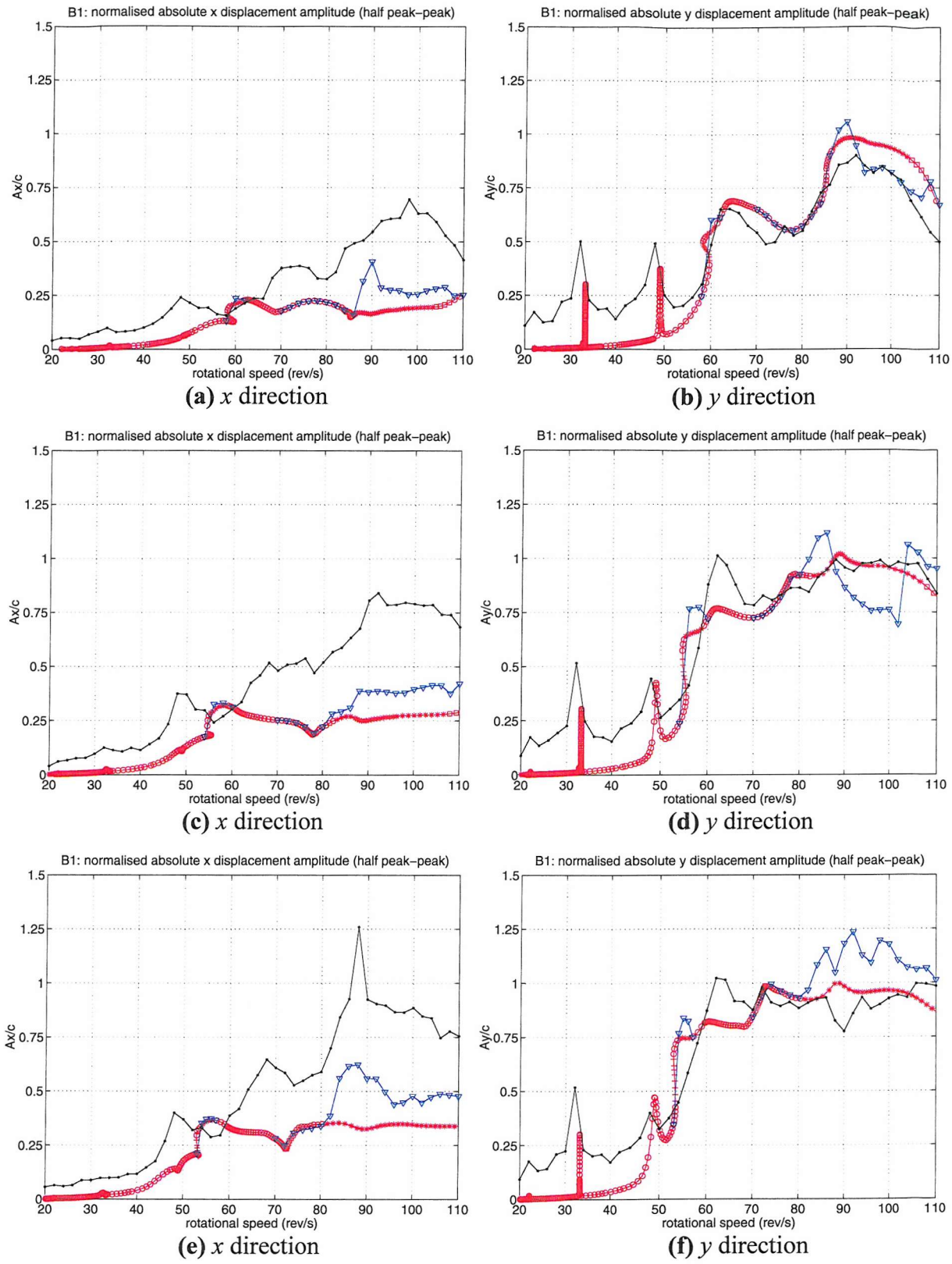

(a) x direction **(b)** y direction

(c) x direction **(d)** y direction

(e) x direction **(f)** y direction

Figure 8.20: *Response of* B_1 *for three states of unbalance* (first three rows of Table 8.4: **(a)**, **(b)** row 1; **(c)**, **(d)** row 2; **(e)**, **(f)** row 3). Measurements – black. RHB $N = 1$, $m = 10$ – red: "o" stable, "+" unstable (λ_I real, positive), "□" unstable (λ_I real, negative), "*" unstable (λ_I complex); numerical integration – blue. Vertical axes show ratio of half peak-to-peak displacement to c.

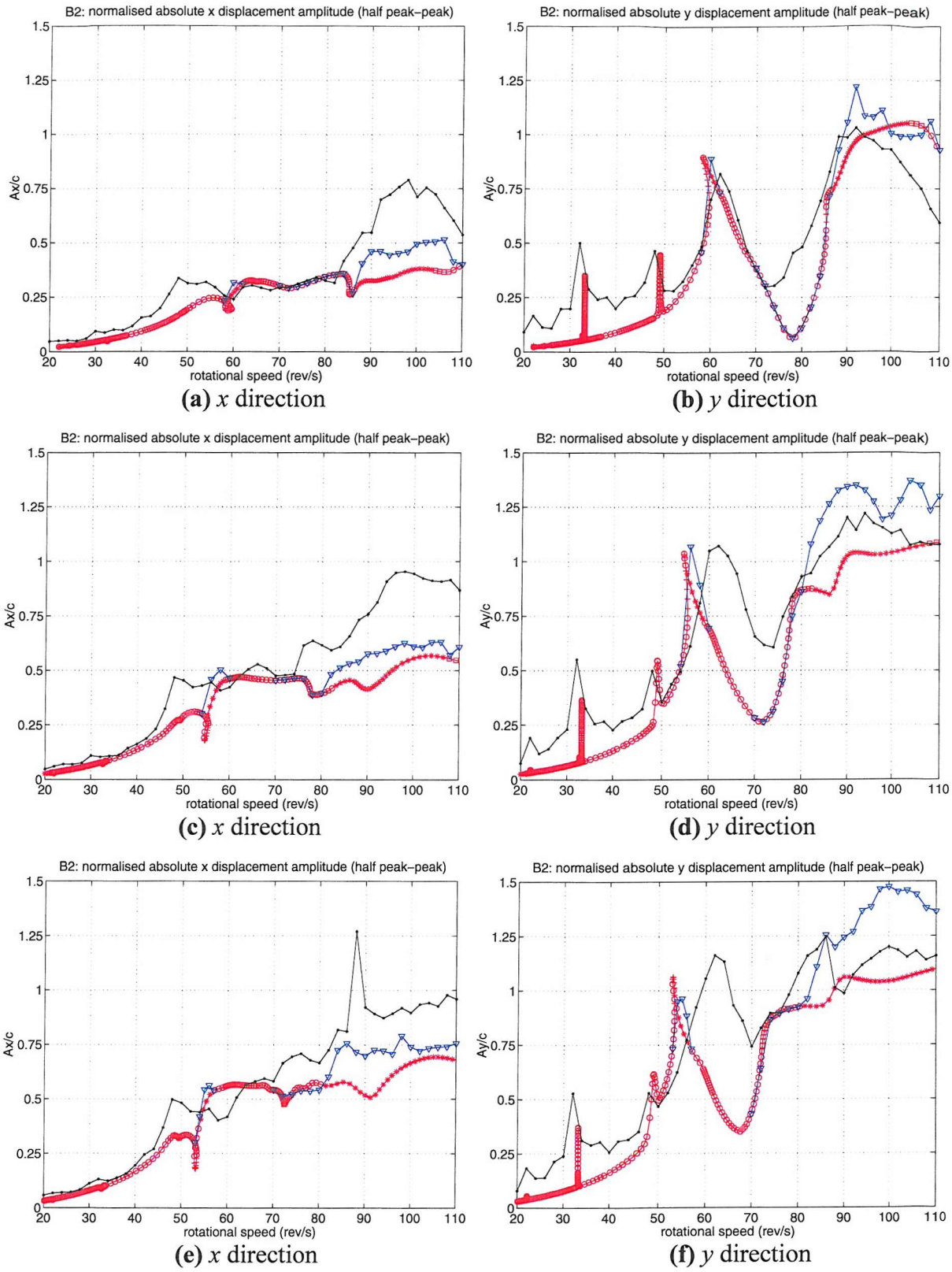

Figure 8.21: *Response of* B_2 *for three states of unbalance* (first three rows of Table 8.4: **(a)**, **(b)** row 1; **(c)**, **(d)** row 2; **(e)**, **(f)** row 3). Measurements – black. RHB $N = 1$, $m = 10$ – red: "o" stable, "+" unstable (λ_l real, positive), "□" unstable (λ_l real, negative), "*" unstable (λ_l complex); numerical integration – blue. Vertical axes show ratio of half peak-to-peak displacement to c.

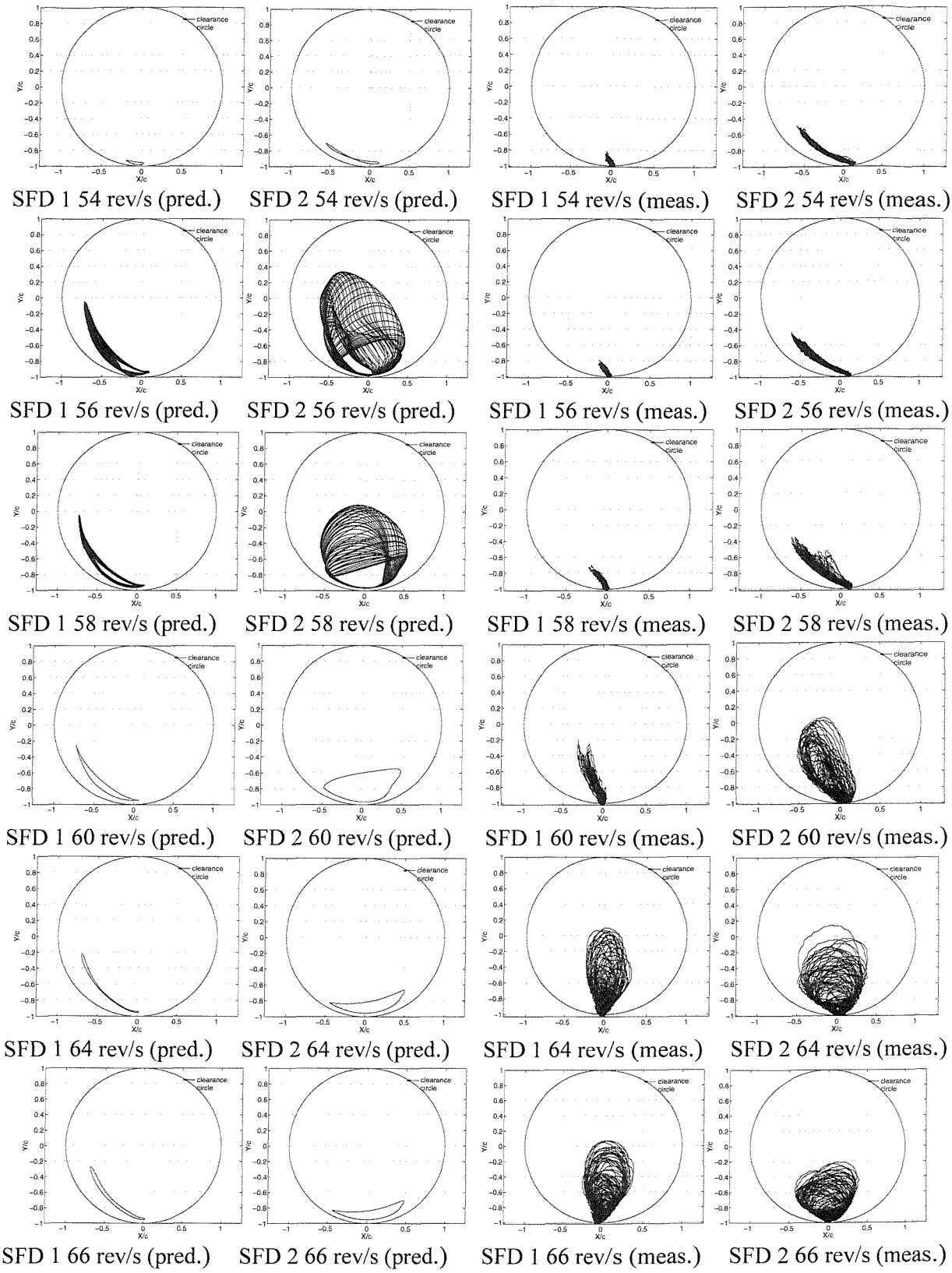

Figure 8.22: *Predicted and measured orbits* (over 2 s) *of* J_{1m} *relative to* B_1 *and* J_{2m} *relative to* B_2 *around the first bounce critical speed* (unbalance as in row 2 of Table 8.4)
(Figure continues on the following page)

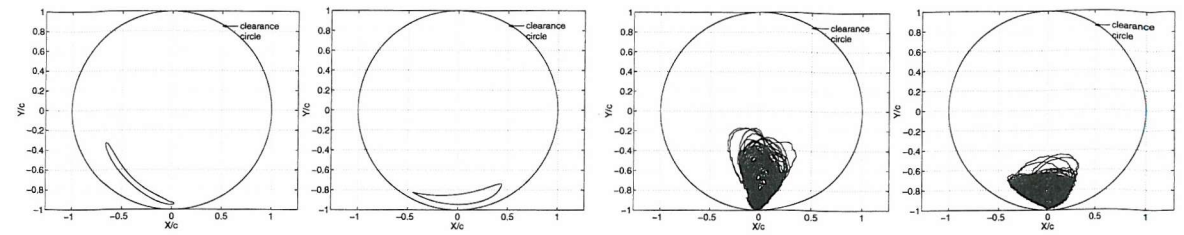

SFD 1 68 rev/s (pred.) SFD 2 68 rev/s (pred.) SFD 1 68 rev/s (meas.) SFD 2 68 rev/s (meas.)

Figure 8.22 (continued): *Predicted and measured orbits* (over 2 s) *of* J_{1m} *relative to* B_1 *and* J_{2m} *relative to* B_2 *around the first bounce critical speed* (unbalance as in row 2 of Table 8.4)

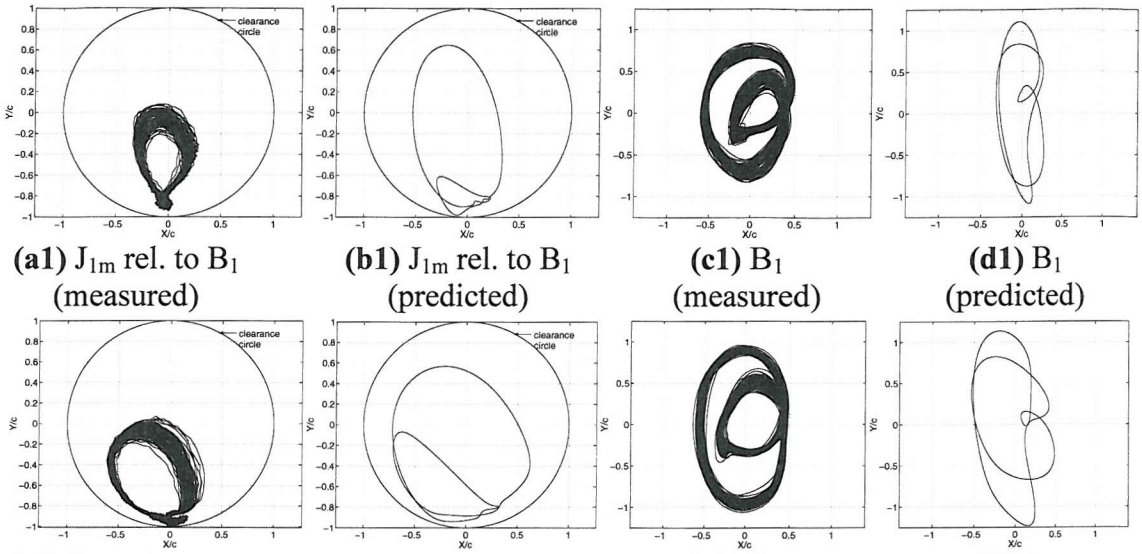

(a1) J_{1m} rel. to B_1 (measured) **(b1)** J_{1m} rel. to B_1 (predicted) **(c1)** B_1 (measured) **(d1)** B_1 (predicted)

(a2) J_{2m} rel. to B_2 (measured) **(b2)** J_{2m} rel. to B_2 (predicted) **(c2)** B_2 (measured) **(d2)** B_2 (predicted)

Figure 8.23: *2T-periodic motion at* 84 *rev/s for* $U_1 = 0$, $U_2 = 10.74 \times 10^{-4}$ *kgm* (i.e. second row of Table 8.4)

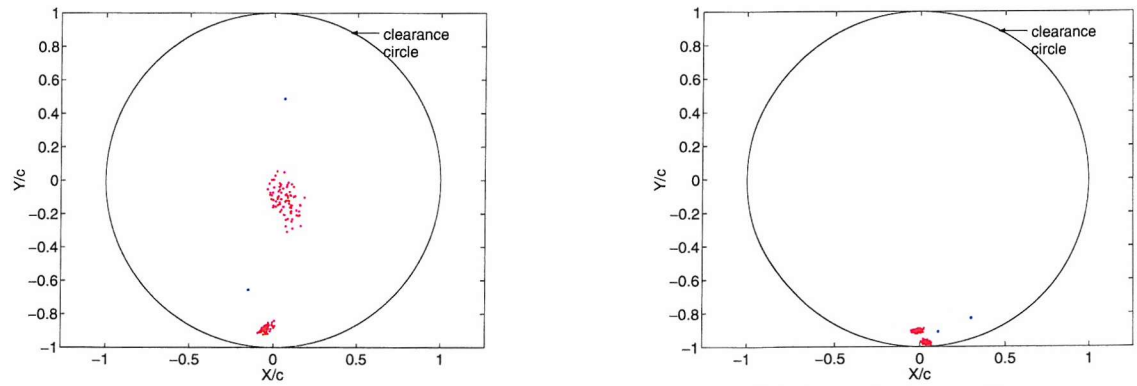

(a) J_{1m} relative to B_1 **(b)** J_{2m} relative to B_2

Figure 8.24: *Poincaré maps of orbital motion in Figure 8.23* ($\Omega t_k = 3\pi/4 + k2\pi$) measured - red (168 ± 1 samples); predicted - blue (100 samples)

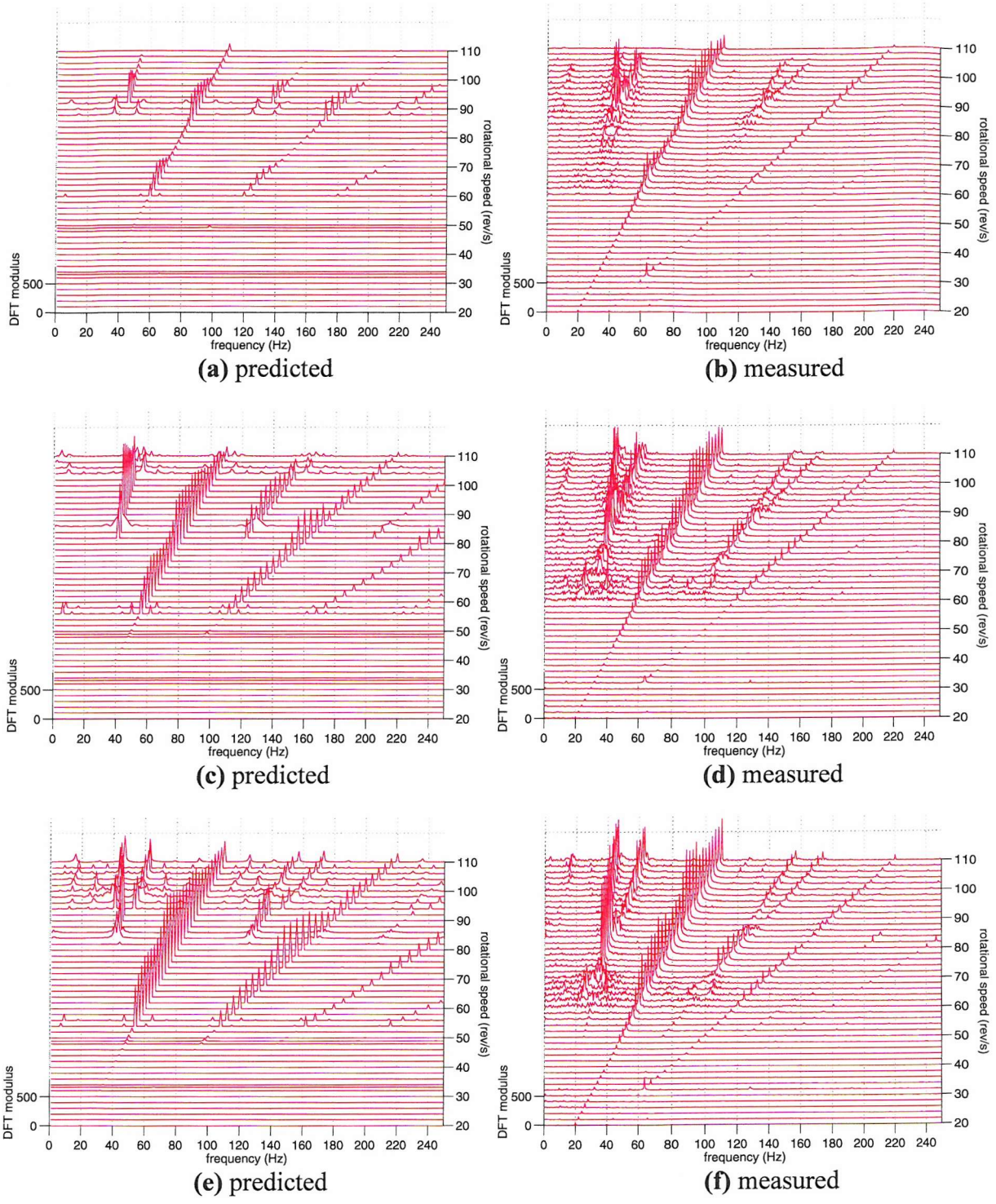

Figure 8.25: *Waterfall diagrams of the frequency spectra of the y displacement response of* J_{1m} *relative to* B_1 *for three states of unbalance* (first three rows of Table 8.4: **(a)**, **(b)** row 1; **(c)**, **(d)** row 2; **(e)**, **(f)** row 3). Data length: 1 s for predictions, 2 s for measurement.

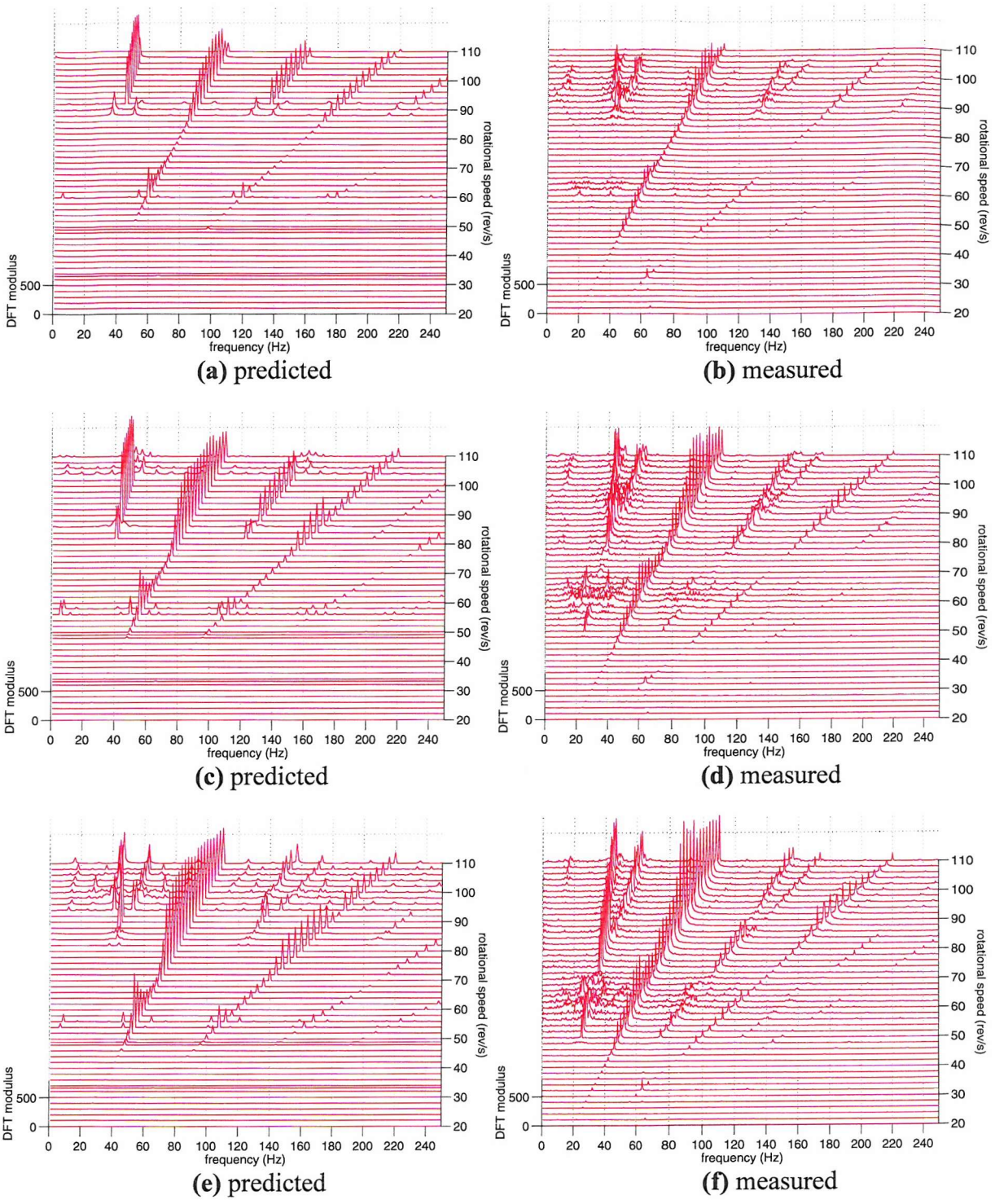

Figure 8.26: *Waterfall diagrams of the frequency spectra of the y displacement response of* J_{2m} *relative to* B_2 *for three states of unbalance* (first three rows of Table 8.4: **(a)**, **(b)** row 1; **(c)**, **(d)** row 2; **(e)**, **(f)** row 3). Data length: 1 s for predictions, 2 s for measurement.

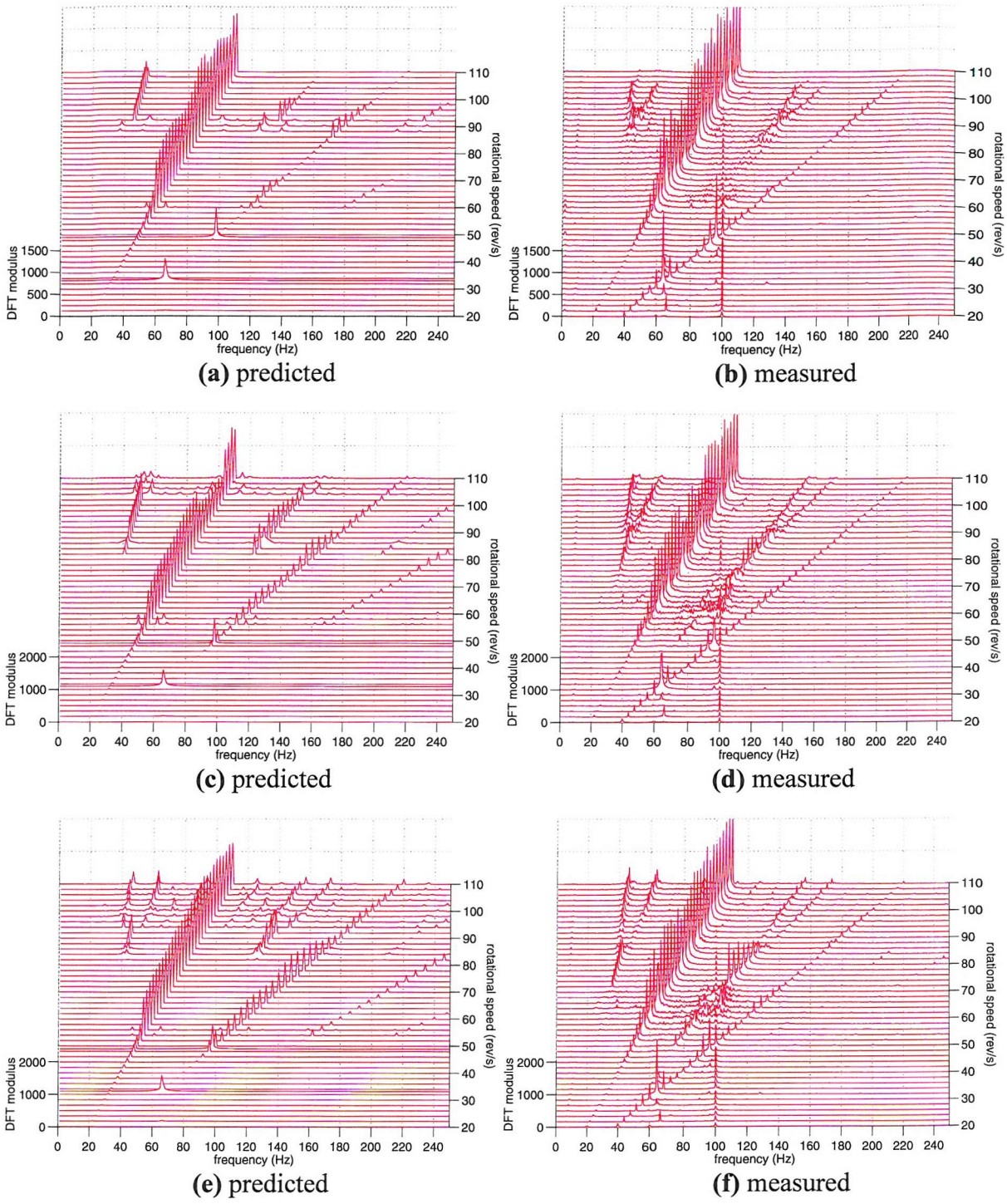

Figure 8.27: *Waterfall diagrams of the frequency spectra of the y displacement response of* B_1 *for three states of unbalance* (first three rows of Table 8.4: **(a)**, **(b)** row 1; **(c)**, **(d)** row 2; **(e)**, **(f)** row 3). Data length: 1 s for predictions, 2 s for measurement.

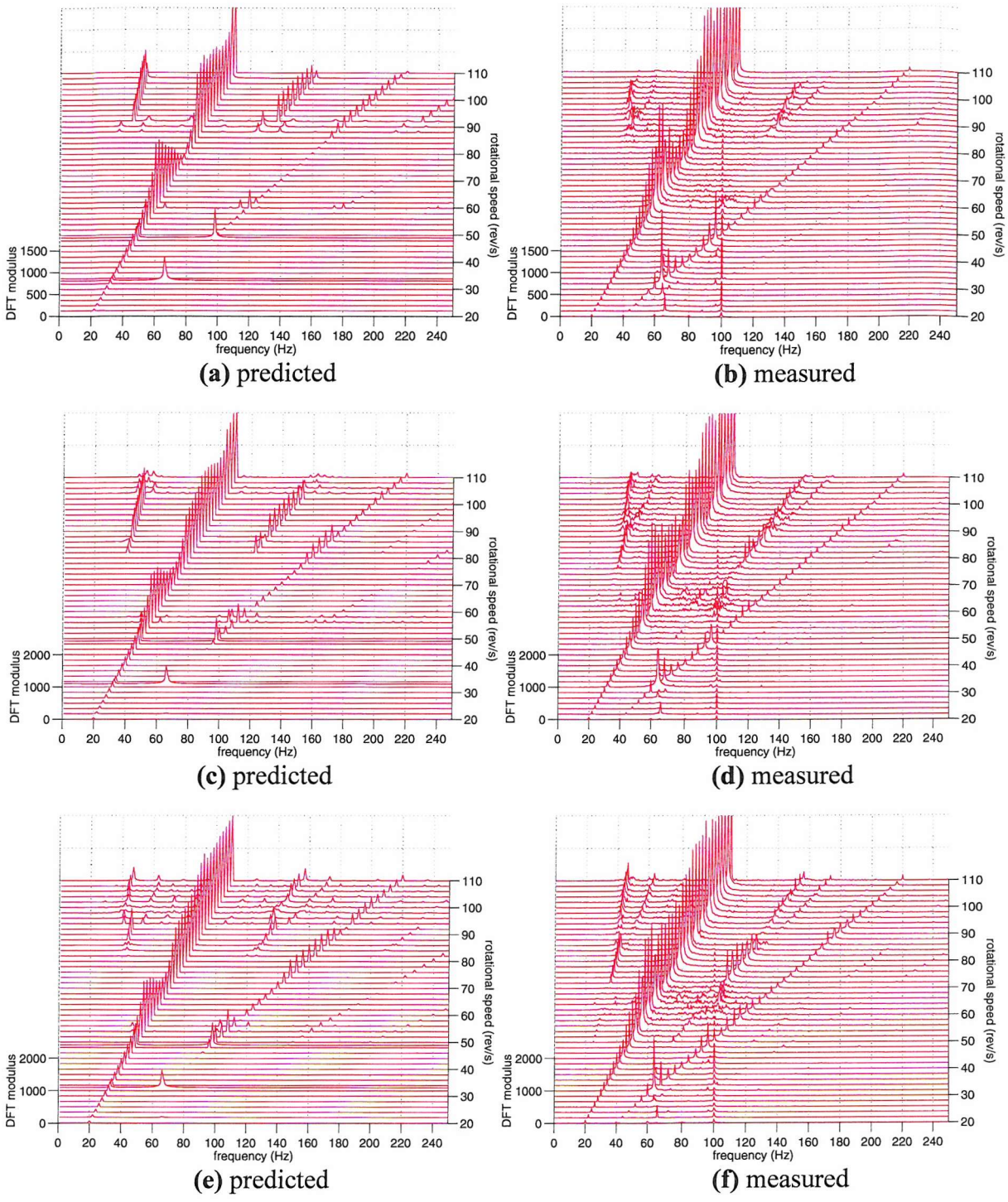

Figure 8.28: *Waterfall diagrams of the frequency spectra of the y displacement response of* B_2 *for three states of unbalance* (first three rows of Table 8.4: **(a)**, **(b)** row 1; **(c)**, **(d)** row 2; **(e)**, **(f)** row 3). Data length: 1 s for predictions, 2 s for measurement.

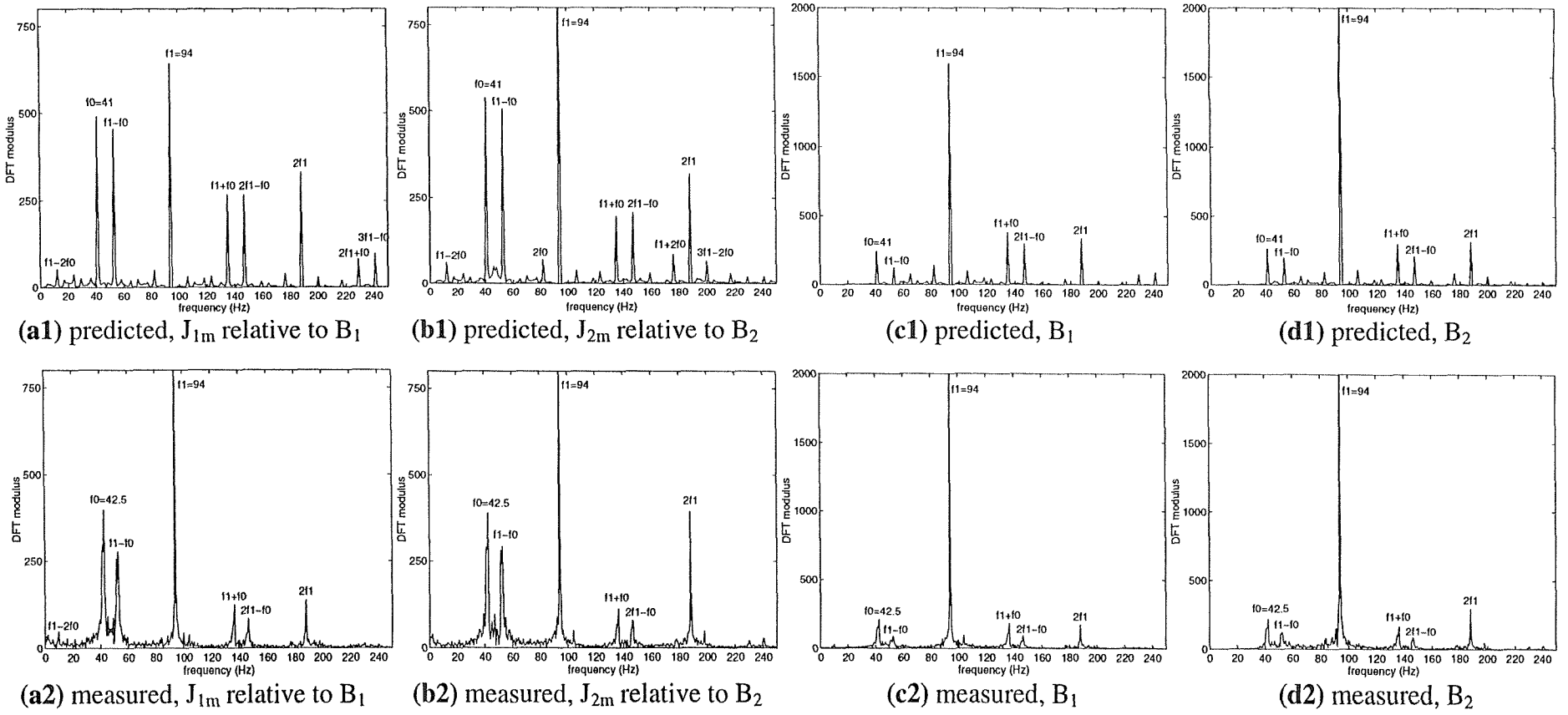

(a1) predicted, J_{1m} relative to B_1 **(b1)** predicted, J_{2m} relative to B_2 **(c1)** predicted, B_1 **(d1)** predicted, B_2

(a2) measured, J_{1m} relative to B_1 **(b2)** measured, J_{2m} relative to B_2 **(c2)** measured, B_1 **(d2)** measured, B_2

Figure 8.29: *Frequency spectra of the y displacement response at* 94 *rev/s* (unbalance as in row 3 of Table 8.4)
Data length: 1 s for predictions, 2 s for measurement.

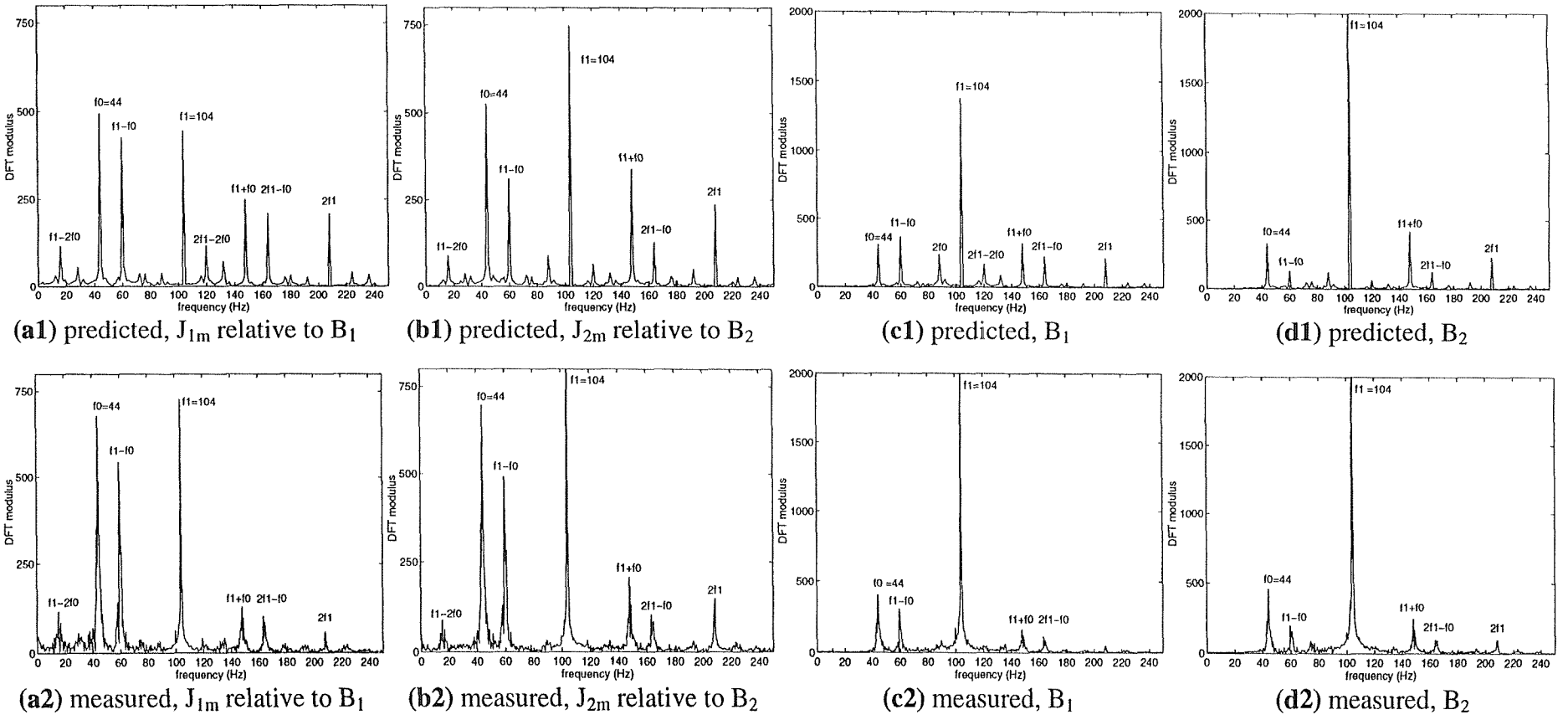

(a1) predicted, J_{1m} relative to B_1 **(b1)** predicted, J_{2m} relative to B_2 **(c1)** predicted, B_1 **(d1)** predicted, B_2

(a2) measured, J_{1m} relative to B_1 **(b2)** measured, J_{2m} relative to B_2 **(c2)** measured, B_1 **(d2)** measured, B_2

Figure 8.30: *Frequency spectra of the y displacement response at* 104 *rev/s* (unbalance as in row 3 of Table 8.4)
Data length: 1 s for predictions, 2 s for measurement.

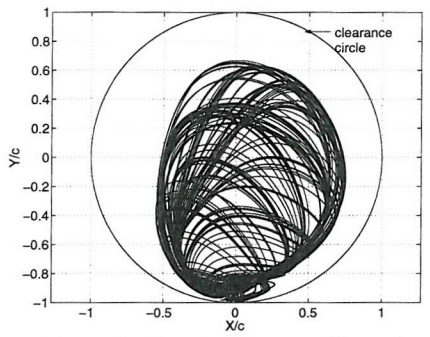

(a1) J_{1m} relative to B_1, predicted

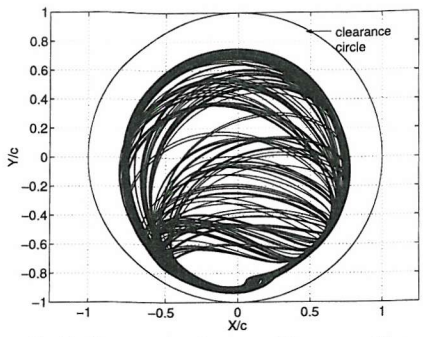

(b1) J_{2m} relative to B_2, predicted

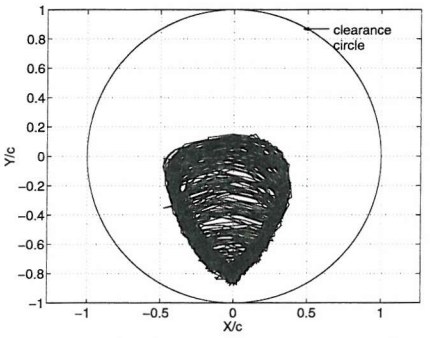

(a2) J_{1m} relative to B_1, measured

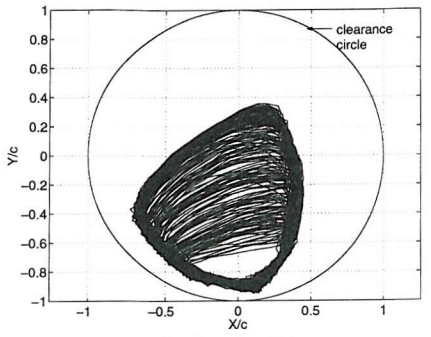

(b2) J_{2m} relative to B_2, measured

Figure 8.31: *Orbital motion at* 94 *rev/s over* 2 *s* (unbalance as in row 3 of Table 8.4)

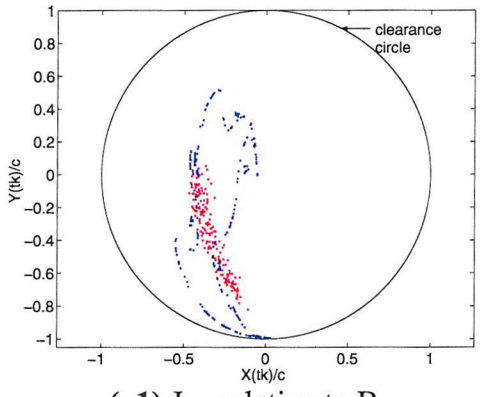

(a1) J_{1m} relative to B_1

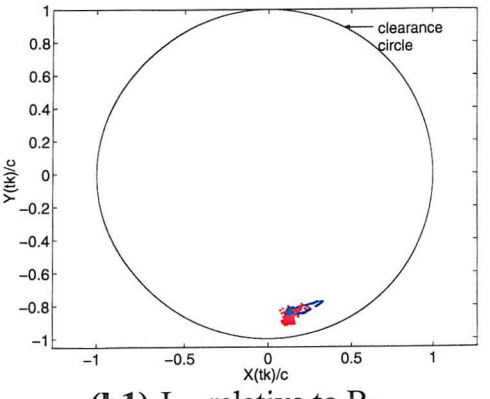

(b1) J_{2m} relative to B_2

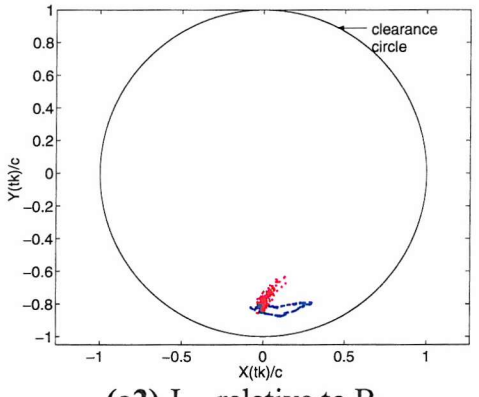

(a2) J_{1m} relative to B_1

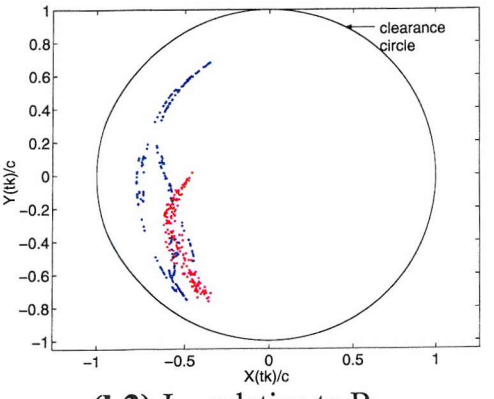

(b2) J_{2m} relative to B_2

Figure 8.32: *Poincaré maps of orbital motion in Figure 8.31 for different phases*: **(a1)**, **(b1)** $\Omega t_k = 3\pi/4 + k2\pi$; **(a2)**, **(b2)** $\Omega t_k = 7\pi/4 + k2\pi$. Measured - red (188 ± 1 samples); predicted - blue (300 samples)

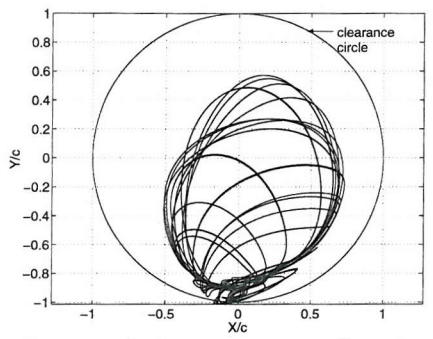

(a1) J_{1m} relative to B_1, predicted

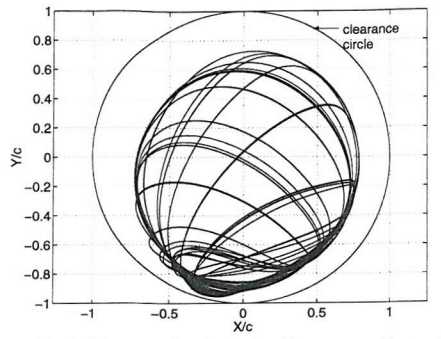

(b1) J_{2m} relative to B_2, predicted

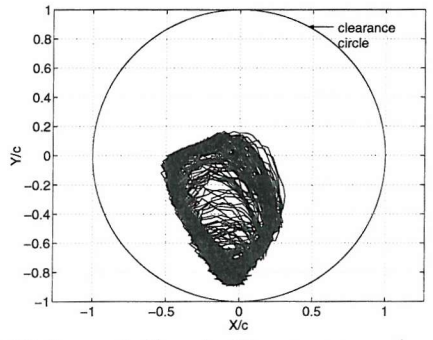

(a2) J_{1m} relative to B_1, measured

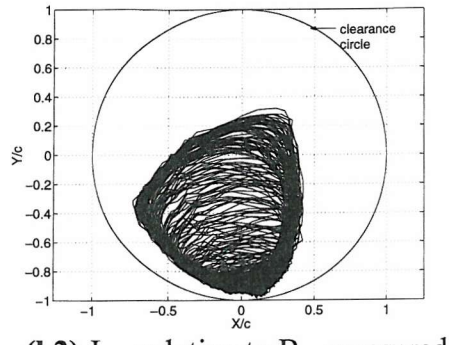

(b2) J_{2m} relative to B_2, measured

Figure 8.33: *Orbital motion at* 104 *rev/s over* 2 *s* (unbalance as in row 3 of Table 8.4)

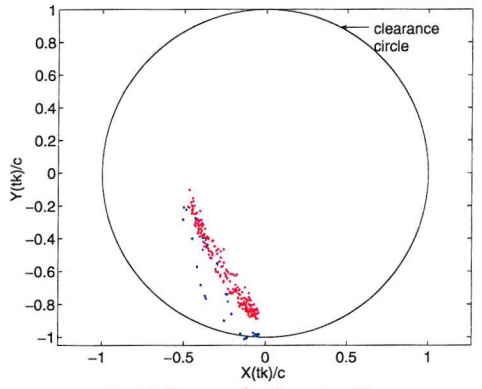

(a1) J_{1m} relative to B_1

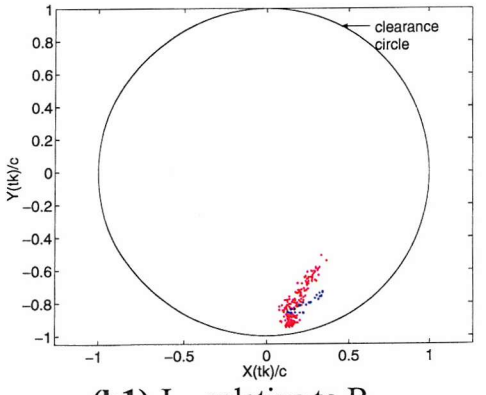

(b1) J_{2m} relative to B_2

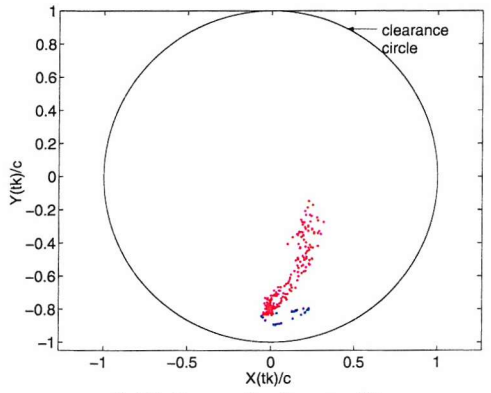

(a2) J_{1m} relative to B_1

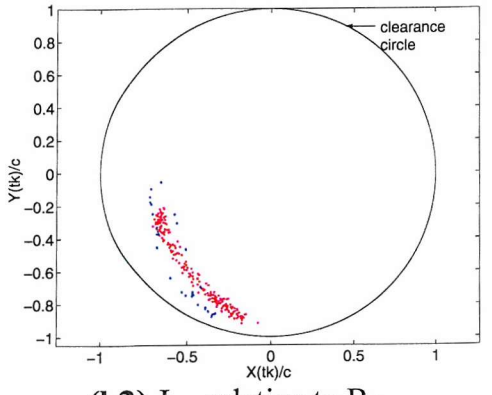

(b2) J_{2m} relative to B_2

Figure 8.34: *Poincaré maps of orbital motion in Figure 8.33 for different phases*: **(a1), (b1)** $\Omega t_k = 3\pi/4 + k2\pi$; **(a2), (b2)** $\Omega t_k = 7\pi/4 + k2\pi$. Measured - red (208 ± 1 samples); predicted - blue (300 samples)

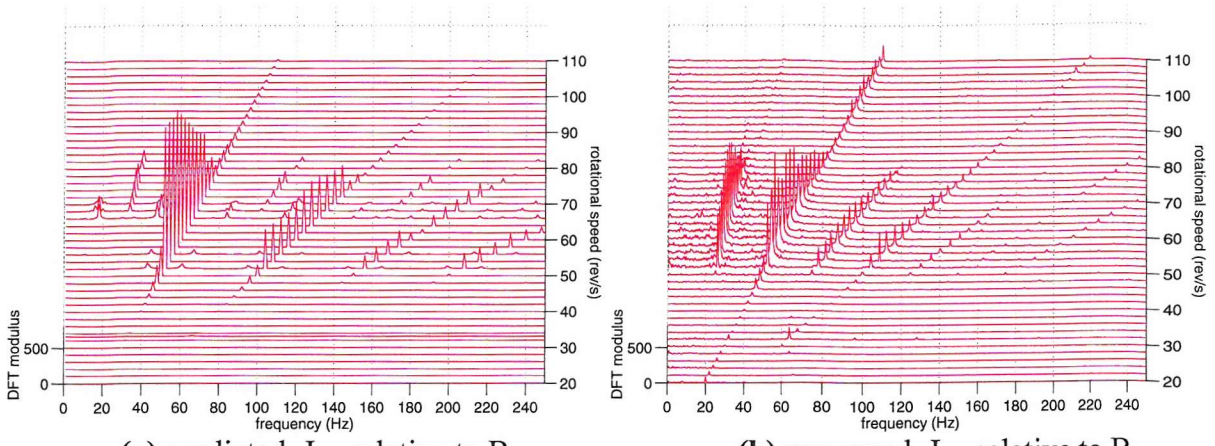

(a) predicted, J_{1m} relative to B_1 **(b)** measured, J_{1m} relative to B_1

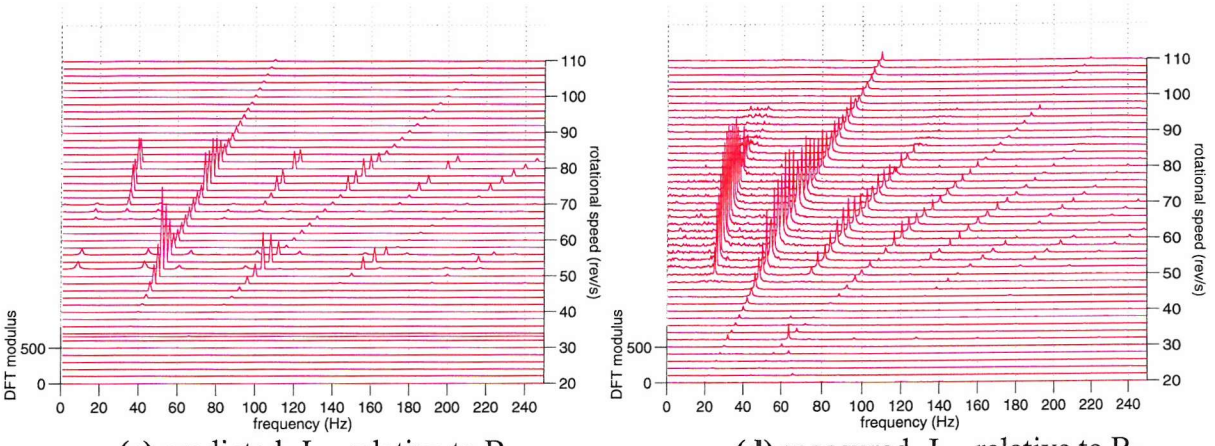

(c) predicted, J_{2m} relative to B_2 **(d)** measured, J_{2m} relative to B_2

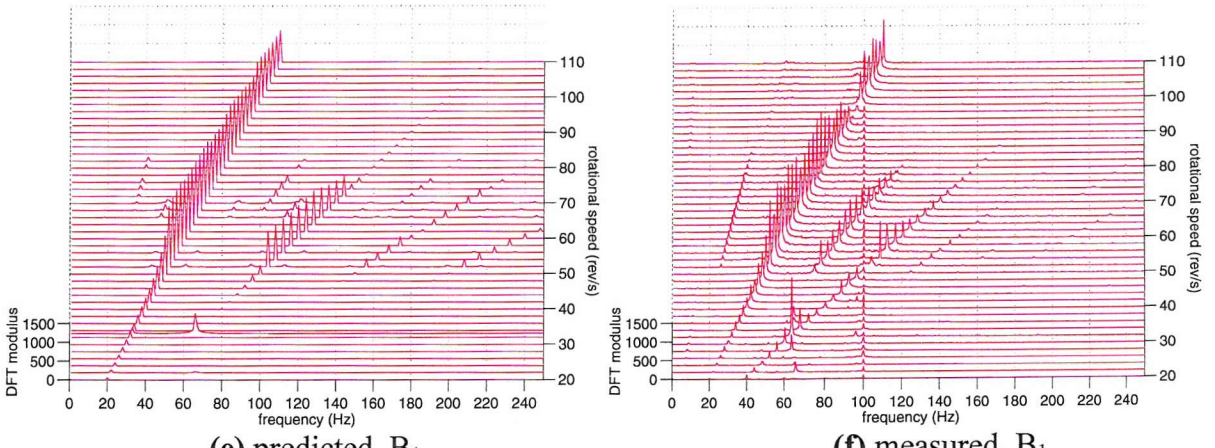

(e) predicted, B_1 **(f)** measured, B_1

Figure 8.35: *Waterfall diagrams of the frequency spectra of the y displacement response for symmetrical unbalance* (last row of Table 8.4). Data length: 1 s for predictions, 2 s for measurement. (Figure continues on the following page)

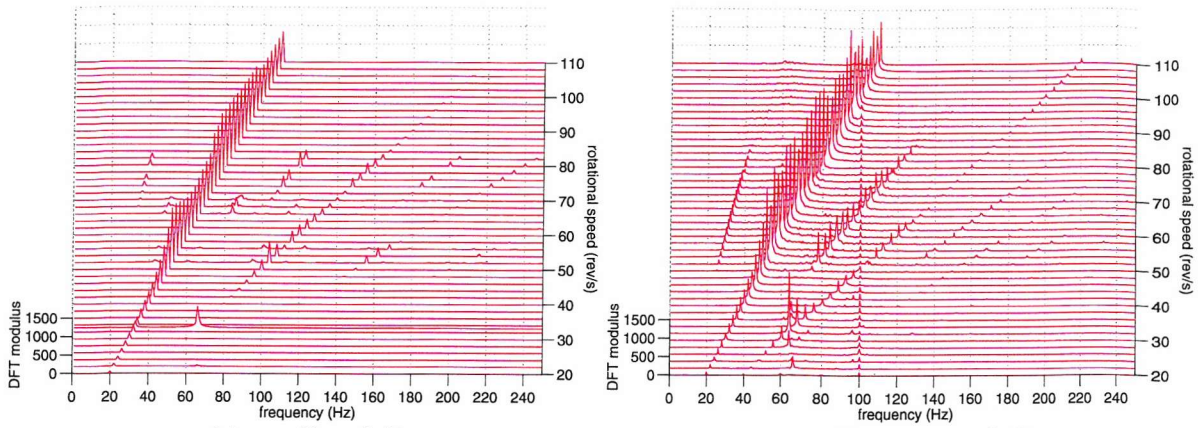

(e) predicted, B_2 **(f)** measured, B_2

Figure 8.35 (continued): *Waterfall diagrams of the frequency spectra of the y displacement response for symmetrical unbalance* (last row of Table 8.4). Data length: 1 s for predictions, 2 s for measurement.

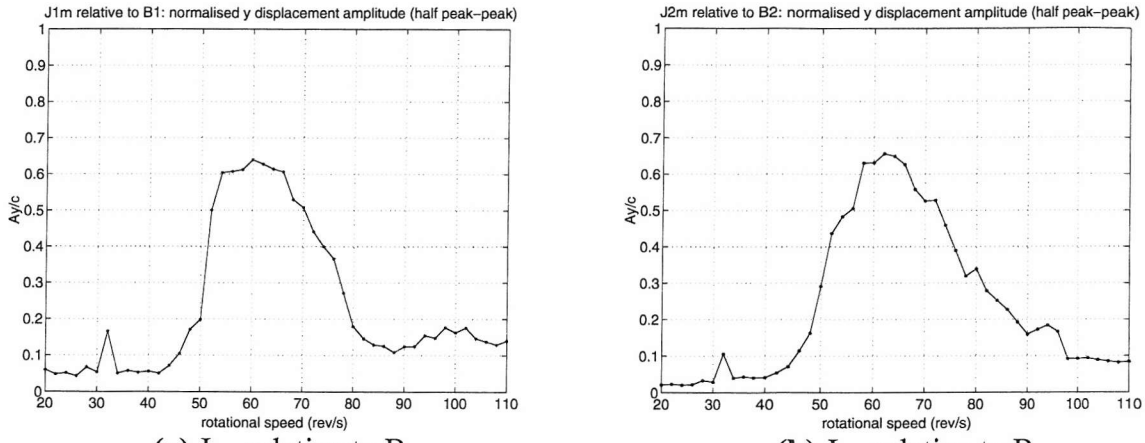

(a) J_{1m} relative to B_1 **(b)** J_{2m} relative to B_2

Figure 8.36: *Measured response at SFDs in y direction for symmetrical unbalance* (last row of Table 8.4). Vertical axes show the ratio of half the peak-to-peak displacement to *c*.

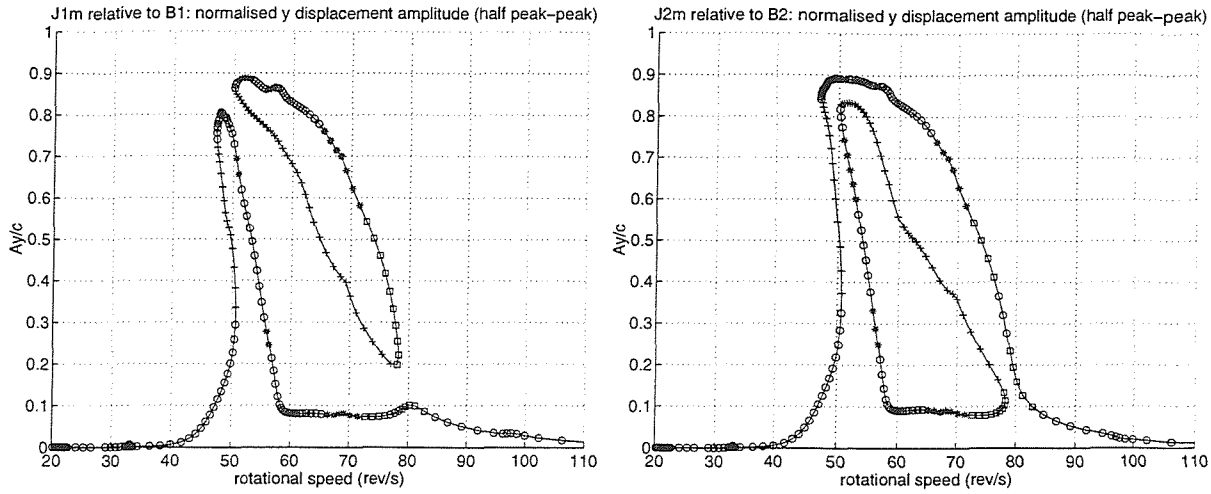

(a) J_{1m} relative to B_1 **(b)** J_{2m} relative to B_2

Figure 8.37: *Predicted T-periodic response at SFDs in y direction for symmetrical unbalance* (last row of Table 8.4). RHB $N=1$, $m=10$: "o" stable, "+" unstable (λ_l real, positive), "□" unstable (λ_l real, negative), "*" unstable (λ_l complex). Vertical axes show ratio of half peak-to-peak displacement to c.

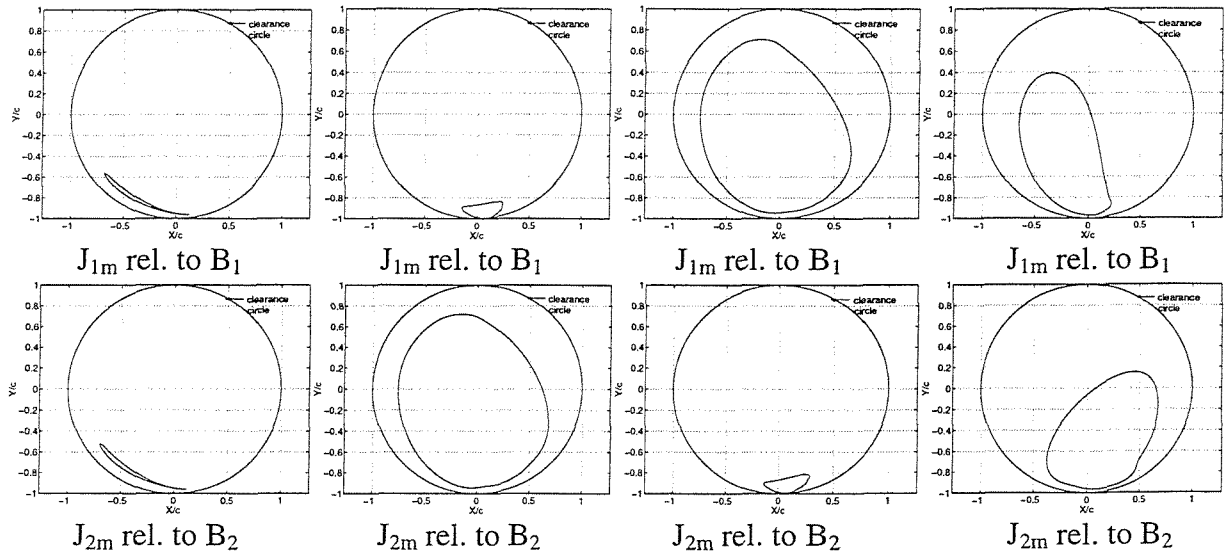

J_{1m} rel. to B_1 J_{1m} rel. to B_1 J_{1m} rel. to B_1 J_{1m} rel. to B_1

J_{2m} rel. to B_2 J_{2m} rel. to B_2 J_{2m} rel. to B_2 J_{2m} rel. to B_2

(a) 50 rev/s (stable) **(b)** 60 rev/s (stable) **(c)** 60 rev/s (stable) **(d)** 60 rev/s (unstable)

Figure 8.38: *Predicted T-periodic orbits of symmetrically unbalanced rig* ($U_1 = U_2 = 10.74\times10^{-4}$ kgm)

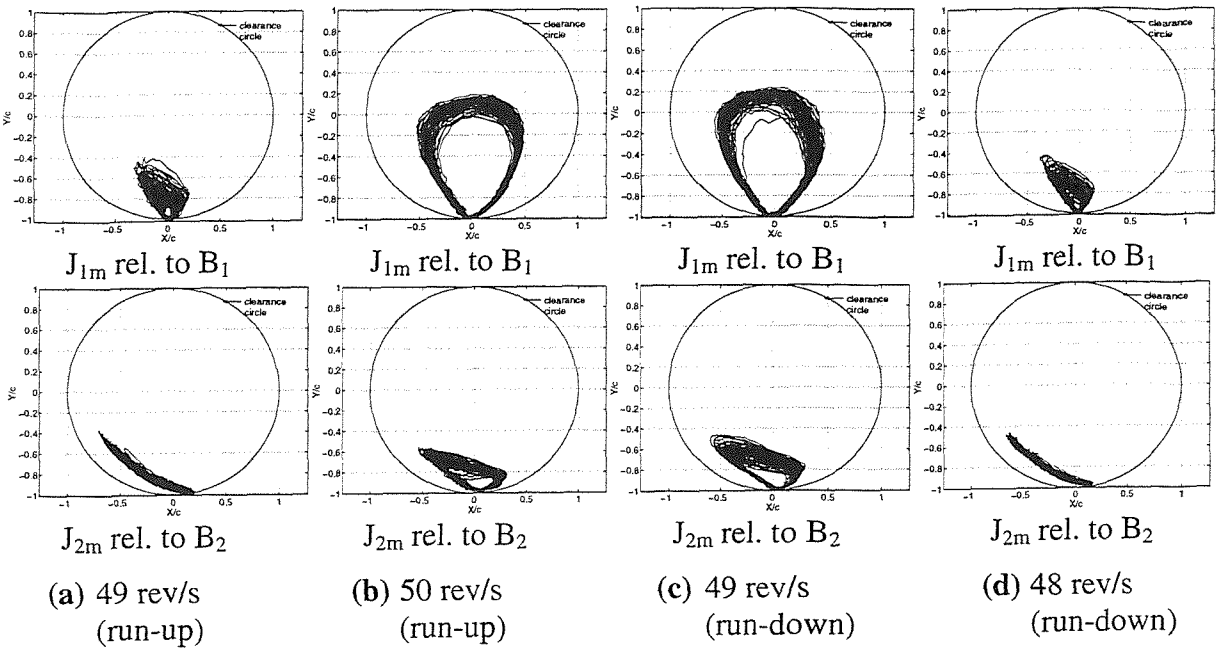

(a) 49 rev/s (run-up) **(b)** 50 rev/s (run-up) **(c)** 49 rev/s (run-down) **(d)** 48 rev/s (run-down)

Figure 8.39: *Hysterisis in measured orbital motion at SFDs for a symmetrical unbalance of* $U_1 = U_2 = 13.15 \times 10^{-4} kgm$

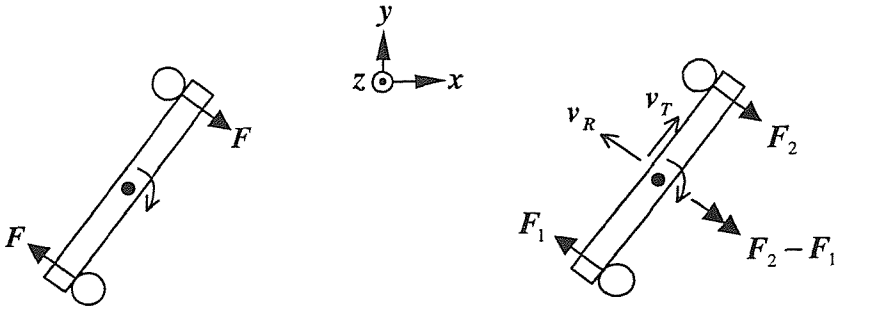

(a) no vibration at LH end **(b)** vibration at LH end

Figure 8.40: *Forces on driven bar of coupling at left hand (LH) end of the shaft*

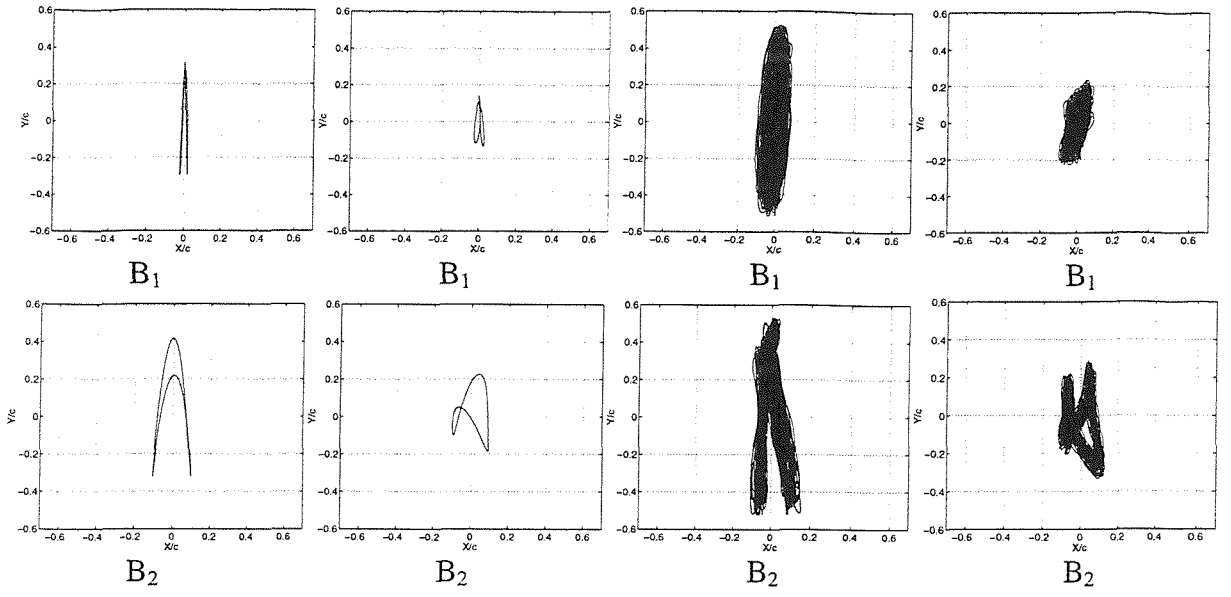

(a) 32.164 rev/s (predicted) **(b)** 32.175 rev/s (predicted) **(c)** 32 rev/s (measured) **(d)** 34 rev/s (measured)

Figure 8.41: *Contrast in bandwidth of predicted and measured super-harmonic resonances* (unbalance as in third row of Table 8.4)

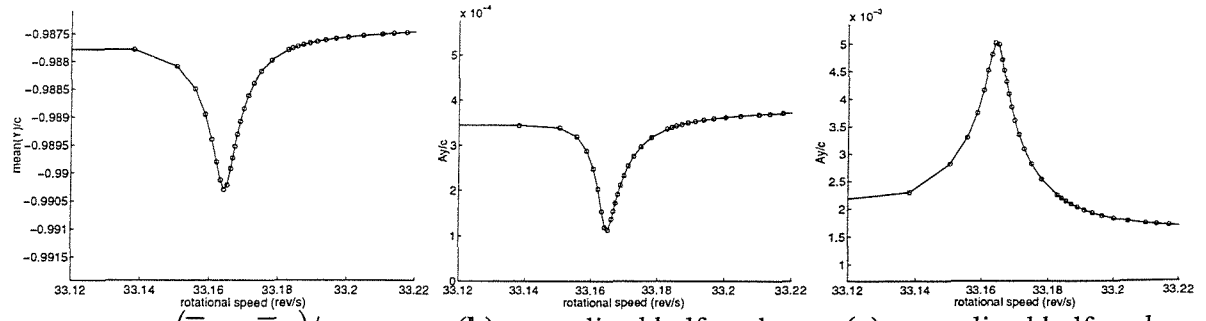

(a) $\left(\overline{Y}_{J_2} - \overline{Y}_{B_2}\right)/c$ **(b)** normalised half peak-to-peak y displacement of J_2 relative to B_2 **(c)** normalised half peak-to-peak y displacement of J_{2m} relative to B_2

Figure 8.42: *Predicted behaviour at SFD in the region of first super-harmonic resonance using RHB* $N = 1,\ m = 10$ (unbalance as in third row of Table 8.4)

9 CONCLUSIONS AND PROPOSALS FOR FUTURE RESEARCH

9.1 CONCLUSIONS

In this thesis an efficient integrated modelling technique has been presented for the full solution of the non-linear response of an unbalanced squeeze film damped rotor-dynamic system. The method was composed of three complementary modelling blocks, each of which is tractable to practical systems that have many degrees of freedom:

(1) receptance harmonic balance for the determination of periodic solutions;

(2) modal Floquet stability analysis of these solutions;

(3) numerical integration of a limited number of the modal equations, where deemed necessary according to the stability analysis results.

The advantages of the individual modelling blocks were discussed in Chapter 5, section 5.8. It suffices to reiterate here that such an approach can be easily interfaced with the current linear state-of-the-art in the rotor-dynamics industry. Linear rotor-dynamic methods can be used to analyse the linear subsystem for receptance functions and modal parameters. These two sets of data can then be used in a detailed non-linear analysis of the whole system that can be implemented using standard mathematical software.

The integrated model was applied to three configurations, of increasing complexity. These configurations were chosen to capture, to a limited extent, the essential features of practical squeeze film damped rotor-dynamic systems, particularly with respect to aero-engine applications:

(A) rigid rotor-flexible support structure;

(B) flexible rotor-rigid support structure;

(C) both rotor and support structure considered flexible.

In each case, the correlation between the three modelling blocks was found to be excellent and no computational difficulties were encountered when implementing the model on a 333 MHz, Pentium II computer, thereby verifying the feasibility of the model. In each case it was found that the best approach was to apply steps (1) and (2) for T-periodic solutions (where T is the period of rotation), using an initial approximation from step (3) at some convenient

speed to start off the arc-length continuation process. Regimes of instability of T-periodic motion were then analysed by step (3).

Experimental work showed that the integrated model was generally successful in predicting and explaining the highly non-linear performance, and reference is made to the specific conclusions of Chapters 6-8 for details. Such a study has bridged the gap that existed between advanced theoretical non-linear studies that lacked experimental validation and more experimentally oriented studies. The important non-linear phenomena encountered in the study are summarised below:

- 2-frequency quasi-periodic motion, wherein the frequency spectrum was composed of combinations of two fundamental frequencies, one being synchronous with the rotational speed, and the other being sub-synchronous. The simulations revealed the possibility of such motion leading to chaotic motion through a frequency-locking route, although this was not formally investigated.
- Sub-harmonic motions i.e. NT-periodic motions where N is an integer greater 1 ($N = 2$ in Chapters 6 and 8, and $N = 3$ in Chapter 7).
- Amplitude jump (of the spring-softening type) with a hysterisis effect; the asymmetric behaviour of a symmetrical unbalanced rotor was conclusively proven theoretically but not experimentally.
- The unusual generation of sub-critical super-harmonic resonance in the absolute motion under conditions where the unsupported squeeze film damper (SFD) ostensibly behaved as a rigid link (i.e. there was very little relative vibration across it).

The above phenomena were obtained with unsupported SFDs, although 2-frequency quasi-periodicity was also observed and predicted with a sprung SFD under conditions of high static offset and unbalance.

To a limited extent, the good correlation with experiment also served to provide additional validation to the model used to compute the SFD forces, which was based on a short incompressible film that cavitated at absolute zero pressure. This was particularly so for the sprung SFD used in configuration (B). The inherent uncertainty in oil film conditions in unsupported SFDs probably degraded speed-for-speed correlation between measurements and prediction. However, even in this case, the measured vibration still evolved largely as predicted over the operating speed range, particularly with respect to its orbital structure and its highly peculiar frequency content.

As shown here and elsewhere in the literature, despite being an economical design, unsupported SFDs can be quite fickle in their performance since this is totally dependent on

their ability to generate a sustained lift to support the static load. Hence, the performance of an unsupported SFD is strongly dependent on the nature of the structure with which it interacts. It was outside the scope of this thesis to provide design recommendations for the use of unsupported SFDs since these would be specific to the configurations studied. However, it is worth mentioning that the analysis conducted showed that such a SFD design provided safe passage through the critical speeds (by attenuating the vibration amplitude) when such speeds corresponded to bounce modes, in which the rotor exhibited much less deflection than the housings (Chapters 6 and 8). For the case where the critical speeds corresponded to flexural modes of the rotor (Chapter 7), the unsupported SFD was found to be highly unsatisfactory as regards vibration attenuation. In fact, it was inferior in all aspects to a badly centralised sprung SFD, even when the oil viscosity was nearly trebled. In the design stage, careful consideration should be given as to whether it would be more economical in the long term to statically off-load the damper either with a parallel retainer spring or leaving it unsprung but off-loading it with some flexible element (support) at a different location. It is believed that the modelling approach developed in this thesis would provide designers with an effective tool in reaching such decisions.

It should be added that the integrated model can be easily adapted to cover other types of motion-dependent non-linearities in rotor-dynamic systems by using the appropriate non-linear forcing functions.

9.2 PROPOSALS FOR FUTURE RESEARCH

It is proposed that the next stage of this project be the application of the modelling technique to a "real" problem, using the receptance functions of a real aero-engine rotor and support structure. Such an assembly might also be statically indeterminate.

Following this, it is proposed to consider the application of a similar modelling approach to dual rotor systems wherein two unbalanced rotors operate at different speeds. Such twin rotor configurations are typical of medium-sized jet engines. As mentioned in Chapter 8, the test rig for configuration C (Figure 8.1) has the facility to couple two independently driven rotors through the housing of the right hand squeeze film damper. With the single rotor configurations considered in this thesis, the *nominal motion* (i.e. the motion prior to the bifurcations) was T-periodic, for which the frequency spectrum was composed of frequencies $k_1 f_1$, where k_1 is an integer and f_1 is the synchronous frequency component ($=1/T$). A secondary Hopf bifurcation resulted in 2-frequency quasi-periodic motion with frequency

spectra composed of frequencies of the form $k_0 f_0 + k_1 f_1$ where k_0 is an integer and f_0 a sub-synchronous fundamental frequency that could only be determined from the time-marching solution. The value of f_0 was generally dependent on the value of the independently controlled synchronous frequency f_1. Although frequency-locking was identified as a potential route to chaotic motion, such motion either did not develop or was mild. With the dual shaft version, it is the nominal motion that has a frequency spectrum composed of the form $k_1 f_1 + k_2 f_2$, where k_1 and k_2 are integers, and the fundamentals f_1 and f_2 are both known and independent of each other, being equal to (and hence synchronous with) the respective speeds of the two shafts. Since the numerical values of f_1 and f_2 are generally rationally independent, the nominal motion is quasi-periodic. The nominal motion is now subject to a tertiary Hopf bifurcation, which ostensibly results in 3-frequency quasi-periodicity with a frequency spectrum composed of frequencies of the form $k_0 f_0 + k_1 f_1 + k_2 f_2$ where k_0 is an integer and f_0 the non-synchronous fundamental frequency that is dependent on both synchronous frequencies f_1 and f_2. As discussed in Chapter 3 (end of section 3.5), 3-frequency quasi-periodicity is thought to be highly unstable and it is highly probable that the motion immediately descends to chaos. Hence, unlike the single shaft version, it is highly likely that the emergence of the non-synchronous fundamental f_0 would mark the onset of chaos.

Since the nominal motion (i.e. the motion prior to the bifurcation) in a dual rotor system is quasi-periodic rather than periodic, the question arises as to what to do with the first two modelling blocks of the integrated model (i.e. periodic solution and stability analysis). Three options are available:

i. Ignore the first two modelling blocks and use the time-marching block only. However, apart from the computational burden, this will exclude unstable equilibrium solution possibilities and hence results in a restricted understanding of the non-linear dynamics involved.

ii. Approximate the nominal motion by an NT-periodic motion where T is chosen as either $1/f_1$ or $1/f_2$. The value of N is determined from the frequency spectrum of a time-marching solution at some speed where the motion is likely to be nominal. From this spectrum one can also establish which of the harmonics of the approximate common fundamental $1/NT$ are relevant to the problem. The Fourier coefficients of this approximate periodic motion are then used to initiate the arc-length continuation

procedure, which will then trace out a curve of NT-periodic solutions over a range of values of f_1 say, while keeping f_2 fixed, and vice-versa. These solutions approximate to the nominal quasi-periodic motion. During this solution process, those RHB equations corresponding to harmonics of $1/NT$ that were initially deemed irrelevant to the problem are simply omitted. The Floquet stability analysis block can then be used on these periodic solutions. In such a case, it is hoped that a secondary Hopf bifurcation of these NT-periodic solutions would correspond to a tertiary Hopf bifurcation of the actual quasi-periodic solutions that they substitute.

iii. Develop a 2-frequency quasi-periodic solution technique with two fundamental frequencies rather than just the one fundamental taken in periodic solution techniques. Such a method would be based on the compound Fourier series of eq. (3.30) (with $K = 2$ fundamental frequencies). Since Floquet theory applies only to the stability of a periodic solution, the stability analysis block would need to be generalised to cover the stability of the 2-torus defined by a 2-frequency quasi-periodic solution [43].

With method (iii), it is envisaged that difficulties will be encountered in the computation of the coefficients of the compound Fourier series expansion for the SFD forces. Moreover, to the author's knowledge, the theory of the stability of a 2-torus has not been developed. Hence, it appears that method (ii) provides the best compromise.

For such a dual rotor project it would also be desirable (though not essential) to devise a reliable method for the estimation of the Lyapunov exponent for use in such applications.

Another interesting project would be the investigation of the role of a squeeze film damper in controlling effects that are due to other sources of non-linearity e.g. rotor-stator rub and spline couplings.

10 REFERENCES

1. S. COOPER 1965 *Squeeze-film bearings*. British Patent No. 1002919.
2. A. H. CRAVEN, R. HOLMES 1972 *International Journal for Numerical Methods in Engineering* **5**, 17-24. The vibration of engine crankshafts - a fast numerical solution.
3. E. J. GUNTER, L. E. BARRETT, P. E. ALLAIRE 1977 *American Society of Mechanical Engineers Journal of Lubrication Technology* **99**, 57-64. Design of nonlinear squeeze-film dampers for aircraft engines.
4. R. A. COOKSON, S. S. KOSSA 1979 *International Journal of Mechanical Sciences* **21**, 334-338. The effectiveness of squeeze film damper bearings supporting rigid rotors without a centralising spring.
5. L. M. GREENHILL, H. D. NELSON 1982 *American Society of Mechanical Engineers Journal of Mechanical Design* **104**(2), 639-650. Iterative determination of squeeze film damper eccentricity for flexible rotor systems.
6. L. J. McLEAN, E. J. HAHN 1983 *American Society of Mechanical Engineers Journal of Lubrication Technology* **105**, 22-28. Unbalance behaviour of squeeze film damped multi-mass flexible rotor bearing systems.
7. L. J. McLEAN, E. J. HAHN 1985 *American Society of Mechanical Engineers Journal of Lubrication Technology*, **107** 402-410. Stability of squeeze film damped multi-mass flexible rotor bearing systems.
8. R. HOLMES, M. DOGAN 1982 *Journal of Mechanical Engineering Science* **24**(3), 129-137. Investigation of a rotor bearing assembly incorporating a squeeze-film damper bearing.
9. E. J. HAHN 1985 *Proceedings of the Institution of Mechanical Engineers* **199**(C1), 57-63. An energy approach to linearising squeeze-film damper forces.
10. S. CHEN, S. LIU 1986 *American Society of Mechanical Engineers Journal of Vibration, Acoustics, Stress and Reliability in Design* **108**, 434-440. Equivalent linearisation of a squeeze film damper.
11. A. EL-SHAFEI, R. V. ERANKI 1994 *American Society of Mechanical Engineers Journal of Engineering for Gas Turbines and Power* **116**, 682-691. Dynamic analysis of squeeze film damper supported rotors using equivalent linearisation.

12. P. Y. P. CHEN, E. J. HAHN, G. Y. WANG 1993 *The 38th ASME Int. Gas Turbine & Aeroengine Cong. & Expo. (Ohio)*, Paper No. 93-GT-428. Subharmonic oscillations in squeeze film damped rotor bearing systems without centralising springs.
13. J. Y. ZHAO, I. W. LINNETT, L. J. McLEAN 1994 *American Society of Mechanical Engineers Journal of Tribology* **116**, 361-368. Stability and bifurcation of unbalanced response of a squeeze film damped flexible rotor.
14. C. NATARAJ, H. D. NELSON 1989 *American Society of Mechanical Engineers Journal of Vibration, Acoustics, Stress, and Reliability in Design* **111**, 187-193. Periodic solutions in rotor dynamic systems with nonlinear supports: a general approach.
15. E. J. HAHN, P. Y. P. CHEN 1994 *American Society of Mechanical Engineers Journal of Tribology* **116**, 499-507. Harmonic balance analysis of general squeeze film damped multidegree-of-freedom rotor bearing systems.
16. R. SEYDEL 1988 *From Equilibrium to Chaos: Practical Bifurcation and Stability Analysis.* New York: Elsevier Science.
17. T. -N. SHIAU, A. -N. JEAN 1990 *American Society of Mechanical Engineers Journal of Vibration and Acoustics* **112**, 501-507. Prediction of periodic response of flexible mechanical systems with non-linear characteristics.
18. A. LIEW, N. S. FENG, E. J. HAHN 1999 *Proc. of ASME Design Engineering Technical Conference: 17th Biennial Conference on Mechanical Vibration and Noise, Sept. 12-15, 1999, Las Vegas*, paper no. DETC99/VIB-8263, 9pp. Application of transfer matrices to non-linear rotor-bearing systems.
19. P. BONELLO, M. J. BRENNAN 2001 *Journal of Sound and Vibration* **239**(3), 445-466. Modelling the dynamic behaviour of a supercritical rotor on a flexible foundation using the mechanical impedance technique.
20. M. PETYT 1998 *Introduction to Finite Element Vibration Analysis.* Cambridge: Cambridge University Press.
21. F. CHU, R. HOLMES 2000 *Tribology International* **33**(2), 81-97. The damping capacity of the squeeze film damper in suppressing the vibration of a rotating assembly.
22. K. H. BECKER, E. STEINHARDT 1990 *J. M. Montalvao e Silva and F. A. Pina da Silva (eds.), Vibration and Wear in High Speed Rotating Machinery*, 263-277. A general method for rotordynamic analysis.
23. R. W. ARMENTROUT, E. J. GUNTER 1999 *SPIE Proceedings* **3727(1)**, 290-296. Transient modal analysis of nonlinear rotor-bearing systems.

24. J. Y. ZHAO, E. J. HAHN 1993 *Proceedings of the Institution of Mechanical Engineers* **207**, 383-392. Subharmonic, quasi-periodic and chaotic motions of a rigid rotor supported by an eccentric squeeze film damper.
25. THE MATHWORKS INC. 1999 *MATLAB®*. Version 5.3.1.29215a (R11.1).
26. F. CHU, R. HOLMES 1998 *American Society of Mechanical Engineers Journal of Engineering for Gas Turbines and Power* **120**, 1-9. The effect of squeeze film damper parameters on the unbalance response and stability of a flexible rotor.
27. J. Y. ZHAO, I. W. LINNETT, L. J. McLEAN 1994 *American Society of Mechanical Engineers Journal of Vibration and Acoustics* **116**, 357-363. Subharmonic and quasi-periodic motions of an eccentric squeeze film damper-mounted rigid rotor.
28. J. E. H. SYKES, R. HOLMES 1990 *Proceedings of the Institution of Mechanical Engineers* **204**, 83-99. The effects of bearing misalignment on the non-linear vibration of aero-engine rotor-damper assemblies.
29. M. C. LEVESLEY, R. HOLMES 1994 *Proceedings of the Institution of Mechanical Engineers*, **208**, 52-66. Experimental investigation into the vibration response of an aero-engine rotor-damper assembly
30. R. HOLMES, S. BOX 1992 *Machine Vibration* **1**, 71-79. On the use of squeeze-film dampers in rotor support structures.
31. R. HOLMES, M. M. DEDE 1989 *Proceedings of the Institution of Mechanical Engineers* **203**, 25-34. Non-linear phenomena in aero-engine rotor vibration.
32. R. HOLMES, J. E. H. SYKES 1996 *Proceedings of the Institution of Mechanical Engineers* **210**, 39-51. The vibration of an aero-engine rotor incorporating two squeeze-film dampers.
33. J. L. NIKOLAJSEN, R. HOLMES 1979 *Journal of Mechanical Engineering Science* **21**(4), 247-252. Investigation of squeeze-film isolators for the vibration control of a flexible rotor.
34. R. C. HILBORN 1994 *Chaos and Nonlinear Dynamics*. New York: Oxford University Press.
35. E. OTT 1993 *Chaos in Dynamical Systems*. Cambridge: Cambridge University Press.
36. M. BOTMAN 1976 *American Society of Mechanical Engineers Journal of Engineering for Power* **98**, 393-400. Experiments on squeeze film dampers for turbomachinery.
37. X. LI, D. L. TAYLOR 1987 *American Society of Mechanical Engineers Journal of Tribology* **109**, 169-176. Nonsynchronous motion of squeeze film damper systems.

38. J. J. THOMSEN 1997 *Vibrations and Stability*. Maidenhead: McGraw-Hill.
39. F. F. EHRICH 1972 *American Society of Mechanical Engineers Journal of Engineering for Industry*, February 1972, 181-184. Sum and difference frequencies in vibration of high speed rotating machinery.
40. F. F. EHRICH 1988 *American Society of Mechanical Engineers Journal of Vibration, Acoustics, Stress, and Reliability in Design* **110**, 9-16. High order subharmonic response of high speed rotors in bearing clearance.
41. F. F. EHRICH 1992 *American Society of Mechanical Engineers Journal of Vibration and Acoustics* **114**, 93-100. Observations of subcritical superharmonic and chaotic response in rotordynamics.
42. P. BONELLO, M. J. BRENNAN, R. HOLMES 2002 *Journal of Sound and Vibration* **249**(4), 743-773. Non-linear modelling of rotor dynamic systems with squeeze film dampers – an efficient integrated approach.
43. G. IOOS, D. D. JOSEPH 1980 *Elementary Stability and Bifurcation Theory*. New York: Springer-Verlag.
44. R. GRIMSHAW 1990 *Nonlinear Ordinary Differential Equations*. Oxford: Blackwell Scientific Publications.
45. C. S. HSU 1972 *American Society of Mechanical Engineers Journal of Applied Mechanics* June 1972, 551-558. Impulsive parametric excitation: theory.
46. C. S. HSU 1973 *American Society of Mechanical Engineers Journal of Applied Mechanics* March 1973, 78-86. Applications of the theory of impulsive parametric excitation and new treatments of general parametric excitation problems.
47. D. J. EWINS 1984 *Modal Testing: Theory and Practice*. Letchworth: Research Student Press.
48. E. KRAMER 1993 *Dynamics of Rotors and Foundations*. Berlin: Springer-Verlag.
49. E. J. GUNTER 1985 *American Society of Mechanical Engineers Journal of Tribology* **107**, 409-410. Discussion.
50. A. WOLF, J. B. SWIFT, H. L. SWINNEY, J. A. VASTANO 1985 *Physica* **16D**, 285-317. Determining Lyapunov exponents from a time series.
51. X. ZENG, R. EYKHOLT, R. A. PIELKE 1991 *Physics Review Letters* **25**, 3229-3232. Estimating the Lyapunov-exponent spectrum from short time series of low precision.
52. K. SHIN 1996 *Ph.D. Thesis, University of Southampton, UK*. Characterisation and identification of chaotic dynamical systems.

53. M. M. DEDE, M. DOGAN, R. HOLMES 1985 *American Society of Mechanical Engineers Journal of Tribology* **107**, 411-418. The damping capacity of a sealed squeeze film bearing.

54. P. BONELLO, M. J. BRENNAN, R. HOLMES 2000 *ISVR Technical Memorandum No.* 857, *University of Southampton, UK.* Modelling the non-linear dynamics of an aero engine low pressure rotor mounted on squeeze film bearings.

55. N. S. FENG, E. J. HAHN 1985 *American Society of Lubrication Engineers Transactions* **29**(3), 361-369. Density and viscosity models for two-phase homogeneous hydrodynamic damper fluids.

56. N. S. FENG, E. J. HAHN 1985 *American Society of Lubrication Engineers Transactions* **29**(3), 353-360. Cavitation effects on squeeze-film damper performance.

57. B. HUMES, R. HOLMES 1978 *Journal of Mechanical Engineering Science* **20**(5), 283-289. The role of subatmospheric film pressures in the vibration performance of squeeze-film bearings.

58. R. HOLMES, M. DEDE 1980 *I. Mech. E. Second International Conference on Vibrations in Rotating Machinery* **C260/80**. Dynamic pressure determination in a squeeze-film damper.

59. N. S. FENG, E. J. HAHN 1987 *American Society of Mechanical Engineers Journal of Tribology* **109**, 149-154. Effects of gas entrainment on squeeze film damper performance.

60. L. SAN ANDRES, J. M. VANCE 1986 *American Society of Mechanical Engineers Journal of Engineering for Gas Turbines and Power* **108**, 332-339. Effects of fluid inertia and turbulence on the force coefficients for squeeze film dampers.

61. C. F. GERALD 1980 *Applied Numerical Analysis.* Second Edition, Reading, Massachusetts: Addison-Wesley Publishing Company.

62. E. J. HEARN 1991 *Mechanics of Materials.* Volume 1, Second Edition, Oxford: Pergamon Press.

63. M. DOGAN 1983 *Ph.D. Thesis, University of Sussex.* Investigation of an Aero-Engine Squeeze-Film Damper.

64. M. BURGHARDT 1998 *M.Sc. Thesis, University of Southampton.* An Investigation of The Squeeze Film Damping of a Super-Critical Rotor.

65. G. DAHLQUIST 1974 *Numerical Methods.* Englewood Cliffs N. J.: Prentice-Hall.

66. S. D. CONTE, C. DE BOOR 1972 *Elementary Numerical Analysis: An Algorithmic Approach.* New York: McGraw-Hill Book Company.

67. BENTLY NEVADA CORPORATION 1993 *3300 8mm Proximity Transducer System.* Revision M, October 1993.

A1 ITERATIVE SCHEME FOR RHB

This appendix presents an algorithm that traces out a speed response curve of NT-periodic solutions (N is a fixed positive integer) of the receptance harmonic balance equations, using the arc-length continuation method i.e. it computes the solutions $\hat{\mathbf{w}}_i = \begin{bmatrix} \hat{\mathbf{v}}_i \\ \hat{\Omega}_i \end{bmatrix}$ of the system of eqs. (5.24)

$$\begin{bmatrix} \mathbf{p}(\hat{\mathbf{v}}, \hat{\Omega}) \\ g(\hat{\mathbf{v}}, \hat{\Omega}, \sigma) \end{bmatrix} = \mathbf{0} \tag{A1.1}$$

at points i, for which $\sigma = \sigma_i$. The system (A1.1) is solved using an iterative predictor-corrector scheme adapted from the theory in [16, 65]. The algorithm is presented with respect to the general system of equations

$$\mathbf{r}(\mathbf{y}, \mu) = \mathbf{0} \tag{A1.2}$$

where the vector of unknowns is $\mathbf{y}$, $\mathbf{r}$ is a non-linear vector function of $\mathbf{y}$, and μ the control parameter. This general form is chosen since, as explained in section 5.3, page 64, the determination of the first point on the speed response curve requires the solution of the original system of equations (5.18):

$$\mathbf{p}(\hat{\mathbf{v}}, \hat{\Omega}) = \mathbf{0} \tag{A1.3}$$

For the determination of the first point on the speed response, eq. (A1.2) represents eq. (A1.3) i.e. $\mathbf{y}$ is $\hat{\mathbf{v}}$, the control parameter μ is $\hat{\Omega}$ and $\mathbf{r}(\mathbf{y}, \mu) = \mathbf{p}(\hat{\mathbf{v}}, \hat{\Omega})$. For subsequent points, eq. (A1.2) represents eq. (A1.1) i.e. $\mathbf{y}$ is $\hat{\mathbf{w}} = \begin{bmatrix} \hat{\mathbf{v}} \\ \hat{\Omega} \end{bmatrix}$, the control parameter μ is σ and $\mathbf{r}(\mathbf{y}, \mu) = \begin{bmatrix} \mathbf{p}(\hat{\mathbf{v}}, \hat{\Omega}) \\ g(\hat{\mathbf{v}}, \hat{\Omega}, \sigma) \end{bmatrix}$.

A1.1 ALGORITHM

The following algorithm finds the solutions $\hat{\mathbf{w}}_i = \begin{bmatrix} \hat{\mathbf{v}}_i \\ \hat{\Omega}_i \end{bmatrix}$ at $\sigma = \sigma_i$, $i = 1 \ldots n_{totalsol}$ where σ_1 is arbitrarily set to 0. Let $\mathbf{y} = \mathbf{y}_i$ be the unknown solution of eq. (A1.2) for $\mu = \mu_i$: $\mathbf{y}_i^{(k)}$ is the k^{th} iterate for $\mathbf{y}_i$.

FOR $i = 1 \ldots n_{totalsol}$ DO STEPS A, B, C

A. SPECIFY EQUATION AND CURRENT VALUE OF CONTROL PARAMETER

If $i = 1$

Eq. (A1.2) represents eq. (A1.3)

Choose non-dimensional starting speed $\hat{\Omega}_1$

If $i > 1$

Eq. (A1.2) represents eq. (A1.1)

Choose arc length interval $\Delta\sigma$

$\mu_i = \mu_{i-1} + \Delta\mu$

B. PREDICTOR STEP

For $i = 1$:

In the case of a non-degenerate rotor, if $N = 1$ and $\hat{\Omega}_1$ is low, from eq. (5.26):

$$\hat{\mathbf{y}}_1^{(0)} = \begin{bmatrix} \mathbf{h}_0 / c \\ \mathbf{0} \end{bmatrix}$$

otherwise,

$\hat{\mathbf{y}}_1^{(0)}$ is determined by performing the time-marching solution at $\hat{\Omega} = \hat{\Omega}_1$ and computing the Fourier coefficients of the SFD response(s).

For $i = 2$:

$\mathbf{y}_2^{(0)}$ determined from a tangent predictor [16]:

$$\mathbf{y}_2^{(0)} = \mathbf{y}_1 + (\mu_2 - \mu_1)(d\mathbf{y}/d\mu)\big|_{\mu=\mu_1}$$

The evaluation of the tangent vector $(d\mathbf{y}/d\mu)\big|_{\mu=\mu_1}$ is explained in section A1.2.

For $i > 2$:

$\mathbf{y}_i^{(0)}$ determined from a secant predictor [16]:

$$\mathbf{y}_i^{(0)} = \mathbf{y}_{i-1} + \left(\frac{\mu_i - \mu_{i-1}}{\mu_{i-1} - \mu_{i-2}} \right) (\mathbf{y}_{i-1} - \mathbf{y}_{i-2})$$

C. CORRECTOR STEP

C1. Compute the Jacobian matrix of $\mathbf{r}(\mathbf{y}, \mu)$ with respect to $\mathbf{y}$ at $\mathbf{y} = \mathbf{y}_i^{(0)}$, $\mu = \mu_i$:

$$\mathbf{J}_i^{(0)} = \partial \mathbf{r} / \partial \mathbf{y} \Big|_{\mathbf{y}=\mathbf{y}_i^{(0)}, \mu=\mu_i}$$

$k = 0$

C2. Apply the damped Newton-Raphson method [65]:

$$\mathbf{y}_i^{(k+1)} = \mathbf{y}_i^{(k)} - \chi \mathbf{H}_i^{(k)} \mathbf{r}_i^{(k)}$$

where: $\mathbf{r}_i^{(k)} = \mathbf{r}(\mathbf{y}_i^{(k)}, \mu_i)$, $\mathbf{H}_i^{(k)} = (\mathbf{J}_i^{(k)})^{-1}$, $0 < \chi \leq 1$ is the damping factor

C3. Increase k by 1

C4. While $\left| \mathbf{y}_i^{(k)} - \mathbf{y}_i^{(k-1)} \right| \leq tol$ do steps C4.1-C4.3:

C4.1. Update $\mathbf{H}_i^{(k)}$ using Broyden's method [65]:

$$\mathbf{H}_i^{(k)} = \mathbf{H}_i^{(k-1)} - \frac{(\mathbf{H}_i^{(k-1)} \mathbf{b} - \mathbf{a}) \mathbf{a}^{\mathrm{T}} \mathbf{H}_i^{(k-1)}}{\mathbf{a}^{\mathrm{T}} \mathbf{H}_i^{(k-1)} \mathbf{b}}$$

where: $\mathbf{a} = \mathbf{y}_i^{(k)} - \mathbf{y}_i^{(k-1)}$, $\mathbf{b} = \mathbf{r}_i^{(k)} - \mathbf{r}_i^{(k-1)}$

C4.2. Compute $\mathbf{y}_i^{(k+1)}$ using damped Newton –Raphson method, step C2

C4.3. Increase k by 1

C5. While $\left(\left| \mathbf{y}_i^{(k)} - \mathbf{y}_i^{(k-1)} \right| \leq eps \right)$ or $\left(\left| \mathbf{r}_i^{(k)} \right| \leq eps \right)$ do steps C5.1-C5.3:

C5.1. Update $\mathbf{H}_i^{(k)}$ using step C4.1

C5.2. Compute $\mathbf{y}_i^{(k+1)}$ using undamped Newton-Raphson method: step C2 with

$\chi = 1$

C5.3. Increase k by 1

C6. $\mathbf{y}_i = \mathbf{y}_i^{(k)}$

C7. If $i = 1$ (i.e. solved eq. (A1.2) is eq. (A1.3))

$\hat{\mathbf{v}}_1 = \mathbf{y}_1$ and $\hat{\Omega}_1 = \mu_1$

$$\hat{\mathbf{w}}_1 = \begin{bmatrix} \hat{\mathbf{v}}_1 \\ \hat{\Omega}_1 \end{bmatrix} \text{ and } \sigma_1 = 0$$

If $i > 1$ (i.e. solved eq. (A1.2) is eq. (A1.1))

$\hat{\mathbf{w}}_i = \mathbf{y}_i$ and $\sigma_i = \mu_i$

In step C1 the Jacobian matrix is defined as follows:

If $\mathbf{y} = \begin{bmatrix} y_1 & \cdots & y_{n_y} \end{bmatrix}^T$ and $\mathbf{r}(\mathbf{y}, \mu) = \begin{bmatrix} r_1(y_1, \ldots, y_{n_y}, \mu) & \cdots & r_{n_y}(y_1, \ldots, y_{n_y}, \mu) \end{bmatrix}^T$, then the Jacobian of $\mathbf{r}$ with respect to $\mathbf{y}$ is

$$\frac{\partial \mathbf{r}}{\partial \mathbf{y}} = \begin{bmatrix} \partial r_1/\partial y_1 & \cdots & \partial r_1/\partial y_{n_y} \\ \vdots & \vdots & \vdots \\ \partial r_{n_y}/\partial y_1 & \cdots & \partial r_{n_y}/\partial y_{n_y} \end{bmatrix} \tag{A1.4}$$

The Jacobian was evaluated using the *MATLAB*® function *numjac*© [25]. The "or" in step C5 is a Boolean operator. In the damped Newton-Raphson method, $\chi = 1$ corresponds to the undamped condition, whereas $\chi = 0$ corresponds to the fully damped condition, wherein the iteration is stalled. For steps C2 and C4.2, the damping factor used in the model applications of Chapters 6-8 was in the range $0.02 \le \chi \le 0.05$ for $i = 1$, and in the range $0.05 \le \chi \le 0.2$ for $i > 1$. For steps C4.1-C4.3 $tol = 10^{-8}$. In step C5, $eps = 2 \times 10^{-16}$, the smallest number registered by the computer. The absolute value of the arc-length increment $\Delta\sigma$ used in step A was around 0.1. Occasionally, this value had to be reduced for certain regions of the speed response curve. Notice that the sign of $\Delta\sigma$ determines the sense in which the speed response curve is traced out from the first point $\hat{\mathbf{w}}_1$; hence, after generating $(n_{totalsol} - 1)$ points with $\Delta\sigma > 0$, the speed response curve can be extended "backwards" from $\hat{\mathbf{w}}_1$ by repeating the calculations with $\Delta\sigma < 0$.

A1.2 COMPUTATION OF THE TANGENT VECTOR

This section explains the determination of the tangent vector $(d\mathbf{y}/d\mu)_{\mu=\mu_1}$ used in the tangent predictor of step B, case $i = 2$, of the algorithm of section A1.1. In this case, the system being solved is eq. (A1.1), hence, $d\mathbf{y}/d\mu = d\hat{\mathbf{w}}/d\sigma$. Now

$$\frac{d\hat{\mathbf{w}}}{d\sigma} = \lim_{\Delta\sigma \to 0} \left(\frac{\Delta\hat{\mathbf{w}}}{\Delta\sigma} \right) = \lim_{|\Delta \mathbf{w}| \to 0} \left(\frac{\Delta\hat{\mathbf{w}}}{|\Delta\hat{\mathbf{w}}|} \right) \tag{A1.5}$$

since, from eq. (5.23), $\Delta\sigma = |\Delta\hat{\mathbf{w}}|$ ($\Delta\sigma$ taken as positive). From eq. (A1.1), for small $\Delta\hat{\mathbf{w}} = \begin{bmatrix} \Delta\hat{\mathbf{v}} \\ \Delta\hat{\Omega} \end{bmatrix}$:

$$\begin{bmatrix} \left.\dfrac{\partial \mathbf{p}}{\partial \hat{\mathbf{v}}}\right|_{\hat{\mathbf{w}}=\hat{\mathbf{w}}_1} & \left.\dfrac{\partial \mathbf{p}}{\partial \hat{\Omega}}\right|_{\hat{\mathbf{w}}=\hat{\mathbf{w}}_1} \end{bmatrix} \begin{bmatrix} \Delta\hat{\mathbf{v}} \\ \Delta\hat{\Omega} \end{bmatrix} = \mathbf{0} \tag{A1.6}$$

The number of unknowns in the above system (A1.6) is one more than the number of equations. Dividing both sides of (A1.6) by $\Delta\hat{\Omega}$ and adding an extra trivial equation:

$$\begin{bmatrix} \left.\partial \mathbf{p}/\partial \hat{\mathbf{v}}\right|_{\hat{\mathbf{w}}=\hat{\mathbf{w}}_1} & \left.\partial \mathbf{p}/\partial \hat{\Omega}\right|_{\hat{\mathbf{w}}=\hat{\mathbf{w}}_1} \\ 0 \quad \cdots\cdots\cdots & 0 \quad 1 \end{bmatrix} \begin{bmatrix} \Delta\hat{\mathbf{v}}/\Delta\hat{\Omega} \\ 1 \end{bmatrix} = \begin{bmatrix} \mathbf{0} \\ 1 \end{bmatrix} \tag{A1.7}$$

Now $\Delta\hat{\mathbf{w}} = \Delta\hat{\Omega}\begin{bmatrix} \Delta\hat{\mathbf{v}}/\Delta\hat{\Omega} \\ 1 \end{bmatrix} = \Delta\hat{\Omega}\mathbf{d}$ where $\mathbf{d} = \begin{bmatrix} \Delta\hat{\mathbf{v}}/\Delta\hat{\Omega} \\ 1 \end{bmatrix}$. Hence, from the relations in eq. (A1.5):

$$\left.\frac{d\mathbf{y}}{d\mu}\right|_{\mu=\mu_1} = \left.\frac{d\hat{\mathbf{w}}}{d\sigma}\right|_{\sigma=\sigma_1} = \frac{\mathbf{d}}{|\mathbf{d}|} \tag{A1.8}$$

where, from eq. (A1.7):

$$\mathbf{d} = \begin{bmatrix} \left.\partial \mathbf{p}/\partial \hat{\mathbf{v}}\right|_{\hat{\mathbf{w}}=\hat{\mathbf{w}}_1} & \left.\partial \mathbf{p}/\partial \hat{\Omega}\right|_{\hat{\mathbf{w}}=\hat{\mathbf{w}}_1} \\ 0 \quad \cdots\cdots\cdots & 0 \quad 1 \end{bmatrix}^{-1} \begin{bmatrix} \mathbf{0} \\ 1 \end{bmatrix} \tag{A1.9}$$

A2 MECHANICAL IMEDANCE MODEL OF LINEAR PART

A2.1 OVERVIEW

The mechanical impedance (MI) method is used to compute the receptance functions relating points on the rotor part of the linear subsystem. This method is analogous to the dynamic stiffness method, but works with impedance rather than dynamic stiffness frequency response functions. The method is described in [19] where the MI model of a rotor that is linearly connected to a flexible support structure is described. The MI model used for the linear subsystem of rigs B and C is a simplified version of that in [19] since:

(a) The support structure is not considered – it is either rigid (configuration B), or is uncoupled from the rotor (configuration C). Hence, the impedance model is applied either to a point supported rotor (configuration B) or one that is fully unrestrained (configuration C).

(b) Gyroscopic effects are neglected.

The shaft is divided into beam-like elements that rotate about their longitudinal axis and bend harmonically at frequency ω rad/s in the *xz* and *yz* planes. Due to the simplification (b), the vibrations in the two planes can be treated separately and the frequency response functions are independent of rotational speed. For each such plane (see Figure A2.1), the impedance matrix $\mathbf{Z}_k(\omega)$ of a shaft element no. *k* is given by

$$\begin{bmatrix} \tilde{f}_{ki} \\ \tilde{M}_{ki} \\ \tilde{f}_{k(i+1)} \\ \tilde{M}_{k(i+1)} \end{bmatrix} = \mathbf{Z}_k(\omega) \begin{bmatrix} \tilde{v}_i \\ \tilde{\Omega}_i \\ \tilde{v}_{i+1} \\ \tilde{\Omega}_{i+1} \end{bmatrix} \tag{A2.1}$$

where the instantaneous forces and moments acting on element no. *k* at terminal no. *i* are given respectively by $f_{ki}(t) = \mathrm{Re}\left(\tilde{f}_{ki} e^{j\omega t}\right)$, $M_{ki}(t) = \mathrm{Re}\left(\tilde{M}_{ki} e^{j\omega t}\right)$, and the instantaneous velocities and angular rotation rates (in the plane) at terminal no. *i* are given by $v_i(t) = \mathrm{Re}\left(\tilde{v}_i e^{j\omega t}\right)$, $\Omega_i(t) = \mathrm{Re}\left(\tilde{\Omega}_i e^{j\omega t}\right)$.

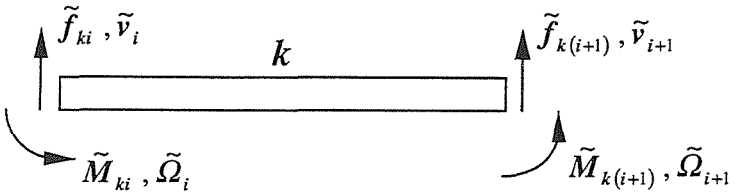

Figure A2.1: *Shaft element notation*

The matrix $\mathbf{Z}_k(\omega)$ can be obtained from [19]. It is based on the exact dynamic deflection curve of a uniform section beam element of distributed inertia. Hence, the impedance matrix of one such element is exact, irrespective of length. The assembly procedure for the shaft elemental matrices is the similar to that in the finite element (FE) technique [19, 48]. Inertia components attached to the shaft are concentrated at the terminals, as are the stiffness of any point supports, and the impedance matrices of these inclusions are inserted at the appropriate areas of the assembled global impedance matrix, as in FE. The global impedance matrix is of size $2n_{term} \times 2n_{term}$ (where n_{term} is the total number of terminals). However, for both rigs B and C, no external moments are applied at the terminals and the rotations there are not required. Hence (as for the FE method in [48]), the global impedance matrix can be deflated to size $n_{term} \times n_{term}$:

$$\tilde{\mathbf{f}}_{\mathbf{red}} = \{z_{ij}(\omega)\}\tilde{\mathbf{v}}_{\mathbf{red}} \tag{A2.3}$$

where $\{z_{ij}(\omega)\}$ is the reduced global impedance matrix, $\tilde{\mathbf{f}}_{\mathbf{red}} = \begin{bmatrix}\tilde{f}_1 & \cdots & \tilde{f}_{n_{term}}\end{bmatrix}^T$ contains the complex amplitudes of the external forces at the terminals, $\tilde{\mathbf{v}}_{\mathbf{red}} = \begin{bmatrix}\tilde{v}_1 & \cdots & \tilde{v}_{n_{term}}\end{bmatrix}^T$ contains the terminal velocity complex amplitudes. The reduced global receptance matrix $\{\alpha_{ij}(\omega)\}$ is given by:

$$\tilde{\mathbf{u}}_{\mathbf{red}} = \{\alpha_{ij}(\omega)\}\tilde{\mathbf{f}}_{\mathbf{red}} \tag{A2.4}$$

where $\tilde{\mathbf{u}}_{\mathbf{red}}$ contains the displacement complex amplitudes. Since $\tilde{\mathbf{v}}_{\mathbf{red}} = j\omega\tilde{\mathbf{u}}_{\mathbf{red}}$, (where $j = \sqrt{-1}$), $\{\alpha_{ij}(\omega)\}$ is given by

$$\{\alpha_{ij}(\omega)\} = \frac{\{z_{ij}(\omega)\}^{-1}}{j\omega} \qquad \text{(A2.5)}$$

A terminal is normally a location where there is a change in cross-section of the shaft, or an attached inertia and/or point support. If a receptance relating positions P and Q is required where one or both positions do not coincide with the above-specified types of locations, then P and/or Q are introduced in the model as additional terminals.

The following sections describe the MI model for rigs B and C. In both rigs, since polar moments of inertia are neglected, the diametral moments of inertia per unit length of the beam elements, and the diametral moments of inertia of the attached components, are also neglected. The impedance matrices of the beam elements include the effect of shear deformation, in addition to bending. Hence, the beam elements are Timoshenko beams with diametral moment of inertia per unit length set to zero [19].

A2.2 RIG B

8 Timoshenko beam elements (see last paragraph of section A2.1) are used to model the linear part of rig B. In configuration B1 (retainer spring fitted), the linear subsystem is the shaft pinned at H and sprung at J (see Figure 7.1). The corresponding MI model is shown in Table A2.1 where:

- The flexible drive coupling is assumed to exert no force and bending moment on the shaft.
- For the shaft elements, Young's Modulus $E = 200\times10^9$ N/m^2 and the density $\rho = 7860$ kg/m^3.
- The point supports at terminal 3 (H) and terminal 6 (J) exert no restraining moments since self-aligning ball bearings are used. The ball bearing stiffness values are taken to be infinitely large. The stiffness value at terminal 6 is that of the retainer spring and was obtained from [21].
- The attached mass at terminal 6 was determined experimentally in [21] and is the combined mass of the ball bearing, damper journal and the effective mass of the retainer spring.
- The mass of the coupling hub at the left hand end of the shaft (Figure 7.1) is shared between terminals 1 and 2 such that its centre of mass coincides with the resultant mass centre of the two lumped masses.

- The disc is lumped at terminal 8.

For configuration B2 (no retainer spring), the linear subsystem is the shaft pinned at H and free at J (see Figure 7.1), so the support stiffness at terminal 6 is omitted from Table A2.1. The attached inertia at this terminal is left unaltered since the aluminium retainer spring has negligible mass.

A2.3 RIG C

9 Timoshenko beam elements (see last paragraph of section A2.1) are used to model the free-free rotor of the linear subsystem of configuration C (Figure 8.1), as shown in Table A2.2. With reference to this table:

- For the shaft elements, Young's Modulus $E = 200\times10^9$ N/m^2 and the density $\rho = 7860$ kg/m^3.
- The redundant terminals 7 and 8 are included to allow the computation of the receptances $\alpha_{J_1U_1}, \alpha_{J_1U_2}, \alpha_{J_2U_1}, \alpha_{J_2U_2}$.
- The attached mass at each terminal 4 and 9 is the combined mass of the corresponding roller bearing and damper journal.

terminal no.	**1**	**2**	**3 (H)**	**4**	**5**	**6 (J)**	**7**	**8 (U)**	**9**
attached mass (kg)	0.1518	0.0692				1.3567		6.4039	
support stiffness (kN/m)			∞			123.4			

shaft element	**1-2**	**2-3**	**3-4**	**4-5**	**5-6**	**6-7**	**7-8**	**8-9**
length (mm)	20.0	29.0	44.0	715.0	262.0	13.0	209.3	12.7
diameter (mm)	16.000	25.405	25.405	50.000	25.405	25.405	25.385	25.385

Table A2.1: *Mechanical impedance model for rig B with retainer spring*

terminal no.	**1**	**2**	**3**	**4 (J_1)**	**5**	**6**	**7 (U_1)**	**8 (U_2)**	**9 (J_2)**	**10**
attached mass (kg)	0.0577	0.2618		1.2950					1.2925	

element	**1-2**	**2-3**	**3-4**	**4-5**	**5-6**	**6-7**	**7-8**	**8-9**	**9-10**
length (mm)	14.17	9.83	24.00	23.50	0.50	78.00	746.00	102.00	24
diameter (mm)	50	50	92	92	50	92	92	92	92

Table A2.2: *Mechanical impedance model for rig C*

A3 COMPUTATION OF MODAL PARAMETERS OF ROTOR

A3.1 OVERVIEW

This appendix considers the analytical determination of the undamped, non-rotational modal parameters of the linear subsystem of rig B and those of the rotor part of the linear subsystem of rig C. In either case, the vibrations in the *xz* and *yz* planes are uncoupled. Moreover, the system considered is isotropic, so the modal parameters are identical in either plane. This work shall concentrate on the *xz* plane. The modal parameters are computed from the receptance frequency response functions. These functions are contained in the receptance matrix of eq. (A2.4), which is computed from the mechanical impedance matrix by eq. (A2.5). Each term in the matrix $\{\alpha_{ij}(\omega)\}$ can be approximated by a modal series, truncated beyond q modes [47]:

$$\alpha_{ij}(\omega) \approx \sum_{r=1}^{q} \frac{A_{ij}^{(xr)}}{\omega_{xr}^2 - \omega^2} \tag{A3.1}$$

where ω_{xr}, $r = 1 \ldots q$, is the undamped natural frequency of the subsystem in mode r and $A_{ij}^{(xr)}$ is the corresponding modal constant, which is given by [47]:

$$A_{ij}^{(xr)} = \phi_i^{(xr)} \phi_j^{(xr)} \tag{A3.2}$$

$\phi_i^{(xr)}$ is the mass-normalised mode shape of mode r in the *xz* plane, evaluated at position i in the x direction.

The natural frequencies ω_{xr} are found by locating the first q zeros of the determinant of the impedance matrix i.e. the roots of the equation

$$\left|\{z_{ij}(\omega)\}\right| = 0 \tag{A3.3}$$

This is done using Muller's iterative algorithm [66]. The input approximations for the roots are obtained from the resonance locations of the frequency response of any typical term $\alpha_{ij}(\omega)$ in $\{\alpha_{ij}(\omega)\}$. Once the natural frequencies have been found, the values of the corresponding mode shapes at selected locations $\breve{i}$ and $\breve{j}$ can be found by performing two modal fits from eq. (A3.1) – first for $\alpha_{\breve{i}\breve{i}}(\omega)$, yielding $A_{\breve{i}\breve{i}}^{(xr)} = \phi_{\breve{i}}^{(xr)}\phi_{\breve{i}}^{(xr)}$, $r = 1\ldots q$, and then for $\alpha_{\breve{i}\breve{j}}(\omega)$, yielding $A_{\breve{i}\breve{j}}^{(xr)} = \phi_{\breve{i}}^{(xr)}\phi_{\breve{j}}^{(xr)}$, $r = 1\ldots q$. Then

$$\phi_{\breve{i}}^{(xr)} = \sqrt{A_{\breve{i}\breve{i}}^{(xr)}}, \quad \phi_{\breve{j}}^{(xr)} = A_{\breve{i}\breve{j}}^{(xr)} \Big/ \sqrt{A_{\breve{i}\breve{i}}^{(xr)}} \tag{A3.4}$$

Each fit is performed as follows. Compute $\alpha_{ij}(\omega)$ at p selected frequencies $\omega_{sel\ k}$, $k = 1\ldots p$, within the chosen frequency range and solve the equations:

$$\begin{bmatrix} \alpha_{ij}(\omega_{sel\ 1}) \\ \vdots \\ \alpha_{ij}(\omega_{sel\ p}) \end{bmatrix} = \begin{bmatrix} \dfrac{1}{\omega_1^2 - \omega_{sel\ 1}} & \cdots & \dfrac{1}{\omega_q^2 - \omega_{sel\ 1}} \\ \vdots & \cdots & \vdots \\ \dfrac{1}{\omega_1^2 - \omega_{sel\ p}} & \cdots & \dfrac{1}{\omega_q^2 - \omega_{sel\ p}} \end{bmatrix} \begin{bmatrix} A_{ij}^{(x1)} \\ \vdots \\ A_{ij}^{(xq)} \end{bmatrix} \tag{A3.5}$$

which can be expressed as

$$\mathbf{r} = \mathbf{E}\mathbf{a}$$

where $\mathbf{r}$ and $\mathbf{a}$ are $p \times 1$ and $q \times 1$ vectors respectively and $\mathbf{E}$ is a $p \times q$ matrix. Now $p \geq q$. If $p = q$ i.e. as many points are taken as unknowns, then

$$\mathbf{a} = \mathbf{E}^{-1}\mathbf{r} \tag{A3.6}$$

If $p > q$ i.e. more points are taken than the number of unknown modal constants

$$\mathbf{a} = \mathbf{E}^{\perp}\mathbf{r} \tag{A3.7}$$

where $\mathbf{E}^{\perp}$ is the pseudo- inverse of $\mathbf{E}$, given by [47]:

$$\mathbf{E}^{\perp} = \left(\mathbf{E}^{\mathrm{T}}\mathbf{E}\right)^{-1}\mathbf{E}^{\mathrm{T}} \tag{A3.8}$$

A3.2 RIG B

In this case, the linear subsystem was the shaft pinned at H and either sprung or unsprung at J (Figure 7.1), corresponding to configurations B1 and B2 respectively. In each case $q = 4$ modes were taken in each plane. The fitting frequency range was 0 Hz to 300 Hz and $p = 4$ equally spaced frequency points $\omega_{sel\,k}$ were taken. $\omega_{sel\,1}$ was adjusted to $2\pi \times 0.1$ from 0 to avoid $\left|\alpha_{ij}\left(\omega_{sel\,1}\right)\right| \to \infty$ for configuration B2. The natural frequencies, and the modal constants obtained by fitting $\alpha_{JJ}(\omega)$, $\alpha_{JU}(\omega)$ are given in Table A3.1 for configuration B1, and Table A3.2 for configuration B2. The values in these tables are refinements on those quoted in [42] (that had been obtained by fitting over the range 0 Hz to 500 Hz with $q = 5$ modes and $p = 5$ equally spaced points).

mode no. r	$\omega_{xr}/(2\pi)$ (Hz)	$A_{JJ}^{(xr)} = \phi_J^{(xr)}\phi_J^{(xr)}$ ($\times 10^{-3}\,\mathrm{kg}^{-1}$)	$A_{JU}^{(xr)} = \phi_J^{(xr)}\phi_U^{(xr)}$ ($\times 10^{-3}\,\mathrm{kg}^{-1}$)
1	13.74	54.220	77.796
2	40.40	38.495	-34.148
3	173.86	251.269	-38.753
4	334.68	106.073	-13.540

Table A3.1: *Undamped modal parameters for configuration B1 in one plane of vibration*

mode no. r	$\omega_{xr}/(2\pi)$ (Hz)	$A_{JJ}^{(xr)} = \phi_J^{(xr)}\phi_J^{(xr)}$ ($\times 10^{-3}\,\mathrm{kg}^{-1}$)	$A_{JU}^{(xr)} = \phi_J^{(xr)}\phi_U^{(xr)}$ ($\times 10^{-3}\,\mathrm{kg}^{-1}$)
1	0	66.771	81.309
2	39.00	31.652	-36.859
3	171.60	248.170	-39.748
4	334.20	103.543	-13.349

Table A3.2: *Undamped modal parameters for configuration B2 in one plane of vibration*

For the evaluation of the time domain response at point M (Figure 7.1), the mode shapes at this location are required and these are found by fitting $\alpha_{JM}(\omega)$.

A3.3 RIG C

In this case, the modal parameters of the rotor were required. $q=3$ modes were taken in each plane, where the first two were rigid body modes. Since $\omega_{Rx1}=\omega_{Rx2}=0$, the first two terms of the series in eq. (A3.1) merged into one:

$$\alpha_{ij}(\omega)\approx-\frac{\breve{A}_{ij}}{\omega^2}+\frac{A_{ij}^{(Rx3)}}{\omega_{Rx3}^2-\omega^2} \tag{A3.9}$$

where

$$\breve{A}_{ij}=A_{ij}^{(Rx1)}+A_{ij}^{(Rx2)} \tag{A3.10}$$

Since $r=1$ defined the pure translation mode,

$$A_{ij}^{(Rx1)}=1/M_R \tag{A3.11}$$

where M_R is the total mass of the rotor. Hence, upon determining $\breve{A}_{ij}$ and $A_{ij}^{(Rx3)}$ by applying the modal fit to eq. (A3.9), the constants $A_{ij}^{(Rx1)}$, $A_{ij}^{(Rx2)}$ were found from eqs. (A3.10) and (A3.11). It was found necessary to use $p=41$ equally spaced frequency points over a range 0 Hz to 600 Hz, with $\omega_{sel\ 1}$ adjusted to $2\pi\times0.1$ from 0 to avoid $\left|\alpha_{ij}(\omega_{sel\ 1})\right|\rightarrow\infty$. The natural frequencies, and the modal constants obtained by fitting $\alpha_{J_1J_1}$, $\alpha_{J_1J_2}$, $\alpha_{J_1U_1}$, $\alpha_{J_1U_2}$ are given in Table A3.3. In Figure A3.1 the exact receptances (computed by MI) are compared with those reconstructed from the corresponding computed modal parameters.

mode no. r	$\omega_{Rxr}/(2\pi)$ (Hz)	$A_{J_1J_1}^{(Rxr)}=\phi_{J_1}^{(Rxr)}\phi_{J_1}^{(Rxr)}$ ($\times10^{-3}$kg^{-1})	$A_{J_1J_2}^{(Rxr)}=\phi_{J_1}^{(Rxr)}\phi_{J_2}^{(Rxr)}$ ($\times10^{-3}$kg^{-1})	$A_{J_1U_1}^{(Rxr)}=\phi_{J_1}^{(Rxr)}\phi_{U_1}^{(Rxr)}$ ($\times10^{-3}$kg^{-1})	$A_{J_1U_2}^{(Rxr)}=\phi_{J_1}^{(Rxr)}\phi_{U_2}^{(Rxr)}$ ($\times10^{-3}$kg^{-1})
1	0	18.048	18.048	18.048	18.048
2	0	43.199	-44.349	33.799	-34.949
3	374.95	41.724	44.580	17.352	20.093

Table A3.3: *Undamped modal parameters for configuration C in one plane of vibration*

For the time domain response at points J_{1m}, J_{2m} (Figure 8.1), the mode shapes at these locations are required, and these are found by fitting $\alpha_{J_1 J_{1m}}(\omega)$, $\alpha_{J_1 J_{2m}}(\omega)$.

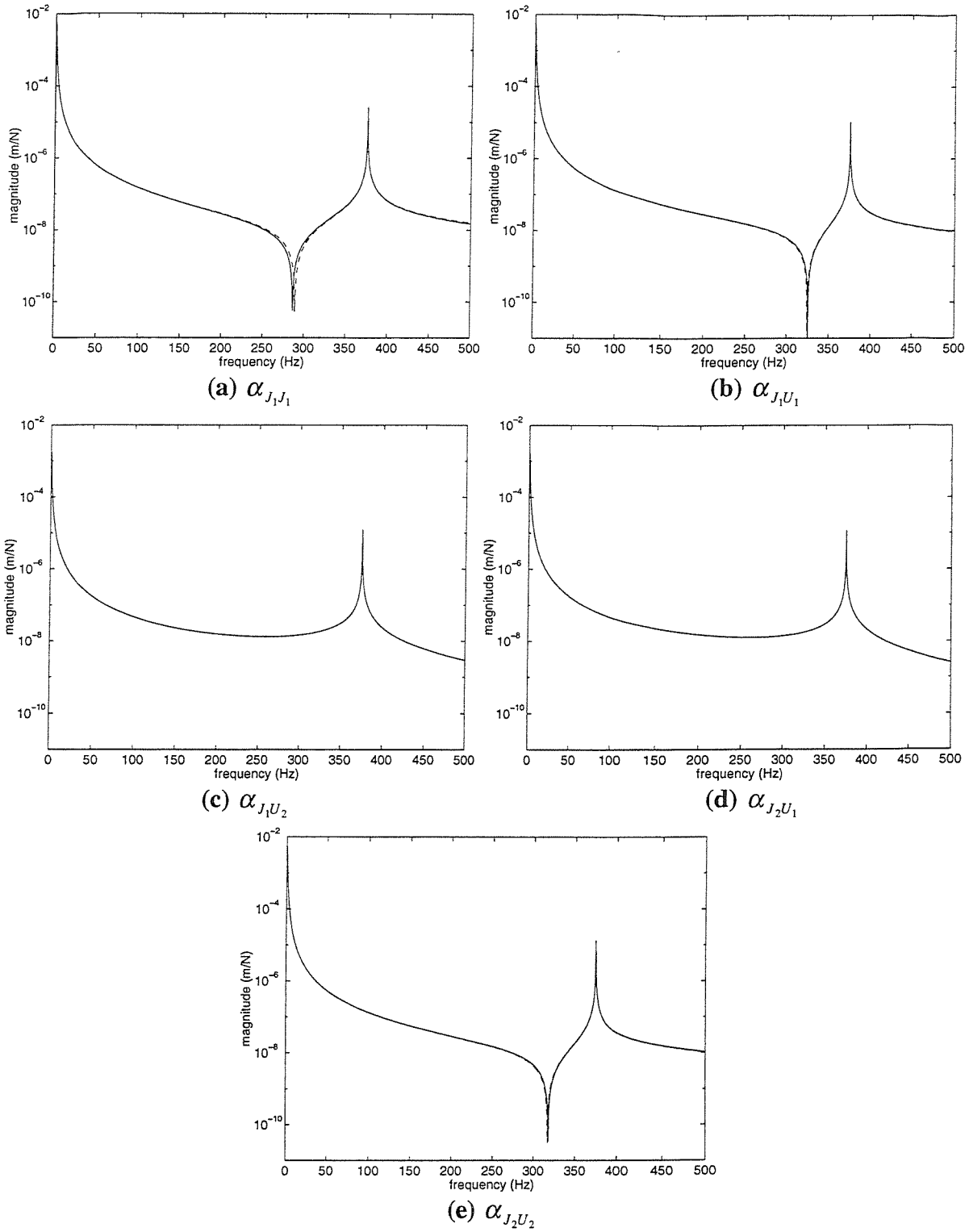

Figure A3.1: *Comparison of exact rotor receptances computed by MI* (——) *with approximations reconstructed from the* 3 *modes in* Figure 8.6(b) (– – –)

A4 TIME-MARCHING SOLUTION

This appendix explains how the coordinates in the modal equations (7.11) and (8.19) are non-dimensionalised prior to integration. The non-dimensionalisation of these coordinates facilitates the choice of a suitable tolerance for the accuracy of the numerical integration solver.

A4.1 RIG B

In eqs. (7.11), non-dimensional modal coordinates $\hat{q}_{xr} = \phi_J^{(xr)} q_{xr}/c$, $\hat{q}_{yr} = \phi_J^{(yr)} q_{yr}/c$ are defined, as well as a non-dimensional time $\varsigma = \Omega t$, where Ω is the rotational speed. Eqs. (7.11) then become:

$$\hat{q}''_{xr} + \left(\frac{\omega_{xr}}{\Omega}\right)^2 \hat{q}_{xr} = \frac{1}{c\Omega^2}\left[A_{JJ}^{(xr)} Q_x + A_{JU}^{(xr)} P_x\right] \tag{A4.1a}$$

$$\hat{q}''_{yr} + \left(\frac{\omega_{yr}}{\Omega}\right)^2 \hat{q}_{yr} = \frac{1}{c\Omega^2}\left[A_{JJ}^{(yr)} Q_y + A_{JU}^{(yr)} P_y\right], \quad \text{where } r = 1\ldots4 \tag{A4.1b}$$

In the above equations, $(\,)'$ denotes differentiation with respect to ς, the modal constants $A_{PQ}^{(xr)}$, $A_{PQ}^{(yr)}$ connecting positions P and Q are defined in Appendix A3, eq. (A3.2), and $A_{PQ}^{(xr)} = A_{PQ}^{(yr)}$. For configuration B2 (no retainer spring), Q_y in eq. (A4.1b) is replaced by $Q_y - W$. Eqs. (A4.1) are expressed as a set of 8 first order differential equations, as in eq. (3.1), with ς replacing *t*, and solved using the *MATLAB*® function *ode*23*s*©.

A4.2 RIG C

We define non-dimensional modal coordinates $\hat{q}_{Rxr} = \phi_{J_1}^{(Rxr)} q_{Rxr}/c$, $\hat{q}_{Ryr} = \phi_{J_1}^{(Ryr)} q_{Ryr}/c$ in eqs. (8.19a,b). In eqs. (8.19c-f) we define non-dimensional coordinates $\hat{X}_{B_1} = \phi_{B_1}^{(Sx1)} q_{Sx1}/c$, $\hat{X}_{B_2} = \phi_{B_2}^{(Sx2)} q_{Sx2}/c$, $\hat{Y}_{B_1} = \phi_{B_1}^{(Sy1)} q_{Sy1}/c$, $\hat{Y}_{B_2} = \phi_{B_2}^{(Sy2)} q_{Sy2}/c$. From eqs. (5.34), (8.6) and

(8.20), $\hat{X}_{B_1} = X_{B_1}/c$, $\hat{X}_{B_2} = X_{B_2}/c$, $\hat{Y}_{B_1} = Y_{B_1}/c$, $\hat{Y}_{B_2} = Y_{B_2}/c$. Defining also a non-dimensional time $\varsigma = \Omega t$, where Ω is the rotational speed, eqs. (8.19) become:

$$\hat{q}''_{Rxr} + \left(\frac{\omega_{Rxr}}{\Omega}\right)^2 \hat{q}_{Rxr} = \frac{1}{c\Omega^2}\left[A^{(Rxr)}_{J_1J_1}Q_{x1} + A^{(Rxr)}_{J_1J_2}Q_{x2} + A^{(Rxr)}_{J_1U_1}P_{x1} + A^{(Rxr)}_{J_1U_2}P_{x2}\right]$$

$$\hat{q}''_{Ryr} + \left(\frac{\omega_{Ryr}}{\Omega}\right)^2 \hat{q}_{Ryr} = \frac{1}{c\Omega^2}\left[A^{(Ryr)}_{J_1J_1}\left(Q_{y1} - W_1\right) + A^{(Ryr)}_{J_1J_2}\left(Q_{y2} - W_2\right) + A^{(Ryr)}_{J_1U_1}P_{y1} + A^{(Ryr)}_{J_1U_2}P_{y2}\right],$$

where $r = 1\ldots3$ (A4.2a,b)

$$\hat{X}''_{B_1} + \left(\omega_{Sx1}/\Omega\right)^2 \hat{X}_{B_1} = -A^{(Sx1)}_{B_1B_1}Q_{x1}/\left(c\Omega^2\right) \quad \text{(A4.2c)}$$

$$\hat{Y}''_{B_1} + \left(\omega_{Sy1}/\Omega\right)^2 \hat{Y}_{B_1} = -A^{(Sy1)}_{B_1B_1}Q_{y1}/\left(c\Omega^2\right) \quad \text{(A4.2d)}$$

$$\hat{X}''_{B_2} + \left(\omega_{Sx2}/\Omega\right)^2 \hat{X}_{B_2} = -A^{(Sx2)}_{B_2B_2}Q_{x2}/\left(c\Omega^2\right) \quad \text{(A4.2e)}$$

$$\hat{Y}''_{B_2} + \left(\omega_{Sy2}/\Omega\right)^2 \hat{Y}_{B_2} = -A^{(Sy2)}_{B_2B_2}Q_{y2}/\left(c\Omega^2\right) \quad \text{(A4.2f)}$$

The modal constants on the right hand side of the above equations are defined in Appendix A3, eq. (A3.2) and in eqs. (8.2). For eqs. (A4.2a,b) only, the modal constants are the same for both planes. Eqs. (A4.2) are expressed as a set of 20 first order differential equations, as in eq. (3.1), with ς replacing *t*, and solved using the *MATLAB*® function *ode*23*s*©.

A5 ADDITIONAL DATA FOR RIG B

A5.1 INSTRUMENTATION DATA

With reference to Figure 7.1, the calibration of the displacement transducers (probes) at the disc (U) and mid-shaft (M) was checked on a workbench using a micrometer screw gauge calibrator and a digital voltmeter. The squeeze film damper (SFD) probes (at J) were calibrated *in situ* (i.e. when in position on the rig), using a digital voltmeter and a micrometer dial indicator at the shaft, situated as close as possible to J. The reason for this was that the lateral clearance of the SFD probes from the bearing housing face, and other surfaces, was within the limits of tolerance recommended by the manufacturer [67]. The calibration curves and sensitivities are given in Figures A5.1(a,b)-A5.3(a,b). A least squares linear fit was used to determine the sensitivities.

In the subsequent experiments, vibration data were acquired from the displacement probes in the form of time histories using a *Hewlett Packard* 35650® spectral analyser (serial number 2911A02485).

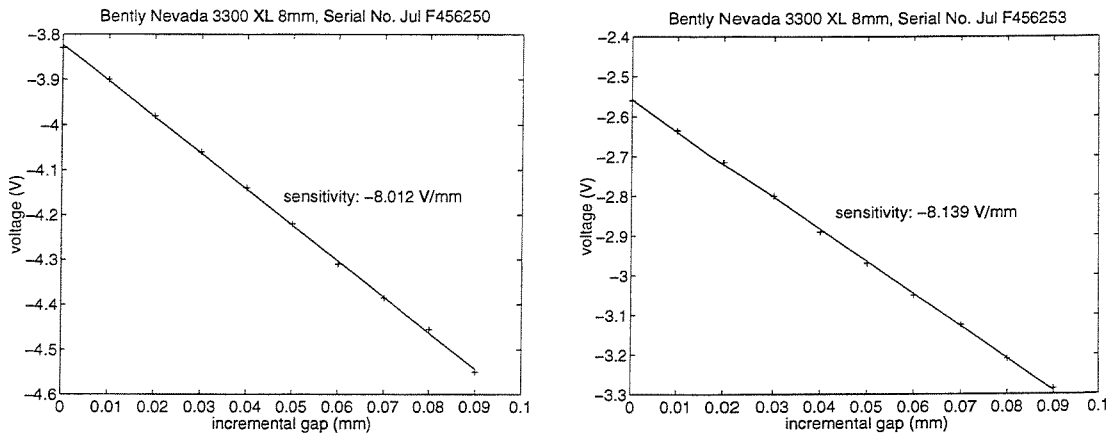

(a) x probe **(b)** y probe

Figure A5.1: *Calibration of displacement transducers at SFD* (J)

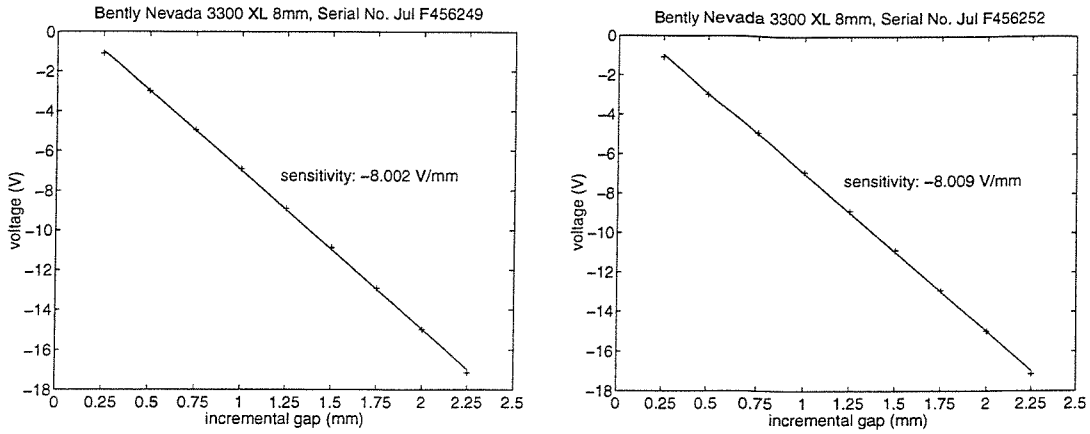

(a) *x* probe **(b)** *y* probe

Figure A5.2: *Calibration of displacement transducers at disc* (U)

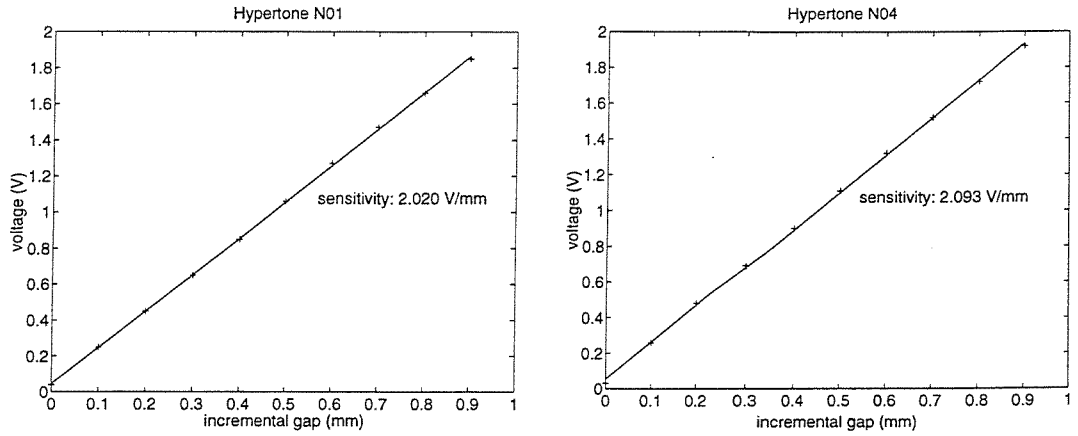

(a) *x* probe **(b)** *y* probe

Figure A5.3: *Calibration of displacement transducers at mid-shaft* (M)

A5.2 STATIC ECCENTRICITY SETTINGS FOR CONF. B1

The SFD static eccentricity adjustment was made at room temperature and checked at the beginning and end of each experiment. The oil temperature at the start of each experiment was at least 25 °C. This temperature was reached after the rig was run for about 30 minutes. Tables A5.1 and A5.2 show static offset conditions at the start and end of two different experiments in which the maximum variation of oil temperature was observed (8 °C). The eccentricity values in these tables were determined by pushing the journal J from the static position until the clearance limits were reached. With reference to Figure 7.2, the journal was pushed up and down for ε_{0y}, and pushed either way laterally for ε_{0x}. The corresponding travels of J were measured using the displacement probes and a digital voltmeter.

θ (°)	ε_{0x}
0	0.04
90	0.05
180	-0.01
270	-0.02
$\bar{\varepsilon}_{0x}$	0.02

(a1) *x* direction, 25 °C

θ (°)	ε_{0y}
0	-0.41
90	-0.60
180	-0.72
270	-0.55
$\bar{\varepsilon}_{0y}$	-0.57

(a2) *y* direction, 25 °C

θ (°)	ε_{0x}
0	0.08
90	0.10
180	0.06
270	0.01
$\bar{\varepsilon}_{0x}$	0.06

(b1) *x* direction, 33°C

θ (°)	ε_{0y}
0	-0.39
90	-0.66
180	-0.79
270	-0.60
$\bar{\varepsilon}_{0y}$	-0.61

(b2) *y* direction, 33°C

Table A5.1: *Static eccentricity conditions for* $\varepsilon_{0x} = 0.0$, $\varepsilon_{0y} = -0.6$

θ (°)	ε_{0x}
0	-0.03
90	0.03
180	-0.03
270	-0.07
$\bar{\varepsilon}_{0x}$	-0.03

(a1) *x* direction, 25 °C

θ (°)	ε_{0y}
0	-0.63
90	-0.84
180	-0.96
270	-0.77
$\bar{\varepsilon}_{0y}$	-0.80

(a2) *y* direction, 25 °C

θ (°)	ε_{0x}
0	0.02
90	0.05
180	0.07
270	-0.05
$\bar{\varepsilon}_{0x}$	0.02

(b1) *x* direction, 33 °C

θ (°)	ε_{0y}
0	-0.66
90	-0.91
180	-1.00
270	-0.86
$\bar{\varepsilon}_{0y}$	-0.86

(b2) *y* direction, 33 °C

Table A5.2: *Static eccentricity conditions for* $\varepsilon_{0x} = 0.0$, $\varepsilon_{0y} = -0.8$

In Table A5.1, the grand means, to one decimal place, are $\varepsilon_{0x} = 0.0$, $\varepsilon_{0y} = -0.6$. In Table A5.2, the grand means, to one decimal place, are $\varepsilon_{0x} = 0.0$, $\varepsilon_{0y} = -0.8$. These values were used in the simulations.

A5.3 MEASUREMENT OF "DC" COMPONENT OF VIBRATION FOR CONF. B1

A data acquisition with the analyser was performed on the stationary rig at the start of each experiment. With the rig stationary, the voltages $V_{0xJ\theta}, V_{0yJ\theta}$ at the locations J, U and M respectively were acquired for the four angular positions of the shaft θ = 0°, 90°, 180°, 270°. This allowed for the static run-out at J. The average static dc voltages in the x and y directions at locations J, U and M were then obtained as:

$$\overline{V}_{0xJ} = \frac{V_{0xJ0^\circ} + V_{0xJ90^\circ} + V_{0xJ180^\circ} + V_{0xJ270^\circ}}{4}, \quad \overline{V}_{0yJ} = \frac{V_{0yJ0^\circ} + V_{0yJ90^\circ} + V_{0yJ180^\circ} + V_{0yJ270^\circ}}{4} \tag{A5.1a,b}$$

Let $V_{xJ}(t), V_{yJ}(t)$ be the x, y voltage measurements at J, acquired at any given speed, and let γ_{xJ}, γ_{yJ} be the sensitivities of the x, y probes at J. The non-dimensional displacements of J from the housing centre B were then given by:

$$\frac{X_J}{c} = \varepsilon_{0x} + \frac{V_{xJ}(t) - \overline{V}_{0xJ}}{\gamma_{xJ} c}, \qquad \frac{Y_J}{c} = \varepsilon_{0y} + \frac{V_{yJ}(t) - \overline{V}_{0yJ}}{\gamma_{yJ} c} \tag{A5.2a,b}$$

The above displacements were directly comparable to the predictions. For added precision the static voltage acquisition was repeated at the end of each experiment with the rig hot. The static voltages used in equations (A5.2a,b) where in fact the averages of the cold and hot values.

A5.4 PHOTOGRAPHS OF TEST RIG B

Photographs of the test rig for configuration B are shown in Figure A5.4.

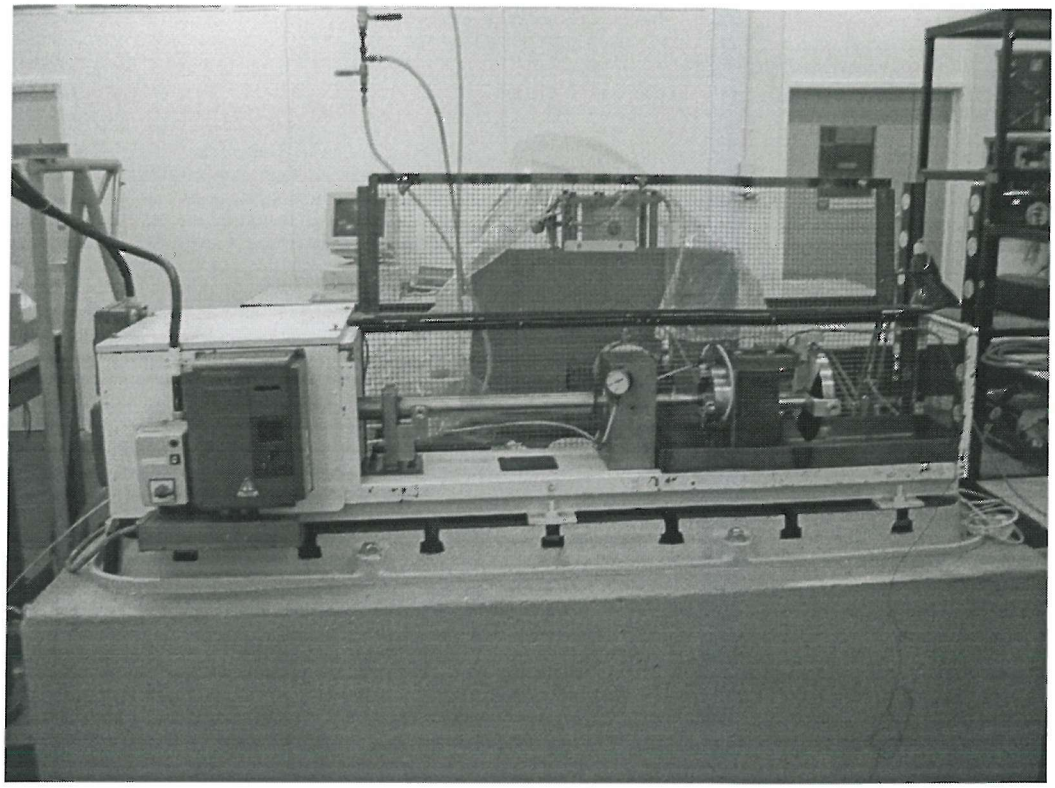

(a) general view

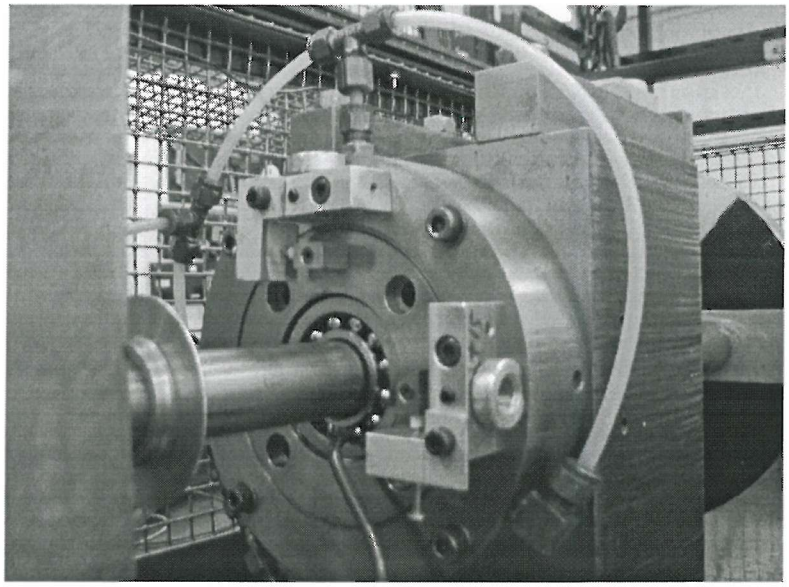

(b) view of SFD (retainer spring removed and anti-rotation bolts in place)

Figure A5.4: *Photographs of test rig B*

A6 ADDITIONAL DATA FOR RIG C

A6.1 EXPERIMENTAL MODAL ANALYSIS OF SUPPORT STRUCTURE

The instrumentation details are given in Table A6.1. In the experiments, the frequency range was 0 Hz to 800 Hz, with a resolution of 0.25 Hz.

instrument	make	serial number
impulse hammer	PCB Piezotronics Inc. Model No. 086C03	12302
voltage amplifier	PCB Piezotronics Inc. Model No. 480E09	23265
accelerometer 1	Bruel & Kjaer, type 4383	1230366
charge amplifier 1	Bruel & Kjaer, type 2635	1690255
accelerometer 2	Bruel & Kjaer, type 4383	1230368
charge amplifier 2	Bruel & Kjaer, type 2635	1690271
spectrum analyser	Hewlett Packard 35650	2911A02485

Table A6.1: *Instrumentation details for modal analysis of support structure*

The modal fitting technique is explained with respect to the receptance $\alpha_{B_1B_1}(\omega)$ (eq. (8.1a)):

$$\alpha_{B_1B_1}(\omega) \approx \frac{A_{B_1B_1}^{(Sx1)}}{\omega_{Sx1}^2 - \omega^2 + j\hat{\eta}_{Sx1}\omega_{Sx1}^2} \tag{A6.1}$$

If "LHS" denotes the left hand side of eq. (A6.1), then the Nyquist plot of LHS (i.e. the plot of Im(LHS) (on y axis) versus Re(LHS) (on x axis)) must be a circle passing through the origin with diameter inclined to the $-y$ axis by an angle $\arg\left(A_{B_1B_1}^{(Sx1)}\right)$ (anti-clockwise positive), where arg( ) is the phase of ( ) [47]. Figure A6.1(a) shows the Nyquist plot of the measurement $\alpha_{B_1B_1}(\omega)$ over the range 100 Hz to 400 Hz, where the frequency increases in the clockwise sense. It is seen that eq. (A6.1) is approximately satisfied and that $A_{B_1B_1}^{(Sx1)}$ can be taken to be real. According to [47], the undamped resonance frequency ω_{Sx1} is equal to the frequency for which the relative angular spacing of the measured data points on the Nyquist

plot is a maximum. Hence, in Figure A6.1(a), the undamped resonance is taken to be the average of the frequencies at the two points marked "*". The loss factor $\hat{\eta}_{Sx1}$ is determined from the formula

$$\hat{\eta}_{Sx1} = (\omega_2 - \omega_1)/\omega_{Sx1} \tag{A6.2}$$

where ω_1 and ω_2 are the half power point frequencies [47], displaced by 90° around the circle from the resonance point, on either side of it. In Figure A6.1(a), the data points marked with a circle and square are those closest to the positions of ω_1 and ω_2 respectively. By repeating the calculation with the circled point replaced by the preceding point as the first half power point, it is ascertained that the accuracy of the estimate for the loss factor is not significantly affected by the relatively course frequency resolution. The real modal constant $A_{B_1B_1}^{(Sx1)}$ is determined from a graph of $\mathrm{Re}(1/\alpha_{B_1B_1}(\omega))$ versus ω^2. From eq. (A6.1), this should yield a straight line of slope $-1/A_{B_1B_1}^{(Sx1)}$ and this is seen from Figure A6.1(b), where the frequency range is 100 Hz to 400 Hz. A straight line through the data points in Figure A6.1(b) is fitted by the least squares criterion using the *MATLAB*® function *polyfit*©. The modal parameters of $\alpha_{B_2B_2}(\omega)$, $\beta_{B_1B_1}(\omega)$, $\beta_{B_2B_2}(\omega)$ are found in a similar fashion.

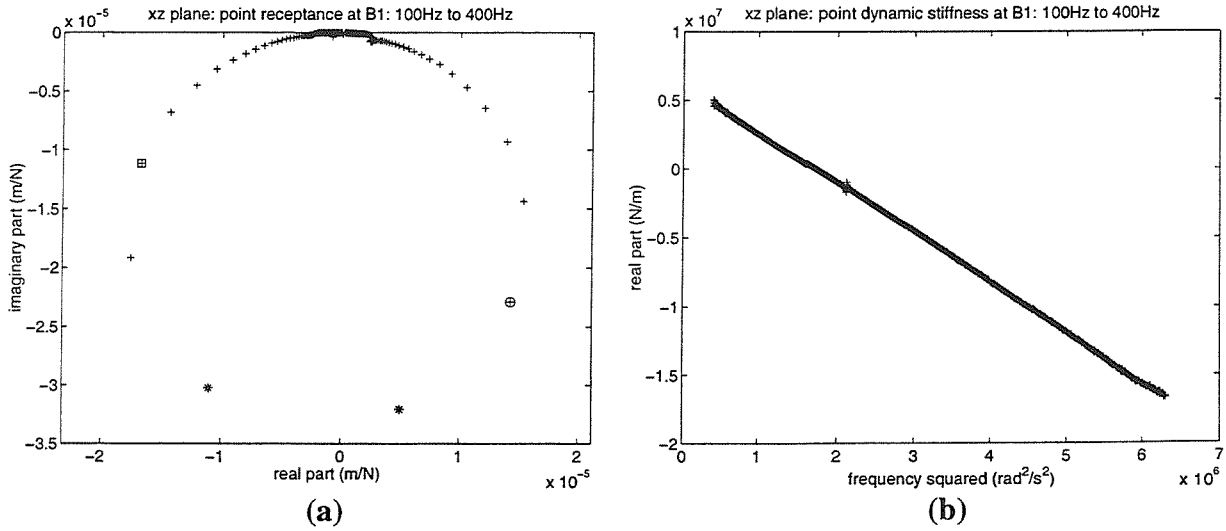

Figure A6.1: *Experimental modal analysis:* **(a)** *Nyquist plot of measured receptance* $\alpha_{B_1B_1}(\omega)$; **(b)** *plot of real part of measured dynamic stiffness* $1/\alpha_{B_1B_1}(\omega)$ *versus* ω^2

A6.2 MI MODEL OF RIG WITH SFDs LOCKED

With the SFDs locked, for each plane *xz*, *yz*, the rig reduces to a beam that is point supported at B_1 and B_2. The MI model used for the predictions in Figure 8.5 is given in Table A6.2, where the first pair of rows refers to the *xz* plane and the second pair to the *yz* plane. In this table:

- The point supports at terminals 4 and 7 are assumed to exert no restraining couple. This is an approximation since the roller bearings are not self-aligning. The stiffness values are taken from Table 8.2. The loss factors in Table 8.2 were also included in the MI model by inputting complex support stiffness values $\tilde{k}_{xB_i} = k_{xB_i}\left(1 + j\hat{\eta}_{xB_i}\right)$ and $\tilde{k}_{yB_i} = k_{yB_i}\left(1 + j\hat{\eta}_{yB_i}\right)$.
- The shaft elements were Timoshenko beam elements (Appendix A2, section A2.1) with diametral moment of inertia ignored. The diametral moments of inertia of the mass attachments were also ignored.
- The mass at each terminal 4 and 7 is the combined mass of the corresponding roller bearing and damper journal (marked (3), (4) in Figure 8.1), effective housing mass (Table 8.2) and housing end-plates.
- For the shaft elements, Young's Modulus $E = 200\times10^9$ N/m^2 and the density $\rho = 7860$ kg/m^3. The predicted rigid rotor resonances in the third row of Table 8.3 can be arrived at by setting E to a very large number in the MI model ($E \rightarrow \infty$).

terminal no.	**1**	**2**	**3**	**4 (B_1)**	**5**	**6**	**7 (B_2)**	**8**
attached mass (kg)	0.0577	0.2618		5.5577			5.4616	
support stiffness (kN/m)				6250			5680	
attached mass (kg)	0.0577	0.2618		5.4701			5.5231	
support stiffness (kN/m)				6200			5850	

shaft element	**1-2**	**2-3**	**3-4**	**4-5**	**5-6**	**6-7**	**7-8**
length (mm)	14.17	9.83	24.00	23.50	0.50	926.00	24.00
diameter (mm)	50	50	92	92	50	92	92

Table A6.2: *Mechanical impedance model in xz and yz planes with SFDs locked*

A6.3 FINAL PARAMETERS OF SUPPORT STRUCTURE

For the non-linear analysis (SFDs operational), the effective mass terms in Table 8.2 need to be increased to cover for the housing end-plates, rotor probe brackets (marked (12) in Figure 8.1) and their probes. The revised effective masses are shown in Table A6.3.

Housing 1		Housing 2	
M_{xB_1} (kg)	4.5094	M_{xB_2} (kg)	4.4158
M_{yB_1} (kg)	4.4219	M_{yB_2} (kg)	4.4773

Table A6.3: *Revised effective masses at housings*

The natural frequencies and non-zero modal constants in Table 8.1 are then revised by working backwards from eqs. (8.3) and (8.4):

$$A_{B_1B_1}^{(Sx1)} = 1/M_{xB_1}\,, \quad \ldots\ldots \text{ etc.}, \quad \omega_{Sx1} = \sqrt{K_{xB_1}/M_{xB_1}}\,, \quad \ldots\ldots \text{ etc.}$$

A6.4 INSTRUMENTATION DATA FOR ROTATION TESTS

The displacement transducers used were *Bently Nevada* 3300 *XL* 8*mm Proximitor*® probes. Their calibration was checked using a micrometer screw gauge calibrator and a digital voltmeter, as illustrated in [67], and was found to be within the manufacturer's specifications. Figures A6.2(a,b) show typical calibration diagrams. A least-squares linear fit was used to determine the sensitivities. Table A6.4 shows the sensitivities of the probes in volts per mm increment in gap.

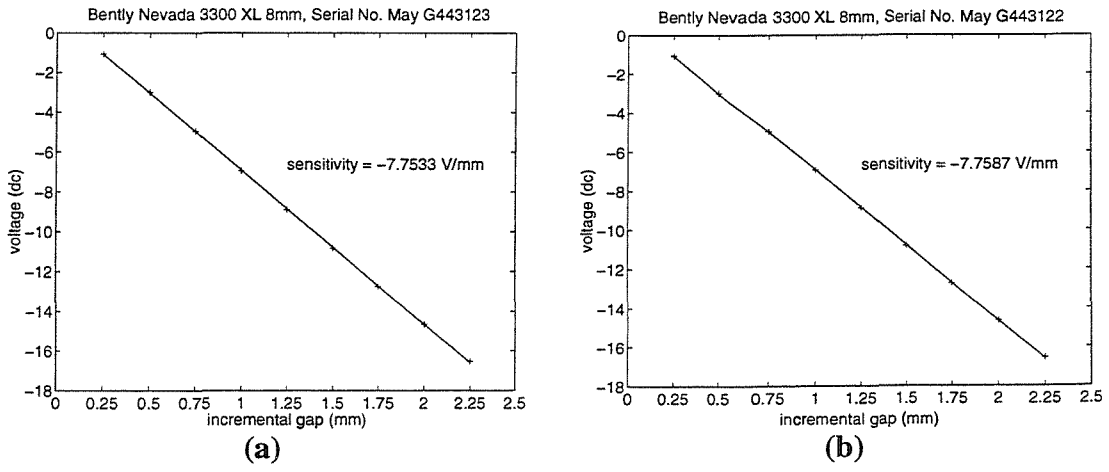

Figure A6.2: *Typical calibration diagrams for displacement transducers of rig C*

measurement location	serial no. (probe)	serial no. (amplifier)	sensitivity (V/mm)
J_{1m} rel. to B_1 (x)	May G443123	FEBG 105272	-7.7533
J_{1m} rel. to B_1 (y)	May G443122	FEBG 105244	-7.7587
J_{2m} rel. to B_2 (x)	May G443124	FEBG 105251	-7.8300
J_{2m} rel. to B_2 (y)	May G443121	FEBG 105267	-7.7600
B_1 (x)	Jul F456250	MARF 114392	-7.6970
B_1 (y)	Jul F456253	APRF 118471	-7.6870
B_2 (x)	Jul F456252	APRF 118593	-7.7750
B_2 (y)	Jul F456249	APRF 118497	-7.7613

Table A6.4: *Table of displacement transducer sensitivities for rig C*

Figure A6.3 shows a schematic of the data acquisition system. The rotor displacement probes (measuring displacements of J_{1m} and J_{2m} relative to B_1 and B_2 respectively) were set to acquire the mean component of the vibration, in addition to the alternating component. The housing displacement probes were set to acquire the alternating component of the vibration only (mean component excluded). The spectral analysers 1 and 2 (Figure A6.3) used to capture the vibration time histories were *Hewlett Packard* 35650® with serial numbers 2911A02485, 2911A01033 respectively.

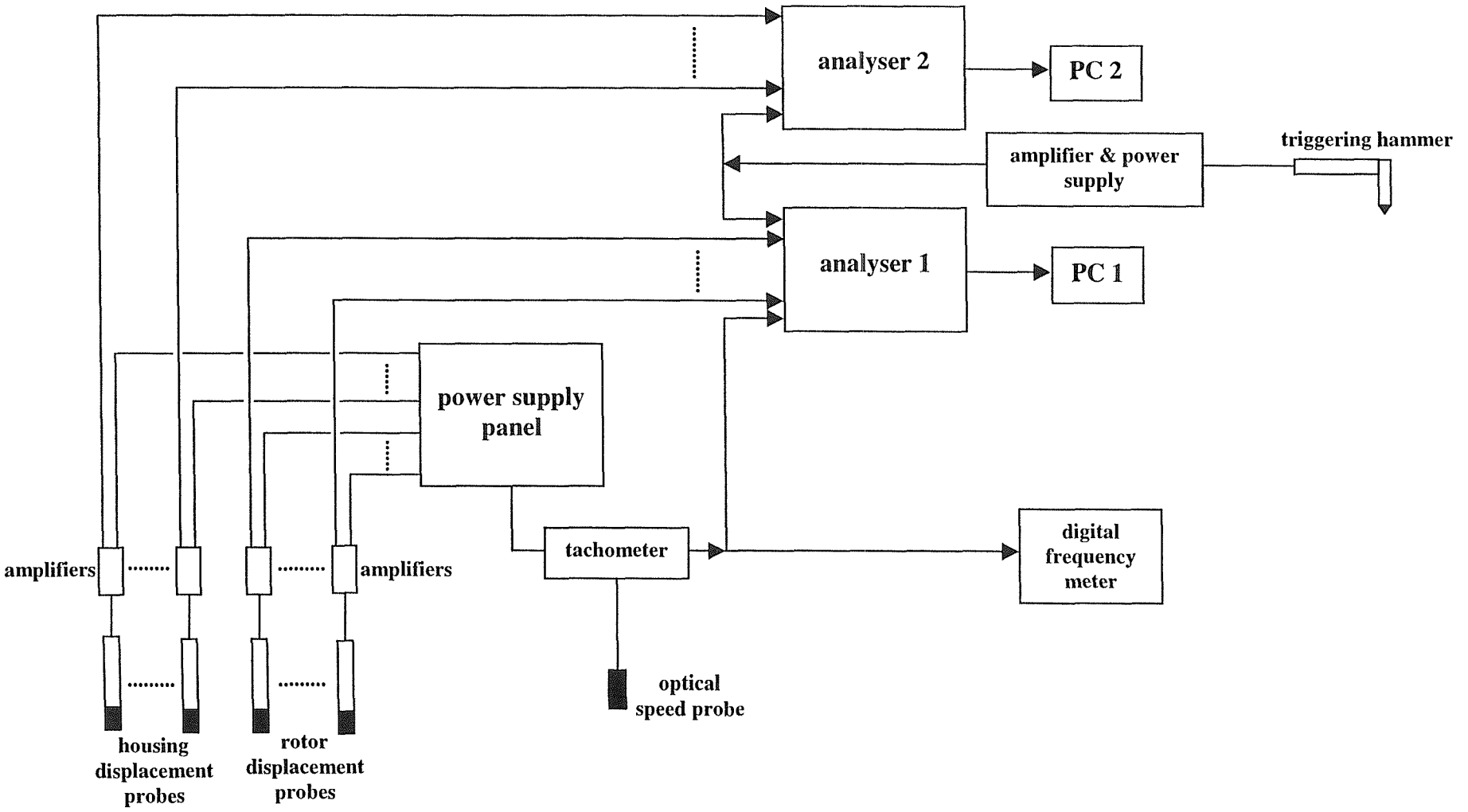

Figure A6.3: *Schematic of data acquisition system for test rig C*

A6.5 WATERFALL DIAGRAMS (*x* direction)

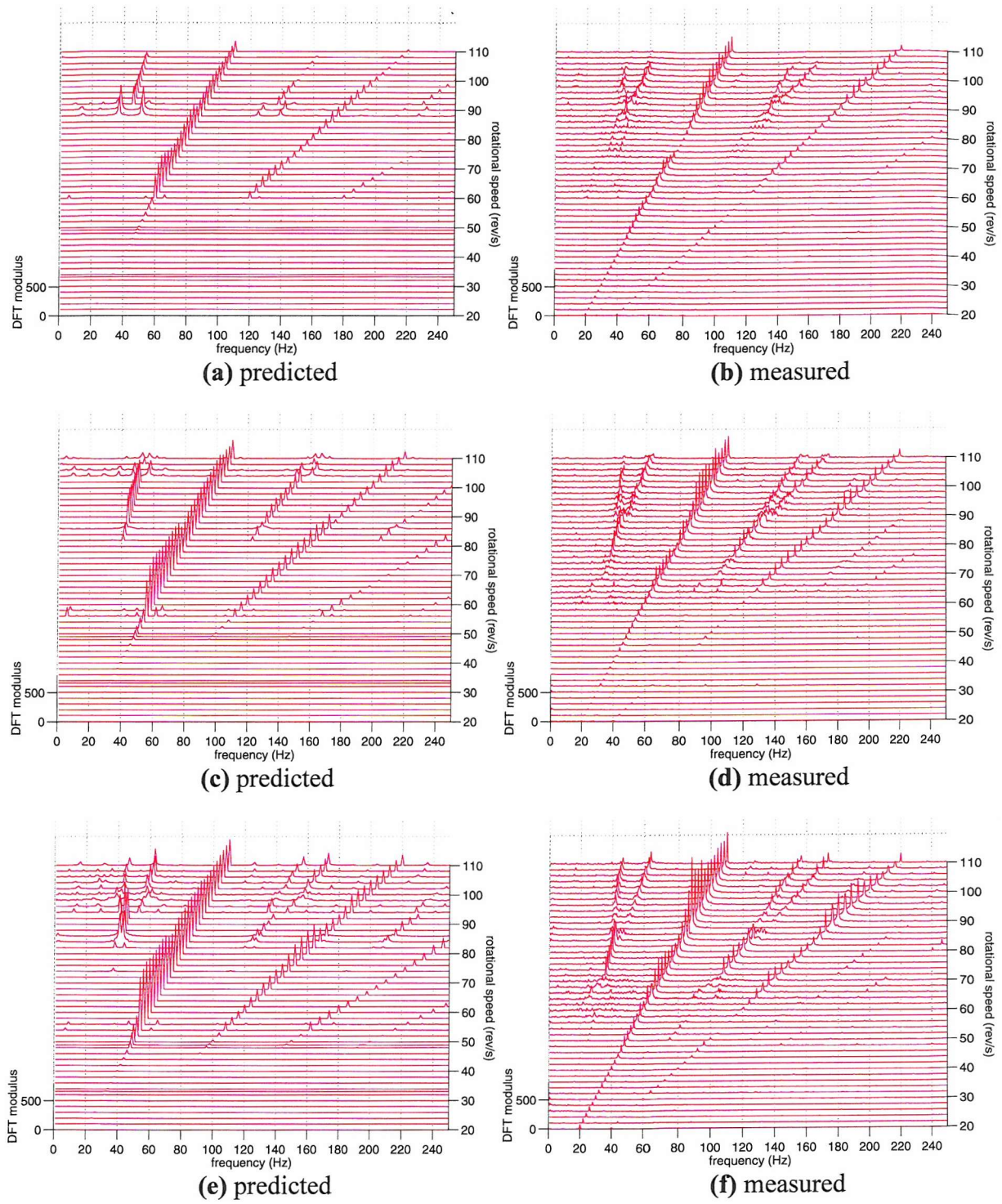

Figure A6.4: *Waterfall diagrams of the frequency spectra of the x displacement response of* J_{1m} *relative to* B_1 *for three states of unbalance* (first three rows of Table 8.4: **(a)**, **(b)** row 1; **(c)**, **(d)** row 2; **(e)**, **(f)** row 3). Data length: 1 s for predictions, 2 s for measurement.

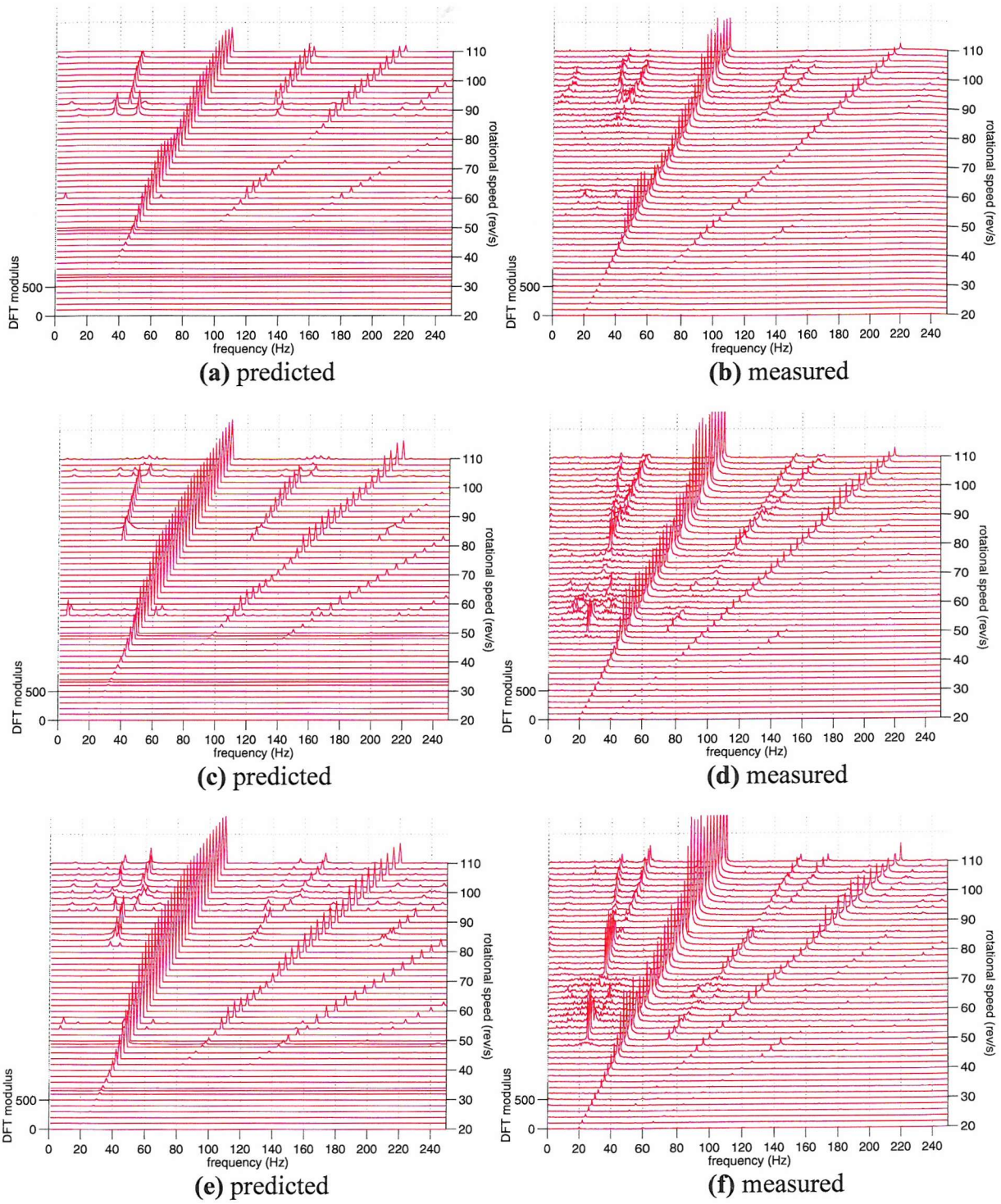

Figure A6.5: *Waterfall diagrams of the frequency spectra of the x displacement response of* J_{2m} *relative to* B_2 *for three states of unbalance* (first three rows of Table 8.4: **(a)**, **(b)** row 1; **(c)**, **(d)** row 2; **(e)**, **(f)** row 3). Data length: 1 s for predictions, 2 s for measurement.

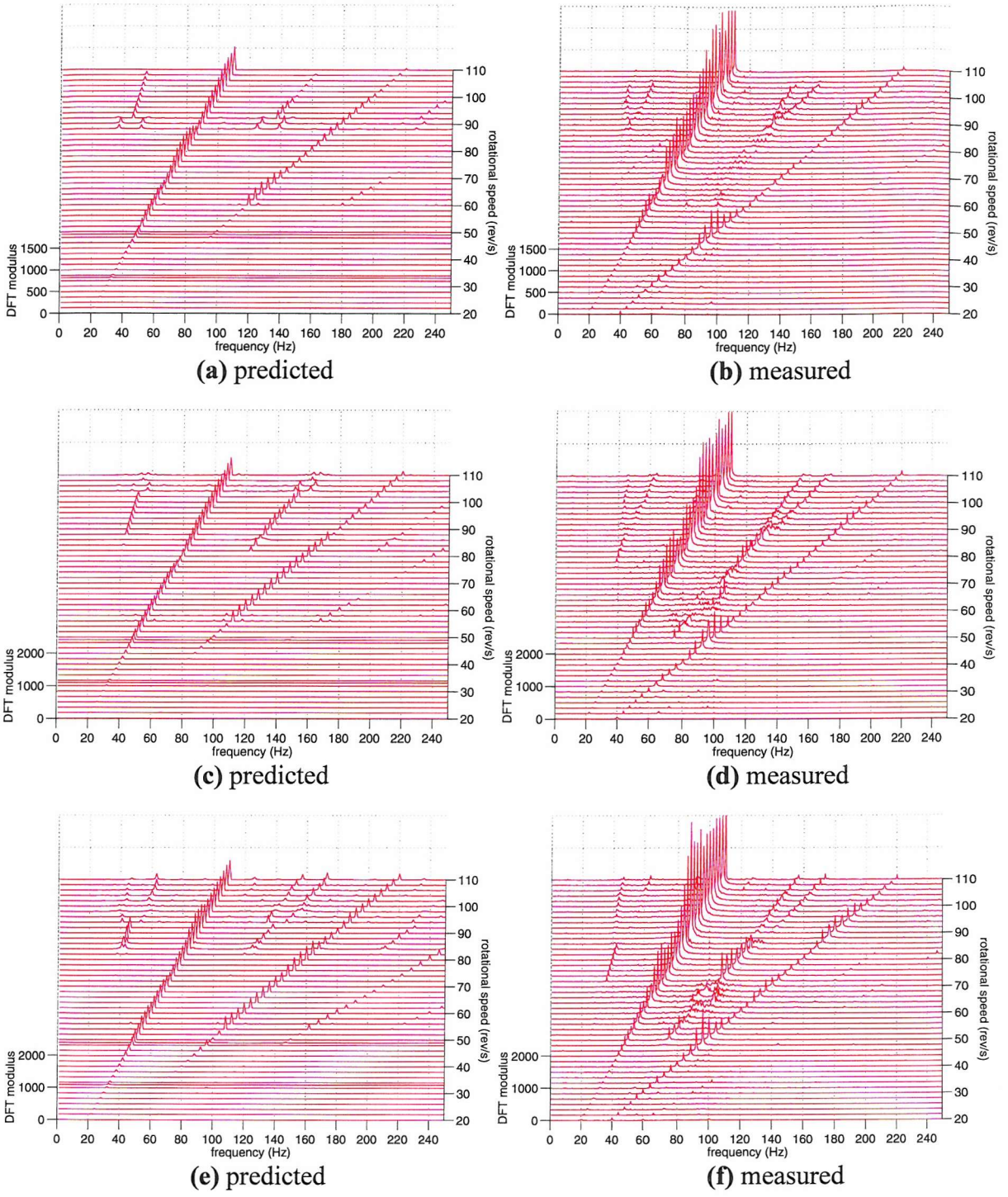

Figure A6.6: *Waterfall diagrams of the frequency spectra of the x displacement response of* B_1 *for three states of unbalance* (first three rows of Table 8.4: **(a)**, **(b)** row 1; **(c)**, **(d)** row 2; **(e)**, **(f)** row 3). Data length: 1 s for predictions, 2 s for measurement.

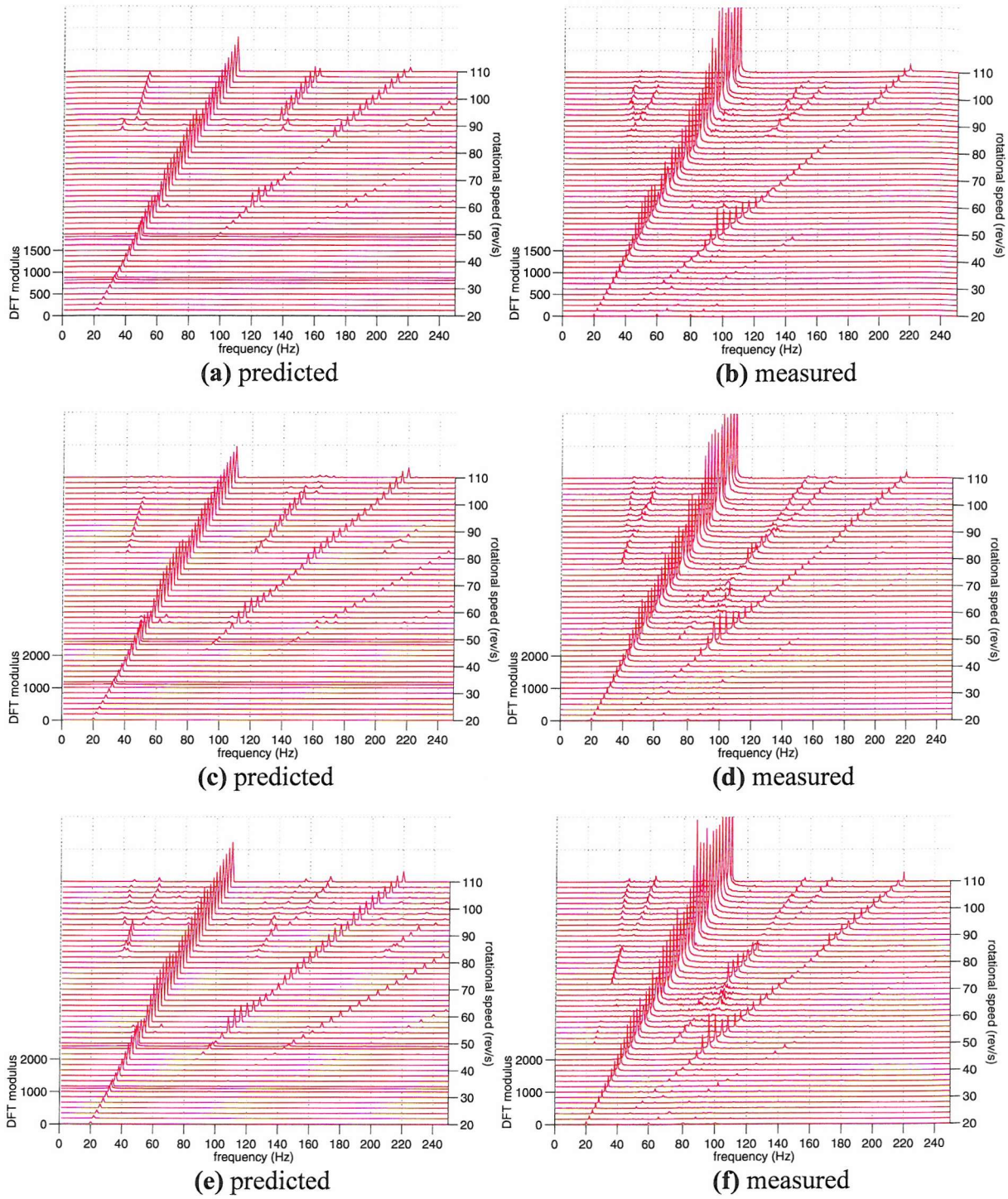

Figure A6.7: *Waterfall diagrams of the frequency spectra of the x displacement response of* B_2 *for three states of unbalance* (first three rows of Table 8.4: **(a)**, **(b)** row 1; **(c)**, **(d)** row 2; **(e)**, **(f)** row 3). Data length: 1 s for predictions, 2 s for measurement.

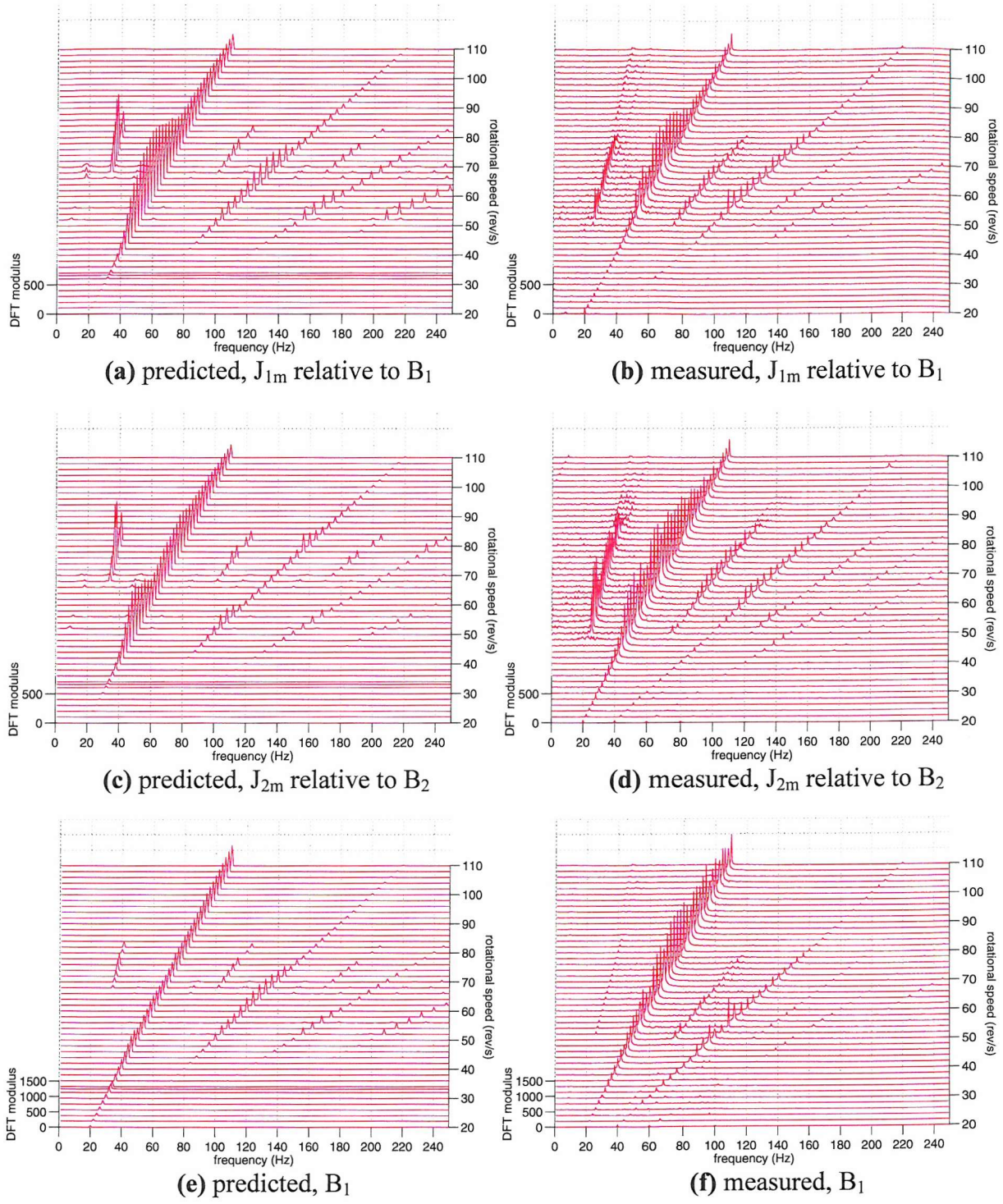

(a) predicted, J_{1m} relative to B_1

(b) measured, J_{1m} relative to B_1

(c) predicted, J_{2m} relative to B_2

(d) measured, J_{2m} relative to B_2

(e) predicted, B_1

(f) measured, B_1

Figure A6.8: *Waterfall diagrams of the frequency spectra of the x displacement response for symmetrical unbalance* (last row of Table 8.4). Data length: 1 s for predictions, 2 s for measurement. (Figure continues on the following page)

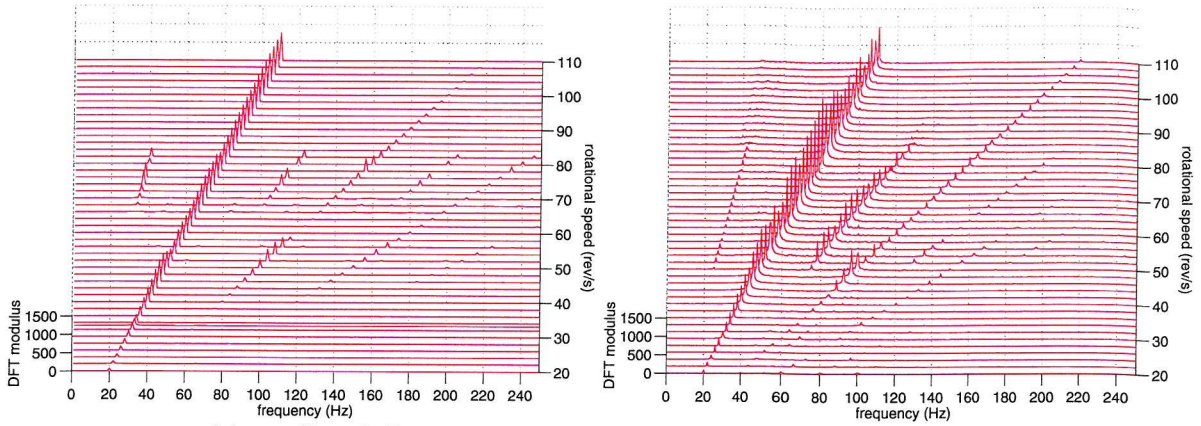

(e) predicted, B_2 **(f)** measured, B_2

Figure A6.8 (continued): *Waterfall diagrams of the frequency spectra of the x displacement response for symmetrical unbalance* (last row of Table 8.4). Data length: 1 s for predictions, 2 s for measurement.

A6.6 PHOTOGRAPHS OF TEST RIG C

Figure A6.9 (following page) shows photographs of the test rig for configuration C.

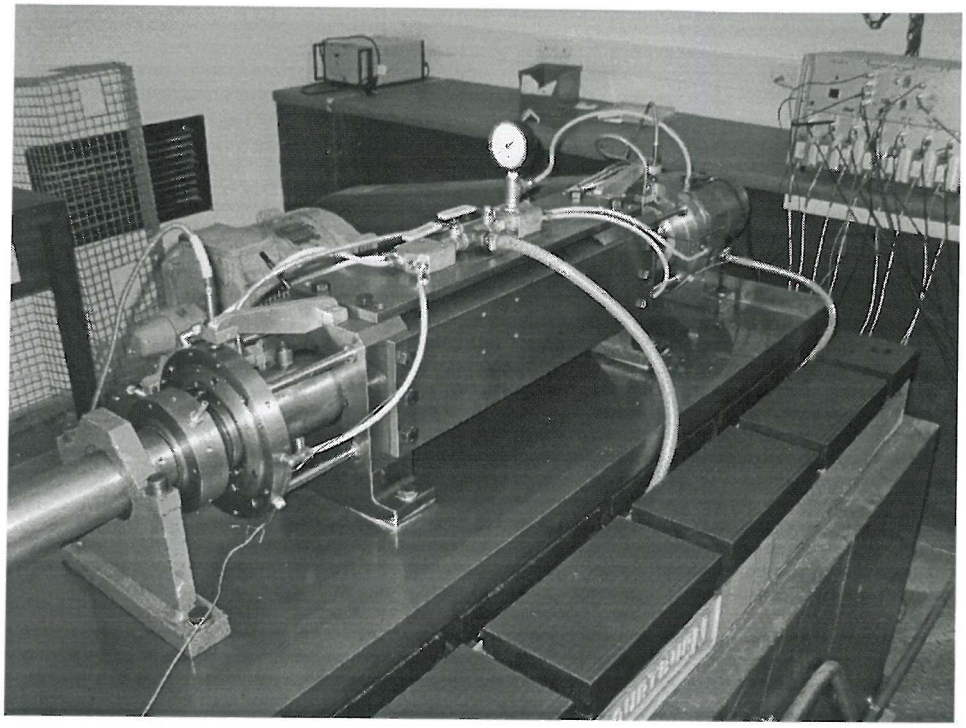

(a) general view (non-rotating "HP" rotor at near end)

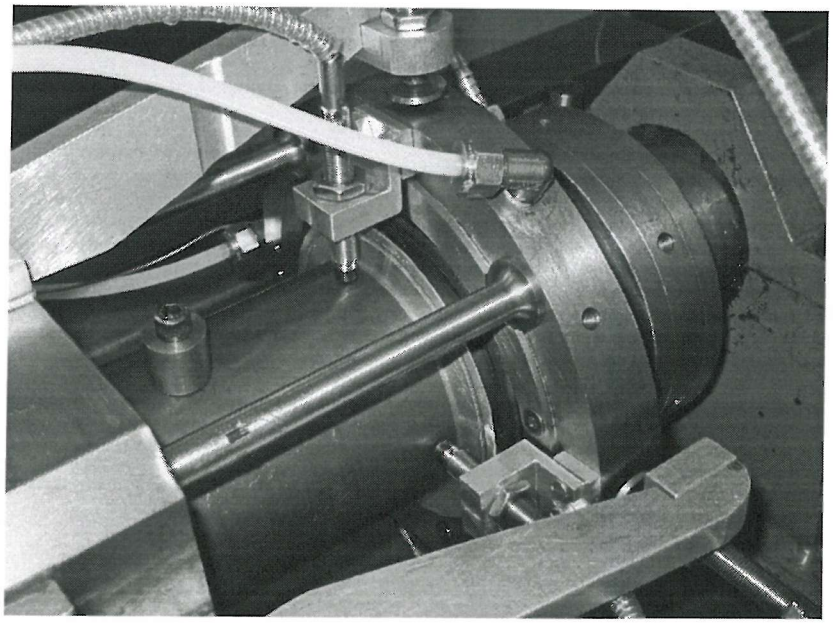

(b) view of the SFD at the right hand end in Figure 8.1

Figure A6.9: *Photographs of test rig C*